Laser-Induced Electron Tunneling and Diffraction

Dissertation
zur Erlangung des Doktorgrades
der Naturwissenschaften

vorgelegt beim Fachbereich Physik
der Johann-Wolfgang-Goethe-Universität
in Frankfurt am Main

von
Moritz Meckel
aus Frankfurt

Frankfurt 2011

(D30)

Vom Fachbereich Physik der

Johann Wolfgang Goethe - Universität als Dissertation angenommen.

Dekan: Prof. Dr. M. Huth

Gutachter: Prof. Dr. R. Dörner, Prof. Dr. H. Schmidt-Böcking

Datum der Disputation:

Summary

The work in hand explores the ionization of nitrogen and oxygen molecules in strong, off-resonant laserlight pulses. The three-dimensional momentum vectors of electrons and ions were measured by means of a so-called COLRIMS spectrometer.

The main interest was aimed at the ionization channel leading to stable molecular single ions (N_2^+ / O_2^+). Due to the absence of dissociations, one cannot use the flight directions of ionic fragments to infer the orientation of the molecular axis prior to ionization. In order to access the dependence of the ionization process on the angle between the molecular axis and the polarization of the ionizing light pulse, one has to actively control the alignment of the molecule in the laboratory frame.

In order to achieve this, a technique called "non-adiabatic molecular alignment" [1] was applied. A first, relatively weak light pulse provided for the alignment. A second, highly intense pulse subsequently ionized the aligned molecules.

In a first experiment, momentum distributions of electrons were measured for two different distributions of molecular axes. Comparison between these cases yielded two main results:

1. In the region of low momentum in the directions perpendicular to the ionizing pulse polarization, the "fingerprint" of the ionized orbital is revealed.

2. At higher electron momenta, structures were observed which can be explained as double-slit diffraction. After being freed, an electron propagates in the oscillating electric field caused by the intense light. It may be driven back to its parent ion and "re-scatter" [2]. We consider the case of elastic re-scattering. In a rough approximation, the constituents of the diatomic ion act like a double-slit, diffracting the electron wave.

In a second, very similar experiment, the direction of alignment was rotated step-by-step. Both the effects of electrons diffracting from their parent ions and - with limitations - the trace of the ionized orbital were observed once again.

The latter is determined by a projection of the orbital in momentum space in the directions perpendicular to the polarization of the ionizing light [3, 4]. Hence, the measurements of the patterns under different alignment angles corresponds to a recording of different projections. The obtained dataset was intended for a tomography-type reconstruction of the orbital's electron density distributions. Work by collaborators in this direction is in progress.

The observed diffraction of the re-scattered electron makes it possible to infer the positions of the nuclei within the molecular ion. There is some hope information on the scattering potential beyond the simple double-slit model can be extracted in the future. On the other hand, re-scattering of more energetic electrons should enable an improved spatial resolution.

Both pieces of information, orbital and diffraction image of the ion, are obtained simultaneously in one measurement. Temporal resolution is solely determined by optical parameters (light wavelength and pulse length). It can be improved to the region of one femtosecond or below by application of ultrashort, phase-stabilized light pulses.

Zusammenfassung

In der vorliegenden Arbeit wird die Ionisation von Stickstoff- und Sauerstoff-Molekülen in starken, nicht-resonanten Laserlicht-Pulsen untersucht. Die dreidimensionalen Impulsvektoren der freigesetzten Elektronen und Ionen wurden mittels eines sogenannten COLTRIMS Spektrometers vermessen.

Das Hauptaugenmerk galt dem Kanal der Einfachionisation, der ein stabiles Molekülion (N_2^+ / O_2^+) erzeugt. Da in diesem Fall keine Dissoziation des Ions stattfindet, kann nicht aus der Flugrichtung ionischer Fragmente auf die Ausrichtung der Molekülachse geschlossen werden. Die Abhängigkeit des Prozesses vom Winkel zwischen der Molekülachse und der Polarisationsrichtung des ionisierenden Lichtes ist nur dann zugänglich, wenn die Ausrichtung der Molekülachsen vor dem Zeitpunkt der Ionisation aktiv kontrolliert werden kann.

Hierzu wurde die Technik der "nichtadiabatischen Molekülausrichtung" ("nonadiabatic molecular alignment") [1] angewandt. Ein erster, mäßig intensiver Lichtpuls bewirkte die Ausrichtung der Molekülachsen im Laborsystem. Sodann wurden die ausgerichteten Moleküle von einem zweiten, hochintensiven Puls ionisiert.

In einem ersten Experiment wurden Elektronen-Impulsverteilungen für zwei verschiedene Molekülausrichtungen bestimmt. Ein Vergleich der Verteilungen brachte zwei wichtige Ergebnisse:

1. Im Bereich niedriger Elektronen-Impulse senkrecht zur Polarisationsrichtung des ionisierenden Lichtpulses wird der "Fingerabdruck" des ionisierten Molekülorbitals sichtbar.

2. Bei höheren Impulsen zeigten sich Strukturen, die als Doppelspalt-Interferenz interpretiert werden können. Ein ionisiertes Elektron propagiert im oszillierenden elektrischen Feld des Laser-Pulses. Von diesem kann es auf das Ion hin zurück beschleunigt werden und dort streuen[2]. Wir betrachten den Fall elastischer "Rückstreuung". In erster Näherung wirken die Bestandteile des diatomaren Molekülions wie ein Doppelspalt, an dem die streuende Elektronen-Welle gebeugt wird.

In einem zweiten, dem ersten sehr ähnlichen Experiment wurde die Molekülausrichtungs-Richtung in kleinen Schritten variiert. Sowohl der Effekt der Elektronenbeugung am Ion, als auch - mit Einschränkungen - die Abbildung des ionisierten Orbitals wurde erneut beobachtet.

Letztere ist durch eine Projektion des Orbitals in den Impulsraum senkrecht zur Laser-Polarisationsrichtung bestimmt [3, 4]. Die Messung der Strukturen

unter verschiedenen Molekül-Ausrichtungen im zweiten Experiment entspricht daher der Aufnahme verschiedener Projektionen des Orbitals. Der so gewonnene Datensatz sollte prinzipiell eine Rekonstruktion der dreidimensionalen Elektronen-Dichteverteilung des ionisierten Molekülorbitals mittels eines Tomographie-Algorithmus ermöglichen. Entsprechende Entwicklungen sind bei Kooperationspartnern im Gange.

Die beobachtete Beugung des rückgestreuten Elektrons ermöglicht den Rückschluss auf die Positionen der Kerne im Molekülion. Es besteht die Hoffnung, dass sich in Zukunft detailliertere Informationen über das streuende Potential jenseits des einfachen Doppelspalt-Modells gewinnen lassen. Rückstreuung höherenergetischer Elektronen sollte hingegen eine verbesserte Ortsauflösung ermöglichen.

Beide Informationen - Ionisiertes Orbital und Beugungsbild des Ions - werden simultan in ein- und derselben Messung gewonnen. Die zeitliche Auflösung wird durch rein optische Parameter (Licht-Wellenlänge, Pulslänge) determiniert. Sie kann mittels ultrakurzer, phasenstabiler Laserlicht-Pulse in den Bereich einer Femtosekunde oder darunter verbessert werden.

Contents

Abbreviations and Symbols

Unless otherwise specified, abbreviations and formula symbols have the meaning assigned below. S stands for "Something" to illustrate properties assigned only to symbols.

Symbol	Meaning / Reading
$\hat{S}$	"S Peak": Maximum value of S
$\vec{S}$	S is a vector, usually three-dimensional.
S_x	x component of vector $\vec{S}$, o.d.a.
φ_{xy}	Azimuth angle in xy plane. $\varphi_{xy} = 0 \Rightarrow$ along x axis, o.d.a.
φ_{yx}	Azimuth angle in xy plane. $\varphi_{yx} = 0 \Rightarrow$ along y axis, o.d.a.
ϑ_z	Polar angle with z axis, o.d.a.
γ	Keldysh parameter as defined in equation (2.3).
τ	FWHM of a light pulse.
ω	Unless otherwise stated: Carrier frequency of laser light
ATI	Above Threshold Ionization; cf. chapter 2.2.1.
a.u.	Atomic units
B	Magnetic field
d	Distance, e.g. between slits, atoms, ...
E	Electric field
$FWHM$	Full width at half maximum
HOMO	Highest occupied molecular orbital
I	Intensity
I_P	Ioinization potential (for single ionization unless stated otherwise)
o.d.a.	"Other directions accordingly."
p	Momentum
$p_{\parallel}$	Momentum parallel to ionizing laser polarization (z axis)
$p_{\perp}$	Momentum perpendicular to ionizing laser polarization (z axis)
t	Time
TOF	Time of flight
U_P	Ponderomotive potential as defined in equation (2.15)
V	Electrostatic potential
v	Velocity
W	Energy

Atomic Units

Dimension	Formula	SI Units
Mass	m_e	$9.10938 \cdot 10^{-31}$ kg
Charge	q_e	$1.60218 \cdot 10^{-19}$ C
Length	a_0	$5.29177 \cdot 10^{-11}$ m
Velocity	v_0	$2.18769 \cdot 10^{6}$ m s^{-1}
Time	a_0/v_0	$2.41888 \cdot 10^{-17}$ s
Momentum	$m_e v_0$	$1.99285 \cdot 10^{-24}$ kg m s^{-1}
Angular Momentum	$\hbar = a_0 m_e v_0$	$1.05457 \cdot 10^{-34}$ kg m^2 s^{-1}
Frequency	$v_0/(2\pi a_0)$	$6.57969 \cdot 10^{15}$ Hz
Angular Frequency	v_0/a_0	$4.13414 \cdot 10^{16}$ Hz
Energy	$q_e^2/(4\pi\epsilon_0 a_0)$	27.2116 eV = 1 hartree
Action	$\hbar = q_e^2/(4\pi\epsilon_0 v_0)$	$1.05457 \cdot 10^{-34}$ J s
Electric Field	$q_e/(4\pi\epsilon_0 a_0^2)$	$5.14221 \cdot 10^{11}$ V/m
Magnetic Field	$\hbar/(q_e a_0^2)$	$2.35052 \cdot 10^{5}$ T
Intensity	$1/2\ c\epsilon_0(q_e/(4\pi\epsilon_0 a_0^2))^2$	$3.50953 \cdot 10^{16}$ W/cm^2

Constant	Formula	SI Units	Atomic units
Planck's Constant	h	$6.62608 \cdot 10^{-34}$ J s	2π
Dirac Constant	$\hbar$	$1.05457 \cdot 10^{-34}$ J s	1
Elementary Charge	q_e	$1.60218 \cdot 10^{-19}$ C	1
Electron Mass	m_e	$9.10938 \cdot 10^{-31}$ kg	1
Proton Mass	m_p	$1.67262 \cdot 10^{-27}$ kg	1836.15
Atomic Mass Unit	$amu = \frac{1}{12}m(^{12}C)$	$1.66054 \cdot 10^{-27}$ kg	1822.89
Velocity of Light	c	$2.99792 \cdot 10^{8}$ m/s	137.04
Influence Constant	ϵ_0	$8.85419 \cdot 10^{-12}$ As/(Vm)	$1/(4\pi)$
Induction Constant	$\mu_0 = 1/(c^2\epsilon_0)$	$4\pi \cdot 10^{-7}$ Vs/(Am)	$4\pi/137.04^2$

Based on [5].

1. Introduction

Molecules are the entities connecting all of the three natural sciences. Biology is composed of them and molecular biology deals with them in particular. In chemical synthesis, the formation and destruction of molecules is explored, employed and optimized. Molecular physics and physical chemistry / spectroscopy have a large area of overlap. Here the structure of molecules and the nature of their bonds is either determined experimentally or theoretically modeled.

Electrons are the glue holding the atomic constituents of a molecule in place. They are organized into molecular orbitals. To fully characterize the state of a molecule one has to know know about both the positions of the nuclei and the orbitals occupied by the electrons. The same is true during a chemical reaction but with the complication of the parameters changing. Time becomes a crucial factor. Making "reaction movies" has been a dream ever since. We found a technique that is able to access both of the desired observables in a very direct manner.

A common technique for the determination of structure is diffraction. Here, a sample is bombarded with a beam of photons, electrons, or even neutrons. Structural information is (i.e. the positions of the nuclei are) reconstructed from the pattern imprinted on the projectiles by the interaction with the sample. The spatial resolution of this method is, in principle, only limited by the DeBroglie wavelength of the projectile applied. However, timing information in the order required for watching reactions is not provided by conventional diffraction techniques.

Currently two different approaches are pursued to overcome this deficit. On the one hand, X-ray free electron lasers (XFELs) are becoming operational. These will provide high-intensity, sub-100 fs pulses of high-energy photons, promising a wealth of new opportunities for time-resolved measurements. First results are encouraging[1]. On the down side, XFELs are expensive large-scale facilities. They leave significant space for smaller, less costly alternatives.

Such an alternative may be diffraction with ultrashort electron bunches. A technique where bursts of electrons are released from a cathode by pulses of laser light and then accelerated towards a separate sample has been termed "ultrafast electron diffraction" (UED) and applied to some molecular systems [7]. However, this technique is experimentally challenging. The generation of electron bunches of a duration down to a value 15 as (attoseconds, 10^{-18} s) has been reported [8].

---

[1]The (static) imaging of a large biomolecule by means of XFEL radiation with 8.5 Å resolution has been reported very recently [6].
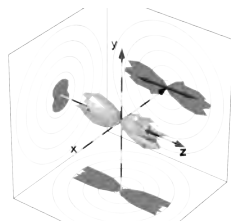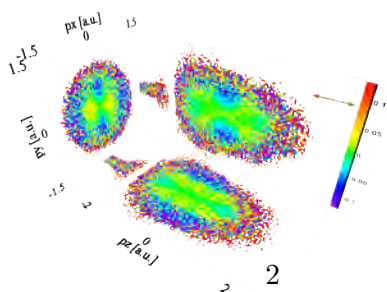
The achievement of a timing resolution in this order of magnitude in an actual diffraction experiment is still pending.

A third way towards time-resolved diffraction imaging of molecules has been proposed by theory [9, 10]. In this scheme, the sample serves as its own photocathode. We provided the first experimental proof of this concept in [11]. This is also a major topic of the work in hand.

Another interesting property of a molecule is the shape of its electron cloud. In the case of solids and molecules adsorbed on a surface, this can be traced out as a tunneling current with a scanning tip microscope (STM). The second aspect of our findings closely relates to this. We will "scan" and measure a tunneling current, too, but in the gas phase and yielding some extra information.

In our experiments, we did not resolve time. Nevertheless, all steps determining temporal resolution are of a purely optical nature. Therefore the route towards time resolution on the order of femtoseconds (1 fs = 10^{-15} s) seems straightforward.

This work emerged in the context of a collaboration between the "Atom" group at the Institut für Kernphysik, J. W. Goethe Universität Frankfurt, Germany (Prof. R. Dörner) and the "Atto" group of the Steacie Institute for Molecular Sciences, National Research Council (NRC), Ottawa, Canada (Prof. P. B. Corkum). All data were taken in Ottawa using a spectrometer developed and built in Frankfurt.

Finally a hint for all those who cannot wait to learn about the flip-book feature of the work in hand: It is explained in chapter 5.2.3 (page 120).
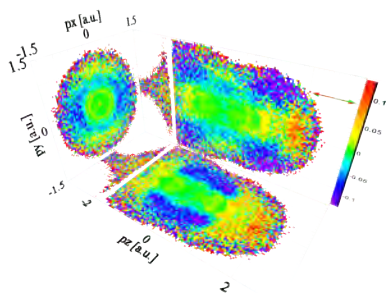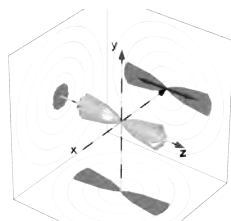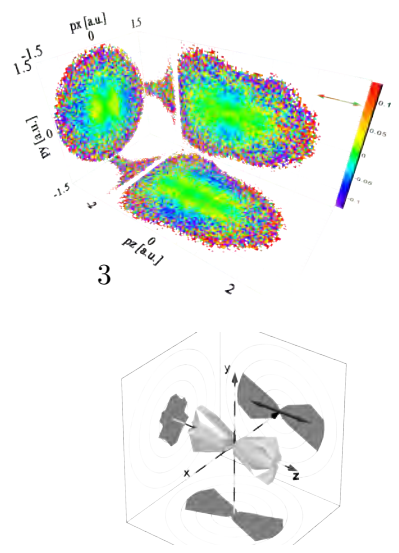
2. Background

This chapter compiles some facts of importance with regard to the understanding of the experiments presented later in this work. It is organized into six sections. After recalling the properties of ultraintense light, we will explore how an electron can be freed from an atom or molecule by this kind of radiation. In section 2.3, a brief discussion of the electron's motion after being ionized will follow. We will see that the electron may, under certain conditions, re-encounter with its parent ion and "re-scatter". Therefore, a brief discussion of of electron-molecule scattering will ensue in section 2.4. We will then review some effects in re-scattering, mostly concentrating on the case of elastic re-scattering. And finally, we will give an introduction to the technique used in the experiment to control the orientation of molecular axes in section 2.6.

2.1. Ultraintense Laserlight Pulses

This work is about the interaction of ultraintense pulses of laser light. But what is ultraintense light, actually?

2.1.1. The Wave Picture

In the classical picture, light is treated as an electromagnetic wave [12]. Neglecting the magnetic component, we can describe a light pulse by its oscillating electric field

$$E(t) = E_0(t) \cdot \cos(\omega t + \varphi_{CE}). \tag{2.1}$$

$E_0(t)$ is the pulse's envelope, $\omega = 2\pi \frac{c}{\lambda}$ its carrier frequency and φ_{CE} the so-called *carrier-envelope* (CE) *phase*. The envelope can be, for example, of Gaussian shape, i.e.

$$E_0(t) = \hat{E}e^{-\frac{t^2}{2\sigma^2}} \tag{2.2}$$

with $\sigma = \tau/\sqrt{8 \cdot \ln 2}$ being the Gaussian's standard deviation, whereas τ is its full width at half maximum, usually referred to as pulse length. The peak electric
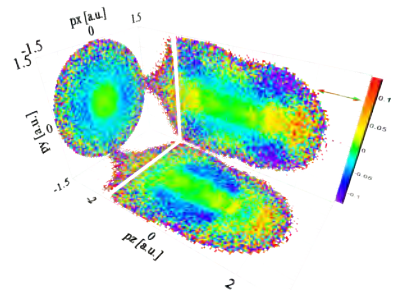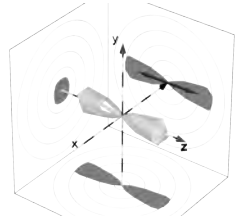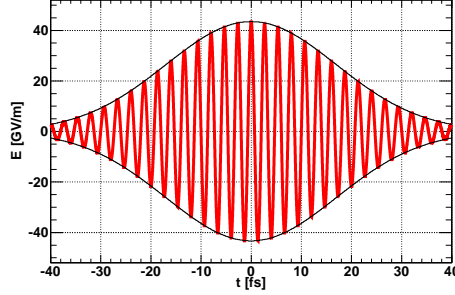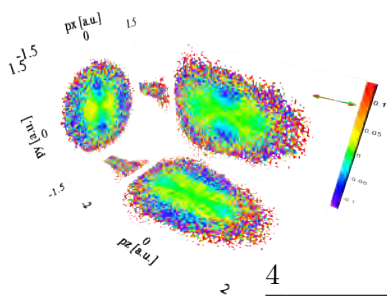
Figure 2.1.: Electric field of a typical $\lambda = 800$ nm, linearly polarized pulse as used in the experiment: $\hat{I} = 2.5 \cdot 10^{14}\ \frac{\text{W}}{\text{cm}^2}$, leading to a peak electric field of $\hat{E} = 43 \cdot 10^9\ \frac{\text{V}}{\text{m}}$. Gaussian envelope with a width of $\tau = 40$ fs.

field at peak intensity $\hat{I}$ is

$$\hat{E} = \sqrt{\frac{2\hat{I}}{c\epsilon_0}}.$$

In the experiments, we used peak intensities of $\hat{I} \sim 10^{14}\ \frac{\text{W}}{\text{cm}^2}$ at a pulse length of $\tau \approx 40$ fs and a carrier wavelength of $\lambda = 800$ nm. The electric field of a typical pulse is graphed in figure 2.1. This field will loosely be called "laser field" in the following.

The carrier-envelope phase plays no role at the pulse length we are going to in the experiments. For many considerations it is also sufficient to assume a constant pulse envelope:

$$E_0(t) = \hat{E} = const.; \qquad \varphi_{CE} = 0.$$

We will refer to this case as the continuous wave or *CW approximation*.

2.1.2. The Photon Picture

Alternatively, light can be described as a current of photons, each carrying the energy

$$W_{Ph} = h \cdot \frac{c}{\lambda} = \hbar\omega$$

with h being Planck's constant, $\hbar = h/2\pi$ Dirac's constant and c being the speed of light.

2.2. Photoionization in Ultraintense Laserlight Pulses

The photon picture is usually applied to describe "conventional" photoionization. In that case, exactly one photon couples to an electron. The latter can be released only if W_{Ph} is at least equal to the ionization potential (I_p) of the system.
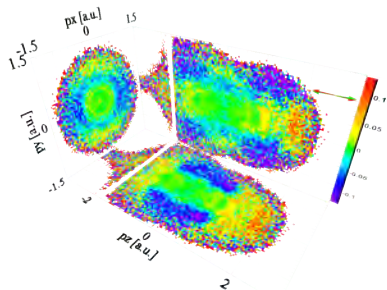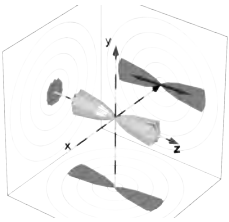
2.2.1. Multiphoton Ionization / ATI

However, if one exposes an atom or molecule to an ultraintense pulse of long-wavelength light, i.e. an extreme density of low-energy photons, it can absorb multiple light quanta and ionize although the energy of a single photon would be insufficient. The resulting electron energy spectra show distinct peaks separated by the energy of one photon. An intuitive explanation is that n photons are absorbed, transferring an energy of $n \cdot W_{Ph}$ into the system. If this more energy than needed to free an electron from the binding potential (a process referred to as *above threshold ionization*, or *ATI*), the excess energy

$$W_{e^-_{ATI}} = n \cdot W_{Ph} - I_P - W_{Stark}$$

will be carried by the electron. Here, W_{Stark} is a Stark shift induced by the laser field.

A classic review of quantitative ATI models and experimental tests thereof can be found in [13], while [14] is recent.

2.2.2. Tunneling Ionization

If intensity is further increased, the ATI peaks in a photoelectron energy spectrum get blurred and finally vanish. A different model of ionization becomes appropriate: The *tunneling picture*. Light can now be described as an electromagnetic wave.

The electrostatic potential binding the outermost electron of a neutral, unperturbed atom can be approximated as a Coulomb potential

$$V_C(r) = -\frac{q_e^2}{4\pi\epsilon_0}\frac{1}{|r|}.$$

The electron is trapped by this potential at the altitude corresponding to its ionization potential (see illustration in figure 2.2(a)). The oscillating electric field caused by the intense light superposes with it, leading to a time-dependent total potential of

$$V_{tot}(r,t) = -\frac{q_e^2}{4\pi\epsilon_0}\frac{1}{|r|} - q_e \cdot r \cdot E(t),$$

showing a barrier which can be tunneled through by the electron. This is illustrated by figure 2.2(b). At sufficient intensity, the laser-induced potential at its maximum can completely suppress the barrier, leading to *over barrier ionization* (OBI, figure 2.2(c)).

2.2.3. The Keldysh Parameter

In order to give a quantitative criterion which one of the above pictures applies, *Keldysh* defined the parameter [15]
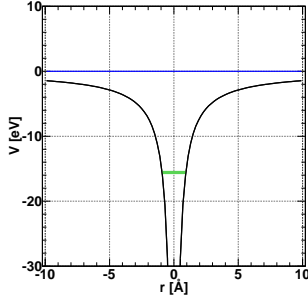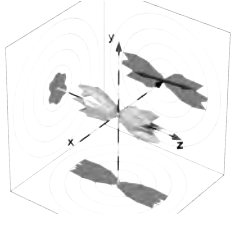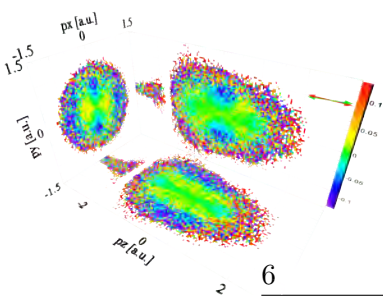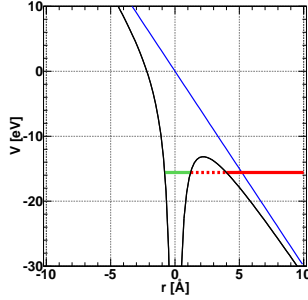
$$\gamma := \sqrt{\frac{I_P}{2U_P}} \tag{2.3}$$
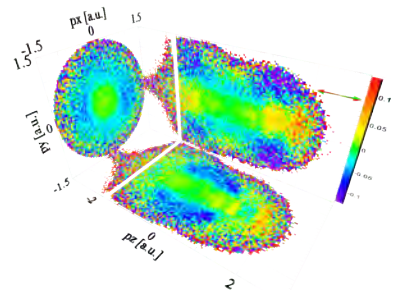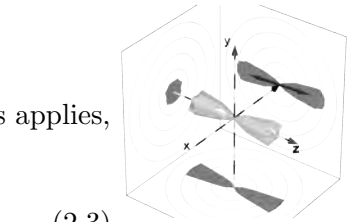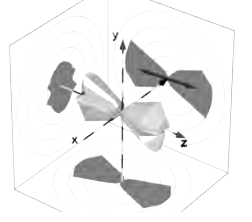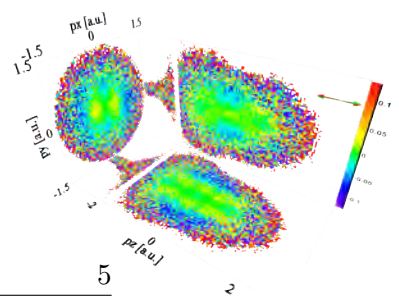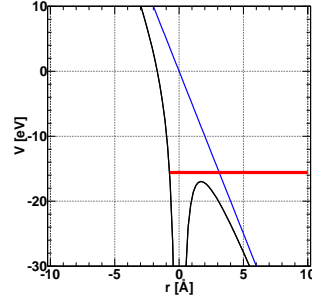
(a) $E = 0 \; \frac{V}{m}$ (b) $E = 30 \cdot 10^9 \; \frac{V}{m}$ (c) $E = 50 \cdot 10^9 \; \frac{V}{m}$

Figure 2.2.: Illustration of tunneling ionization of N_2. (a): The outermost electron is symbolized by a green line drawn in an unperturbed Coulomb potential (*black* curve) at the value corresponding to the ionization potential of N_2 ($I_p = 15.6$ eV). (b): An external electric field of $E = 30 \cdot 10^9 \; \frac{V}{m}$ is applied. The corresponding field-induced potential is shown a the *blue* line. The bound electron (*green* line) can escape by tunneling through the barrier. (c): The electric field of $E = 50 \cdot 10^9 \; \frac{V}{m}$ completely suppresses the barrier. Classically, the electron could freely escape while quantum mechanically, it is still scattered by the potential step.

which was later named after him. Here,

$$U_p = \frac{I}{\omega^2} \frac{q_e^2}{2 m_e \epsilon_0 c} \tag{2.4}$$

is the so-called ponderomotive potential. The physical meaning of the latter will become clear in section 2.3.1 in the vicinity of equation (2.15).

If $\gamma \ll 1$, ionization can be described by tunneling, while $\gamma \gg 1$ implies that the multiphoton picture is appropriate. It has been shown that there is a co-existence of the models in the "no man's land" in between [4]. The tunneling model continues to make accurate predictions around $\gamma \approx 1$ although ATI peaks are visible as well.

2.2.4. ADK Theory

In 1986, *Ammosov*, *Delone* and *Krainov* published their "quantitative theory of tunnel ionization", now commonly called "ADK theory". According to this the overall tunnel ionization rate of an atom with the ionization potential I_p in a linearly polarized electric field E is (all parameters in atomic units) [16]:

$$\Gamma_{ADK} = \sqrt{\frac{3 n^{*3} E}{\pi Z^3}} \cdot \frac{E D^2}{8 \pi Z} \cdot \exp\left(-\frac{2 Z^3}{3 n^{*3} E}\right) \tag{2.5}$$

with Z being the charge of the ion staying behind,

$$n^* := \frac{Z}{\sqrt{2 I_p}}$$
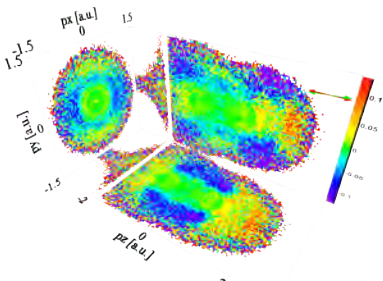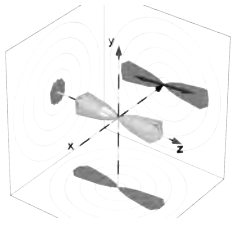
and

$$D := \left(\frac{4q_e Z^3}{En^{*4}}\right)^{n^*}.$$

2.2.5. Momentum Distributions from Atoms

For the rate of obtaining electrons from atoms with the momenta $p_\parallel$ and $p_\perp$ the equation

$$\Gamma(p_\parallel, p_\perp) = \Gamma_0 \cdot \exp\left[-\frac{1}{3}p_\parallel^2 \omega^2 \left(\frac{\sqrt{2I_p}}{E}\right)^3 - p_\perp^2 \frac{\sqrt{2I_p}}{E}\right] \tag{2.6}$$

has been found [16]. $p_\parallel$ is the final electron momentum parallel and $p_\perp$ the one perpendicular to the laser polarization, while

$$\Gamma_0 = \frac{p\omega^2 D^2}{8\pi^3 n^* E} \exp\left(-\frac{2(2I_p)^{3/2}}{3E}\right).$$

It has to be emphasized that equation (2.6) already includes the interaction between the electron and the laser field after tunneling. Therefore it predicts the final, measured momenta after the laser pulse is off. See [16] for the history of these formulae and references.

Equation 2.6 can be used to deduce the light intensity from the width of momentum distributions in an experiment.

2.2.6. MO-ADK Theory

ADK theory was extended to molecules by *Lin* and *Tong* in 2002 [17]. Their so-called "MO-ADK theory" yields ionization rates $\Gamma(E, \vec{R})$, depending on the driving electric field E and the set of Euler angles $\vec{R} = (\alpha, \beta, \gamma)$ between the direction of the electric field and the molecular axis. The idea behind is to assume tunneling from two atomic centers and calculate the coherent sum of the asymptotic electron wavefunctions. The instantaneous ionization rate caused by the static electric field E is
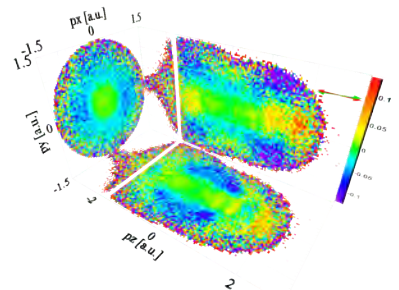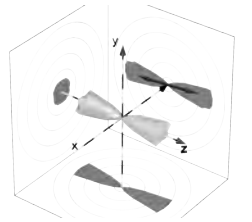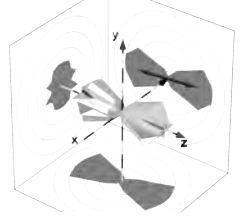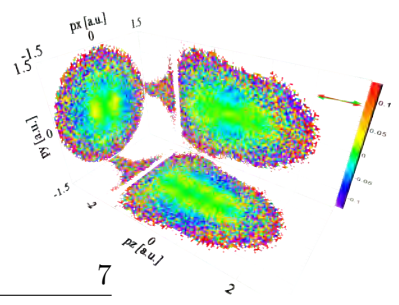
$$\Gamma(E, \vec{R}) = \sum_{m'} \frac{B^2(m, m', \vec{R})}{2^{|m'|}|m'|!} \frac{1}{\kappa^{2Z_c/\kappa-1}} \cdot \left(\frac{2\kappa^3}{E}\right)^{2Z_c/\kappa-|m'|-1} e^{-2\kappa^3/3E} \tag{2.7}$$
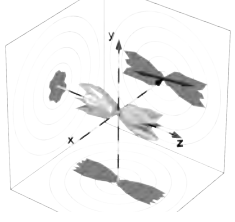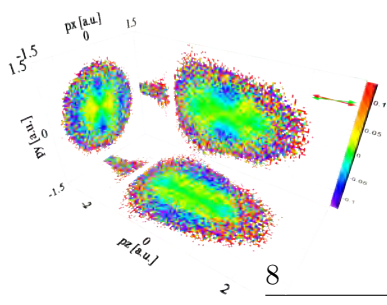
with $\kappa = \sqrt{2I_P}$, Z_c being the effective Coulomb charge, I_p the effective ionization potential and the magnetic quantum number along the molecular axis m.

$$B(m, m', \vec{R}) = \sum_l C_l D_{m',m}^l(\vec{R}) Q(l, m'),$$

where

$$Q(l, m) = (-1)^m \sqrt{\frac{(2l+1)(l+|m|)!}{2(l-|m|)!}}.$$

Species	I_P [eV]	C_0	C_2	C_4
N_2	15.58	2.02	0.78	0.04
O_2	12.03	0	0.62	0.03

Table 2.1.: Effective ionization potentials I_p and coefficients C_l in MO-ADK theory for the species relevant in this work. From [17].

C_l are the species-specific expansion coefficients of the molecular orbital in atomic wavefunctions. They are tabulated in table 2.1. $D^l_{m',m}(\vec{R})$ is a rotation matrix. According to [18], a representation for such a matrix is

$$D^j_{m',m}(\vec{R}) = e^{-im'\alpha}e^{-im\gamma}\sqrt{(j+m')!(j-m')!(j+m)!(j-m)!} \times$$
$$\times \sum_s \frac{(-1)^{m'-m+s}[\cos(\beta/2)]^{2j+m-m'-2s}}{(j+m-s)!s!(m'-m+s)!} \cdot \frac{[\sin(\beta/2)]^{m'-m+2s}}{(j-m'-s)!} \quad (2.8)$$

The ionization rate averaged over a half-cycle is [19]

$$< \Gamma(E,\vec{R}) > = \sqrt{\frac{3E}{\pi\kappa^3}} \cdot \Gamma(E,\vec{R}).$$

The MO-ADK theory makes no predictions concerning electron momentum distributions.

Angle-dependent ionization rates, relative to those at an angle of 0°, are shown for some intensities in figure 2.3. In [19], an intuitive conclusion was suggested, based on MO-ADK rates for N_2 and O_2: Molecules tend to ionize most likely if the laser field pulls along the direction of highest electron density in the valence orbital, while ionization is suppressed in the direction of reduced electron density.

2.2.7. Electron Momentum Distributions from Molecules

If the system being ionized is not an atom but a molecule, the wave packet of tunneled electrons can be approximated as

$$\Psi_{wp,\perp} \propto \langle p_\perp \mid \Psi_i \rangle \exp\left(-\frac{p_\perp^2}{E}\sqrt{\frac{I_p}{2}}\right) \quad (2.9)$$

[3, 4]. Here, $|\Psi_i\rangle$ is the electron's wave function in position space before tunneling, i.e. the orbital being ionized. $\Psi_{wp,\perp}$ is the component of the free electron wave packet in the direction perpendicular to the driving laser field immediately after tunneling, prior to further propagation. The relationship is formulated with a certain level of intuition in [4]. The exponential factor is similar to the $p_\perp$-dependent part of the atomic tunneling rate in equation (2.6). It acts like a filter, suppressing higher lateral momenta. Symmetry of the initial state is
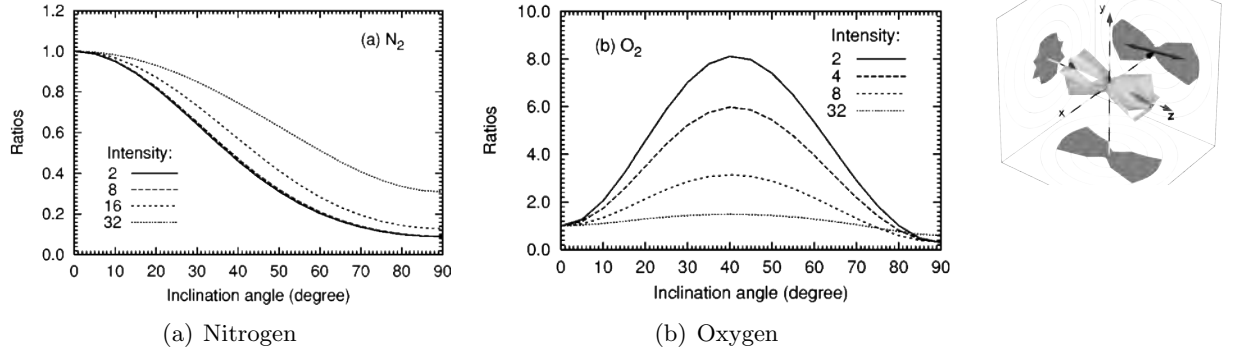
(a) Nitrogen

(b) Oxygen
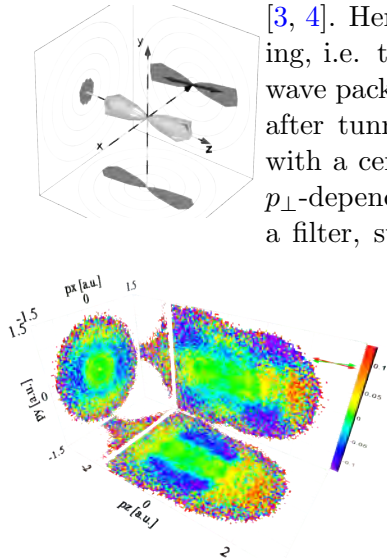
Figure 2.3.: Ionization rates calculated with MO-ADK, depending on the angle between the laser polarization (*horizontal* axis) from N_2 (a) and O_2 (b) as a fraction of the rate at zero degrees (*vertical* axis). The figures contain plots for several light intensities, which are given in the legends in $10^{13} \frac{W}{cm^2}$. From [19].

preserved by tunneling. Hence, "it appears very reasonable to complement the Gaussian shapes [...] with the Fourier transform of the initial state [...]" [4].[1]

In other words, the electron wave function at the exit of the tunnel is the projection of the orbital it tunnels from into momentum space, filtered by a Gaussian. In order to obtain the final, detectable electron momentum distribution, one has to take the propagation of the wave packet in the oscillating laser field into account; see section 2.3. However, in linearly polarized light the component of the wave function treated here is perpendicular to the field and therefore not influenced by it.

2.2.8. Partial Fourier-Transform Approach

Recently, *Murray et al.* published a description of their "partial Fourier-transform approach to tunnel ionization" [20], yielding momentum distributions in all directions for atomic systems. The basic idea is to consider a wave function $\Phi(p_x, p_y, z)$ that depends on momenta in the direction perpendicular to the laser field (p_x, p_y) and on the real-space coordinate z along the field. Such a "mixed representation" enables the authors to treat the bound-state and the continuum part separately. The bound-state wave function can be given either algebraically or numerically while its continuum counterpart is derived within the WKB approximation. As a boundary condition, both wave functions have to match in some point z_0 between the "entrance" and the "exit" of the tunnel. A method for achieving this even for a field-free bound and an in-field continuum wave function is described.

---

[1]In [4], the authors also include the position of the exit of the tunnel, which is set to zero throughout the work in hand.
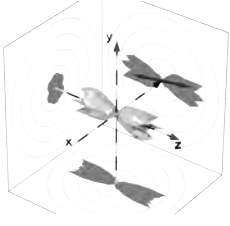
Very recently, the model has been applied to molecules [21]. The authors state that MO-ADK is a limiting case of their theory and show angle-dependent ionization rates for CO_2 which are closer to the experiment ([22], see below) than MO-ADK calculations. They claim the notion inspired by MO-ADK that molecules ionize most likely if the laser field pulls along the direction with the highest electron density gives accurate results only in some special cases but is generally wrong.

A computer code based on the approach is available[2]. This program takes numerical grids containing "Dyson orbitals" as input and outputs angle-dependent ionization rates. However, for the experimentalist the problem of obtaining a Dyson orbital not distributed in the package persists. The program so far does not output momentum distributions, just absolute rates.

2.2.9. Angle-Dependent Ionization Rates: Experiment

Pavicic et al. experimentally determined the dependence of ionization rates on the angle between the molecular axis and the ionizing laser field for N_2, O_2 and CO_2 [22]. Their procedure involved alignment of the molecules as explained in chapter 2.6. In a first step, they measured the alignment distributions by means of Coulomb explosion imaging. In a second step, they recorded the rate of single ionization while rotating the alignment distribution. They then deconvolved the measured alignment angle-dependent rate and the alignment distribution, yielding the angle-dependent single ionization probability of the molecule. Results are compared to MO-ADK (see above). Agreement is good in case of N_2, excellent for O_2 and poor for CO_2; see figure 2.4. It is not clear where the latter disagreement comes from. Nevertheless, the work in hand is dealing with the former species, for which the experiment confirms the validity of MO-ADK.

2.3. Electron Propagation After Tunneling

After tunneling, the freed electron wave packet propagates in the oscillating electric field as prescribed by classical electrodynamics [2]. The electric field $\vec{E}$ of linearly polarized light exerts an electrostatic force of

$$m_e \frac{\mathrm{d}\vec{v}_z}{\mathrm{d}t} = -q_e \vec{E}(t)$$

to the electron. We assume that the latter has a negligible initial velocity in the field direction upon tunneling. If it follows the field freely, i.e. without interaction with the ion, its momentum $\vec{p}(t_i, t)$ can be calculated by integrating the above equation:

$$\vec{p}(t_i, t) = -q_e \int_{t_i}^{t} \vec{E}(\tilde{t}) \, \mathrm{d}\tilde{t} \tag{2.10}$$

with t_i being the time when the electron tunneled.

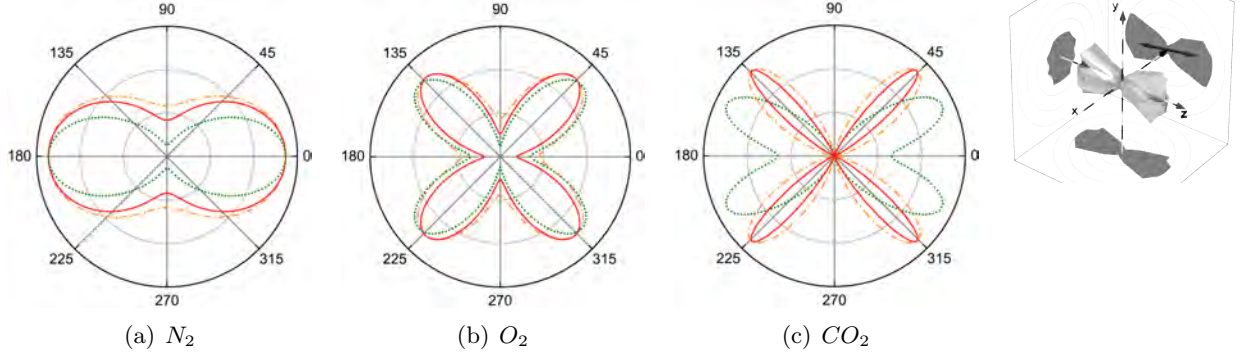[2]http://qols.ph.ic.ac.uk/pymolion

(a) N_2 (b) O_2 (c) CO_2
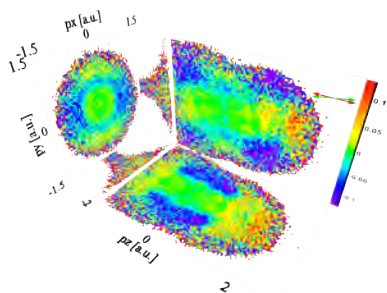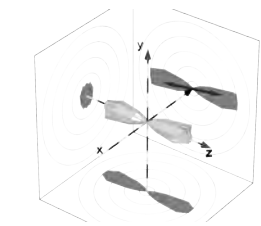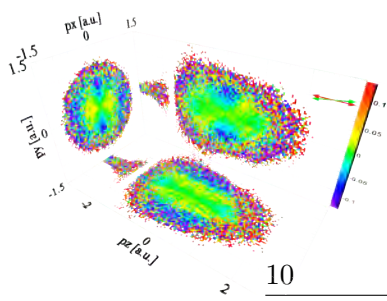
Figure 2.4.: From [22]: Angle-dependent ionization rates of N_2 at an intensity of $I = 1.5 \cdot 10^{14} \frac{W}{cm^2}$ (a), O_2 at $I = 1.3 \cdot 10^{14} \frac{W}{cm^2}$ (b) and CO_2 at $I = 1.1 \cdot 10^{14} \frac{W}{cm^2}$ (c) after deconvolution. *Red* and *orange* curves: Experimental data, analyzed with different assumptions. *Green* dotted curves: MO-ADK rates. The $\lambda = 820$ nm laser field was polarized horizontally.

2.3.1. Streaking by the Field

The electron reaches the detector at virtually infinite time, so its detected velocity in the polarization direction is

$$\vec{p}_{streak}(t_i) = -q_e \int_{t_i}^{\infty} \vec{E}(\tilde{t}) \, d\tilde{t} = q_e \vec{A}(t_i). \tag{2.11}$$

Here, $\vec{A}(t_i)$ is the magnetic vector potential [23]. The effect of the laser field giving the electron a boost it keeps even after the pulse is off is referred to as *streaking*; $p_{streak}(t_i)$ is the streaking momentum. We are assuming that $\vec{E}$ is along the z axis. Hence, streaking proceeds only in this direction and only the z-component of $\vec{A}$, from now on denoted as A, is non-zero.

In general, $\vec{A}$ has to be calculated numerically. However, for a relatively long pulse, streaking momentum can be approximated by

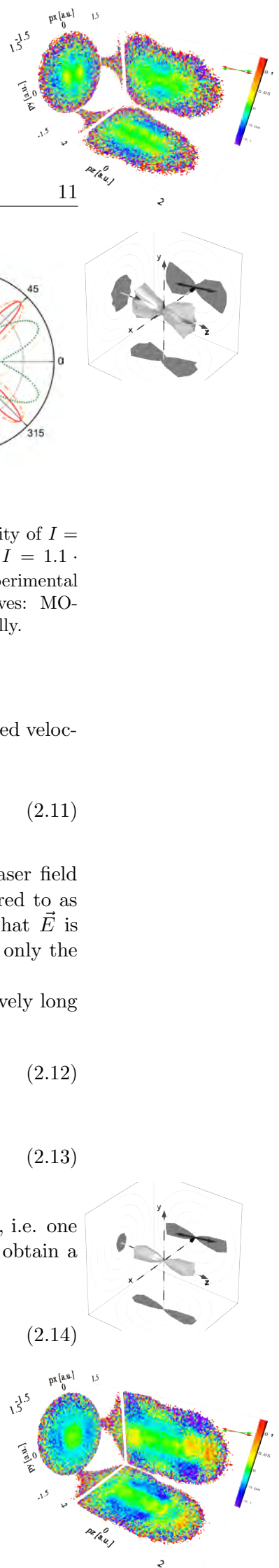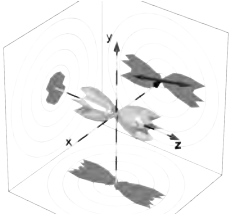$$p_{streak}(t_0) = q \cdot A(t_0) \approx p_{osc} \sin \omega t_0 \tag{2.12}$$

with

$$p_{osc} := \frac{q_e \hat{E}}{\omega}. \tag{2.13}$$

This is shown in appendix D.

Given it tunnels with a negligible initial velocity, a "direct" electron, i.e. one that does not re-encounter with its parent ion (cf. section 2.3.2) can obtain a maximum final kinetic energy

$$W_{dir,max} = \frac{p_{osc}^2}{2m_e} = 2U_P \tag{2.14}$$

it will keep after the end of the pulse. The so-called "ponderomotive potential" U_p already defined in equation (2.4) is the average kinetic energy an electron would have if its quivering motion took place in a CW field:

$$U_P := \frac{1}{2m_e} < p(0,t)^2 >_t = \frac{p_{osc}^2}{4m_e}. \tag{2.15}$$

Streaking is exploited in a method called the "attosecond streak camera" [24]: Depending on the phase of an infrared laser pulse at the instant of ionization, electrons ejected by an attosecond pulse receive different streak velocities. This can be used to characterize the attosecond pulse.

2.3.2. Re-Collision / Re-Scattering

Before reaching the detector, the electron performs a quivering motion which may, under certain circumstances, lead back to its parent ion where it can scatter. As the most significant effects can be expected to happen within the central laser cycle[3] and the change of our experimental envelope $E_0(t)$ is not significant within this short timespan, we will assume a CW field in the following:

$$E(t) = \hat{E} \cos \omega t.$$

In this case, equation (2.10) can be solved as

$$p(t_i, t) = p_{osc} \cdot (\sin \omega t_i - \sin \omega t). \tag{2.16}$$

If we integrate once more, we obtain the trajectory of the electron:

$$r(t_i, t) = \frac{1}{m_e} \int_{t_i}^t p(t_i, \tilde{t}) \, d\tilde{t} = \frac{p_{osc}}{m_e \omega} [\omega(t - t_i) \sin \omega t_i + \cos \omega t - \cos \omega t_i] + r_i$$

Here r_i is the position where the electron starts its motion. In all discussions we assume this to be zero, while really it is the coordinate of the "exit of the tunnel". If the condition

$$r(\varphi_i, \varphi_r) = \frac{p_{osc}}{m_e \omega} [(\varphi_r - \varphi_i) \sin \varphi_i + \cos \varphi_r - \cos \varphi_i] + r_i = 0 \tag{2.17}$$

can be satisfied for a given ionization phase $\varphi_i = \omega t_i$, the electron *re-collides* with its parent ion at the corresponding re-collision phase $\varphi_r = \omega t_r$.

We will only analyze the first re-collision. Equation (2.17) has to be solved numerically. The relationship between φ_r and φ_i is graphed as a blue line in figure 2.5, assuming $r_i = 0$. Within one cycle a solution exists only for $0^o < \varphi_i < 90^o$. Electrons tunneling at the rising quarter-cycle of the electric field do not re-scatter. Instead, they escape towards the detector directly. We will

---

[3]I.e. the cycle at the maximum of the pulse envelope, showing the maximum peak intensity and electric field strength.
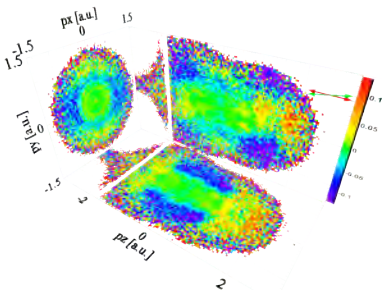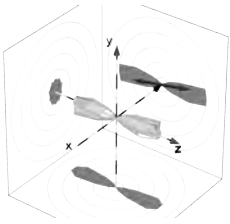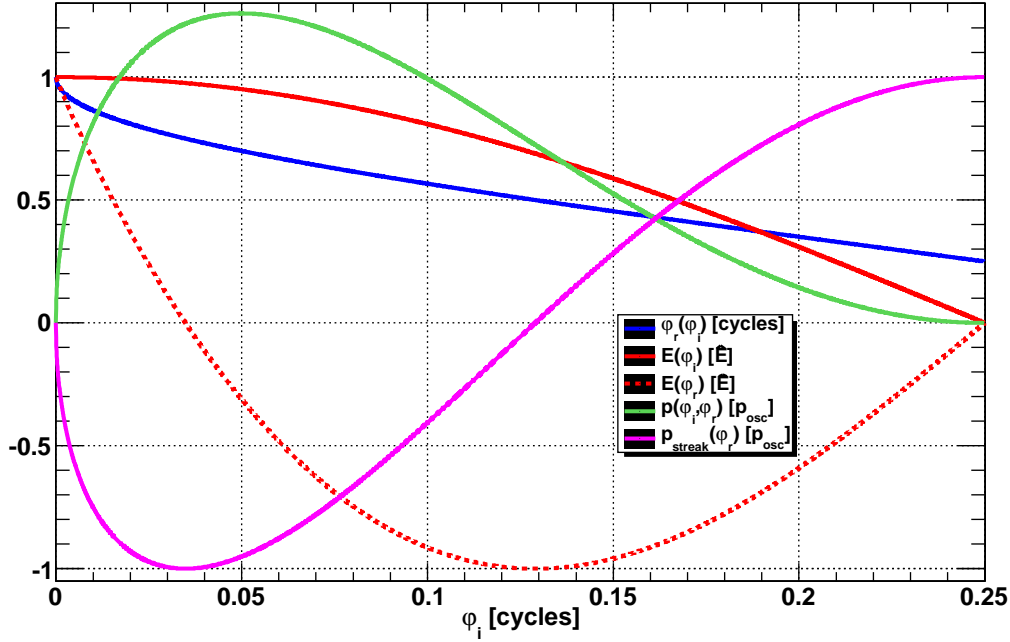
Figure 2.5.: Plot of all relevant factors discussed before. *Horizontal axis*: Phase upon
tunneling φ_i in laser cycles ($= 1/360^o = 1/2\pi = 1/\lambda$). *Blue line:* Re-
collision phase in laser cycles (solution of equation (2.17)). *Full red line:*
Electric field by laser upon tunneling in units of $\hat{E}$. *Dashed red line:* Elec-
tric field upon re-collision. *Green line:* Re-collision momentum in units
of p_{osc} according to equation (2.16). *Pink line:* Streaking momentum
$p_{streak}(\varphi_r)$ after equation (2.12). Please note that light intensity is ac-
counted for by the choice of units.

therefore refer to them as *direct electrons*. They are subject to streaking only.
In the said figure, the momentum of an electron that was born at the phase φ_i
at the instant of re-collision according to equation (2.16) is plotted as a green
line. It can be seen that the maximum re-collision momentum is $p_{rec,max} =
1.26 p_{osc}$, corresponding to a maximum re-collision energy of[4] $W_{rec,max} = 3.17 U_P$,
occurring at an ionization phase of $\varphi_{i,recmax} = 18^o$ and a re-collision phase of
$\varphi_{r,recmax} = 252^o$.[5]

Any re-collision momentum below $p_{rec,max}$ can occur at two different ionization
(and re-collision) phases. If $\varphi_i < \varphi_{i,recmax}$, the corresponding re-collision phase
is later than $\varphi_{r,recmax}$. Hence, more time elapses between ionization and re-
collision. This case is referred to as "*long trajectories*". In contrast, if $\varphi_i >
\varphi_{i,recmax}$, the resulting re-collision phase is $\varphi_r < \varphi_{r,recmax}$, leading to "*short*

---

[4]Please note that in all considerations we are ignoring the parent ion's Coulomb potential.

[5]It shall be acknowledged that the value $\varphi_{i,recmax} = 18^o$ calculated here does not exactly
match the figure reported in [2], which is 17°. Chen et al. even assume 13° ([25], p. 3),
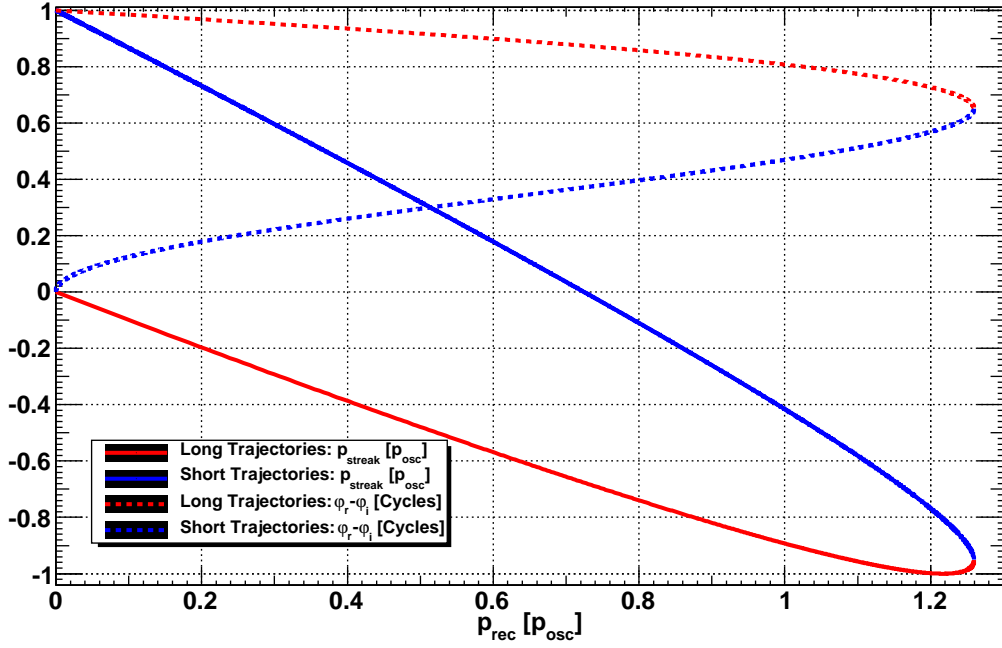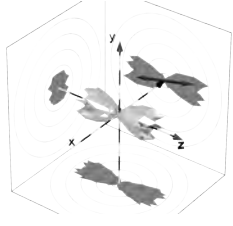which is clearly a deviation beyond rounding errors.
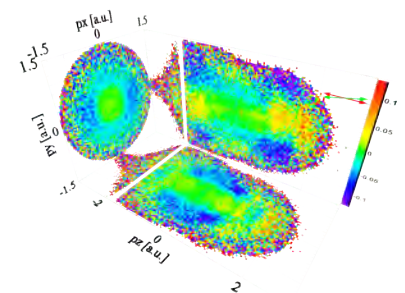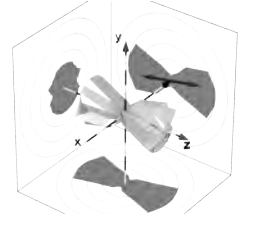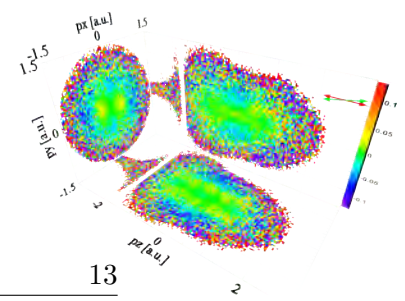
Figure 2.6.: Dependence of streaking momentum in units of p_{osc} (full lines) and the wave packet's time of flight between ionization and re-collision $\varphi_r - \varphi_i$ in laser cycles (dashed lines) on the re-collision momentum (*horizontal* axis, in units of p_{osc}). Red lines: "Long" trajectories ($\varphi_i < 18^o$); blue lines: "Short" trajectories ($\varphi_i > 18^o$).

trajectories". The relationship between re-collision and streaking momenta for short and long trajectories is analyzed in figure 2.6.

2.3.3. Propagation of Elastically Re-Scattered Electrons

In this work, we are going to deal with elastic re-scattering. This means that electrons of our interest do not exchange energy with their parent ion. Instead, the re-colliding electron wave packet is expected to carry information about the ion, such as a diffraction image. Literature on this topic will be reviewed in section 2.5.3. Here we will focus on the interaction between the electron and the laser field.

We will restrict our considerations to two dimensions now. In the following vectors, the first component will correspond to the direction perpendicular and the second to the one parallel to the incident electron's direction, which is along the laser field. The momentum of an incident electron born at the phase φ_i at the instant directly before scattering $\varphi_r - \epsilon$ ($\epsilon > 0$) is

$$\vec{p}(\varphi_i, \varphi_r - \epsilon) = p_{rec} \begin{pmatrix} 0 \\ 1 \end{pmatrix}$$
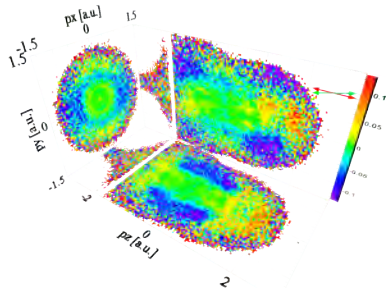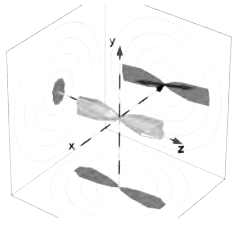
with $p_{rec} = p(\varphi_i, \varphi_r)$ as defined in equation (2.16). Elastic scattering changes the electron's momentum vector by an angle α such that, at the instant $\varphi_r + \epsilon$ after scattering,

$$\vec{p}(\varphi_i, \varphi_r + \epsilon) = p_{rec} \begin{pmatrix} \sin \alpha \\ \cos \alpha \end{pmatrix}.$$

To obtain the final, measurable momentum, we have to account for the effect of the oscillating laser field. An electron scattered at some phase φ_r is subject to the same conditions as one that was born at just that instant with the same initial momentum. Hence, we have to add the respective streaking momentum according to equation (2.12), yielding

$$\vec{p}_f := \vec{p}(\varphi_i, \infty) = p_{rec} \begin{pmatrix} \sin \alpha \\ \cos \alpha \end{pmatrix} + \begin{pmatrix} 0 \\ p_{osc} \sin \varphi_r \end{pmatrix}. \tag{2.18}$$

$\vec{p}_f$ is the final momentum we will actually detect. Its angle with the direction of the incident electron (and the driving electric field) is

$$\alpha' = \angle(\vec{p}_f, \vec{p}_{rec}) \neq \alpha.$$

However, it is important to note that the laser phase at the instant of re-scattering φ_r depends on the tunneling phase φ_i. Hence, φ_i, the scattering angle α and the light intensity $\hat{I}$ (leading to a specific electric field) completely determine the final momentum of an electron. Another important thing to note is that re-scattered electrons can reach energies beyond $2U_p$, which is the maximum energy a direct electron can gain from streaking. Backscattered electrons ($\alpha = 180^o$) can reach a final kinetic energy of up to $\approx 10U_P$ [26]. Hence, energy is a parameter that can be used to distinguish between direct and re-scattered electrons.

In [3], Spanner et al. suggested that one can remove streaking and reveal effects of scattering in experimental data by analyzing them along circles of the radius p_{rec} whose centers are offset along the laser polarization direction by p_{streak}. Since then, the method has been used successfully in various works, e.g. [27, 11, 28].

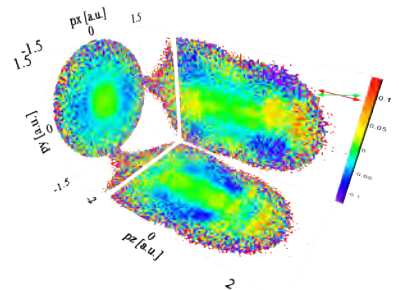*Chen* et al. noticed that, in case of long trajectories, the relationship between p_{rec} and p_{streak} (cf. figure 2.6) is about linear with
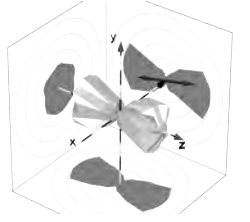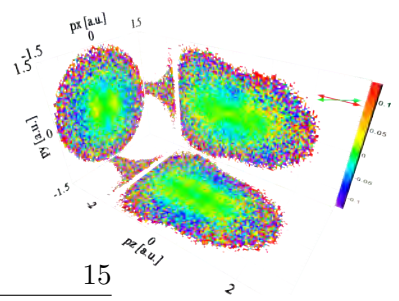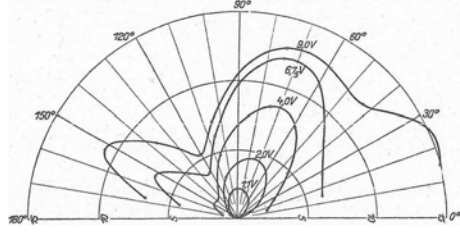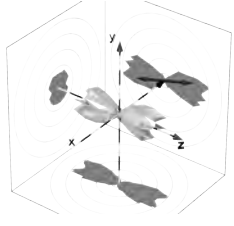
$$p_{rec} \approx -1.26 p_{streak}$$

in the region of high re-collision momenta [25]. Based on this approximation, they obtain

$$\tan \alpha' = \frac{\sin \alpha}{1/1.26 - \cos \alpha} \tag{2.19}$$

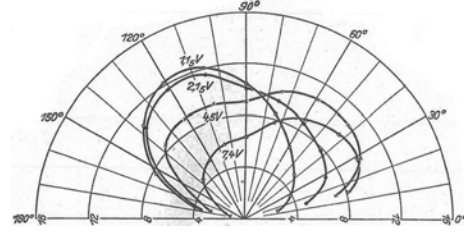and

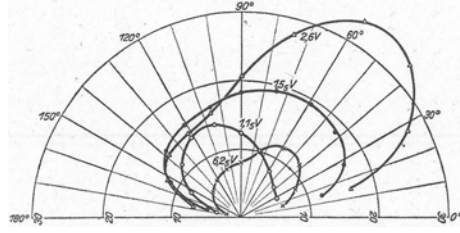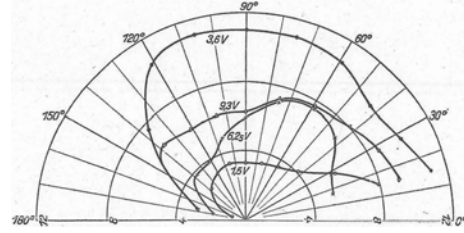$$|\vec{p}_f|^2 = p_{rec}^2 \cdot (1.63 - 1.59 \cos \alpha). \tag{2.20}$$

(a) Argon Atoms

(b) Hydrogen Molecules

(c) Carbon Monoxide Molecules

(d) Carbon Dioxide Molecules

Figure 2.7.: Differential electron scattering cross sections for various electron energies, which are denoted by the numbers attached to curves in electron volts. An angle of 180° corresponds to backscattering. These experimental results were published by *Ramsauer* and *Kollath* in 1932 [31].
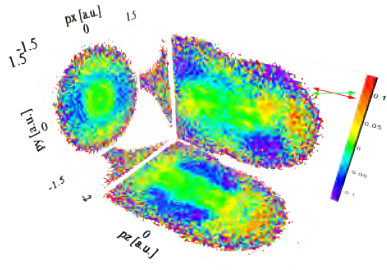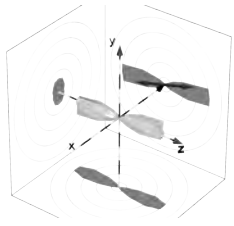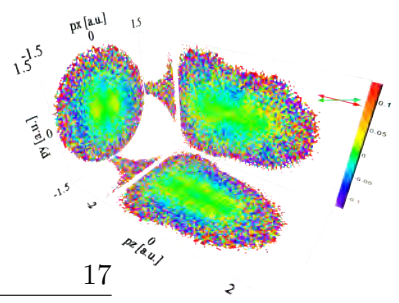
2.4. Elastic Electron-Molecule Scattering

Already starting in the early 1920s, *Ramsauer* explored low-energy electron scattering at various species (e.g. [29, 30, 31]). He found peculiar structures both in the total and differential scattering cross sections (see examples in figure 2.7), changing significantly with varying electron energy. By the time, this phenomenon could not be explained.

It can only be understood quantum mechanically. The intuitive explanation is that any atom has a Coulomb potential, shielded by its bound electrons. The scattering electron wave penetrates through the atom's electron cloud, accelerates on the way down and decelerates while moving back up the potential well. If the wavefront was plane before scattering, it is no more thereafter. The potential introduces phase shifts and makes partial waves interfere, causing peculiar scattering cross sections.

In order to reproduce experimental findings for low incident electron energies (less than 100 eV), theorists have to take into account the time-dependent polarization inflicted upon the target atom's or molecule's electron cloud by the projectile electron. The exchange interaction also plays a significant role. These complications prevent an algebraic treatment already for simple atoms. Molecules are even more involved. [32]

The situation simplifies significantly at higher electron energies. If the elec-

tron cloud of the scatterer cannot follow the fast electron anymore, the effective potential becomes static. A further simplification for molecules is the "static independent atom model" (IAM): The molecular potential is approximated as the sum of (static) atomic potentials.

In standard high-energy gas-phase electron diffraction, within the static IAM, the wavefunction of an electron after elastically scattering with a rigid molecule becomes [33]

$$\Psi(\vec{s}) \propto \sum_{i=1}^{n} f_i(|\vec{s}|)e^{i(\vec{s}\cdot\vec{r}_i)}.$$

Here,

$$\vec{s} = \frac{1}{\hbar}(\vec{p}_s - \vec{p}_r)$$

is the momentum transfer with $\vec{p}_r$ being the momentum of the incoming and $\vec{p}_s$ the momentum of the scattered, outgoing electron. f_i is the scattering amplitude of the ith atom, while $\vec{r}_i$ is its position. That is, spherical waves coming from the atoms interfere in the point of observation.

If we consider a homonuclear, diatomic molecule with the internuclear distance vector $\vec{d}$, this collapses to

$$\Psi(\vec{s}) \propto f(|\vec{s}|)\left(1 + e^{i\Delta\varphi}\right)$$

with the phase difference (in radians)

$$\Delta\varphi = \frac{1}{\hbar}\vec{d}\cdot(\vec{p}_s - \vec{p}_r) \tag{2.21}$$

between the partial waves coming from the two atoms. If the atomic scattering factor f is constant, this results in Young-type double-slit diffraction.

2.5. Re-Scattering Physics

Three distinct effects may take place upon re-collision: The electron can either be re-captured, scatter inelastically or elastically. There are several reviews on these topics [34, 35, 36, 23].

2.5.1. Re-Capturing

If the electron is re-captured by its parent ion, its kinetic energy plus the binding energy of the state it is captured into is emitted as a single photon [2]. The wavelength of this photon is typically in the extreme ultraviolet. In analogy to ATI in case of emitted electrons, the energy spectrum of such photons shows distinct peaks which are - due to selection rules - usually separated by twice the photon energy of the driving laser. This is why the phenomenon is called "high harmonics generation". Details beyond the very simple picture just given enabled the
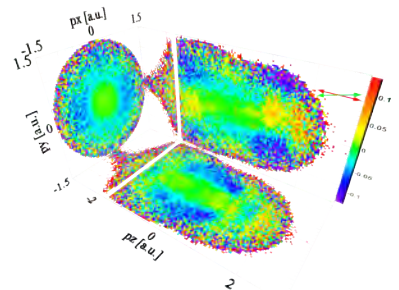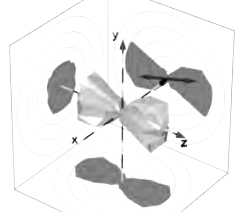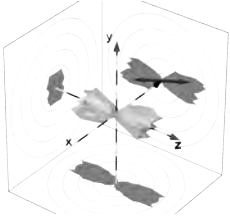
generation of ultraviolet light pulses with a duration in the order of attoseconds [37]. Another spectacular application is the tomographic reconstruction of the HOMO of N_2, including the sign of the wave function [38].

A further special case of re-absorption of the re-colliding electron has been recently observed and termed "frustrated ionization" [39]: The electron can be captured into a highly excited (Rydberg) state, with the resulting system staying stable until detection.

2.5.2. Inelastic Re-Scattering

In other cases, the electron scatters inelastically without being captured. Instead, it can free a second electron. This is the explanation of a process called "non-sequential double ionization" (NSDI) [2].[6]

2.5.3. Elastic Re-Scattering

In this section, we will review literature on elastic re-scattering of electrons in strong laser fields. It can be noted that in the period pre-2008, various theoretical predictions and simulations were published. Publication frequency increased dramatically in 2008, when experimental results appeared in journal articles.

Already in 1996, *Zuo et al.* showed both algebraically and numerically that the angular distribution of ATI electrons from the ionization of aligned H_2^+ shows a diffraction-like modulation [9]. They named this effect "Laser-Induced Electron Diffraction" (LIED). Although this "diffraction" originates from direct electrons, the authors note that re-scattering does exist and re-scattered electrons may be used to retrieve information about the ion. Nowadays, the diffraction of re-colliding electrons rather than interference in direct ones is referred to as LIED.

In 2002, *Niikura et al.* determined the current density of the re-colliding electron using non-sequential double ionization (i.e. inelastic re-scattering) of H_2 [40]. They also remarked that elastically re-scattered electrons can be expected to carry a diffraction image of the molecule.

Lein et al. reported quantum mechanically calculated electron distributions from the ionization of H_2^+ in strong laser pulses in the same year [10]. These were obtained by solving the time-dependent Schrödinger equation (TDSE) in two dimensions numerically for a ten-cycle, trapezoidally shaped, $I = 5\cdot10^{14}\ \frac{\text{W}}{\text{cm}^2}$, $\lambda = 780$ nm pulse. The ion's electrostatic potential was taken into account for grid points inside a box in real-space of 1106×369 a.u. and neglected otherwise. The authors found that the angular distributions of high-energy electrons matched a simple model wherein a re-scattering electron wave is diffracted by the ion acting as a double-slit. The model assumes that the electron's DeBroglie wavelength relevant for diffraction corresponds to its energy upon re-scattering plus its ionization potential. A comparison between TDSE results and the diffrac-

---
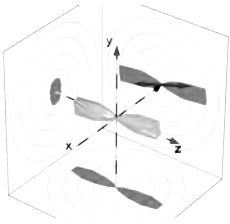
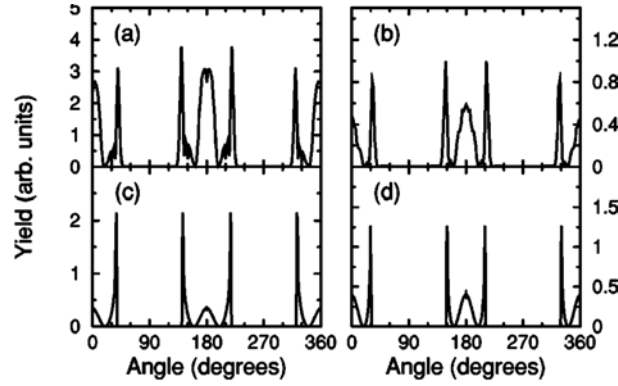[6]NSDI is opposed to "sequential double ionization", where two electrons tunnel successively.
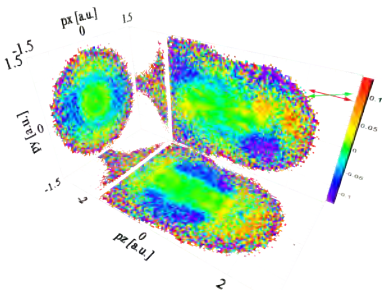
Figure 2.8.: From [10] (*Lein* et al.): Angular distribution of ATI electrons from H_2^+ with an internuclear distance of 2 a.u., ionized by an $I = 5 \cdot 10^{14} \, \frac{W}{cm^2}$, $\lambda = 780$ nm 10-cycle laser pulse. Both the molecular axis and the laser polarization are fixed at 0° / 180°. *Top* row: Quantum mechanical calculations (2D-TDSE). *Bottom* row: Double-slit diffraction model. *Left*-hand column: Electron energy of $7U_p$; *right*-hand column: $8U_p$ electrons. Agreement between the quantum mechanical and model calculations is good regarding the shape of the curves and excellent with respect to peak positions.

tion model is reproduced in figure 2.8 and shows excellent agreement regarding peak positions.

Spanner et al. suggested a "recipe" how to analyze experimental data with respect to diffraction in 2004 [3]. It consists of the following elements:

1. Analyzing the data along circular cuts offset along the polarization direction by the streaking momentum as derived above.

2. Using as short as possible, phase-stabilized pulses to avoid contributions by different cycles.

They checked their method against a quantum mechanical simulation assuming a single-cycle cosine field as an approximation of a laser pulse that is linearly polarized with $I = 7 \cdot 10^{14} \, \frac{W}{cm^2}$, $\lambda = 800$ nm. The TDSE solution was based on the one by Lein et al. discussed above. Results are shown in figure 2.9. In addition to diffraction peaks, a "holographic-type interference" between direct and re-scattered electrons was identified and suggested to be a probe for both magnitude and phase of the scattering amplitude. The authors also analyzed the interference between long and short trajectories, concluding that this leads to a high-frequency modulation in the resulting electron spectra without masking the diffraction pattern, which remains clearly visible.

Also in 2004, *Yurchenko et al.* published results of a numerical solution of the three-dimensional TDSE [41]. They assumed single-cycle, constant envelope, $\lambda = 400$ nm pulses that are turned off after one period and model H_2^+ molecules
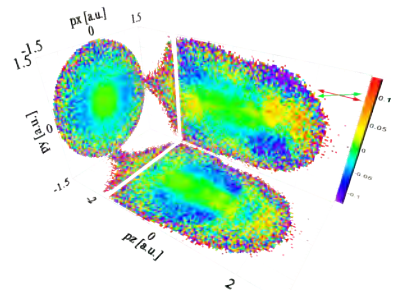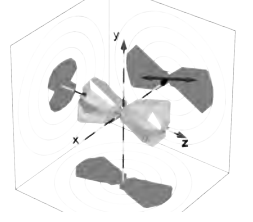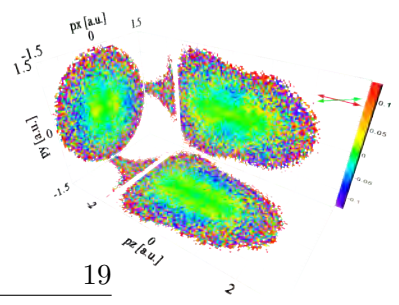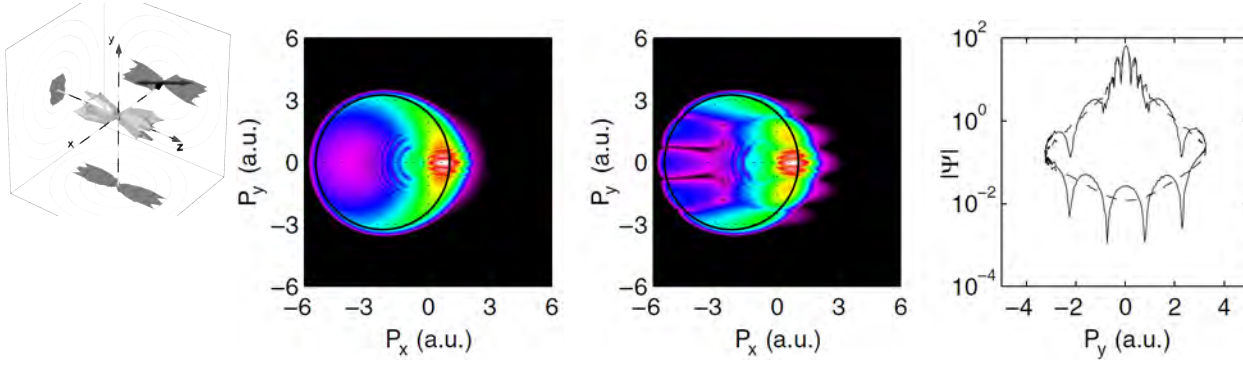
Figure 2.9.: Simulations from [3]: *Centre panel*: An H_2^+-like model molecule is aligned along the vertical axis while the laser polarization is along the horizontal. The color code gives the magnitude of the electron wave-packet on a logarithmic scale. $I = 7 \cdot 10^{14} \frac{W}{cm^2}$, $\lambda = 800$ nm. The black circle is offset along the horizontal axis by the streaking momentum and has a radius equaling the re-collision momentum for electrons born at a phase of $\varphi_i = 17^o$. *Left-hand panel*: Same for a model atom. *Right-hand panel*: Cuts along the circles for the atom (dashed) and the molecule (solid line). The low-frequency modulations present only in the molecular case are attributed to double-slit diffraction. In contrast, the high-frequency ones around $p_y \approx 0$ are visible both in case of the molecule and the atom. These are explained as a "holographic-type interference" between direct and re-scattered electrons. See text for details.

with bond lengths of $d = 6$ a.u. and $d = 8$ a.u.. The real-space electron density distributions at different times are shown in figure 2.10. The authors also suggested a new means of analyzing diffraction images in electron momentum distributions: The rapid reduction of scattering amplitude with increasing scattering angle is recognized as an obstacle. They define the parameter

$$\mu(p) := \frac{\int |\Psi(p, p_y, p_z)|^2 \mathrm{d}p_y \mathrm{d}p_z}{\int |\Psi(p_x, p, p_z)|^2 \mathrm{d}p_x \mathrm{d}p_z} \tag{2.22}$$

of which they show it conserves the diffraction pattern (see figure 2.11) but cancels the envelope. Here p_z is the direction of the laser polarization, p_x parallel and p_y the direction perpendicular to the molecular axis. μ is the ratio of the electron momentum distributions along and perpendicular to the molecular axis with the respective remaining directions integrated over. Furthermore, the effect of the re-colliding electron wave packed being diffracted is explicitly called "laser-induced electron diffraction", which is different from the use of the term by *Zuo et al.* [9] (see above) but now standard.

Hu and *Collins* published results from another 3D-TDSE calculation in 2005 [42]. Their model molecule was K_2^+ at various bond lengths, including its equilibrium one. They exposed it to single-cycle $\lambda = 800$ nm, $I = 1 \cdot 10^{14} \frac{W}{cm^2}$, linearly polarized pulses and confirmed that, assuming double-slit diffraction, they were

(a) After one laser half cycle.

(b) At the end of the pulse.

(c) 152 as after the pulse's end.

(d) 261 as after the pulse's end.
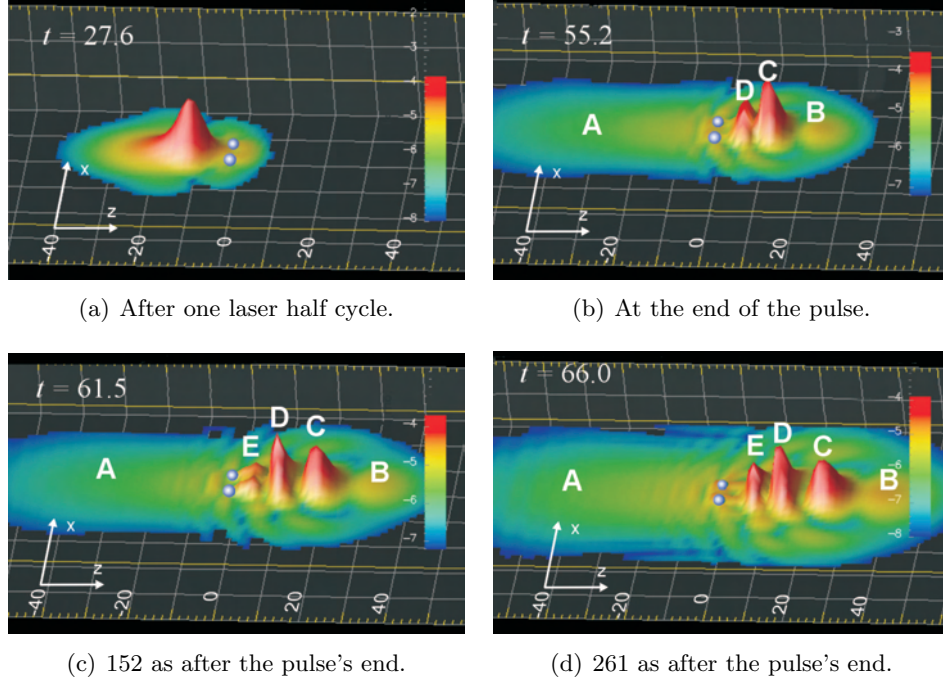
Figure 2.10.: [41]: Different temporal snapshots from a 3D-TDSE simulation of spatial electron density from an H_2^+-like model ion with a bond length of $d = 6$ a.u., aligned along the x-direction. It is ionized by a $\lambda = 400$nm, $I = 3 \cdot 10^{14} \frac{W}{cm^2}$, single-cycle, constant envelope laser pulse polarized along the z (horizontal) direction. The color code is logarithmically scaled.
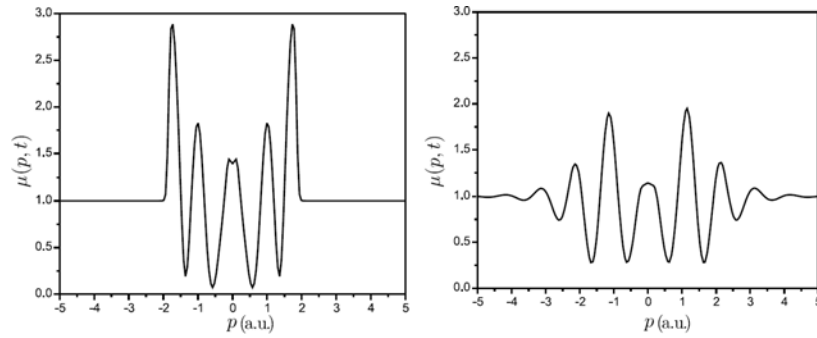
Figure 2.11.: From [41]: *Right*: $\mu(p)$ as defined in equation (2.22) after a full laser cycle; simulated with the same parameters as fig. 2.10. See subscript there. *Left*: Diffraction of a Gaussian-shaped electron wave packet modeled to match the re-collision momentum in the full simulation. The identity of the peak positions in both spectra shows that the double-slit diffraction pattern is present in the ratio μ.
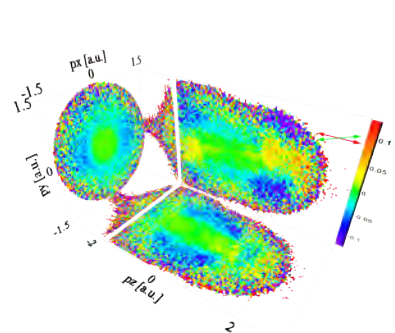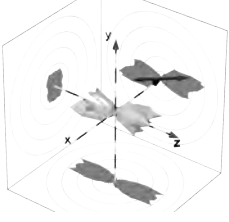
able to retrieve accurate bond lengths from the simulated electron momentum distributions.

In [43] (*Diplomarbeit*), we found structures in the electron momentum distributions from aligned oxygen molecules. However, by the time, we could only speculate their origin might be LIED.

Hetzheim et al. based model calculations on the SFA and included a zero-range potential to analyze elastic re-scattering effects [44], published in 2007. They calculated angle-dependent electron energy spectra for linearly polarized light and diatomic model molecules of different internuclear distances. The authors found an interference structure caused by re-collision in the angular distributions of high-energy electrons which carries information about the internuclear distance.

In January 2008, the article [28] appeared. In this publication, *Morishita* et al. showed that elastic electron scattering cross sections at atomic single ions can be reconstructed from the angular distribution of high-energy, backscattered re-collision electrons. They established this by comparing results from a TDSE simulation of photoelectron spectra from argon, neon, xenon and hydrogen atoms to differential scattering cross sections obtained with a partial wave Ansatz. They showed that the re-colliding electron wave packet is mostly independent of the atomic species. Additionally, the authors demonstrated that photo recombination cross sections can be extracted from the spectrum of high harmonic photons emitted in case of the electron being re-captured by the ion (HHG). The same authors extended their conclusions to fixed-in-space molecular hydrogen, benzene, nitrobenzene, acetylene and vinylidene in another paper published in February 2008 [45]. Doubly differential electron scattering cross sections were presented (reproduced in case of H_2^+ in figure 2.12). *Morishita* et al. now termed the method of analyzing high-energy electron spectra nearby the cutoff within circles / spheres offset by the streaking momentum "laser induced electron microscopy" (LIEM).

An experimental realization for the atomic case by *Ray* et al. became public in April 2008 [27]. The authors reported the retrieval of elastic electron-Ar^+, -Kr^+ and -Xe^+ cross sections and compared them to model calculations. They measured two-dimensional electron momentum distributions with a time of flight spectrometer, rotating the polarization of the ionizing laser pulse. The latter had a peak intensity between 0.4 and $0.9 \cdot 10^{14}$ $\frac{\text{W}}{\text{cm}^2}$ and a duration of 7 fs. The data were analyzed as suggested in [3] and explained in section 2.3.3. Results are reproduced in figure 2.13.
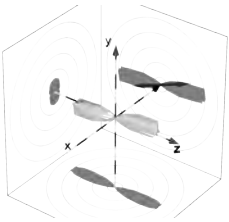
Busuladzic et al. made another extension to the molecular strong-field approximation in order to include re-scattering. Their first paper on this was published in May 2008 [46]. They calculated angular dependent electron energy spectra for different orientations of N_2 and O_2 (reproduced in figure 2.14). These show remarkable minima caused by "two-center interference", depending on the orientation of the molecules (marked as dashed lines in fig. 2.14). The authors established that these minima survive focal averaging and suggested they could
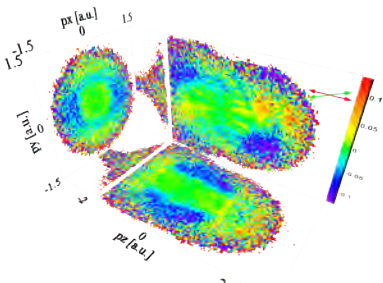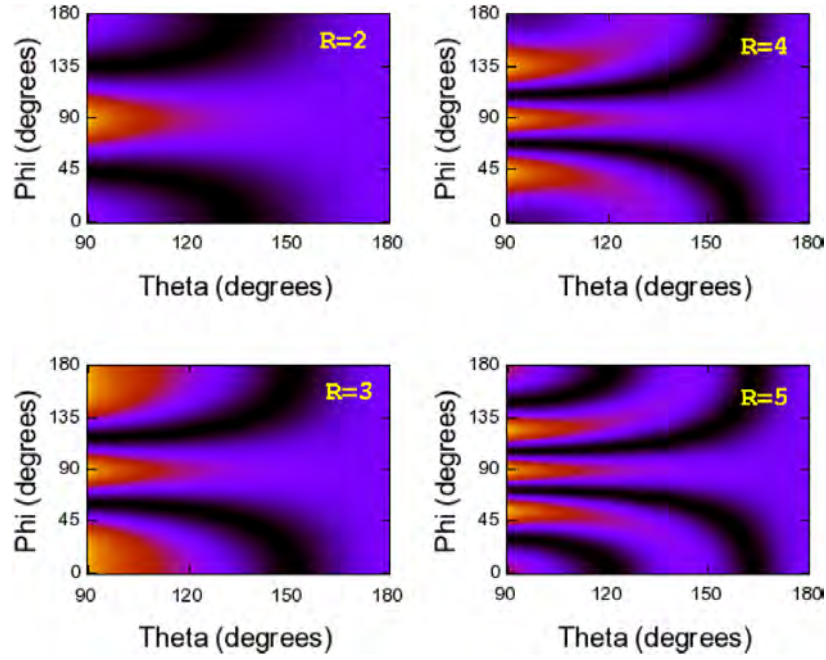
Figure 2.12.: Results by Morishita et al. [45]: Doubly differential electron scattering cross sections of fixed-in-space H_2^+ at internuclear distances of 2 a.u., up to 5 a.u.. The angle ϑ is the scattering angle

be used to retrieve the internuclear separation. This was repeated in greater detail by the same authors in [47].

A very similar study by *Okunishi* et al. [48] appeared in the same volume of Phys. Rev. Lett., back to back with the article by Ray et al. The authors measured elastic electron-ion scattering cross sections from Xe, Kr and Ar with 100 fs laser pulses.

Our article [11] was published in June 2008. Therein, we experimentally showed that diffraction patterns are present in the distributions of high-energy photoelectrons from aligned N_2 and O_2 molecules. Details will be presented in chapter 5.1 of the work in hand.

In another article [49] by *Okunishi* et al., together with Buzuladzic et al., angle-resolved photoelectron energy spectra from N_2 and O_2 molecules were reported. As before, the authors obtained their experimental data with a small-aperture time of flight spectrometer and $\lambda = 800$ nm, $\tau = 100$ fs laser light pulses in the intensity range of a few times $1 \cdot 10^{14}$ $\frac{W}{cm^2}$. No attempts were made to align the molecules. They compared their results with simulations based on the above-mentioned extension of the SFA by Busuladzic et al. [46]. The article was published in early October 2008.

In July 2009, one more paper by *Okunishi* et al. was published [50]. The authors once again compared angle resolved experimental electron energy spectra from non-aligned N_2 and O_2 with the theory by Busuladzic et al.. Laser

(a) Xenon at various p_{rec}.　(b) Various species at $p_{rec} = 1.03$ a.u.
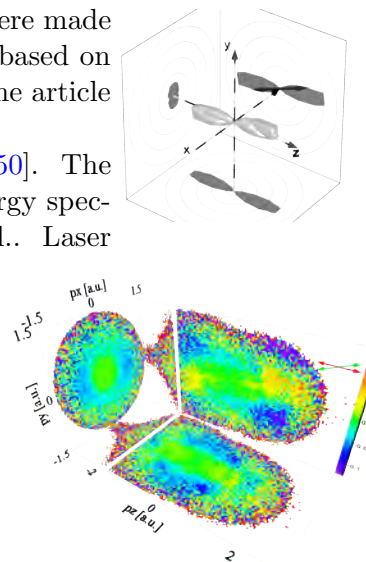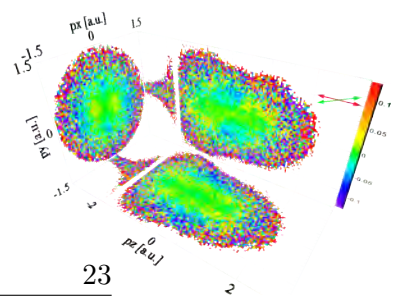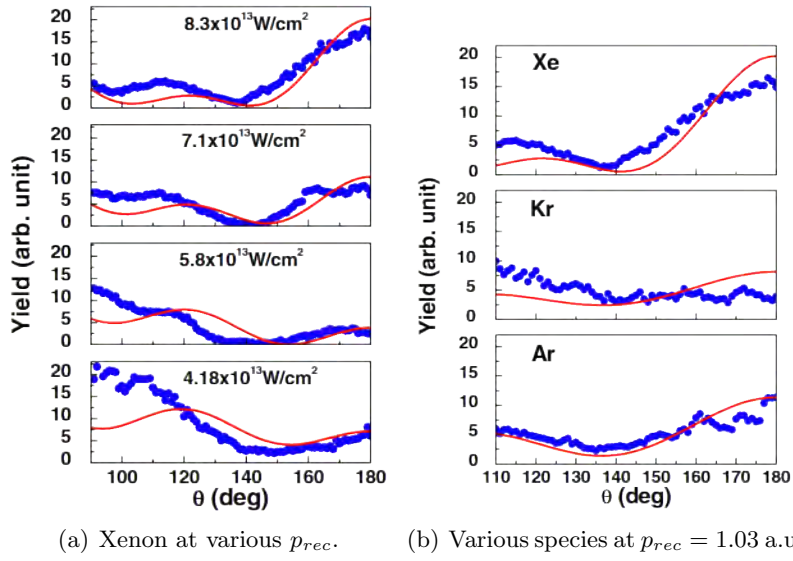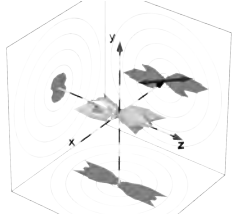
Figure 2.13.: Elastic electron-ion scattering cross sections from [27]. *Blue* points are experimental data while *red* curves are calculated. (a): Data from Xenon taken at the various intensities given in the panels. These correspond to re-scattering electron momenta of (*top to bottom*) 1.03 a.u., 0.95 a.u., 0.86 a.u. and 0.74 a.u.. (b): Data from *Xe* (*top*), *Kr* (*middle*) and *Ar* (*bottom*) taken under condition such that the re-scattering electron momentum is $p_{rec} = 1.03$ a.u.. In all plots, the electron scattering angle θ equals our angle α as defined in section 2.3.3.
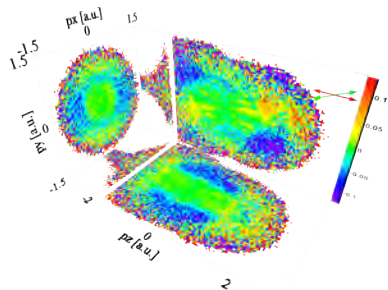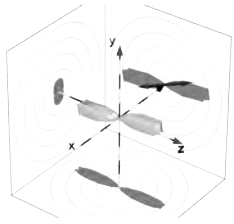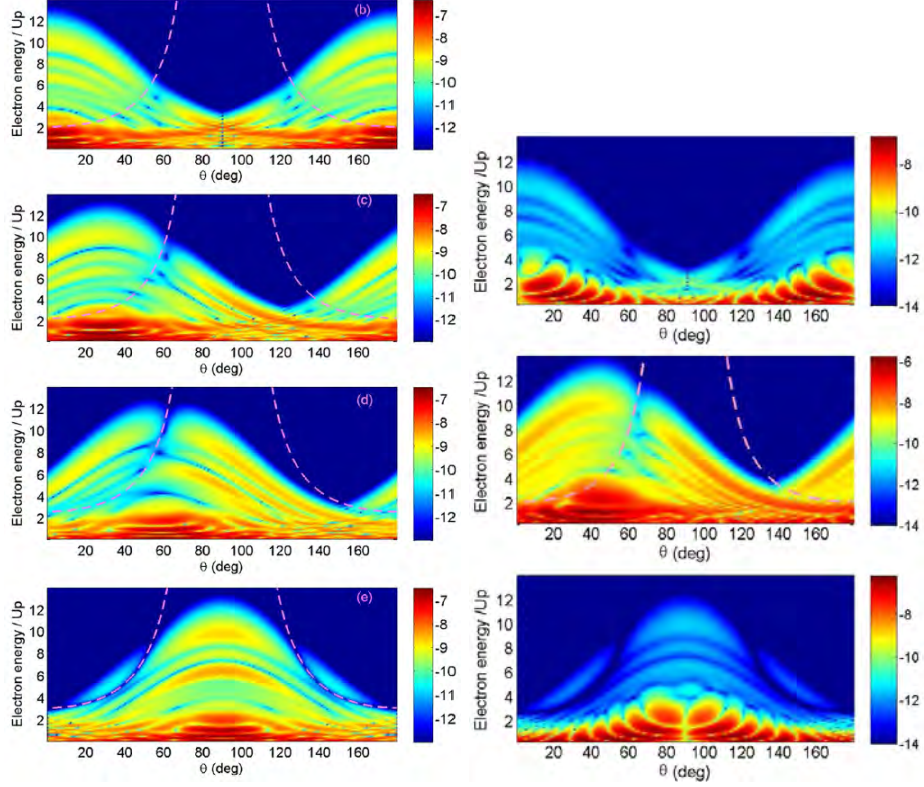
Figure 2.14.: Results by Busuladzic et al., as published in [46]: Simulations of angular-dependent electron energy spectra based on the SFA with re-scattering included. The horizontal axis shows the angle between the emission direction and the laser polarization while the electron energy is plotted along y and ionization rate is color coded. *Left*: N_2, with alignment angle from top to bottom row: 0°, 30°, 60°, 90°. *Right*: O_2 with alignment angles: 1° (top), 45° (middle), 89° (bottom image). $I = 1.68 \cdot 10^{14} \frac{W}{cm^2}$; $\lambda = 800$ nm. The dashed lines denote the expected positions of two-center interference minima.
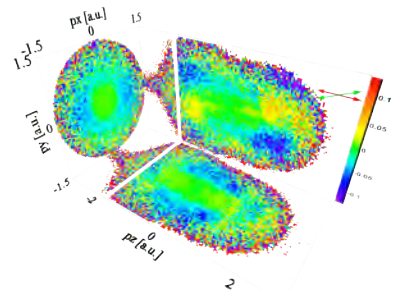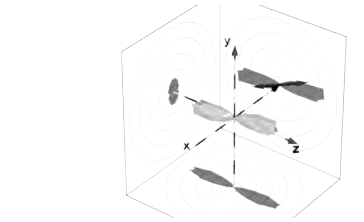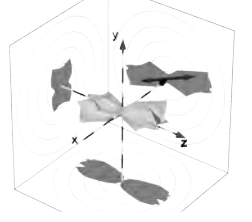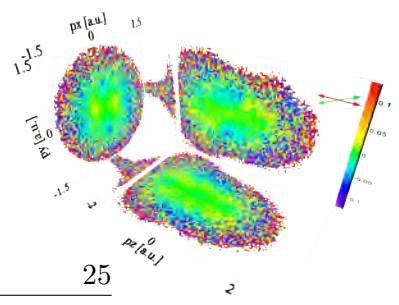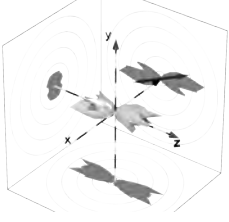
intensity was slightly lower than before. This time, they saw a minimum in the electron distribution from O_2 they had not observed before. They interpreted this minimum as double-slit interference.[7]

Also in July 2009, *Cornaggia* reported elastic singly differential electron scattering cross sections for argon and CO_2, obtained with the same method as Ray and Okunishi [51].

The idea of using the original simple man's / re-scattering model in conjunction with exact cross sections (be it elastical, inelastical or recombination cross sections) has been termed "quantitative re-scattering theory" by the group of C.-D. *Lin* [52]. They produced a whole flurry of articles on this subject, which is summarized in the given reference.

Most recently, in February 2011, *Okunishi* et al. reported differential elastic electron-ion scattering cross sections, extracted from strong-field ionized electrons for O_2^+ and CO_2^+ [53]. They did not actively align their samples but the angle-dependent ionization probabilities of the explored species provided for some "partial alignment" of the molecular distributions contributing to the signals. They ran several measurements at different pulse lengths and peak intensities. The data were then analyzed as suggested in [25] to retrieve the energy- and angle-dependent scattering cross sections. After normalization, comparison between calculated cross sections and the experiment yielded good agreement.

2.6. Non-Adiabatic Molecular Alignment

In the experiment, we had to align molecules, i.e. control the orientation of the molecular axes in the laboratory frame. To accomplish this, we employed a technique called "non-adiabatic", "transient" or "impulsive" molecular alignment [54, 1, 55, 56, 57]. Technically, this means that we shone a pre-pulse into our target that was too weak to ionize. This "pump" pulse was supposed to align the sample before the "probe" pulse ionized at a specific subsequent instant. The ideas behind shall be presented in the following, assuming a rigid rotor.

2.6.1. Exerting a Torque to Non-Polar Molecules

In order to rotate a molecule, one has to apply a torque. We measured non-polar molecules, so there was no static dipole moment that could serve as a handle. Nevertheless, the polarizabilities of N_2 and O_2 are non-isotropic. The component $\alpha_\parallel$ along the molecular axis is larger than the one perpendicular to the molecular axis $\alpha_\perp$ in both cases. If an external electric field $\vec{E}$ is applied, this leads to an

---

[7]In [49] (published in J. Phys. B), the authors properly cited [11]. This reference does not appear in [50] (Phys. Rev. Lett.), though. Interestingly, they now claimed novelty for the observed interference.
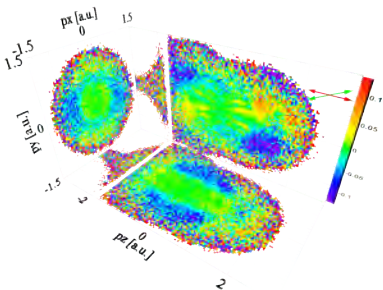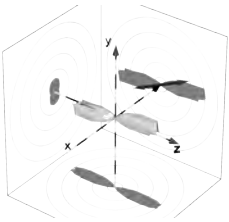
induced dipole moment

$$\vec{p}_{induced} = \begin{pmatrix} \alpha_\perp E_\perp \\ \alpha_\parallel E_\parallel \end{pmatrix} = E \begin{pmatrix} \alpha_\perp \sin\theta \\ \alpha_\parallel \cos\theta \end{pmatrix}.$$

Here, the components of $\vec{E}$ are with respect to the molecular axis and θ is the angle between the electric field and the molecular axis. $\vec{p}_{induced}$ is aligned with $\vec{E}$ only if the molecular axis is either along or perpendicular to the electric field. In any other case, there is an angle between $\vec{p}_{induced}$ and $\vec{E}$, leading to a torque

$$\vec{M} = \vec{p}_{induced} \times \vec{E}$$

rotating the molecular axis into the direction of the electric field. We used the electric field of a linearly polarized laser pulse. The oscillation of this field is not an issue because the induced dipole moment follows the oscillation.

2.6.2. Prompt Alignment

The pulses used for impulsive alignment are short - 40 to 60 fs in our case - while the timescale of molecular rotations is picoseconds. This means the pulse can only "kick" a molecule, i.e. make it spin. The pulse is off before the molecule has rotated by a significant angle. However, it continues rotating. Molecules initially lying at different angles reach alignment with the polarization direction at some instant t_0, which happens to be the same for all initial angles. This can be understood as being due to the angle-dependence of the torque exerted to the molecules.

2.6.3. Revivals

The molecules still rotate when passing the desired orientation along the polarization direction and there is nothing to stop them. Hence, the alignment dissipates quickly. However, it "revives" at defined periods due to the quantization of angular momentum. In case of the so-called "full revivals", this can be understood easily. A molecule in the rotational state $|J, M\rangle$ rotates with the angular frequency

$$\omega_J = \frac{1}{2}J(J+1)\omega_1$$

where $J = 0, 1, \ldots$ is the rotational quantum number and

$$\omega_1 = 4\pi B_0 c$$

the common fundamental frequency of all possible rotational states [54]. B is the molecule's rotational constant in wavenumbers (cm^{-1}). Values for N_2 and O_2 are given in table 2.2. The initial alignment returns at times

$$T_i = \frac{2\pi}{\omega_1}, \qquad\qquad (2.23)$$
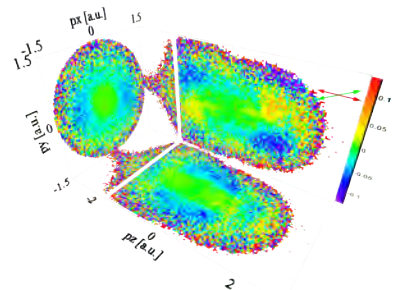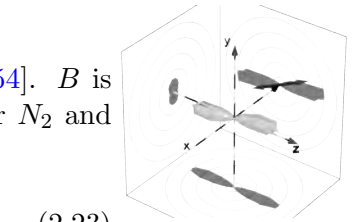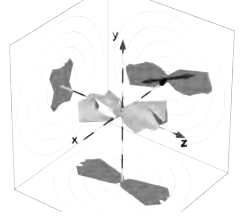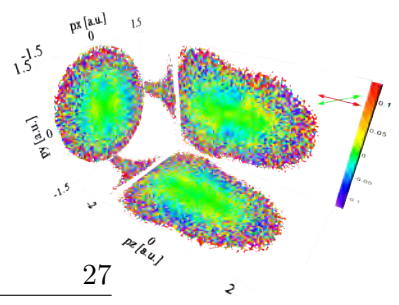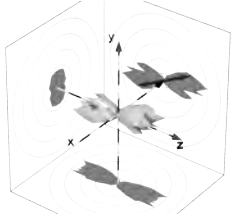
		$^{14}N_2$	$^{16}O_2$
Ionization Potential	I_P [eV]	15.581	12.0697
Bondlength	r_e [Å]	1.09768	1.2156
Rotational Constant	B_e [cm^{-1}]	1.99824	1.4264
Revival Time	T_1 [ps]	8.3464	11.693

Table 2.2.: Some constants of N_2 and O_2 in their ground state from [58]. The revival times were calculated according to equation 2.23.

which is the time it takes a molecule with $J = 1$ to rotate by 360°. If molecules are aligned in a certain direction at the time t_0, they will point along the same direction at all times $t_n = n \cdot T_1 + t_0$, with n being a natural number, regardless of their rotational quantum number J. Some even more intriguing features are found in a quantum mechanical treatment of the problem. The aligning laser pulse populates a coherent superposition of rotational states, called a *rotational wave packet*, which evolves in time:

$$\psi(t) = \sum_{J,M} a_{J,M} e^{-i(W_J/\hbar)t} \left| J, M \right\rangle .$$

Here, the rotational energy is

$$W_J = hcBJ(J + 1)$$

and the coefficients $a_{J,M} = |a_{J,M}| e^{-i\phi_{J,M}}$ contain the amplitude and relative phase of each respective state [55]. $\left| J, M \right\rangle$ are essentially the spherical harmonics. Hence, the evolution of the angular distribution of molecules is an interference between spherical harmonics. The relative phases are locked with respect to each other. If the components of the wave packet interfere constructively, molecules are aligned along the pump polarization as explained above. We will be referring to this case as "alignment" throughout this work. Such a distribution of molecules is sketched in figure 2.15(b). However, at or nearby fractions of the revival time, the case of "anti-alignment" occurs (sketch in fig. 2.15(c)), where different $\left| J, M \right\rangle$-states interfere such that the alignment direction is forbidden and molecules are distributed within a plane perpendicular to it. Factors limiting the quality of alignment are the initial, incoherent population of rotations (i.e. the rotational temperature of the target molecules) and the number of rotational states that can be populated by the aligning pulse without exceeding an intensity that would lead to ionization.
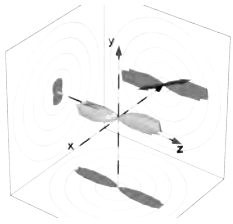
2.6.4. Alignment Parameter

A common measure for the kind and quality of alignment is the ensemble-averaged value

$$< \cos^2 \vartheta >,$$

(a) Random   (b) Alignment   (c) Anti-Alignment
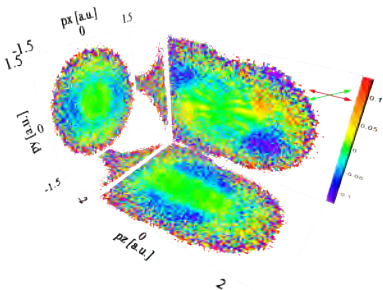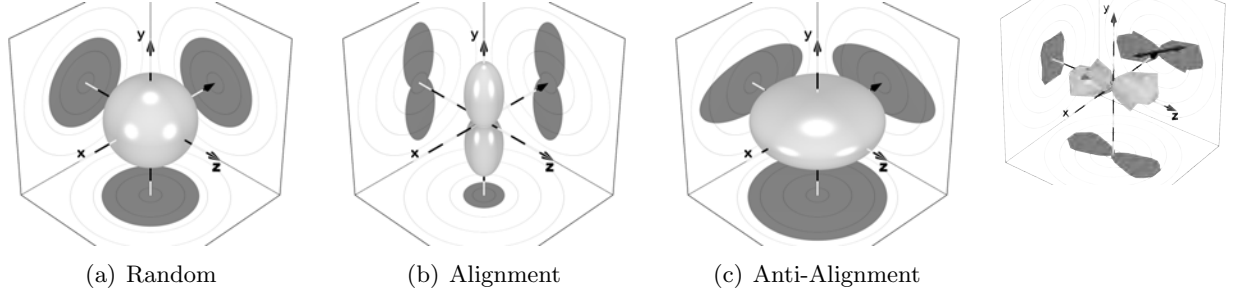
Figure 2.15.: Sketches of distributions of molecular axes: *Random* (a), *aligned* (b) and *anti-aligned* (c). The polarization of the aligning pulse (alignment direction) is along the y axis, i.e. vertical.

$< \cos^2 \varphi_{yx} >$	Name	Meaning	Sketch
0.5	Random	isotropic distribution	2.15(a)
1	Alignment	$\parallel$ alignment axis	2.15(b)
0	Anti-alignment	$\perp$ to alignment axis.	2.15(c)

Table 2.3.: Meaning of the alignment parameter as used in this work.

where ϑ is sometimes indeed the angle between the molecular axis and the aligning laser field in three dimensions. However, particularly in experiments, an angle within a coordinate plane is frequently used rather than a polar one [54, 55, 56, 43]. In this work, we will also use an azimuth angle within a plane. We will label it as φ_{yx}. Some prominent values of the alignment parameter in the definition used throughout this work are explained in table 2.3. The dependence of the alignment parameter on the delay between aligning and probing laser pulses nicely shows the rotational revival structure of the molecule; see figure 2.16.
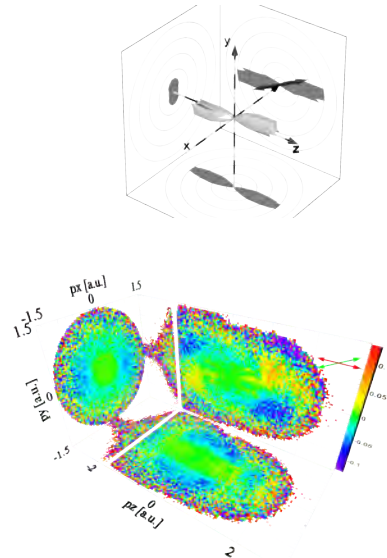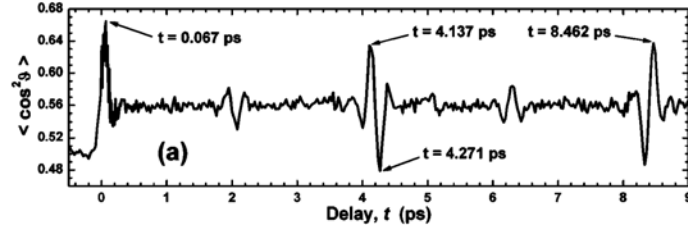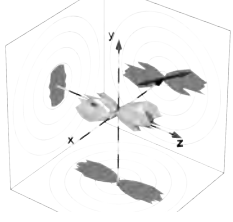
(a) Nitrogen up to its full revival.
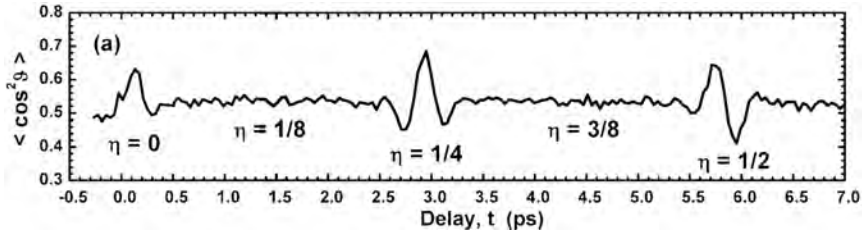
(b) Oxygen up to its half revival.

Figure 2.16.: Revival structures of N_2 (a) and O_2 (b) from [54]. The delay between an aligning and a probing laser light pulse is plotted along the horizontal axis, whereas the vertical shows the alignment parameter as defined in the text. "Peaks" indicate alignment, while "dips" correspond to anti-alignment.
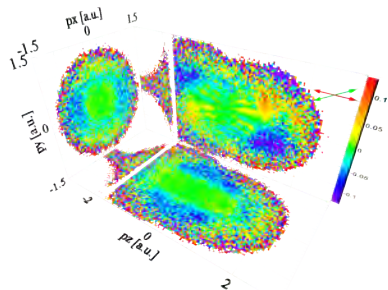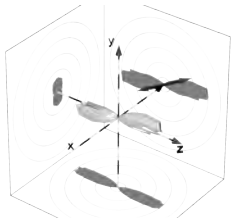
3. Experimental Setup

> A few weeks of development
> and testing can save a whole
> afternoon in the library.
>
> *(Dirk Zeidler)*

We performed two different experiments, now called experiment A and B. The setup used for experiment A is precisely the one used for the measurement of the author's Diplomarbeit [43] and has already been described there. The same machinery was used for experiment B, with some minor modifications.

Accordingly, sections 3.1 trough 3.6 were adopted from [43] with changes only made where they seemed necessary or appropriate.[1]

After presenting the "hardware" used in sections 3.1 to 3.5, we will give an overview of the formulae for detector-level data analysis in section 3.6. The equations used to convert detector coordinates to particle momenta are derived in section 3.7. Calibration aspects will be the subject of chapter 4.

3.1. Overview

An overview of the experimental setup is given in figure 3.1. Light pulses with a wavelength of 800 nm, an energy of ≈ 5 μJ and a duration of ≈ 40 fs were generated by a laser system (see details in section 3.2) and fed into a Mach-Zehnder interferometer (section 3.3.1). There, each one of them was split into an aligning "pump" and an ionizing "probe" pulse. The latter was delayed by an adjustable amount of time τ. After being split and recombined, the beam was focused into a gas target inside a so-called COLTRIMS chamber. Sophisticated particle detection devices described in section 3.4 determined the momenta of resulting electrons and ions. The observables to be captured for each event were:

- Ion momentum vector(s) in three dimensions

- Electron momentum vector in three dimensions

---

[1] These modifications are not marked as such, as a continuous sequence of "begin citation" / "end citation" markings would be nonsensical. The above-mentioned sections in this work shall be considered as a revised and extended edition of sections 3.1 to 3.6 of [43].
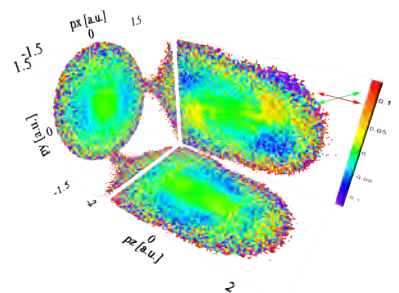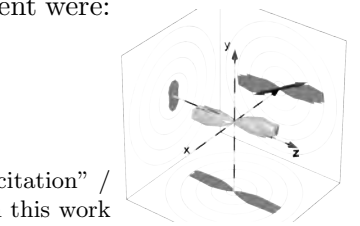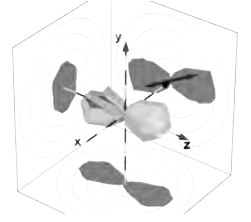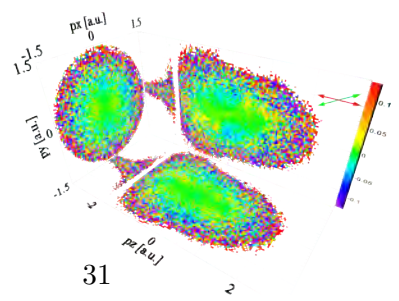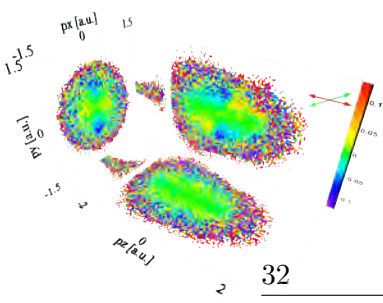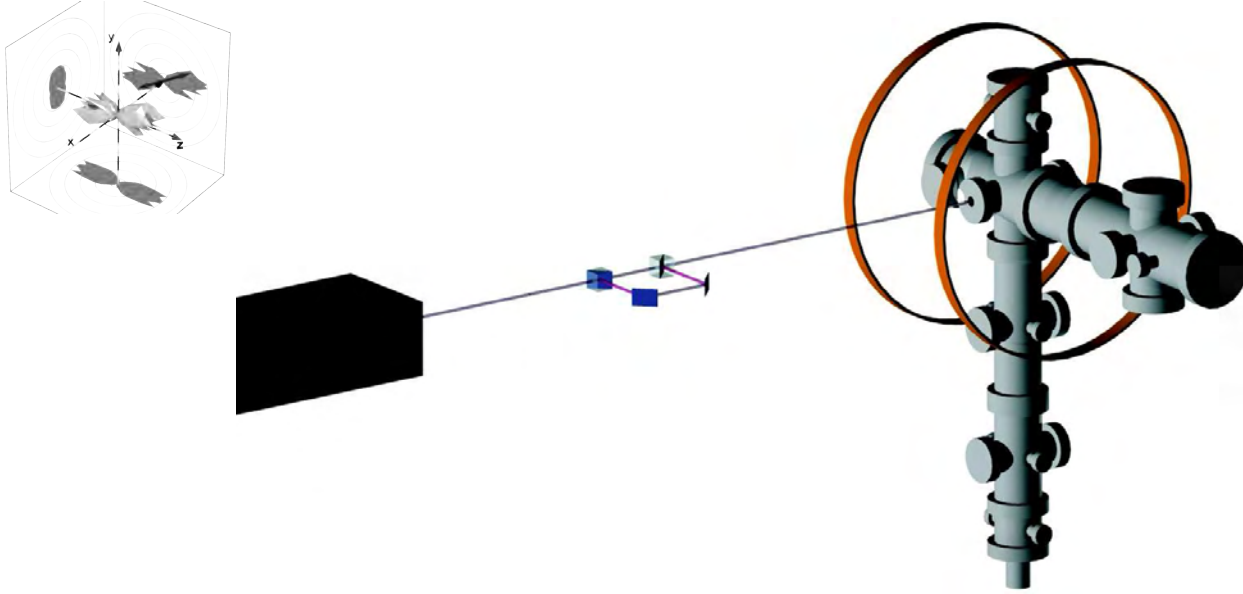
Figure 3.1.: Overview of the setup. Femtosecond light pulses generated by a laser
system (left) are fed into a Mach-Zehnder interferometer (middle). The
resulting pump and probe pulses interact with gas molecules in a so-called
COLTRIMS chamber (right). The momenta of resulting electrons and ions
are determined.
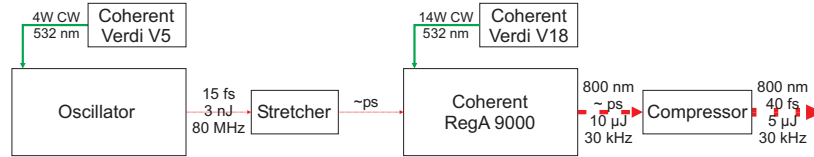
Figure 3.2.: Diagram of the NRC's high repetition rate femtosecond laser system as
used for experiment A. Short light pulses are generated by a Kerr lens
modelocking oscillator and dispersed by a grating stretcher. The chirped
pulses are amplified by a Coherent RegA 9000 regenerative amplifier sys-
tem. Finally, they are re-compressed with a grating compressor. The os-
cillator and the amplifier were pumped by separate solid state CW lasers
(Coherent Verdi series). In case of experiment B, both the oscillator and
the amplifier were pumped by the V18.

- Pump-probe delay.
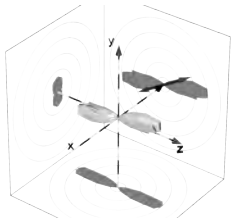
3.2. Laser

Note: A review including the techniques behind the laser system used can be
found in [59]. What follows is basically common knowledge in the laboratory, so
detailed references are omitted.
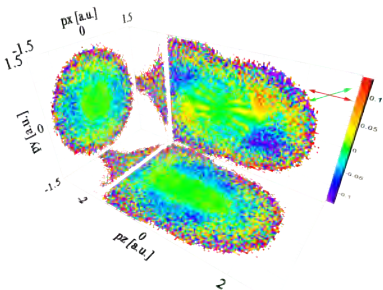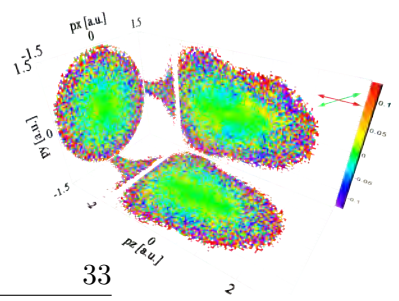
Figure 3.2 shows the principal components of the NRC's laser system. A Kerr lens modelocking oscillator produced weak ($\approx$ 3 nJ) but short ($\approx$ 15 fs) light pulses at a very high repetition rate ($\approx$ 80 MHz). These were stretched by a grating stretcher and fed into a Coherent RegA 9000 Ti:Sa regenerative amplifier system. After amplification, pulses were re-compressed to $\approx$ 40 fs. Their central wavelength was $\lambda = 800$ nm. After compression, the typical pulse energy at a repetition rate of 30 kHz was $\approx$ 5 μJ. In the spatial domain, such a pulse is 12 μm long and performs 15 cycles. The beam diameter was approximately 7 mm. Hence, the system emitted thin "light discs", ideally with a Gaussian profile in all directions.
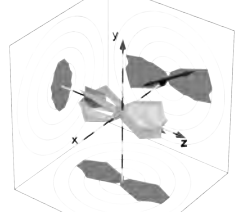
3.2.1. Oscillator

Short pulse generation started in the oscillator. This part of the system entirely depends on the optical Kerr effect.

3.2.1.1. Kerr Lenses

The refractive index of many materials changes if an electric field E is applied:

$$n(\lambda, E) = n_0(\lambda) + S_1(\lambda) \cdot E + S_2(\lambda) \cdot E^2 + \dots$$

The case where the squared term in E dominates over all other powers is known as Kerr effect. A light wave has an electric field, depending on its intensity: $I \propto E^2$. So, as one might expect, there is an "optical Kerr effect": The refractive index depends on the light intensity via

$$n(\lambda, I) = n_0(\lambda) + n_1(\lambda)I.$$

Hence, if $n_1(\lambda) > 0$, a medium constitutes a larger optical path length for high intensity light than for lower intensities. In general, one has to deal with beam profiles showing a high intensity on the beam axis and an intensity drop off-axis, e.g. gaussians. In media showing the optical Kerr effect, those pulses create a "Kerr lens" for themselves; see figure 3.3. The λ-dependence of the refractive index causes dispersion which has to be compensated for.

3.2.1.2. Modelocking

An oscillator built on this principle is basically just a laser with a high-bandwidth gain medium also acting as a Kerr lens. A Ti:Sa crystal like the one used in the NRC's system can serve as a laser medium for a relatively wide range of optical wavelengths ($\approx$ 800 nm $\pm$ 100 nm FWHM [59]). Therefore all cavity modes within this window can be amplified. If they interfere constructively once, this leads to a pulse forming. Normally this pulse would quickly disappear due to dispersion. But in the crystal, it will be Kerr lens focused, enhancing its intensity. The gain in the pumped material (below saturation) rises with intensity. Hence,
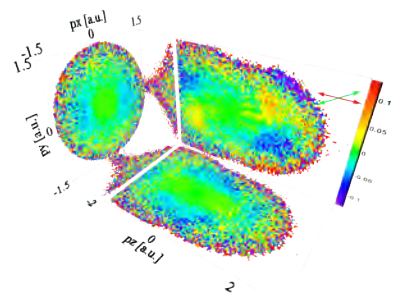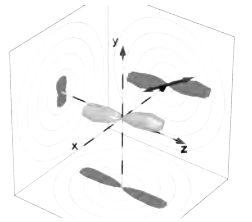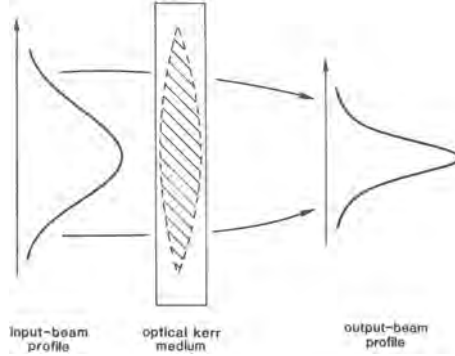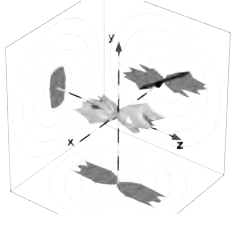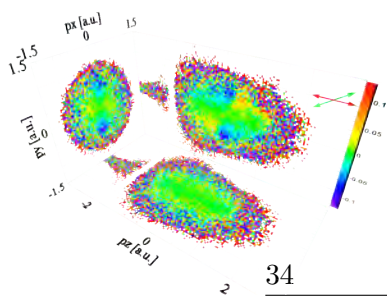
Figure 3.3.: Effect of a "Kerr lens": The spatial profile of an incoming pulse turns a medium into a lens, leading to self-focusing. From [60].

	Specification
Oscillator Type	Kerr lens modelocking Ti:Sa
Output Repetition Rate	80 MHz
Output Pulse Energy	3 nJ
Output Pulselength	15 fs bandwidth limit
Pump Laser Type	Coherent Verdi V5 diode-pumped solid state
Pumping Wavelength	532 nm
Pumping Power	≈ 4 W

Table 3.1.: Specifications of the oscillator.

the constructively interfering modes forming a pulse are strongly favored over modes with arbitrary relative phases. The pulse is amplified much stronger than continuous wave (CW) modes, which makes the pulselength (full width at half maximum) decrease. The phenomenon of pulseforming modes staying together at a constant phase is called *modelocking*. Just like a laser, an oscillator contains a partially reflecting cavity mirror which makes it emit some of the circulating light. But in contrast to a CW laser where a continuous flow of photons fills the whole cavity, there is just the oscillating pulse. So the oscillator emits pulses.

3.2.1.3. Limitations
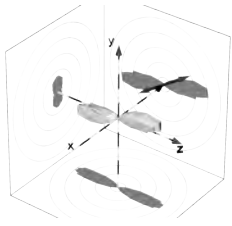
The gain medium's bandwidth limits the pulselength achievable in principle. Additionally, dispersive effects have to be compensated for. (In our case, two prisms were used to accomplish this.) The maximum pulse intensity achievable is constrained by saturation in the gain medium. An oscillator's output repetition rate is inherently fixed to the circulating pulse's roundtrip time.

Specifications of the system used for this work are summarized in table 3.1.
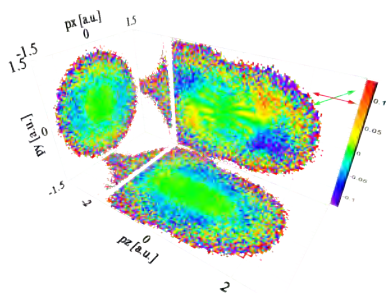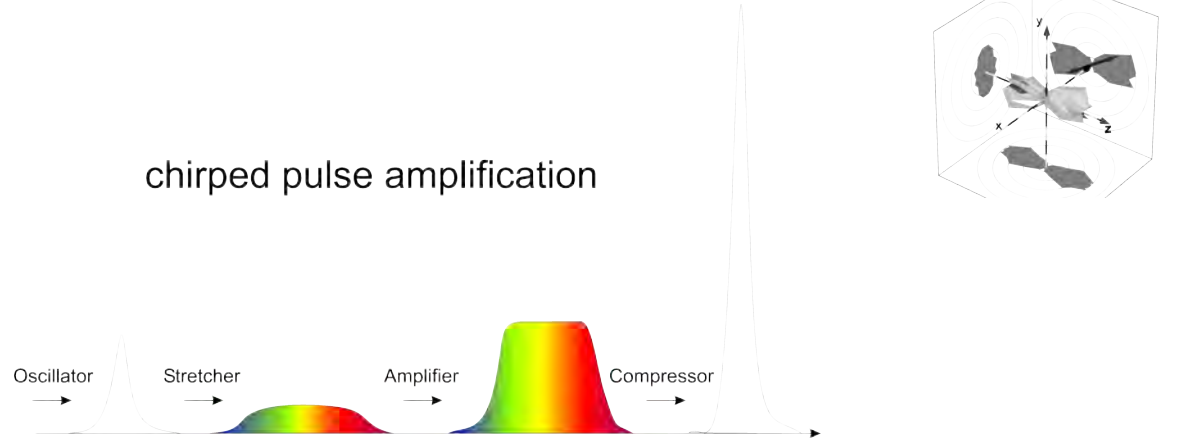
Figure 3.4.: Scheme of Chirped Pulse Amplification (CPA): A short but low-energy
pulse from the oscillator is stretched by means of dispersion. The now
long pulse is then amplified to higher energy. After this step, it is re-
compressed by a negatively dispersive medium. This allows for a final
peak intensity far beyond the damage threshold of the amplifier. Image
from [5].

3.2.2. Chirped Pulse Amplification

Pulse energies that can be provided by an oscillator are much too weak for
strong-field experiments. Those pulses have to be amplified. Every amplifier
has a damage threshold intensity. Therefore, one is interested in stretching
pulses temporally and / or spatially before amplifying them to achieve large
pulse energies at low intensities inside the amplifier. After amplification, pulses
have to be compressed again.

In the frequency domain, a pulse consists of a band of frequencies. Ideally, all
these waves have the optimal relative phase which leads to a pulse that is "Fourier
limited", meaning that it is as short as possible at a given bandwidth. But in
a medium with a wavelength dependent refractive index $n = n(\lambda)$, the Fourier
components quickly disperse. Their maxima do not match in time anymore
which leads to a longer pulse. In case of normal (positive) dispersion, smaller
wavelengths are delayed more than larger ones. The opposite happens in case
of anomalous (negative) dispersion. The result is called a "chirp" in analogy to
the acoustical representation of the resulting pulses.

Hence, it is possible to stretch pulses by, for example, positively chirping them.
The stretched pulses can be strongly amplified without causing damage and
afterwards compressed by negative dispersion (or vice versa). This scheme is
called "*Chirped Pulse Amplification*"(CPA) [61]. In the laser system used here,
a grating stretcher and a grating compressor served as dispersive media. The
principle of CPA is illustrated in figure 3.4.
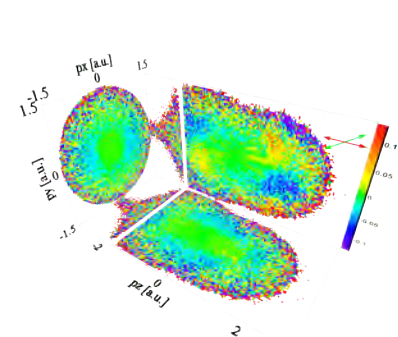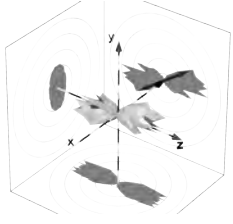
| | Experiment A | | Experiment B | | |
Pulse	W_{pulse} [μJ]	Polarization	W_{pulse} [μJ]	Polarization	τ [fs]
Incident	5.3	adjustable	5.8	adjustable	
Pump	1.2	along y	0.7	adjustable	60
Probe	3.0	along z	1.3	along z	40

Table 3.2.: Input and output of the interferometer. Pulse energies W_{pulse} were measured as beam powers with a calorimetric power meter. Polarization directions are given in the coordinate system of the COLTRIMS measurement; cf. section 3.6.1 / figure 3.17. The pulse lengths τ given are estimates for the focus inside the target chamber, not the interferometer.

3.2.3. Amplifier

The stretched oscillator pulses were amplified by a Coherent RegA 9000 regenerative amplifier. This system's main feature is its widely adjustable pulse repetition rate. Throughout this work a pulse repetition rate of 30 kHz was used but everything between 10 kHz and 250 kHz would have been possible, from some point on at the cost of shrinking pulse energy. Amplified pulses had an energy of ≈ 10 μJ. The compressor absorbed about 50%. So, the whole system's net output were pulses with an energy of 5 μJ at a repetition rate of 30 kHz. The pulse length was not measured especially for this work but estimated to be ≈ 40 fs, in agreement with previous experiments.

3.3. Optics

3.3.1. Interferometer

As mentioned before, the light emitted by the laser system was split into pump and probe pulses in a Mach Zehnder interferometer (see figure 3.5). The pump beam was fed through the fixed arm of the interferometer and the probe pulses' excess path length could be varied by a computer-controlled translation stage. Aligning pulses were stretched by chirping with a 15 mm quartz block. This was intended to keep the pump intensity below the ionization threshold of the target gas while still providing a reasonable pump energy. The latter was adjusted such that the pump beam without probe did not ionize the target.

3.3.1.1. Experiment A

In case of experiment A, the pump beam was additionally clipped with an iris. The latter was hoped to help achieve a larger focal volume for pump than for probe pulses, making sure only "pumped" molecules were ionized. Pulse parameters are summarized in table 3.2.

We used a polarizer cube to split the beam. This enabled us to adjust the splitting ratio by rotating the polarization plane of the (linearly polarized) incident
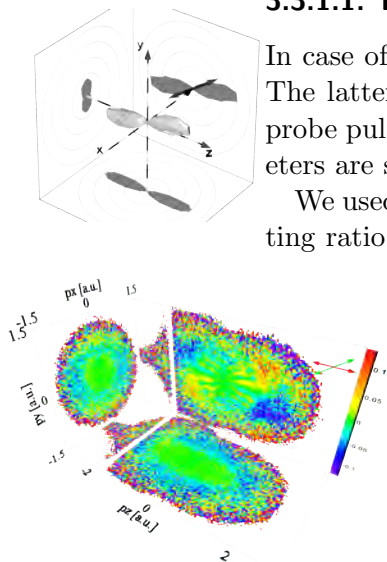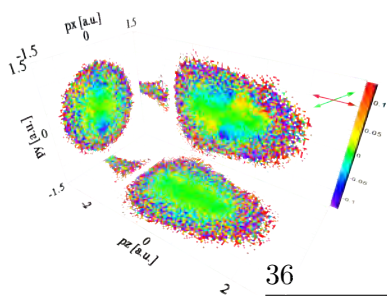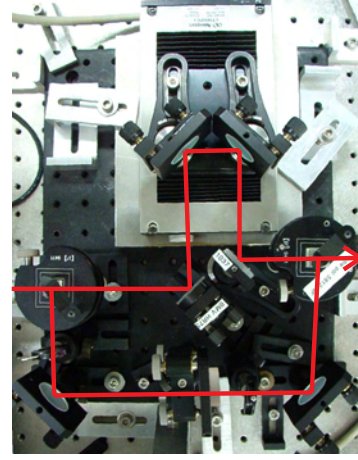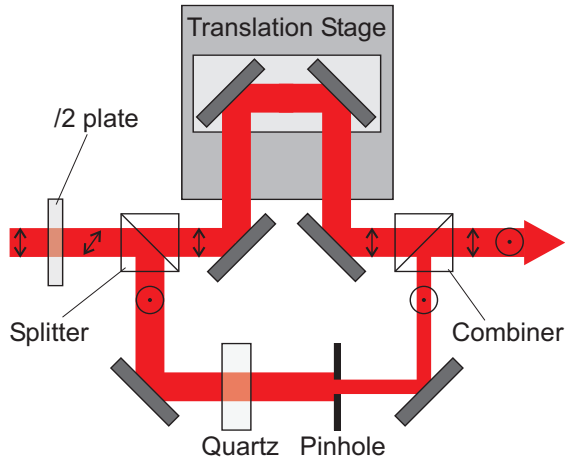
Figure 3.5.: The interferometer as used for experiment A, schematically and as a photo. The beam (coming from the left) is split by a polarizer cube, enabling us to choose the splitting ratio with a $\lambda/2$ plate. The path length of the probe beam can be adjusted via a computer-controlled translation stage. Aligning pulses are stretched by a 15 mm quartz block and, in case of experiment A, clipped by a pinhole. For experiment B we removed the latter and added another $\lambda/2$ plate, mounted in a computerized rotation stage. The beam combiner was another polarizer cube in case of experiment A and a non-polarizing beamsplitter in B. Arrows in the sketch symbolize the polarization direction. In experiment B, we rotated the pump polarization in front of the beam combiner.
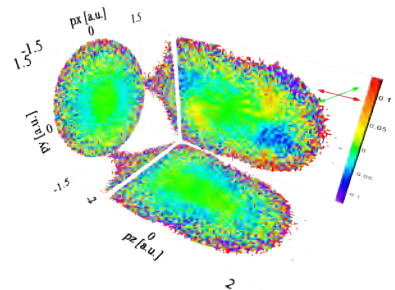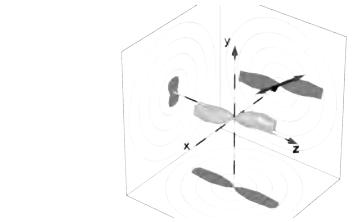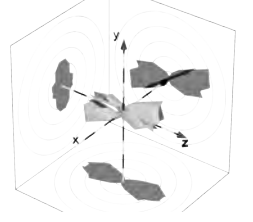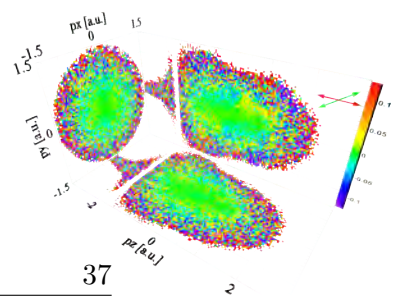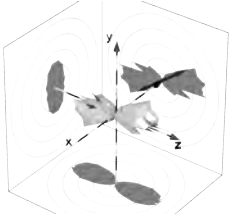
light.

The beams were recombined by another polarizer cube. This enabled us to combine the beams without losing pulse energy. On the down side, the recombining polarizer forced the polarizations of aligning and ionizing pulses to be perpendicular to each other, allowing for only one alignment direction in experiment A.

The excess path length of ionizing over aligning pulses was adjustable and measurable with the translation stage in the interferometer, driven by a programmable stage controller. We programmed the controller to autonomously change the position of the stage. The positions to be taken were those corresponding to the pump-probe delays leading to alignment of N_2, anti-alignment of N_2, alignment of O_2 and anti-alignment of O_2. After maintaining one such delay for ten seconds, the stage was moved to the next. The exact program performed by the stage dontroller can be found in the appendix, section E.1.

By switching between delays we became insensitive to any potential drift in the systems, as such instabilities should affect data taken under all delays alike. We did not observe any instabilities, though.

3.3.1.2. Experiment B

Experiment B was intended to lift the restriction of aligning and ionizing pulses being polarized perpendicular to each other. We replaced the polarizing beam combiner by a non-polarizing one. This came at the expense of an extra 50% loss in pulse energy. We removed the clipping iris from the pump arm of the interferometer to save energy. A $\lambda/2$ wave plate mounted in a computer-controlled rotation stage enabled us to rotate the polarization of the pump beam. The beam combiner used was specified to have a polarization-independent reflectivity within a small margin in the wavelength region of our pulse (800 nm); see figure 3.6. We checked this with a power meter.

In the experiment, we now maintained a constant pump-probe delay corresponding to alignment of the species being measured. We made the rotation stage rotate the pump polarization in increments of 2° after every three seconds from 0° to 360° (i.e. the waveplate was rotated from 0° to 180° in 1° increments). The precise stage program is again given in the appendix, section E.1.

3.3.2. Laser Focus

The last optical device interacting with the laser beam was a parabolic mirror with a focal length of $f = 50$ mm mounted inside the COLTRIMS chamber to focus the light into a jet of molecules (see figure 3.7).

The peak intensity of a focused light pulse of the temporal length τ and a gaussian spatial profile is [5]

$$I(r,x) = \frac{2W_{pulse}}{\tau\pi w(x)^2} \cdot e^{-2\frac{r^2}{w(x)^2}} \tag{3.1}$$
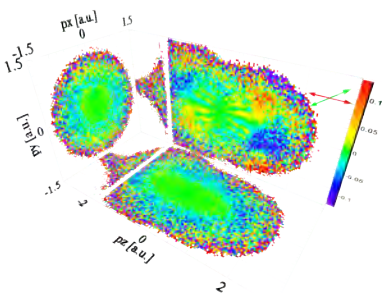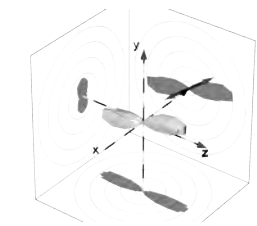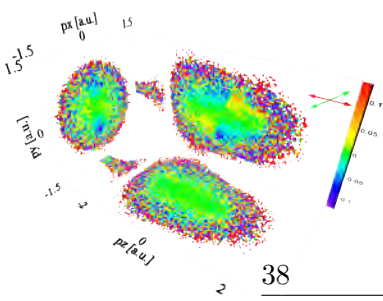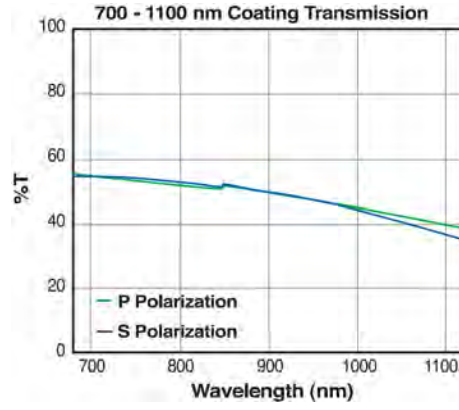
Figure 3.6.: Specified transmission characteristics of the beam combiner used in experiment B of type ThorLabs BS011. The central wavelength of our light was at 800 nm, where the transmission of s- (perpendicular) and p- (parallel to the surface) polarized light is virtually identical. From [62].
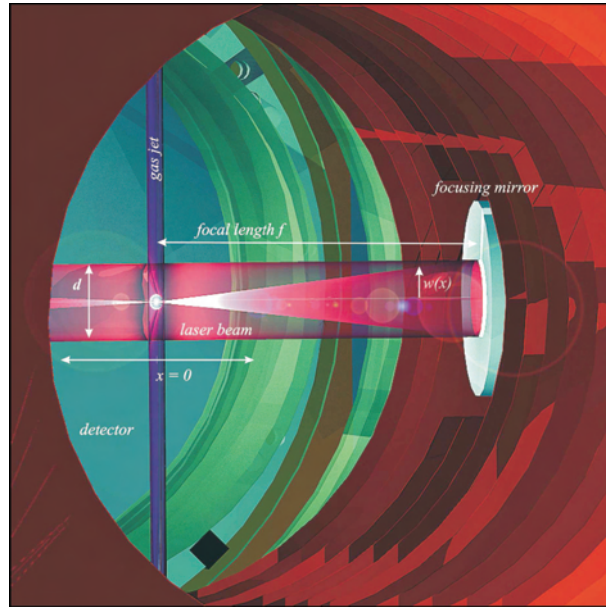
Figure 3.7.: Laser light is focused into a gas target by an $f = 50$ mm parabolic mirror inside the COLTRIMS chamber. Image from [5].
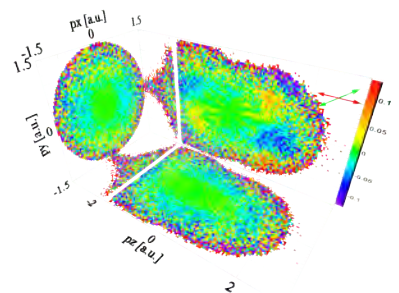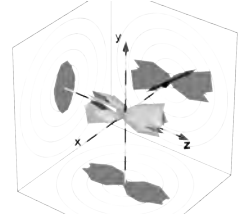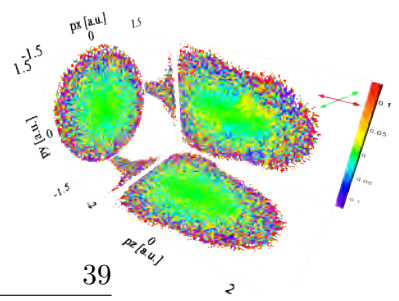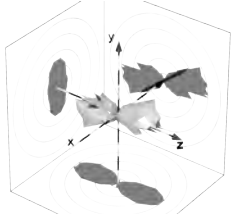
	$x\ [\mu\mathrm{m}]$	$r\ [\mu\mathrm{m}]$	$\hat{I}\ \left[10^{14}\frac{\mathrm{W}}{\mathrm{cm}^2}\right]$
Experiment A: Pump	566	10.0	0.18
Experiment A: Probe	124	4.7	3.0
Experiment B: Pump	124	4.7	0.47
Experiment B: Probe	124	4.7	1.3

Table 3.3.: Numerical findings from the calculations in figure 3.8: Dimensions of the focal spots for all pulses. The offsets from the center of the focus x along and r perpendicular to the beam axis are FWHM values of the intensity distributions. Beam diameters were not measured. We adjusted them such that the calculated probe intensities matched their known values (cf. chapter 4.2.1 for intensity calibration). The diameter of the pump in experiment A is estimated.

where W_{pulse} is the pulse energy, r denotes the lateral and x the longitudinal distance from the focal spot. The beam waist $(1/e^2)$ is

$$w(x) = w_0 \cdot \sqrt{1 + \left(\frac{x}{x_r}\right)^2}$$

with the minimum beam waist

$$w_0 = 2 \cdot \frac{\lambda f}{\pi d}$$

and the Rayleigh length (distance from the focus along the beam axis where intensity dropped by half)

$$x_R = \pi \cdot \frac{w_0^2}{\lambda}$$

with d being the unfocused beam's diameter. This yields the maximum intensity in focus $(x = r = 0)$

$$I_{max} = \frac{\pi}{2}\frac{W_{pulse}d^2}{\tau f^2 \lambda^2}. \tag{3.2}$$

Spatial intensity distributions calculated according to equation (3.1) are shown for pump and probe pulses in figure 3.8. Table 3.3 summarizes numerical findings from this simulation.

3.4. COLTRIMS
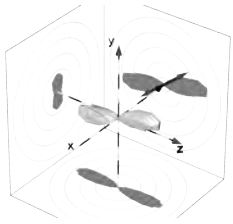
The acronym COLTRIMS stands for COLd Target Recoil Ion Momentum Spectroscopy. A cold gas jet serves as target. Particle detectors measure quantities allowing the reconstruction of three-dimensional initial momentum vectors for electrons and ions created in ionization events in correlation, event by event. This is what distinguishes COLTRIMS from other techniques: The aim of kinematically complete reaction imaging. The COLTRIMS chamber used in this work is sketched in figure 3.9.
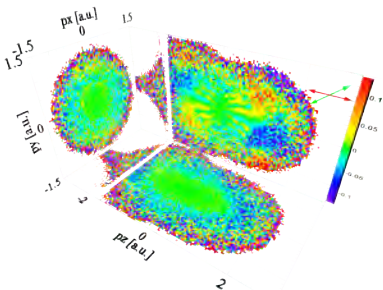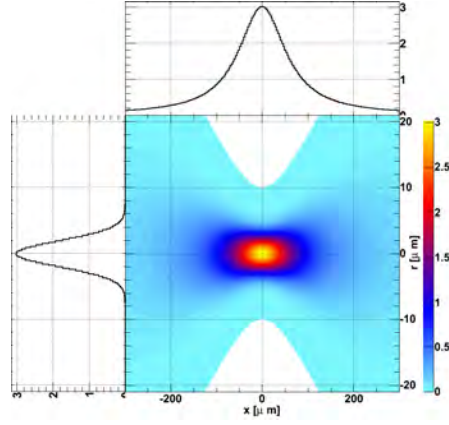
(a) Experiment A, Probe Pulse: $W = 3.0 \; \mu$J, $\tau = 40$ fs, $d = 6.4$ mm.
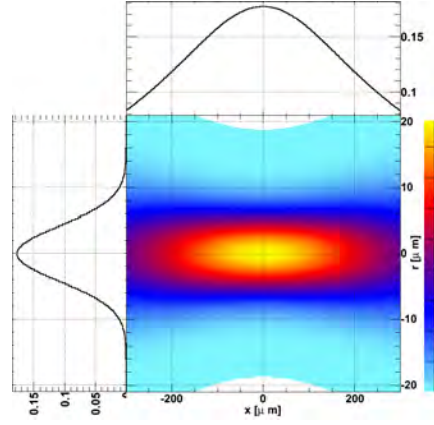
(b) Experiment A, Pump Pulse: $W = 1.2 \; \mu$J, $\tau = 60$ fs, $d = 3$ mm.
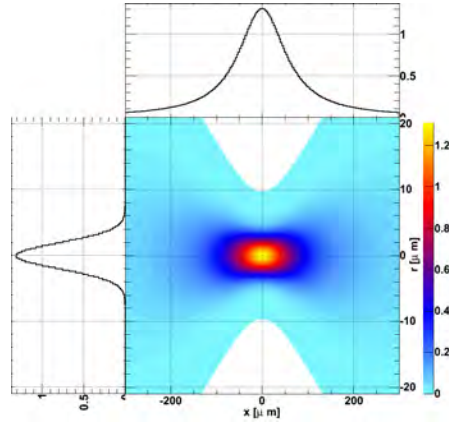
(c) Experiment B, Probe Pulse: $W = 1.3 \; \mu$J, $\tau = 40$ fs, $d = 6.4$ mm.
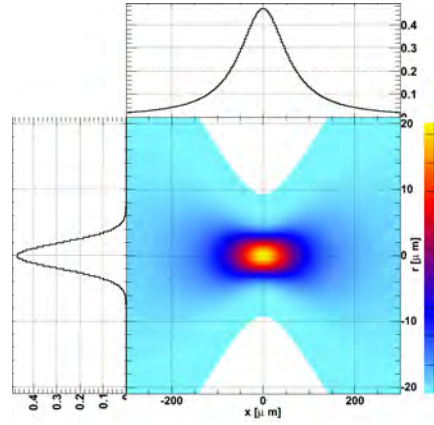
(d) Experiment B, Pump Pulse: $W = 0.7 \; \mu$J, $\tau = 60$ fs, $d = 6.4$ mm.

Figure 3.8.: Intensity distributions in $10^{14} \; \frac{\text{W}}{\text{cm}^2}$ (*color*-coded), depending on the offset from the center of the focus along (*horizontal*) and perpendicular to the beam direction (*vertical* axes). The diameter of the probe beam in experiment A (a) was adjusted such that the peak intensity matched the value obtained in the calibration chapter. The same diameter was assumed for both pulses of experiment B ((c) and (d)). The respective value for the clipped pump beam of experiment A (b) was estimated. Dimensions of the foci are summarized in table 3.3. The intensity obtained for the pump in experiment B 3.8(d) ($\approx 0.5 \cdot 10^{14} \; \frac{\text{W}}{\text{cm}^2}$) seems a bit high.
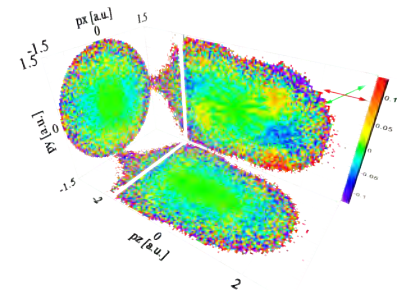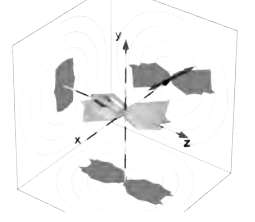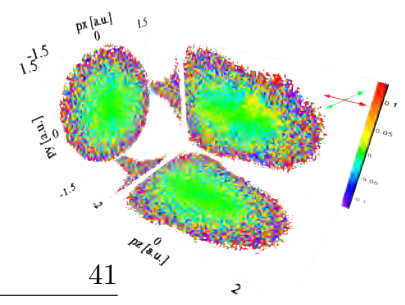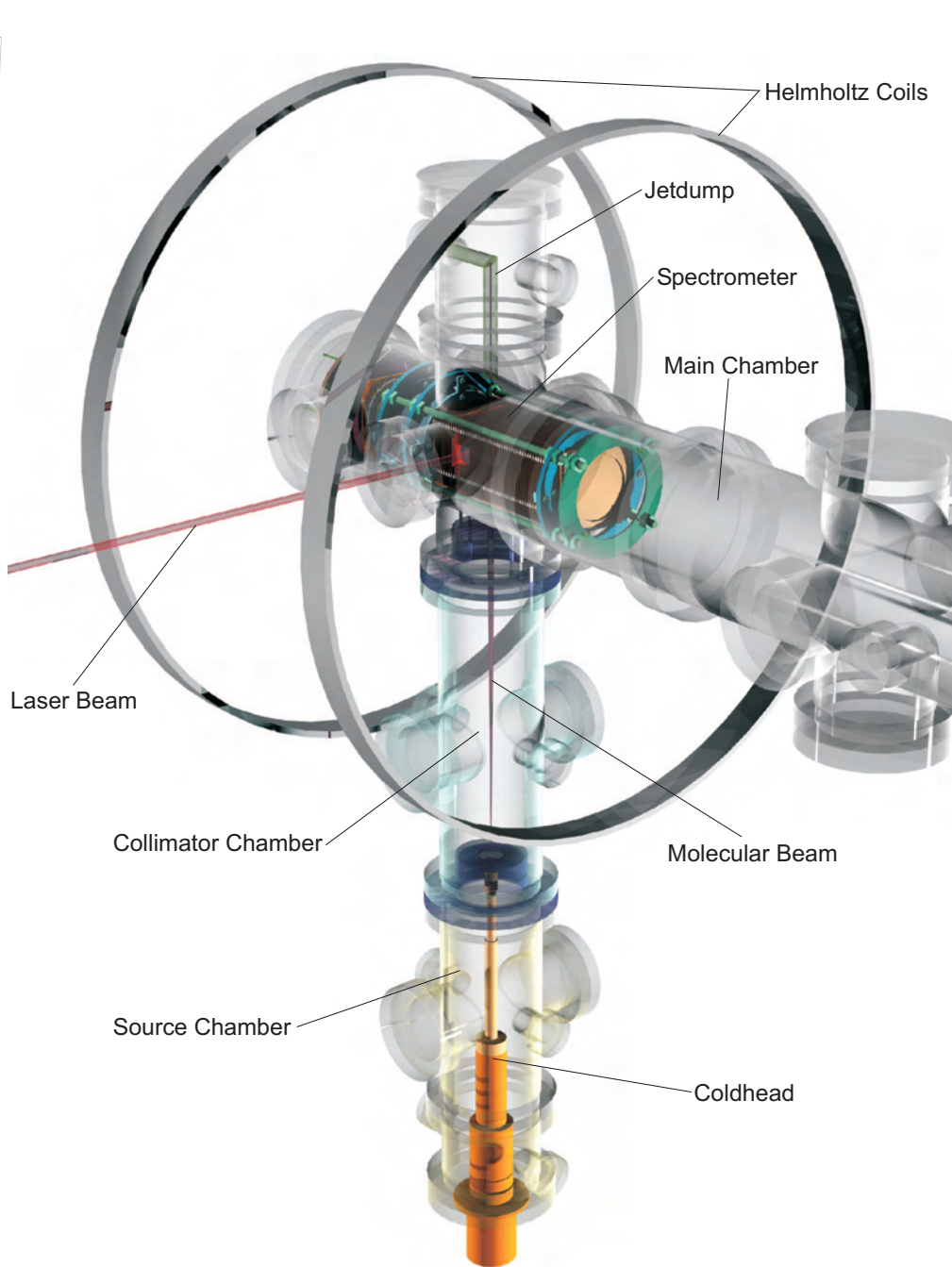
Figure 3.9.: Overview of the COLTRIMS chamber used in this work. The horizontal
main chamber houses the spectrometer. The vertical tube below contains
the jet setup. In these "source chambers" a cold beam of molecules is
created and fed through the laser focus in the main chamber. The many
turbo pumps needed to maintain good vacua in operation were omitted
from the drawing for clarity.
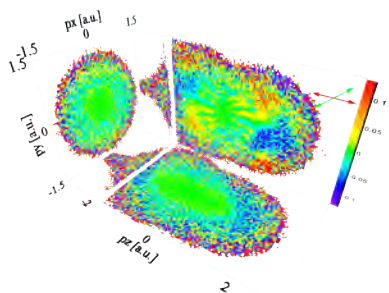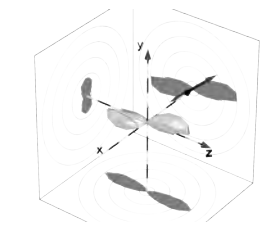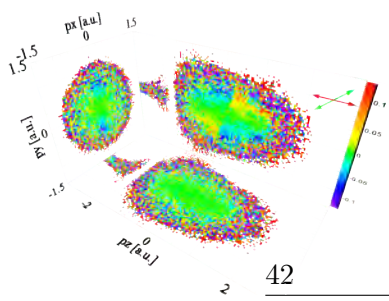
3.4.1. The Jet

The average thermal energy of gas molecules is about 26 meV at room temperature. This corresponds to a momentum of ≈ 10.6 a.u. for an O_2 molecule. It is clear that an intrinsic momentum spread in this order of magnitude is unacceptable for high precision experiments. Additionally, the achievable degree of alignment is higher for a rotationally cold target than for incoherently spinning molecules.

If some gas expands into vacuum, the "cloud" resulting from such a supersonic expansion has an inner structure such as the one shown in figure 3.10. Essentially, there is a beam of molecules with high but directed, narrowly distributed velocities and little rotations on the nozzle axis, separated from "warm" regions by the so-called "zone of silence". This is exploited for cooling purposes by cutting out the warm regions with a skimmer.

Figure 3.11 outlines the jet setup used in the experiment. The nozzle (diameter: 10 μm) was cooled down to 110 K by a cryo coldhead. In addition to the skimmer, a second aperture kept molecules with transverse velocities outside the main chamber which helped maintain a good vacuum there. The resulting cold beam of molecules was fed through the laser focus in the UHV chamber and finally pumped off in the jetdump.

3.4.2. The Spectrometer

Figure 3.12 sketches the spectrometer. Electrons and Ions were born in the laser focus. In the extraction zone, an electric field accelerated them towards their respective position and time sensitive detector. A homogeneous magnetic field parallel to the spectrometer axis confined electrons to spiraling trajectories. This prevented them from missing the detector's active area or escaping from the spectrometer otherwise, even in case of moderate electric fields.
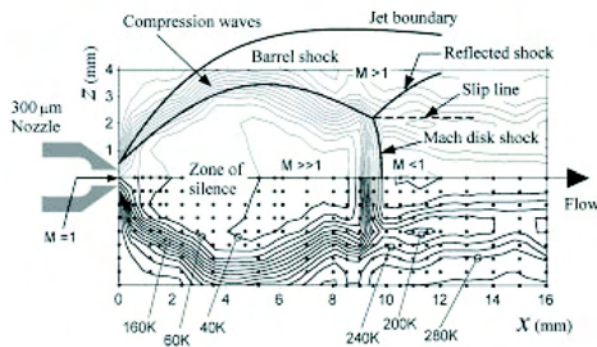
Figure 3.10.: Raman mapping of rotational temperatures in a supersonic jet of CO_2 under a stagnation pressure of 2 bars. Isothermal lines are depicted at steps of 20 K. [63]
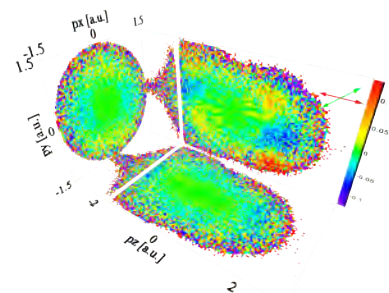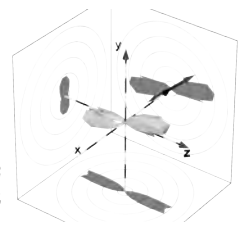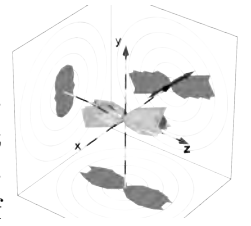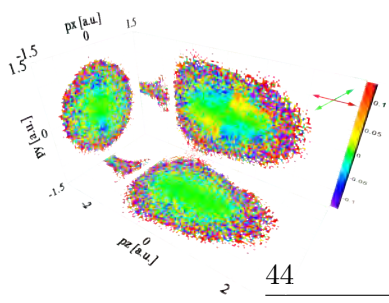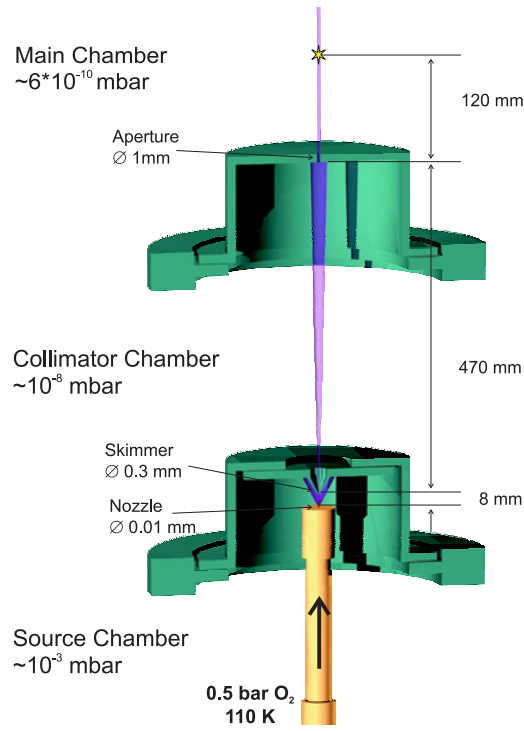
Figure 3.11.: The jet setup. During the experiment, the target gas was pushed through the nozzle, which was cooled to 110 K by a cryo coldhead. Adopted from [5].
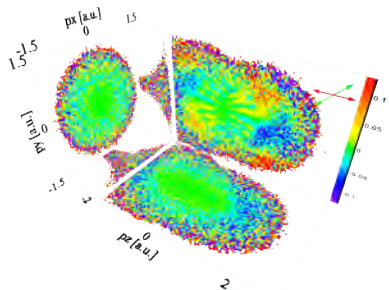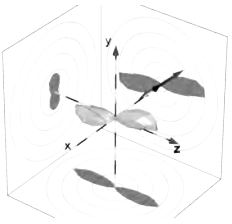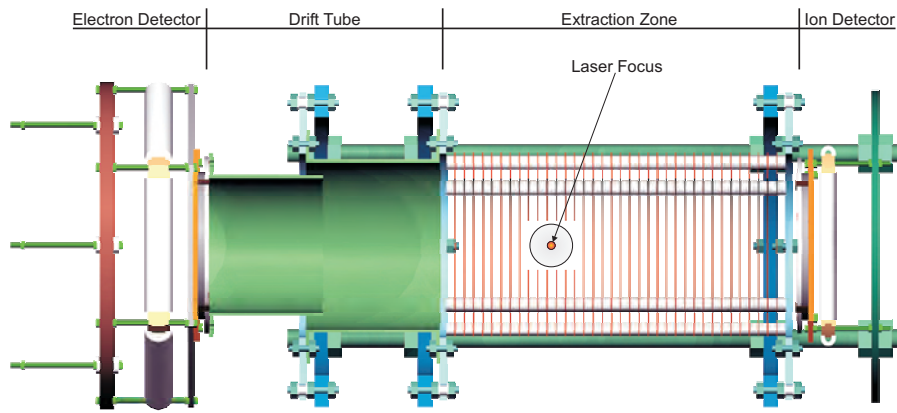
Figure 3.12.: Sketch of the spectrometer. Electrons and ions are born in the laser focus. An electric field E accelerates positively charged ions towards the position sensitive detector on the right hand side. Electrons are guided to the detector on the left hand side, via a drift tube. A magnetic field parallel to the spectrometer axis confines them to spiralling trajectories. The fields are supposed to be homogeneous. But in order to make focusing of the laser beam into the jet with an $f = 50$ mm parabolic mirror possible, a few spectrometer plates had to be cut out. The mirror is conductive and therefore acts as an equipotential surface, distorting the electric field. Image from [5].
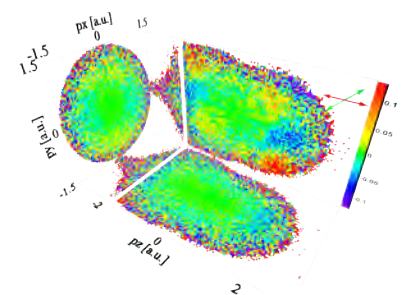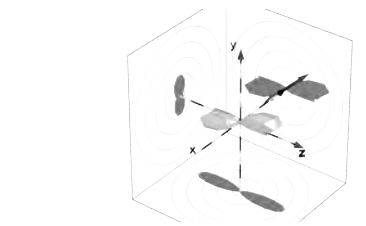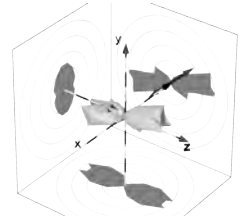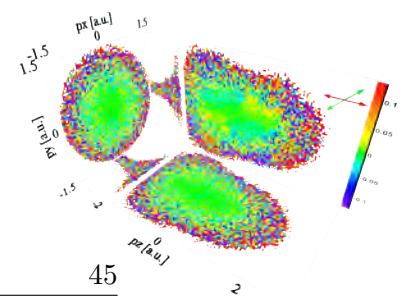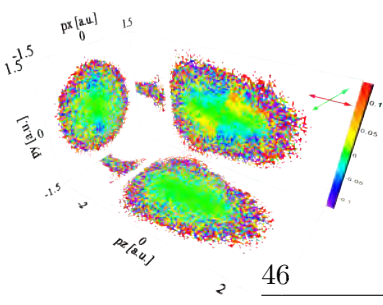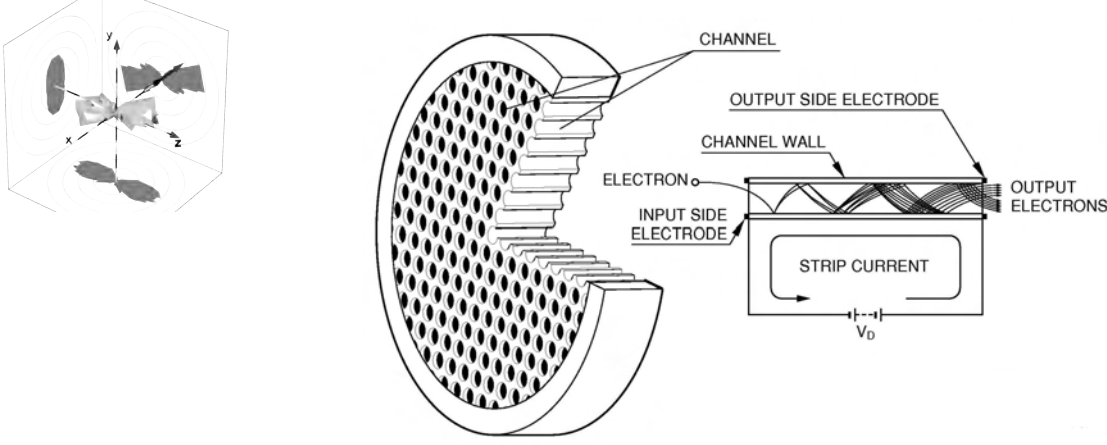
Figure 3.13.: Sketch of a microchannel plate (MCP). Each single channel acts as a secondary electron multiplier. If an incident particle hits a channel wall, an avalanche is started, which can be measured as a strip current I_{MCP}. This is used for time encoding. Secondary electrons leaving the MCP provide position encoding. Image from [64].

For position and time of flight encoding, microchannel plate detectors with delayline readout were used.

3.4.2.1. Microchannel Plate Detectors

A microchannel plate (MCP) is, in principle, an array of millions of microscopic secondary electron multipliers. In practice, an MCP is a thin disc of lead glass with many tiny channels (figure 3.13). The distance between two channel openings is typically some 10 μm. Lead glass has a high resistance. The disc surfaces are metal coated to act as electrodes. The inner surfaces of the channels are processed to show semiconducting behavior [65]. If a voltage in the order of $U_{MCP} \approx 1$ kV is applied over an MCP and a charged particle strikes a channel wall with sufficient kinetic energy, secondary electrons are released from the material and accelerated by U_{MCP} to strike the channel wall at another position and release further electrons by themselves and so forth. An avalanche is started. To make sure any incident or secondary particle strikes a wall, the channels are oriented at an angle to the MCP surface. Additionally, it is common to use stacks of at least two MCPs with channels tilted in opposite directions, resulting in v-shaped net channels. This also prevents any positive ions released from the second MCP's back side from escaping into the spectrometer ("ion feedback"). We used double stacks. These can typically produce between 10^6 and 10^8 secondary electrons per incident particle [65].

Seen from the power supply's perspective, an electron avalanche is a current pulse I_{MCP} through the MCP. In our detectors, the MCPs were connected to their power supplies via resistors. Therefore, each particle starting an avalanche
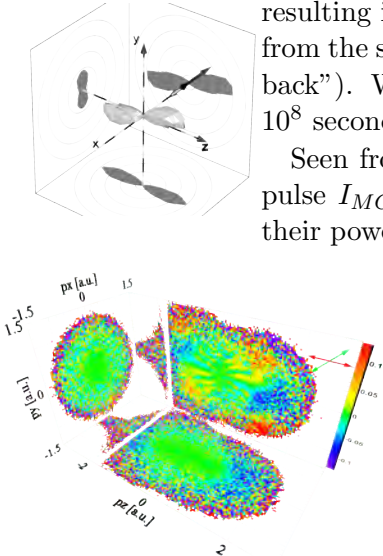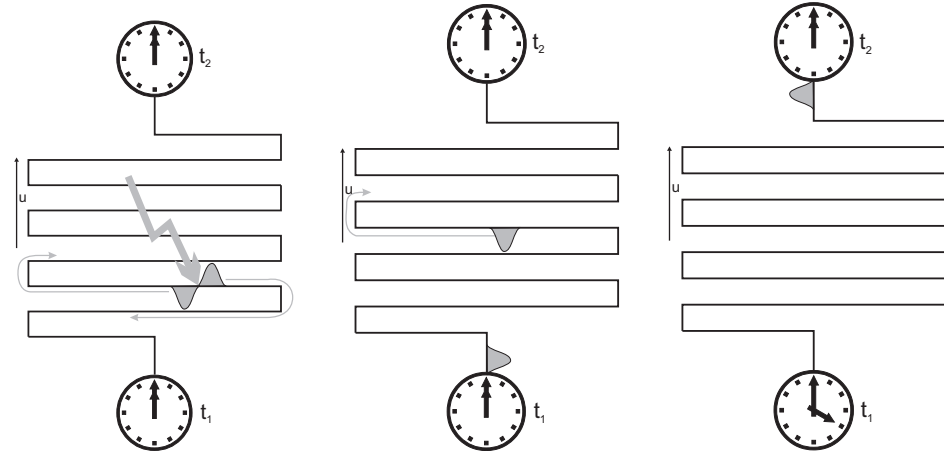
(a) Electrons accumulate on the delayline at the position u_0. Two pulses propagate towards the ends of the wire.

(b) The first pulse reaches the end of the line and triggers a "clock" t_1.

(c) The second pulse triggers its "clock" t_2. From now on, $\Delta t = t_1 - t_2$ corresponds to u_0.

Figure 3.14.: Illustration of the delayline principle. Nota bene: In reality, the electron cloud spreads and strikes more than one meander. This makes the resolution better than the separation between neighboring turns!

caused a voltage drop over the resistor which could be used to measure the particle's time of arrival on the detector.

3.4.2.2. Delayline Readout

The principle underlying a delayline anode is illustrated in figure 3.14. If electrons created by an MCP accumulate on a wire at the position u_0, this leads to two voltage pulses propagating from this position towards the ends of the wire with a constant velocity v_p. If the times of arrival at the wire ends t_1 and t_2 are known, the position where the charge was applied can be calculated in the delayline's coordinate system via

$$u = f \cdot (t_1 - t_2) \tag{3.3}$$

with $f = v_p/2$ being a scale factor. Technically, a delayline consists of a pair of wires ("signal" and "reference") which are wound around a holder. Together they form a Lecher line, showing a defined impedance. The "signal" wire is charged positively with respect to its "reference" companion to attract significantly more electrons. In conjunction with a differential amplifier, this geometry greatly suppresses noise.

The signal propagation direction to be observed is not the one directly along the wires but, as shown in figure 3.14, along the edge of the holder, perpendicular to the wire. This lowers the effective velocity of signal propagation, resulting
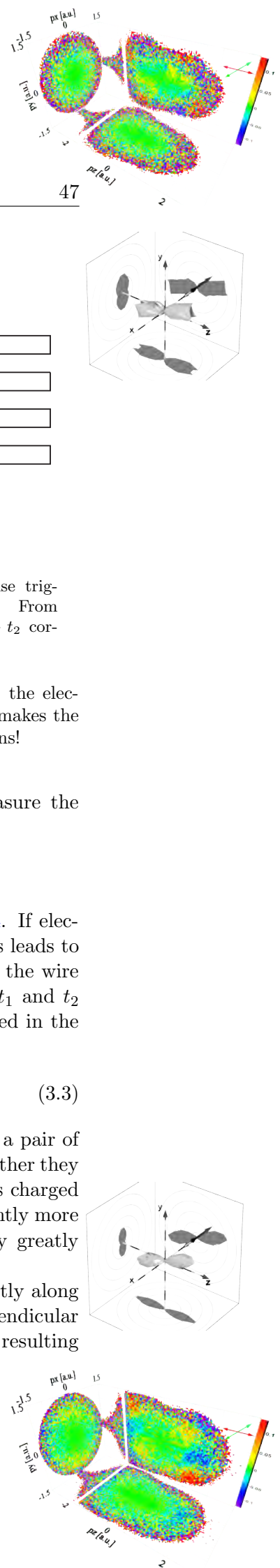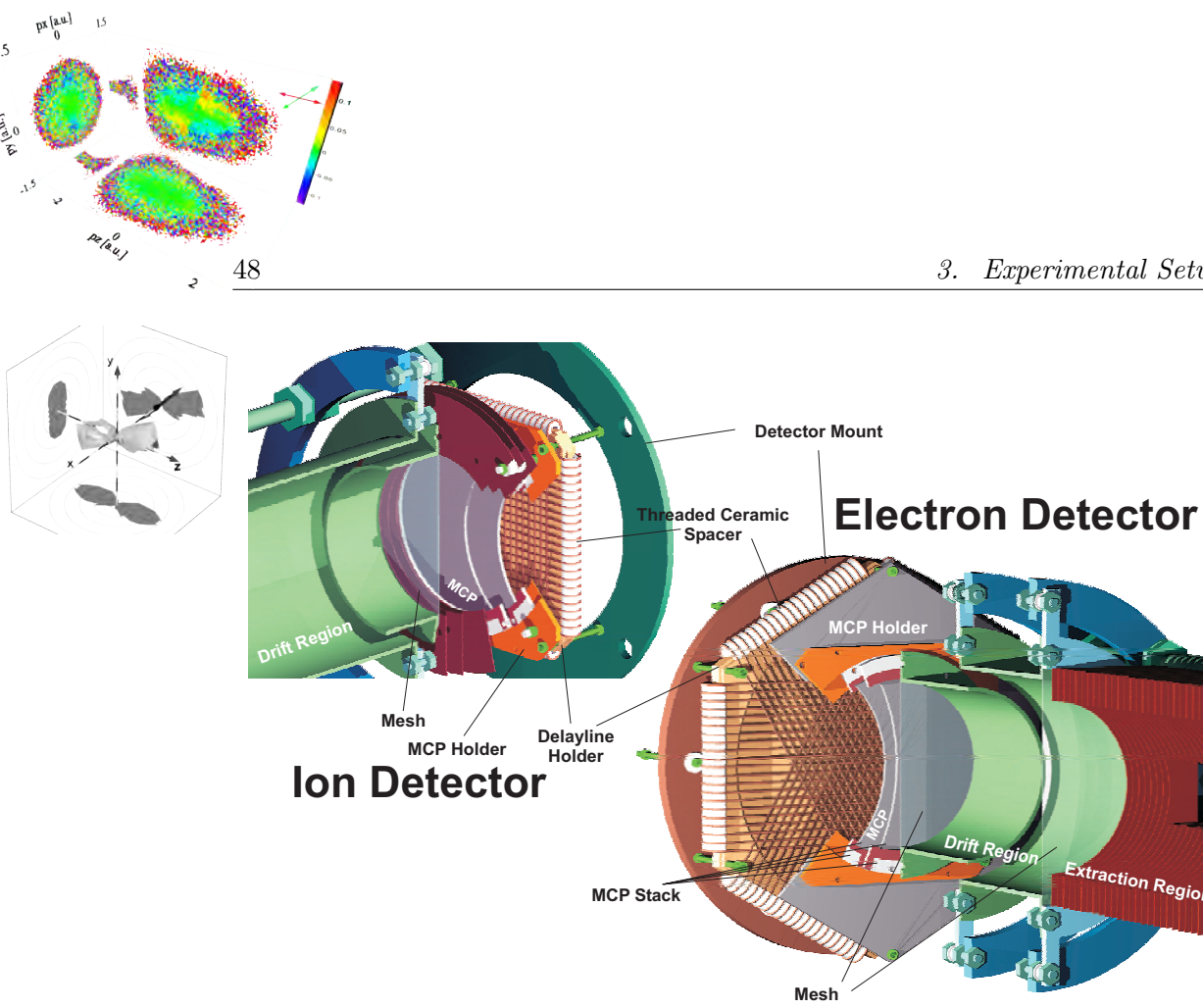
Figure 3.15.: Sketches of the delayline detectors used for this work and adjacent spec-
trometer parts. The ion detector was a rectangular DLD80 and the elec-
tron detector was a HEX 80 hexagonal anode by RoentDek. For clarity,
the spacing between neighbouring meanders of the wires was exaggerated.
Adopted from [5].

in an improved spatial resolution at a given accuracy of pulse arrival times.
Additionally, one lets the electron cloud spread over more than one meander.
Signal processing electronics only deal with the voltage pulse's center of mass.
Due to this "physical interpolation", the detector's spatial resolution can be
better than the separation of neighboring meanders.

At least two independent delayline layers with different orientations are used
for two-dimensional position encoding.

The detectors used for the experiment presented here are sketched in fig. 3.15.
The ion detector was a model DLD80 by RoentDek GmbH with an 80 mm
MCP double stack and two perpendicular delayline layers. A RoentDek HEX80
"hexanode" served as electron detector. Behind an 80 mm MCP double stack,
this model features three delaylines u_e, v_e and w_e at an angle of 60° to each
other. The benefit are improved deadtime characteristics and redundancies in
the data. For further details visit www.roentdek.com.
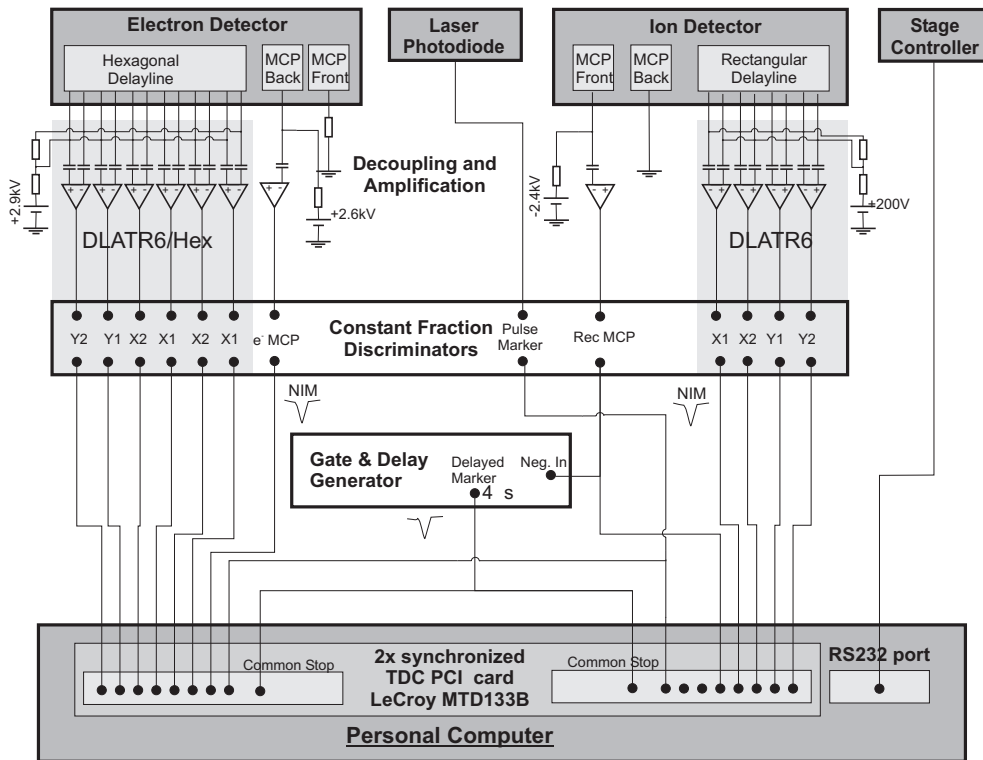
Figure 3.16.: Signal decoupling, signal processing and data acquisition in experiment A. Delayline signals were capacitively decoupled, differentially amplified and digitized in RoentDek DLATR boxes. Non-differential amplifiers and stand-alone CFDs were used for MCP and laser diode signals. All times were "computerized" by two synchronized RoentDek TDC8PCI2 TDCs. A delayed copy of the ion MCP signal served as common stop. The delaystage position was polled by the computer system via a serial line (57.6 kbaud). Based on [5].
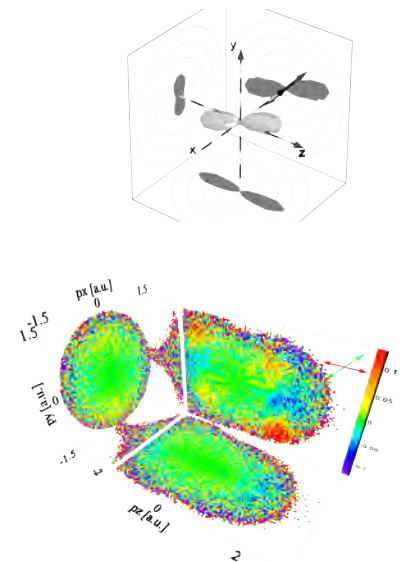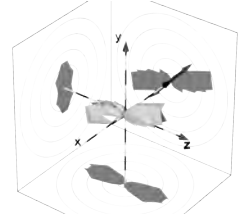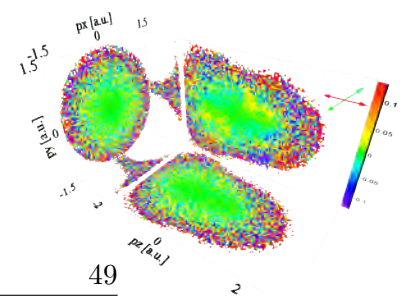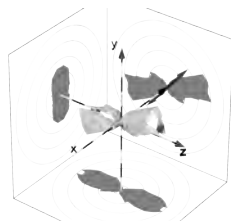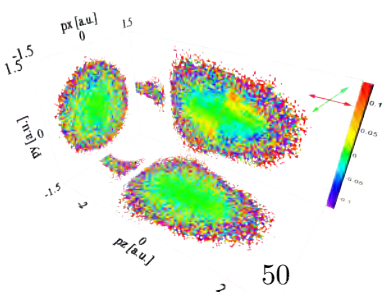
3.5. Data Acquisition Electronics

Figure 3.16 gives an overview of the signal decoupling, signal processing and data acquisition electronics as used in experiment A.

3.5.1. Constant Fraction Discriminators

All measurands in a standard COLTRIMS setup are times. These are, at the detector level, marked by analogue voltage pulses. Real-world analogue pulse heights are variable within a certain range. Purely pulseheight-dependent triggering would therefore lead to large uncertainties.

The solution to this problem are so-called constant fraction discriminators (CFDs) which trigger at a fixed fraction of any pulse's amplitude. This is accomplished by superposing a pulse with a delayed and inverted copy of itself. The zero transition of the superposition, occurring at a constant fraction of the original pulse's height, is used to trigger. In our setup, logical pulses conforming to the NIM standard were generated by the CFDs.

3.5.2. Time to Digital Converters

The NIM signals were fed into a time to digital converter (TDC). Basically, a TDC channel (in common stop mode) can be thought of as an array of high precision stop watches which are started individually and stopped together. The first pulse arriving at the TDC channel starts the first clock, the second one starts the second clock, and so forth. If the stopping line is triggered, all clocks freeze and readout by the host computer is initiated.

In experiment A, we made use of two synchronized RoentDek TDC8PCI2 cards. Each one of them featured eight TDC channels of which each one could keep up to sixteen hits [66] (i.e. consisted of sixteen "clocks"). Anyways, only four hits per channel were read out for efficiency reasons. All channels of such a card had a common stopping line (COM). The resolution was 0.5 ns, the maximum time coverable 32 μs. Due to synchronization, the two eight channel cards could be used as one sixteen channel TDC. A copy of the ion MCP signal delayed by four microseconds served as common stop. This made sure only events with at least one detected ion were stored. Within the 4 μs time window after the arrival of the first ion, further fragments (hopefully originating from the same molecule) could be detected.
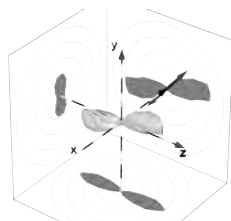
3.5.3. Updated Electronics for Experiment B

We used a different, more recent set of electronics while taking the data for experiment B. The ideas behind remained the same, though.

For differential signal decoupling of the anode wires (see figure 3.16), we now used "pulse trafos" (little current transformers) rather than differential amplifiers. The DLATR boxes from experiment A were replaced by a RoentDek
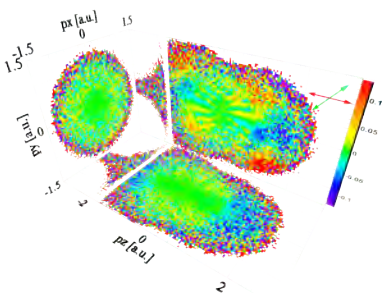
FAMP8 8-channel fast amplifier for the electron- and custom-made "Lothar Schmidt" fast amplifiers for the ion detector. Instead of the CFDs inside the DLATR, we used pre-series models of the RoentDek CFD4b four channel CFD module. Finally and most importantly, timing information was now digitized by two synchronized RoentDek TDC8HP high-precision TDCs, featuring a resolution of 25 ps. We read out up to 16 hits per channel. The TDCs worked in a so-called "group mode". Instead of requiring a dedicated common stop signal, a trigger on an arbitrary channel could initiate readout. And instead of looking only into the past from readout trigger time, the TDC "grouped" all trigger times into an event that fell into a time window around the readout event - both in the positive and in the negative direction.

In contrast to experiment A, we made the electron rather than the ion MCP trigger TDC readout.

3.5.4. Translation and Rotation Stage

As already mentioned before, the translation stage in the interferometer was programmed to change its position autonomously in experiment A, without further intervention by the data acquisition computer. The same was true for the rotation stage in experiment B. Positions could be polled via a serial (RS232) connection with the stage controller. In order to obtain a stage position, the computer had to send the command, e.g. "3TP" ("Tell Position") to the stage controller in order to obtain the position of axis no. 3. Due to bandwidth limitations of the serial line, this could not be done for each and every event without seriously reducing the rate of acquired events. Therefore we made the computer obtain a new delay value only if the age of the last measured one exceeded 15 ms. Given the stages were at rest most of the time, the error introduced by this method is negligible.

3.5.5. Data Acquisition Software

For data acquisition and some rudimentary online analysis, the software CO-BOLD (COmputer Based Online-offline Listmode Dataanalyser) by RoentDek was utilized. This software in its standard configuration reads out TDCs and stores the data in so-called list mode files (LMFs) event by event. Adaptations to specific problems can be made by programming custom data acquisition and data analysis libraries (daq.dll and dan.dll).

For this work, the above-mentioned polling of the translation- and rotation stages were implemented in custom daq.dlls, using the stage controller manufacturer's library.

The specification of the custom list mode file format used for experiment B can be found in the appendix, section E.2.
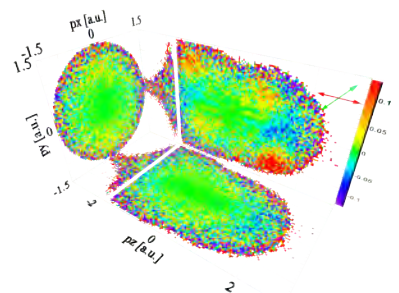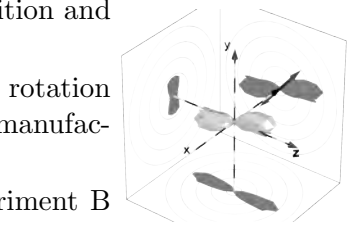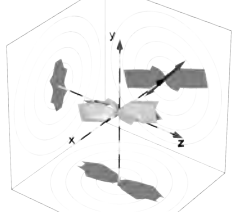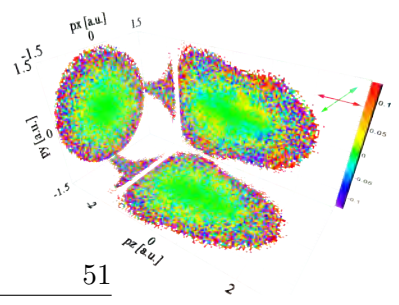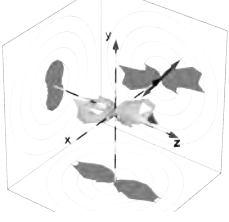
3.6. Reconstruction of Real-Space Coordinates

In a COLTRIMS experiment, all information is encoded in times. As a first
step of data analysis, positions on the detectors and flight times have to be
reconstructed from those raw coordinates. We will show how this is done for
experiment A in the following. The differences for experiment B are minor.

Let us first recall what signals are generated by an event, and realize their
succession.

1. $t = t_{laser}$: The laser emits a pulse. A small fraction of the light shines onto
   a photodiode which generates the laser signal (=pulsemarker).

2. The pulse reaches the jet target. An ion is born and flys towards the ion
   detector.

3. $t = t_{MCP}$: The ion strikes the ion detector's MCP. The MCP signal is
   emitted. Electrons created by the MCP form pulses propagating along the
   delaylines.

4. $t = t_{r_{u_1}}$, $t = t_{r_{u_2}}$, $t = t_{r_{v_1}}$, $t = t_{r_{v_2}}$: The pulses reach the ends (1, 2) of the
   ion detector's delaylines (r_u, r_v) and generate the respective signals.

5. $t = t_{COM} = t_{MCP} + 4\,\mu$s: The delayed ion MCP signal triggers the TDC's
   common stop.

Steps 2 to 4 happen for electrons and multiple ions accordingly, with another
delayline e_w in step 4 for electrons.

All t_i are clock times. But what the TDC stores in case of experiment A is the
time difference θ_i between the channel i triggering and the common stop firing,
plus cable and electronics offsets. In other words: θ_i is the age of event i at
common stop time. Compared to dealing with clock times, this yields a minus
sign in all calculations.

3.6.1. Coordinate System

The coordinate system used is defined as follows (see figure 3.17):

x-Axis: Opposite laser propagation direction

y-Axis: Jet Direction

z-Axis: Time of flight direction, pointing from the electron to the ion detector.

ϑ_a**:** Polar angle with the a axis.

φ_{ab}**:** Azimuthal angle with the a axis in the ab plane.

x and y are determined by positions on the detector and therefore referred to as
"spatial" directions.
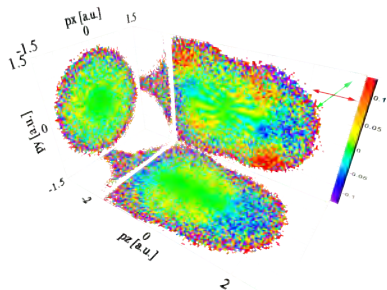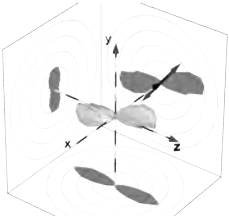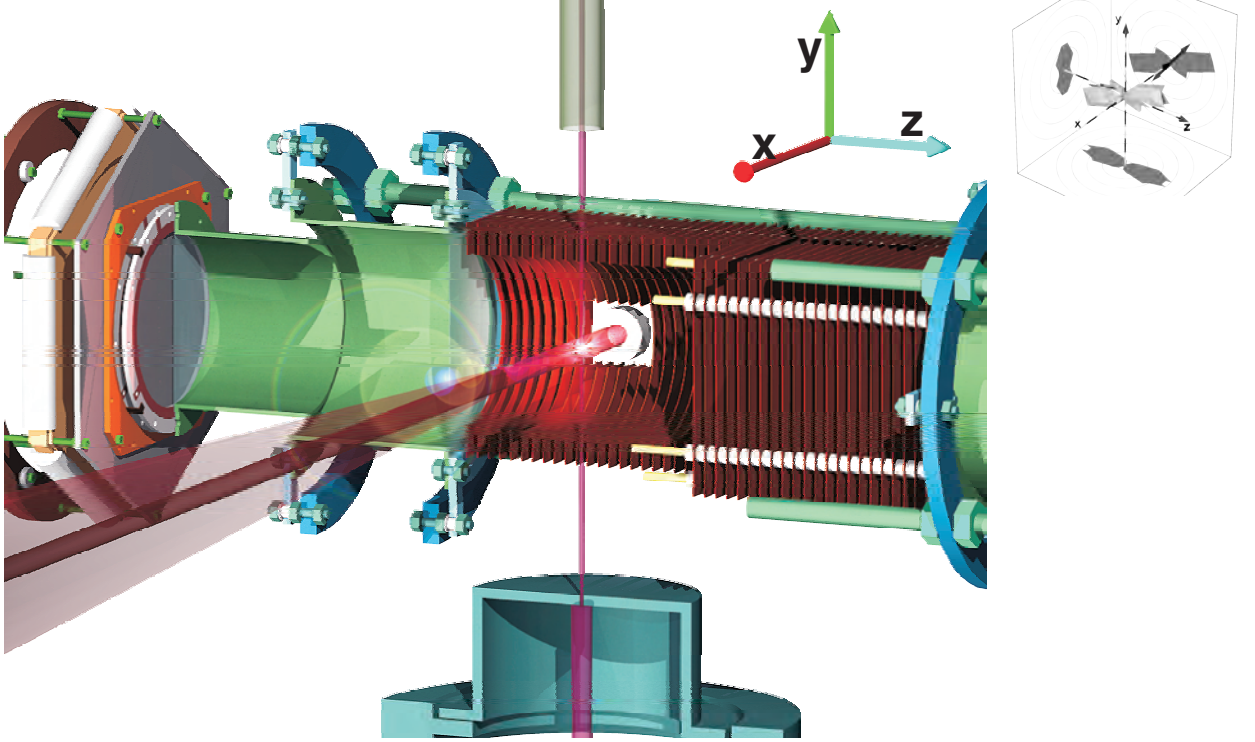
Figure 3.17.: Definition of the coordinate system. The pump pulse polarization is along y; the probe polarization along z. ϑ_a is the polar angle with the a axis while φ_{yx} is the azimuthal angle with tha a axis in the ab plane. Image from [5].

3.6.2. Time of Flight

An ion's time of flight is the time difference between its creation and its arrival at the ion detector's MCP. The ion's birth time is determined by the arrival of a laser pulse in the target, which is - except for a constant offset - defined by the laser signal. Hence, an ion's time of flight is

$$TOF_{Ion} = \theta_{laser} - \theta_{MCP_{ion}} - t_{0_{ion}}. \tag{3.4}$$

Similarly, an electron's time of flight can be calculated via

$$TOF_e = \theta_{laser} - \theta_{MCP_e} - t_{0_e}.$$

3.6.3. Spatial Coordinates

Impact positions of ions and electrons on their respective detectors were calculated using a modified version of the program "lmf2root" by Achim Czasch et al. It contains advanced methods for the calculation of positions and times of flight from delayline detector data. Disarrangements caused by double hits are
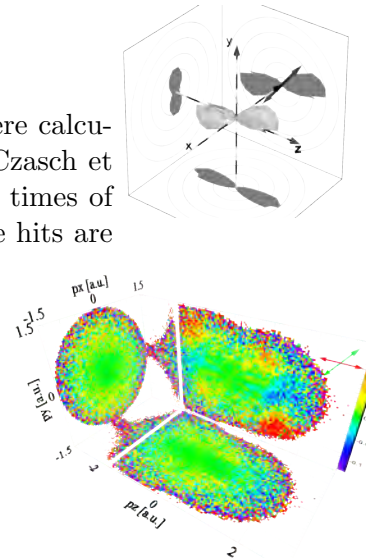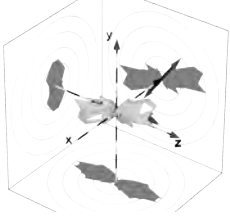
"resorted" and all kinds of redundancies exploited to reconstruct positions, even from the worst data. What follows is a presentation of the underlying principles.

In section 3.4.2.2, it has been established that the position u_0 where a particle hit a delayline detector can be reconstructed in a delayline layer's coordinate system with equation (3.3). Using TDC times, this becomes

$$u = f_u \cdot (\theta_2 - \theta_1)$$

($f_u = v_u/2$: Scalefactor for the u layer with the signal propagation velocity v_u; θ_1, θ_2: TDC times for delayline pulse arrivals).

3.6.3.1. Rectangular Anode

In case of our rectangular ion detector, the delayline coordinates u_r and v_r correspond directly to the cartesian coordinates x_r and y_r:

$$x_r = u_r$$
$$y_r = v_r.$$

3.6.3.2. Hexagonal Anode

The hexagonal electron detector consists of three layers u_e, v_e and w_e at an angle of 60° to each other. Their mapping to cartesian coordinates can be achieved with the formulae

$$x_{uv} = u \tag{3.5}$$
$$y_{uv} = \frac{1}{\sqrt{3}}(2v - u) \tag{3.6}$$
$$x_{uw} = u \tag{3.7}$$
$$y_{uw} = \frac{1}{\sqrt{3}}(2w + u) \tag{3.8}$$
$$x_{vw} = v - w \tag{3.9}$$
$$y_{vw} = \frac{1}{\sqrt{3}}(v + w) \tag{3.10}$$
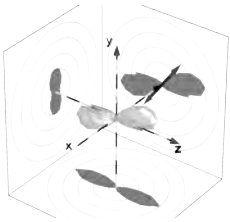
(adopted from [67]). All representations of x and y can be used equally. If, for example, the w layer did not provide a useful signal, x_{uv} and y_{uv} can fill the gap.

3.6.4. Timesums

Any delayline has a fixed length l. The sum of the paths two pulses starting from a common origin travel until they reach opposite ends of a delayline is always l.
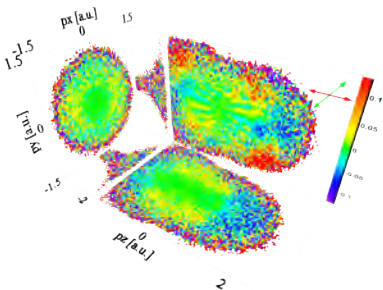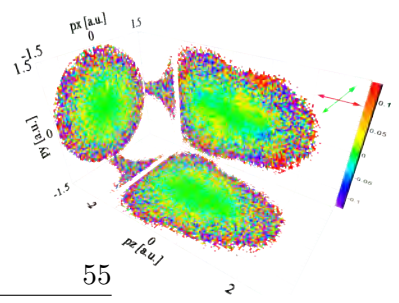
Therefore, provided that their velocity v_p is constant, the sum of their runtimes Θ_1 and Θ_2 must be constant as well:

$$\Theta_1 + \Theta_2 = \frac{l}{v_p} =: TSum = \text{const.}$$

The delay between a particle hitting an MCP and the resulting electrons generating pulses on the anode is constant and therefore negligible. So, the common starting time of the pulses equals t_{MCP}. Expressed in TDC times, the timesum becomes

$$TSum = \frac{l}{v_p} = 2\theta_{MCP} - \theta_{u_1} - \theta_{u_2} \tag{3.11}$$

The timesum is a characteristic constant for each delayline layer. Windows around the known timesum are used as a condition to discriminate against bad events. Alternatively, the knowledge of the correct timesum can be used to reconstruct lost pulse arrival times.
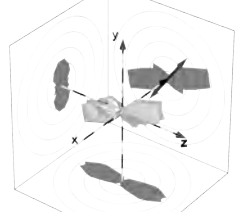
3.7. Calculation of Momenta

The impact positions and times of electrons and ions now have to be converted to initial momenta of these particles. As described above, our spectrometer is supposed to feature a homogeneous electric field $\vec{E}$ and a homogeneous magnetic field $\vec{B}$. The total force these fields cause to a particle of the charge q and velocity $\vec{v}$ is the sum of the Lorentz force $\vec{F_L}$ and the electrostatic force $\vec{F_E}$:

$$
\begin{aligned}
\vec{F} &= \vec{F_E} + \vec{F_L} \\
&= q \cdot \left(\vec{v} \times \vec{B} + \vec{E} \right) \\
&= q \cdot \begin{pmatrix} v_y B_z - v_z B_y + E_x \\ v_z B_x - v_x B_z + E_y \\ v_x B_y - v_y B_x + E_z \end{pmatrix}.
\end{aligned}
$$

Both $\vec{E}$ and $\vec{B}$ are oriented along the time of flight direction z, so

$$\vec{E} = \begin{pmatrix} 0 \\ 0 \\ E \end{pmatrix} \qquad \text{and} \qquad \vec{B} = \begin{pmatrix} 0 \\ 0 \\ B \end{pmatrix},$$

simplifying the above expression to

$$\vec{F} = q \cdot \begin{pmatrix} v_y B \\ -v_x B \\ E \end{pmatrix}. \tag{3.12}$$
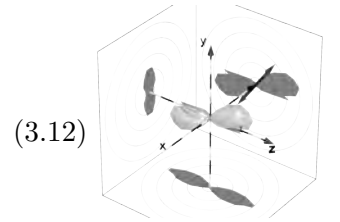
What we would like to reconstruct is the initial momentum $\vec{p} = m\vec{v}$.
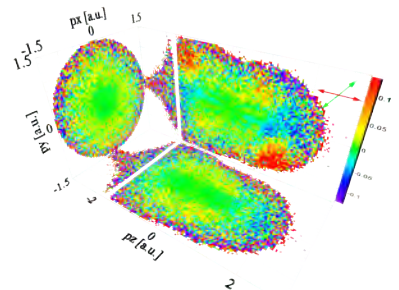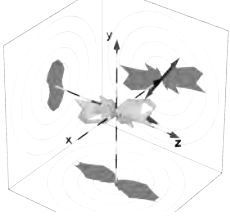
3.7.1. Electrons

On the electron side, our spectrometer consists of an acceleration part of the length $l_{a,e}$ where both $\vec{E}$ and $\vec{B}$ are present, and a drift region of the length $l_{d,e}$ without an electric field.

3.7.1.1. Time of Flight Direction

Hence, an electron's equation of motion in the acceleration region is

$$
\begin{aligned}
l_{a,e} &= \frac{1}{2}\frac{q_e}{m_e}Et_a^2 + v_z t_a \\
\Rightarrow t_a &= -\frac{m_e}{q_e E}\left(v_z - \sqrt{v_z^2 + 2l_{a,e}\frac{q_e}{m_e}E}\right)
\end{aligned}
$$

where t_a ist the amount of time it spends in this region. To pass through the E-field-free drift tube, it takes the time

$$
t_d = \frac{l_{d,e}}{\frac{q_e}{m_e}Et_a + v_z}.
$$

What we detect is the electron time of flight

$$
TOF = t_a + t_d.
$$

Solving that equation for v_z algebraically is inconvenient. Instead, we solved it iteratively for each event with a method developed by Lothar Schmidt.

3.7.1.2. Spatial Directions

In the spatial directions (x,y), according to equation (3.12), only the magnetic field plays a role. Therefore we do not have to distinguish between the acceleration and the drift region, as the B-field is present in both. We solve the differential equation

$$
\begin{pmatrix}\dot{v}_x \\ \dot{v}_y\end{pmatrix} = \frac{q_e}{m_e}B\begin{pmatrix}v_y \\ -v_x\end{pmatrix}
$$

for $(p_x, p_y) = m_e(v_x, v_y)$, yielding [68]

$$
\begin{pmatrix}p_x \\ p_y\end{pmatrix} = \frac{1}{2}m_e\omega_{gyr}\cdot\begin{pmatrix}x/\xi - y \\ y/\xi + x\end{pmatrix} \tag{3.13}
$$
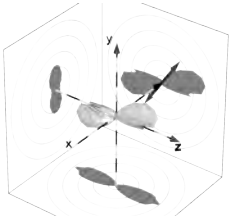
where

$$
\omega_{gyr} = \frac{q_e}{m_e}B = \frac{2\pi}{T_{gyr}}
$$

is the electron's gyration frequency and

$$
\xi = \tan\left(\frac{1}{2}\omega_{gyr}TOF\right).
$$
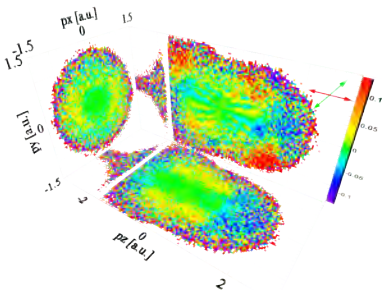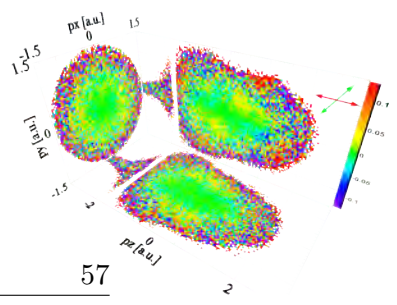
3.7.2. Ions

The ion species with the lowest mass/charge ratio we are going to measure is $^{14}N^+$. The influence by the magnetic fields used ($B < 15$ Gauss) on these and heavier ions is negligible. Our ion spectrometer only consists of an acceleration region of the length $l_{a,i}$. There is no field-free drift area.
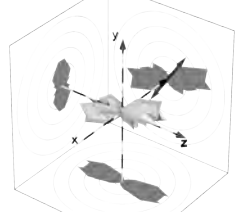
3.7.2.1. Time of Flight Direction

Hence, an ion's equation of motion in the time of flight direction z is

$$l_{a,i} = \frac{1}{2}\frac{q}{m}Et^2 + \frac{p_z}{m}t \tag{3.14}$$

where q is the particle's charge, m its mass, p_z its initial momentum along the z direction and t its time of flight. If our ionization process leads to only one detectable ion per event, we have to solve equation (3.14) for momentum:

$$\boxed{p_z = \frac{l_{a,i}m}{t} - \frac{1}{2}qEt}. \tag{3.15}$$

If two correlated ionic fragments emerge with the parameters (m_1, q_1, t_1) and (m_2, q_2, t_2), obeying momentum conservation (neglecting electrons), we can cancel the spectrometer length, which is the same for both fragments. That is,

$$\begin{aligned}
l_{ai} &= \frac{1}{2}\frac{q_1}{m_1}Et_1^2 + \frac{p_{1_z}}{m_1}t_1 \\
&= \frac{1}{2}\frac{q_2}{m_2}Et_2^2 + \frac{p_{2_z}}{m_2}t_2.
\end{aligned}$$

We assume that momentum is conserved among the ions, neglecting both electron- and center of mass momenta. Hence, $p_z := p_{1_z} = -p_{2_z}$. Using this relation, the above system of equations can be solved to

$$\boxed{p_z = \frac{1}{2}E\frac{m_1q_2t_2^2 - m_2q_1t_1^2}{m_2t_1 + m_1t_2}}, \tag{3.16}$$

which is independent of the spectrometer's length. If the ions have equal mass and charge, i.e. $m_1 = m_2$ and $q := q_1 = q_2$, equation (3.16) collapses to

$$\boxed{p_z = \frac{1}{2}qE(t_2 - t_1)} \tag{3.17}$$

and therefore becomes independent of potential offsets t_0 of the time of flight, too.

Despite its elegance from a calibration point of view, equation (3.16) may not be optimal in case of a relatively warm target. It might be better to infer the
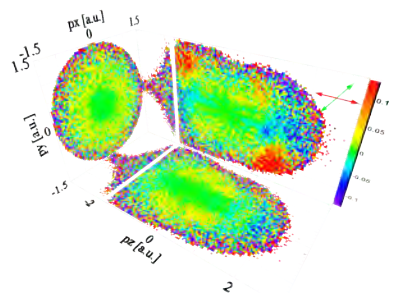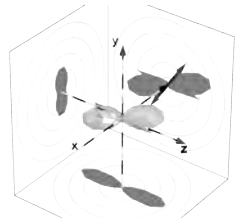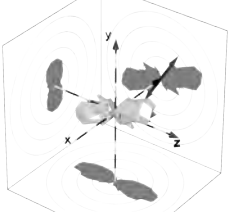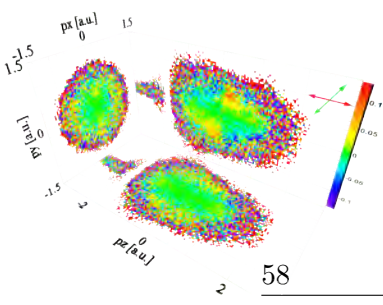
momenta of the two ions individually using equation (3.15) to successively calculate and correct their center of mass momentum (event-by-event). Additionally, electron momenta were neglected. The accuracy of the method is therefore limited by the amount of momentum carried by electrons. It cannot be used if the total electron and ion center of mass momentum is to be exploited, e.g. to infer the momentum of a particle that was not detected.

3.7.2.2. Spatial Directions

If the electric field is aligned along z, ions are not accelerated in the spatial directions x and y. Hence, an ion's impact position on the detector is

$$r_{x,y} = \frac{p_{x,y}}{m} t.$$

and its momentum becomes

$$\boxed{p_{x,y} = m \frac{r_{x,y}}{t}}. \tag{3.18}$$

A major practical disadvantage of equation (3.18) is that any offset $r_{0_{x,y}}$ has a direct impact on the result. When trying to calibrate scalefactors and offsets at the same time this causes trouble.

Ideally, one would only use the differences of detector coordinates of correlated fragments to cancel any constant offset:

$$
\begin{aligned}
r_{2_{x,y}} - r_{1_{x,y}} &= (r_{2_{x,y}} + r_{0_{x,y}}) - (r_{1_{x,y}} + r_{0_{x,y}}) \\
&= v_{2_{x,y}} t_2 - v_{1_{x,y}} t_1 \\
&= p_{2_{x,y}} \frac{t_2}{m_2} - p_{1_{x,y}} \frac{t_1}{m_1}.
\end{aligned}
$$

We once again assume momentum conservation between the ions, so

$$p_{x,y} := p_{2_{x,y}} = -p_{1_{x,y}},$$

obtaining

$$r_{2_{x,y}} - r_{1_{x,y}} = p_{x,y} \left(\frac{t_1}{m_1} + \frac{t_2}{m_2} \right)$$

which can be solved to

$$\boxed{p_{x,y} = m_1 m_2 \frac{r_{2_{x,y}} - r_{1_{x,y}}}{m_2 t_1 + m_1 t_2}}. \tag{3.19}$$

This equation does not suffer from constant detector offsets. However, it does not cancel any ion center of mass momenta (i.e. thermal motion, the jet velocity) either. It is also sensitive to time of flight offsets t_0 and ignores the momenta of electrons.
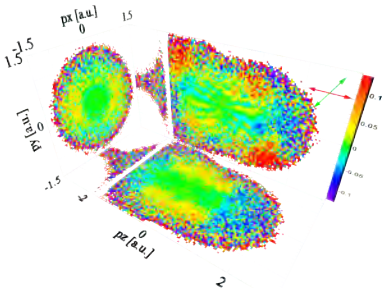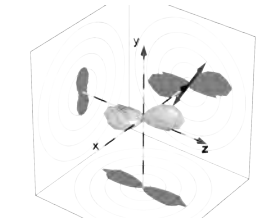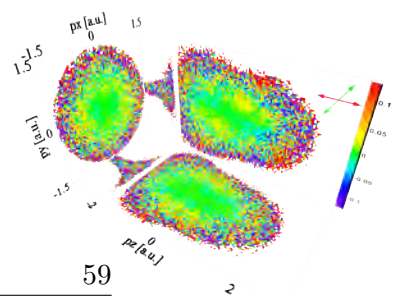
3.7.2.3. Correcting Thermal Motion

We can further refine our momentum resolution in case of correlated fragments by removing thermal motion. We start with the raw momenta $\vec{p}_{1,raw}$ and $\vec{p}_{2,raw}$, calculated according to equations (3.18) and (3.15). We then calculate the center of mass velocity

$$\vec{v}_{cms} = \frac{\vec{p}_{1,raw} + \vec{p}_{2,raw}}{m_1 + m_2}.$$

We neglect the electron recoil on the ion. Then, $\vec{v}_{cms}$ can be interpreted as being due to the finite temperature of the target gas. We correct ion momenta by this per-event offset:

$$\boxed{\vec{p}_i = \vec{p}_{i,raw} - m_i \vec{v}_{cms}} \qquad i = \{1, 2\} \tag{3.20}$$

Unless stated otherwise, if two fragments were available, we used such "thermal motion corrected" ion momenta. Disadvantages of this method are that any wrong offset will affect the result and it cannot be used unless the electrons carry only a negligible amount of momentum.
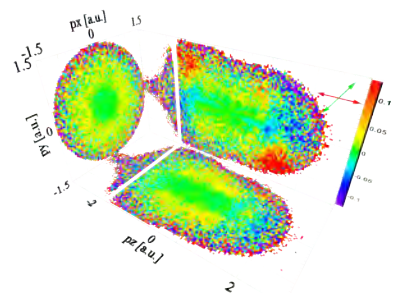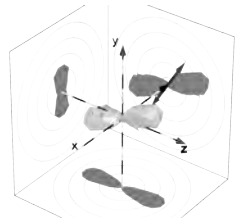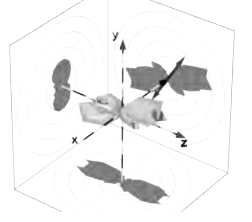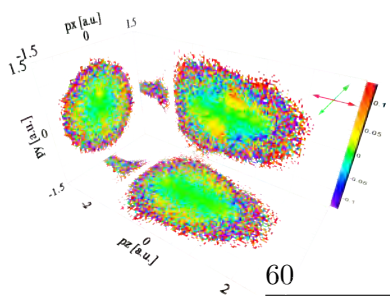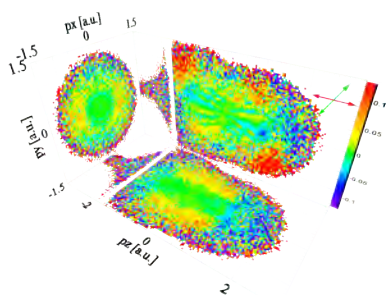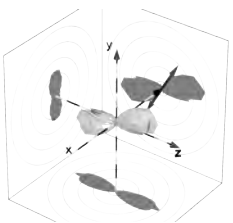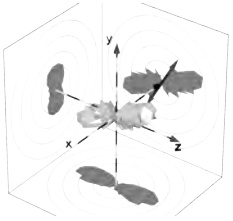
4. Calibration and Data Analysis

Man sollte Exzesse der
Vollkommenheit vermeiden.

(H. M. Enzensberger)

In this chapter, we are going to give an outline of the steps taken to calibrate the experiment. In section 4.3, some special methods and definitions used in the final analysis of the data will be explained.

4.1. Calibration of the COLTRIMS Setup

The COLTRIMS data were analyzed by using custom-made pieces of software written in the programming language C++, based on the data analysis framework ROOT [69]. The analysis proceeded in three distinct stages:

1. Convert TDC data from list mode files to detector coordinates, i.e. impact positions and times of flight. Save these data event-by-event into a file. This was done using the program "LMF2Root", written by Achim Czasch et al.. Adaptations had to be made to meet the specific requirements of the described experiments. The ideas behind have been explained in chapter 3.6.

2. Calculate initial electron and ion momenta from these coordinates, applying the formulae derived in chapter 3.7. This was done using a completely homegrown program. The calibration aspects of this process will be discussed in the following. Data were then filled into histograms.

3. Where applicable, normalize, compare and plot histograms. The definition of particular parameters can be found in section 4.3.

It is a peculiarity of COLTRIMS experiments that almost all calibration information can be inferred from the measured data. In the above-mentioned first level of analysis, TDC trigger times were converted to particle impact positions and times of flight. This process has been automated to some extent by "LMF2Root". We will no further explain the internals.
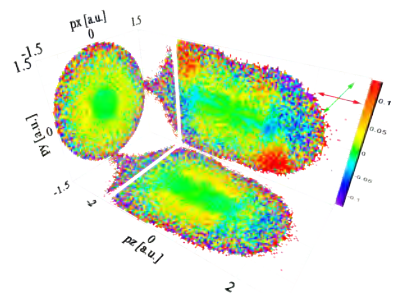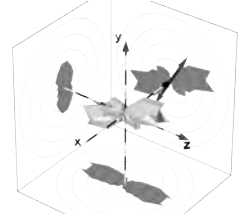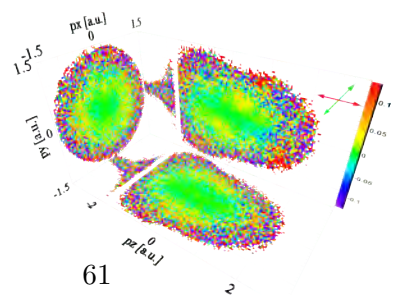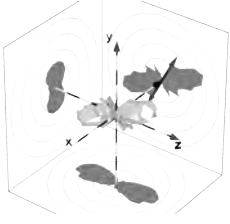
However, detector offsets and scale factors are only roughly correct after this stage of analysis. These have to be derived by using prior knowledge regarding the expected distributions of particle momenta. The strength of the applied fields and the exact dimensions of the spectrometer have to be inferred this way, too.

In the following, we will show how the second level of the analysis can be achieved, using experiment A as an example. Only the necessary steps are presented. In reality, some (in principle unnecessary) sub-steps were done. The real-world order of actions did not necessarily match the presentation, which is aiming for clarity.

4.1.1. Ions: Rough Calibration

In order to carry out a convenient and exact calibration of the ion spectrometer, we are going to use information from correlated fragments produced in Coulomb explosions. However, this only works if we can distinguish real from random coincidences, making a rough pre-calibration necessary. The latter is the subject of this section. Essentially, this is the standard way of calibrating a COLTRIMS; the fine-tuning described in section 4.1.2 is new.

4.1.1.1. Time of Flight Direction

There is no physical reason for a symmetry break along the z axis. Therefore, the ensemble-averaged momentum of ions in this direction is zero, making the positions t_{peak} of peaks in the ion time of flight distribution correspond to ions with zero initial momentum, given there are no dissociations involved. Hence, we can infer from equation 3.14 that

$$t_{Peak} = \sqrt{\frac{m}{q}}\sqrt{\frac{2l_{a,i}}{E}}.$$ (4.1)

For some peaks in the TOF spectrum, the respective ion species could be inferred from relative abundances, shapes and the order of the peaks; see figure 4.1 and the respective figure subscript. Rough time of flight offsets t_0 and the ratio

$$k := \frac{l_{ai}}{E}$$

were obtained by using a linear regression. We know an approximate value of the spectrometer length $l_{a,i}$ from the design of the setup. This is sufficient to calculate rough momenta in the z direction using equation 3.15.
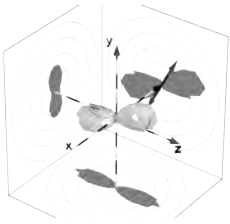
4.1.1.2. Spatial Directions

The symmetry argument made above holds in the spatial directions (x, y), too. Here we have to remove the offset of the ion detector's origin in the "physics frame".
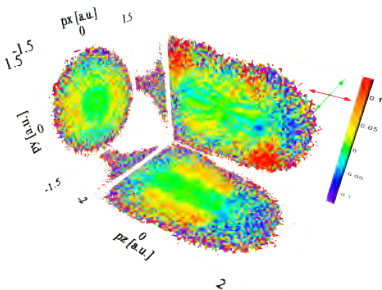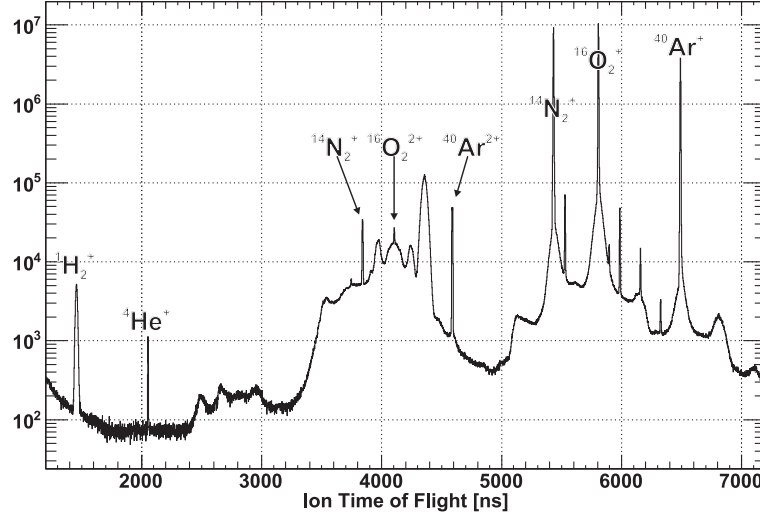
Figure 4.1.: Ion time of flight (TOF) distribution from experiment A. We were using a gas mixture as a target, which was mostly composed of N_2, O_2 and Ar with helium as a buffer gas (cf. table 5.1). We are expecting single ionization to be the most likely process. Hence, the highest peaks in the spectrum can be assigned the mass/charge ratios of 28 ($^{14}N_2^+$), 32 ($^{16}O_2^+$) and 40 ($^{40}Ar^+$). For assignments of mass/charge ratios to the remaining peaks, the reader is referred to figure 5.1 in the results chapter.

The target we ionize is not at rest in the laboratory frame. Instead, molecules propagate along the jet direction (y) at supersonic speed $\vec{v}_{jet}$. This leads to an offset depending on a molecule's time of flight, as can be seen in figure 4.2(a) (marked by black lines). We correct for both the jet velocity and constant detector offsets by applying a linear correction; results are shown in figure 4.2(b). The slopes of the detector offsets (lines in figure 4.2(a)) reflect $\vec{v}_{jet}$ in the detector frame. As we know the jet propagates along the y-axis, this gives us the detector's rotational angle in the laboratory system. We rotate the detector such that $\vec{v}_{jet}$ is along y.

Now we are set to calculate approximate ion momenta according to equation 3.18.

4.1.2. Ions: Fine-Tuning

However, this is still a relatively coarse calibration. It was further refined by exploiting the extra piece of information provided by Coulomb explosions leading to two correlated ions. For this purpose, we have to discriminate against random coincidences. Coulomb exploded fragments fly apart back to back, having (neglecting electrons) zero center of mass momentum. We distinguish real from random coincidences by calculating approximate ion momenta as outlined above
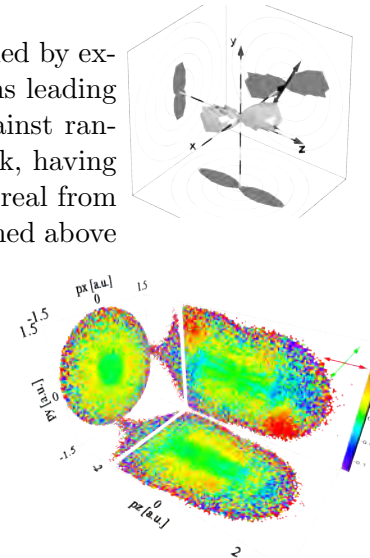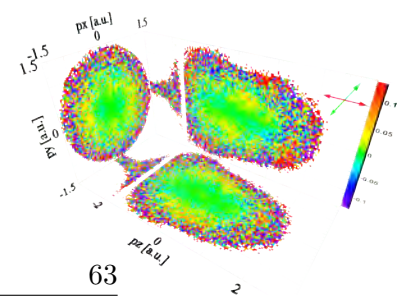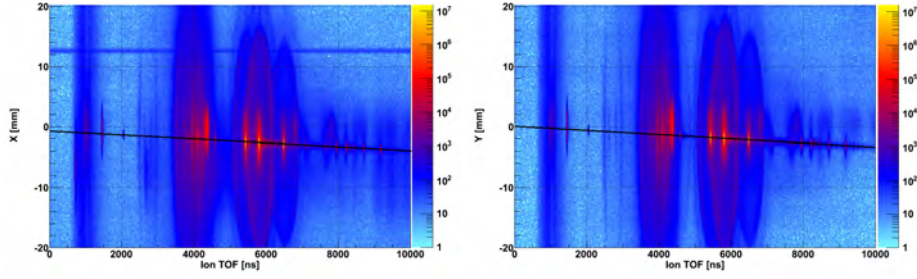
(a) Before Correction. The black lines show the linear correction to be applied.
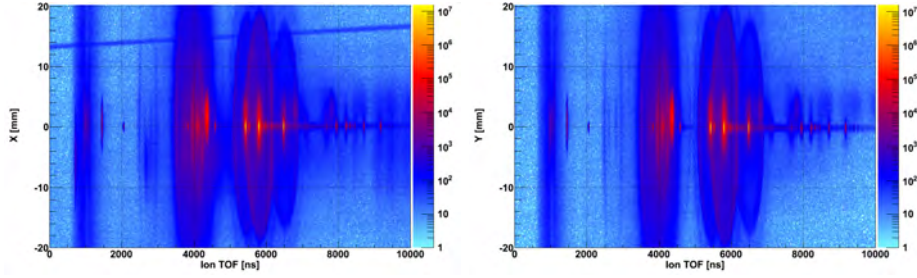
(b) After Correction. Low-momentum ions hit the detector in the origin for all TOFs.

Figure 4.2.: Ion times of flight (*horizontal*) vs. spatial directions (*vertical*; panels on the *left*: x; *right*: y) in the detector frame. (a): Distributions in their original shape. The lines are fit through the positions of low-momentum ions. Their slopes give the jet velocity $\vec{v}_{jet}$ in the detector frame. (b): The same distributions after subtracting the jet velocity and constant detector offset.
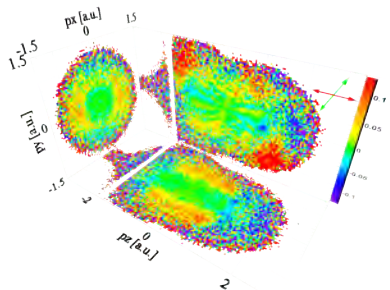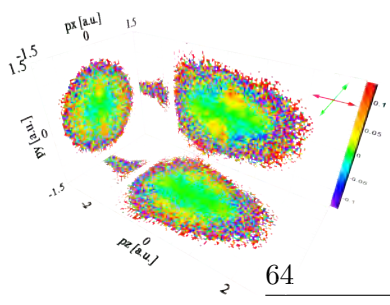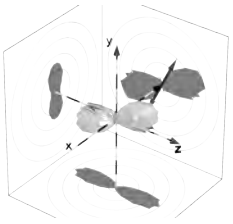
and restricting the ion center of mass momentum

$$\vec{p}_{CMS} = \vec{p}_{ion1} + \vec{p}_{ion2}$$

to a reasonable absolute value (e.g. 20 a.u.).

4.1.2.1. Time of Flight Direction

We will first fine-tune our figure for the electric field strength E. For breakups with equal, correlated fragments ($O^+ + O^+$, $N^+ + N^+$), we calculate the offset-free momentum along the time of flight direction $p_{z,0}$ using equation 3.17. This formula only requires the time of flight difference $\Delta t = t_2 - t_1$ between the two ions and the electric field strength E. Its dependence on Δt rather than absloute TOFs makes it insensitive to offsets t_0. It does not depend on the length of the spectrometer. We calculate the kinetic energy release (KER)[1] for correlated ions lying within a cone around the time of flight axis.

We obtain an improved value for E by matching the largest peak in our $O^+ + O^+$ KER distribution to the literature value of 11.2 eV from [70]. The final distributions after calibration are shown in figure 4.3. The agreement between our $N^+ + N^+$ KER distribution and the one published in [71] confirms the calibration.

This procedure can be considered somewhat problematic as the literature values used were not obtained in laser experiments but in a classical electron scattering experiment, rather. Nevertheless, it has been shown in [72] that the high-resolution KER peaks obtained by inelastic electron scattering in [70, 71] can be seen in a laser-driven experiment, too.

Having an accurate value for E, we also obtain an improved spectrometer length

$$l_{a,i} = k \cdot E.$$

We now vary the ion time of flight offset $t_{0,i}$ such that the momentum distributions of non-dissociated ions (e.g. O_2^+, O_2^{2+}) in the time of flight direction are centered around zero.

However, there is another method of obtaining $t_{0,i}$, involving correlated fragments. Hitherto we know the mass m, charge q and offset-free momentum $p_{z,0}$ of each ion in the z direction according to equation 3.17. In addition, we have so far calibrated the spectrometer length $l_{a,i}$ and the electric field E. We can use these pieces of information to convert offset-free momenta back to offset-free times of flight $t_{calc,i}$ by solving equation (3.14):

$$t_{calc,i} = \frac{1}{qE} \left(\sqrt{p_{z,0}^2 + 2l_{a,i}mqE} - p_{z,0} \right).$$

The distribution of differences $t_{0,i} = t - t_{calc,i}$ between calculated and measured times of flight will peak at the value of the correct time of flight offset.

---

[1]KER stands for Kinetic Energy Release. This is the sum of kinetic energies of all ions in the ion center of mass system.
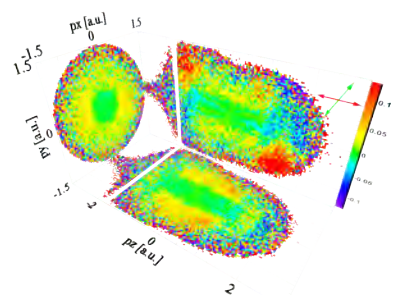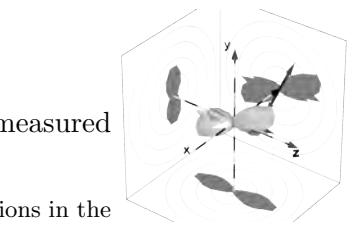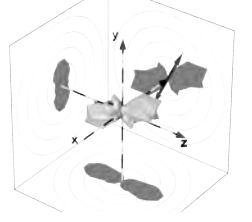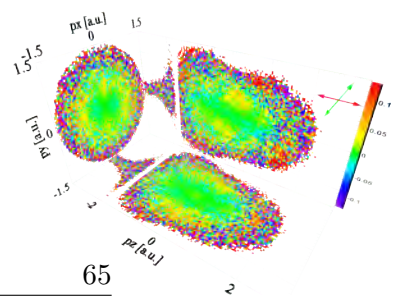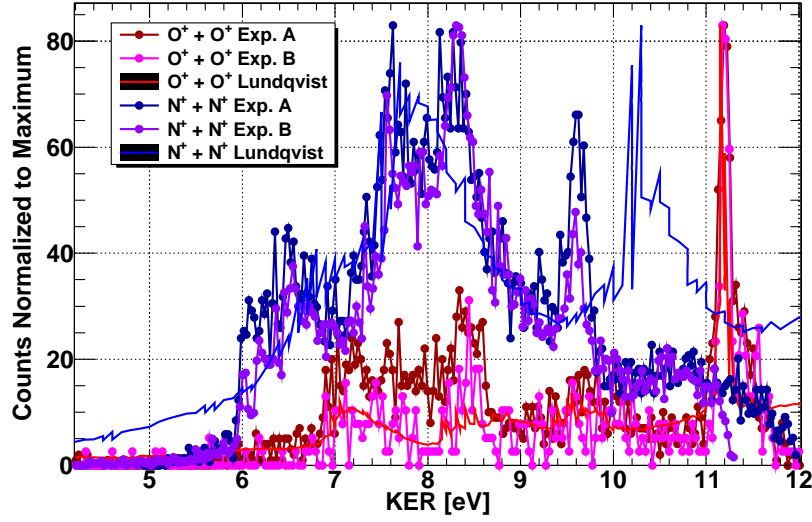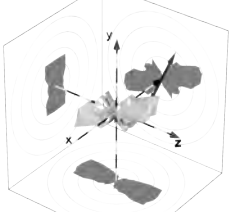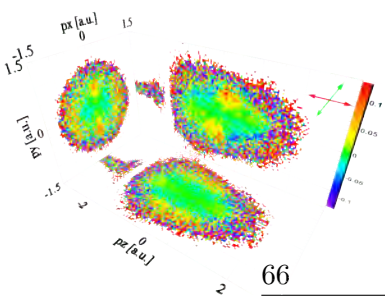
Figure 4.3.: Comparison of KER distributions of Coulomb exploded molecules from our experiments (*circles and lines*) with reference data by Lundqvist et al. from [70] ($O^+ + O^+$, *light red* curve) and [71] ($N^+ + N^+$, *light blue* curve). The momenta leading to our distributions were obtained using equations (3.17) and (3.19). Only correlated fragments are plotted and the condition $\vartheta_z < 10^o$ was imposed in order to minimize the influence by the spatial directions of the detector. The highest maximum of our O^+ distributions (*dark red / pink*) was matched to its companion in the reference curve by adapting the electric field. The basic similarity between our (*dark blue / lavender*) and Lundqvist's curves for N^+ ions (*light blue*) confirms the consistency of the calibrations. The reference curves were obtained in conventional electron-molecule scattering experiments. Therefore, their exact shapes cannot be expected to match those of ours. It is not clear why we see peaks in the nitrogen spectra around 9.6 eV Lundqvist's data do not show. We are missing his structures between 10 and 11 eV, though.
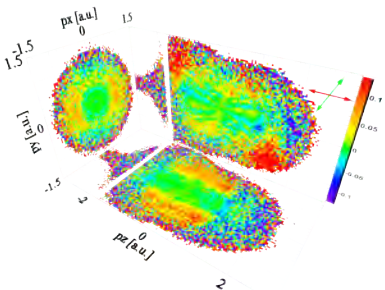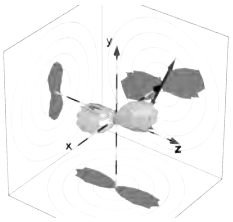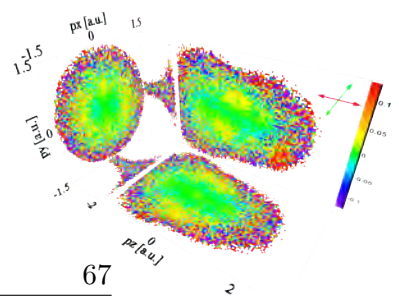
4.1.2.2. Spatial Directions

Now the time of flight direction is fully calibrated, we can turn to the spatial directions (x, y). There are two issues to calibrate here: The spatial offsets of the detector (x_0, y_0) and the detector's scale factors.

We already used the "conventional" method of removing offsets in the approximate calibration by shifting the distributions of stable, low-momentum ions to zero position. However, our detector had some scars in those spots where this kind of ions typically impacts, which made it hard to achieve accurate values. We will now fine-tune by using energetic fragments.

For these, we can calculate offset-free momenta in the spatial directions $p_{xy,0}$ according to equation (3.19). We then convert them to offset-free positions $x_{calc,i}$, $y_{calc,i}$ with equation (3.18) and plot the difference between the measured and the calculated values. These distributions peak at the appropriate values of the offsets x_0 and y_0. By going through this procedure for two different species (e.g. $N^+ + N^+$ and $O^+ + O^+$), we can adjust the jet velocity, too.

Finally we have to calibrate the detector scale factors, using Coulomb explosions another time. The KER peaks caused by such explosions are expected to be constant, regardless of the direction of the explosion within the spectrometer.[2] In a spectrum plotting angle versus KER, a KER peak is therefore supposed to turn into a straight line. We plot the dependence of the $O^+ + O^+$ KER on the angle φ_{yx} within the detector plane in figure 4.4(a). We changed the scale factors of the detector in order to match the strong, sharp line recognized as corresponding to 11.2 eV before to this value and "straighten" it as much as possible.

After these steps, the calibration of the ion spectrometer is complete.

4.1.3. Electrons

In order to calculate electron momenta, in addition to the calibration parameters retrieved for ions, we have to know both the magnitude and sign of the applied magnetic field B.

4.1.3.1. Magnetic Field Magnitude

Electrons perform gyrations on their way to the detector. They start their paths at the spatial origin. If an electron's time of flight t_e matches the gyration period

$$T_{Gyr} = \frac{2\pi}{|B|} \frac{m_e}{q_e} \tag{4.2}$$

---

[2]What may physically show angle-dependencies is the population of KER lines. However, these correspond to dissociative potential curves of ions. It is thinkable that Stark shifts might introduce angle-dependent changes of the potential curves. However, these are most likely far below our measurement accuracy. Hence, as long as KER lines are visible, the KER value of such a line should remain fixed.
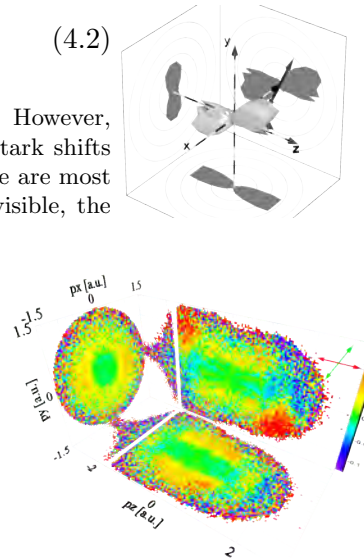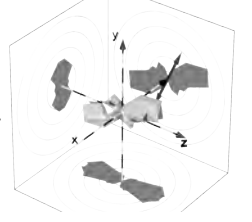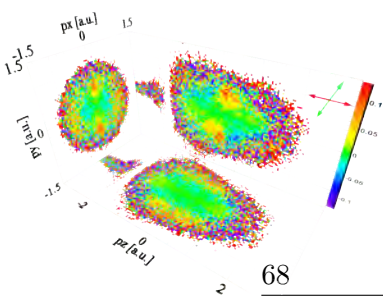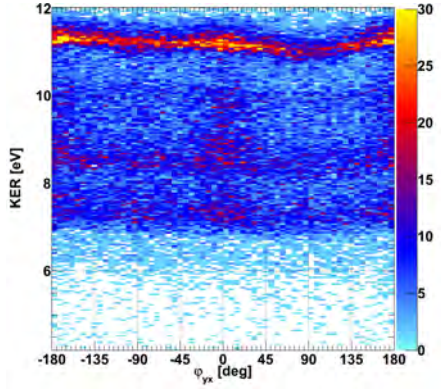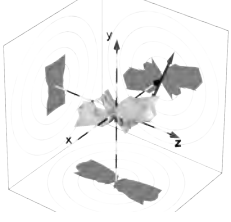
(a) Angle within the detector plane.
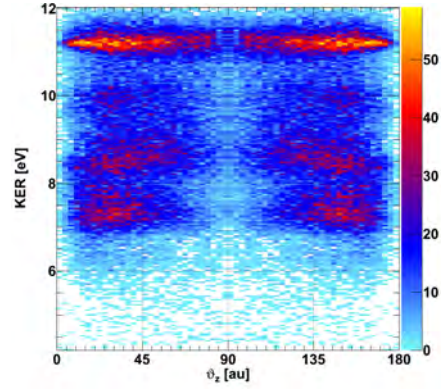
(b) Angle with the TOF axis.

Figure 4.4.: $O^+ + O^+$ breakups from experiment A: Angle-dependence (*horizontal*) of the KER (*vertical* axis). Ideally, the KER lines should not be bent. Detector scale factors were adapted to "straighten" the sharp, highest-energy line as much as possible and match it to the reference value of 11.2 eV from [70]. (a): Dependence on the angle within the detector plane. This is used to calibrate the detector scale factors with respect to each other. (b): Dependence on the angle with the time of flight direction. At $\vartheta_z = 0$, the molecule exploded in the direction perpendicular to the detector. This spectrum confirms the consistency with the z direction. Offset-free formulae were used to calculate KERs.
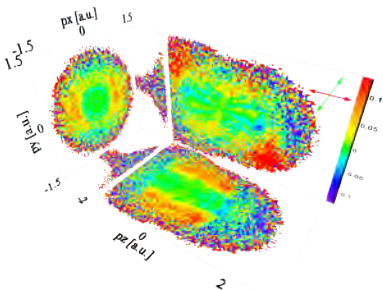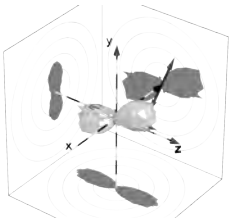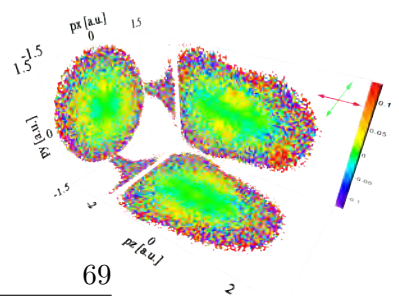
Figure 4.5.: Calibration measurement of experiment A: Electron time of flight (*horizontal* axis) vs. y position on the detector (*vertical*). At times of flight with minimum spread in the y direction, the TOF matches an integer multiple of the gyration period. From the distance between these points, we can calculate the magnetic field strength B; cf. equation (4.2).

or integer multiples thereof, it will hit the detector in the origin. This leads to narrow distributions of electrons on the detector in such cases, which we will refer to as "wiggles". Electrons with different flight times show a greater spread. The more their TOF differs from the closest wiggle time, the larger the spread.

We can therefore calibrate $|B|$ by measuring the difference between two points in time with minimum spatial spread of the electrons. However, in our main experiments, only a single wiggle was visible within our electron distributions.[3] We performed calibration measurements ("wiggle runs") with a reduced electric field to cover various wiggles. The recorded spectrum is shown in figure 4.5.

4.1.3.2. Temporal and Spatial Offsets

Next, we have to remove the electron time of flight offset $t_{0,e}$. Knowing that wiggles occur at $t_{wiggle} = n \cdot T_{Gyr}$, we can extract $t_{0,e}$ from the first visible wiggle in combination with T_{Gyr}. Here we used the time of the first wiggle from the main experiment, as it turned out that it depended on the electric field.

Wiggle positions are not supposed to be E-field dependent, but in practice, they were. In addition, our spectra of electron time of flight vs. position should, in principle, be symmetric around the spatial origin at all times of flight. This was not the case either in reality. We forced the distributions to be roughly symmetric by applying a linear correction in the first place and then generating an offset correction function by fitting Gaussian curves through slices in the spectra along the spatial directions (cf. figure 4.6). The obtained mean values, depending on the time of flight, were subtracted from electron positions. This fixed only the offsets, while the shape of the distributions was still asymmetric, though.

The most likely reason for these flaws is an inhomogeneity of the electric field caused by the focusing mirror in the spectrometer. The latter is conductive and therefore an equipotential surface.

---

[3]This was intentional, as wiggles are blind spots in momentum space. Resolution deteriorates around them.
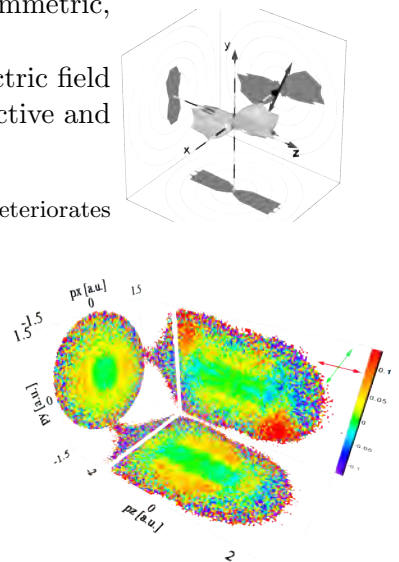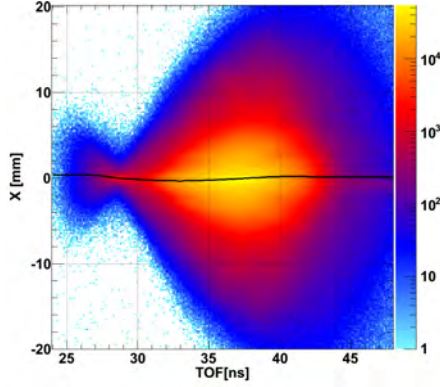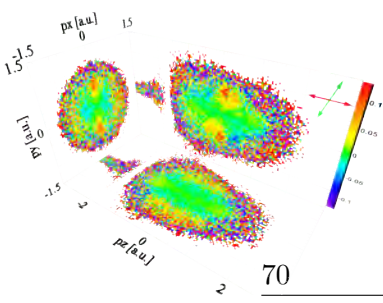
Figure 4.6.: Electron time of flight vs. x position spectrum from experiment A. The slope of the distribution has already been corrected by a linear fit. In a second step, we generated another correction function by fitting Gaussians through slices along the vertical axes and using the resulting mean values as offsets. These are plotted by the black curve. The same was done accordingly for the y coordinate.

4.1.3.3. Magnetic Field Direction and Electron Detector Rotation

Knowing the absolute value $|B|$, we have yet to find out the sign of the magnetic field strength. In fact, this changed between experiments A and B.[4] This sign of the magnetic field is retrieved together with the rotational angle of the electron detector.

We used single ionization events with stable molecular ions as probe. These events should obey momentum conservation in the spatial directions. That is, the distribution of

$$p_{CMS,x/y} = p_{x/y,ion} + p_{x/y,elec}$$

has to be minimized. We chose a sign for B and rotated the electron detector until the widths of the $p_{CMS,x/y}$ distributions were minimum. We used only events with relatively large momenta $p_{x/y}$ in order to maximize visibility of the dependence on the detector angle. After this, we repeated the procedure with B having the opposite sign.

The combination of sign of B and detector angle leading to the narrower distribution of $p_{CMS,x/y}$ was used in the further analysis.

4.1.3.4. Scale Factors

Due to the fact we are using a hexagonal delayline detector, the scale factors of the layers were already automatically calibrated with respect to each other in the first stage of the analysis. What remains is the overall scaling factor of the detector.

---

[4]There is no advantage or disadvantage in making $\vec{B}$ point parallel or anti-parallel to $\vec{E}$. The change happened incidentally, probably during maintenance work.
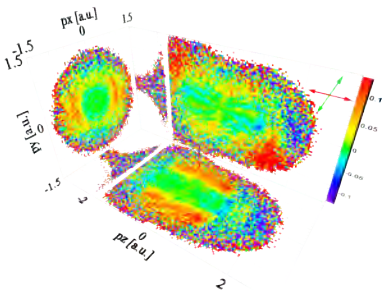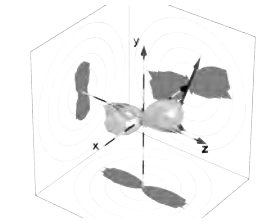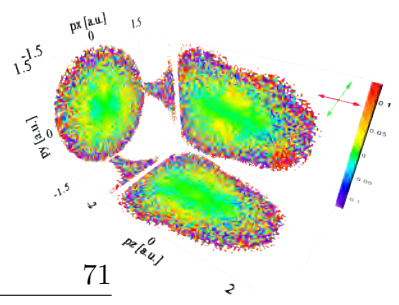
In case of experiment A, we did not resolve any known physical structures in the electron distributions that could have been used for calibration purposes. Hence, we had to rely on a relatively coarse parameter: The known diameter of the MCP.

The situation was more favorable in experiment B. Here, when considering only electrons with small momentum in the time of flight direction ($|p_{z,e}| <$ 0.05 a.u.), we saw distinct electron energy peaks. These were interpreted as ATI. We scaled the detector such that the energy difference between two neighboring peaks matched our photon energy (≈ 1.55 eV).
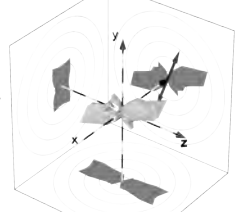
4.1.3.5. Spectrometer Lengths

The last free parameters are the length of the spectrometer's electron extraction region $l_{a,e}$ and the field-free drift $l_{d,e}$. We optimized these, starting with rough values known from the spectrometer design, by matching two conditions:

On the one hand, the electron momentum distribution in the time of flight direction is supposed to be symmetric around zero, as there is no symmetry break (see above).

On the other hand, in case of single ionization, the electron momentum has to take the opposite value of the correlated ion's momentum

$$p_{z,e} = -p_{z,i}$$

due to momentum conservation. This can be checked by plotting the distribution of $p_{z,e}$ vs. $p_{z,i}$, where we expect to see momentum conservation as a diagonal line; cf. figure 4.7.

4.2. Optics

Some optical aspects of the setup also required calibration. This is namely the light intensity in the focus, as well as the delay and polarization between pump and probe pulses.

4.2.1. Probe Pulse Intensity

There are multiple methods to access the intensity of probe pulses.

- If there are detected protons, we can compare their patterns in the time of flight spectrum to tabulated spectra from [73]. In experiment A, a minor amount of background H_2 was ionized. The resulting pattern is consistent with a probe intensity of $I \approx 3 \cdot 10^{14} \frac{W}{cm^2}$.

  Prior to experiment B, we recorded a set of proton spectra at different pulse energies. The results are shown in figure 4.8. A simple thumb formula had been found for the setup before [74]: The intensity in $10^{14} \frac{W}{cm^2}$ roughly

(a) $N_2^+ + e^-$

(b) $O_2^+ + e^-$
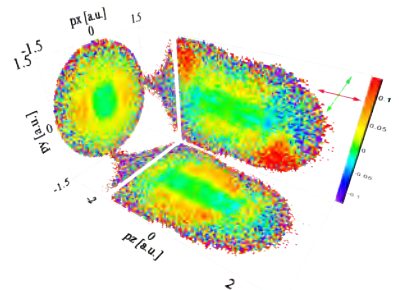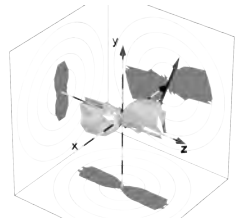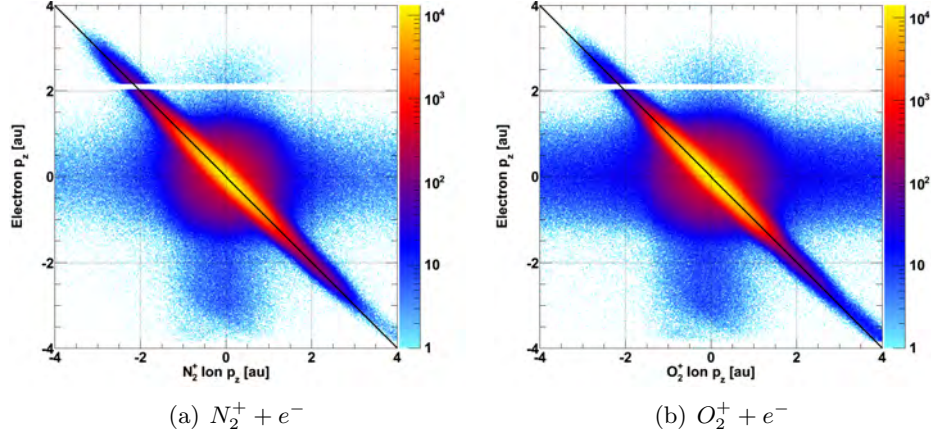
Figure 4.7.: Ion versus electron momentum in the time of flight direction for single ionization channels: $N_2^+ + e^-$ (a) and $O_2^+ + e^-$ (b). Due to momentum conservation, electron and ion momenta have to be antiparallel but equal in magnitude, leading to diagonal lines in the above correlation spectra. The observation of these with a slope of -1 confirms that our values for $l_{a,e}$ and $l_{a,d}$ are reasonable. We did not manage to remove the slight deviations from the diagonal increasing towards the bottom right.

(a) Reference spectra from [73].

(b) Spectra measured before experiment B.
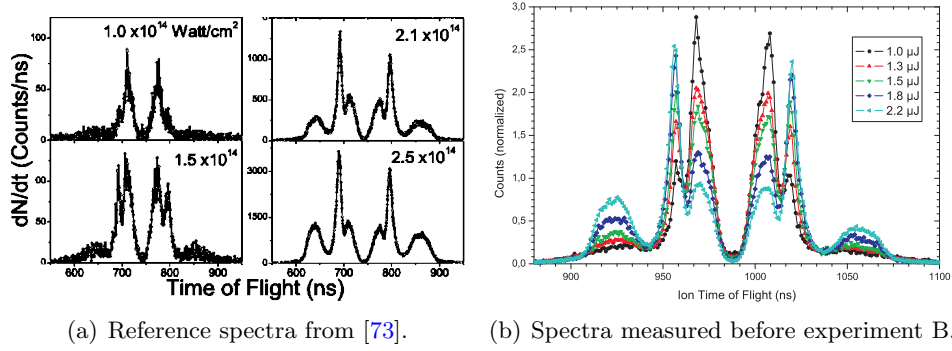
Figure 4.8.: Proton time of flight spectra recorded at different pulse intensities. (a): Reference distributions from [73]. The number given above each curve indicates the corresponding light intensity. By comparing the relative weight of dissociation channels (peaks) between these reference and measured spectra, one can compare light intensity. (b): Proton TOF distributions recorded for this work in a calibration run prior to experiment B. The used pulse energies W_{probe} and intensities inferred by comparison with (a) are: 1.0 μJ (*black* curve) $\Rightarrow 1.0 \cdot 10^{14} \frac{\text{W}}{\text{cm}^2}$; 1.3 μJ (*red*) $\Rightarrow < 1.5 \cdot 10^{14} \frac{\text{W}}{\text{cm}^2}$; 1.5 μJ (*green*) $\Rightarrow \approx 1.5 \cdot 10^{14} \frac{\text{W}}{\text{cm}^2}$; 1.8 μJ (*dark blue*) $\Rightarrow < 2.1 \cdot 10^{14} \frac{\text{W}}{\text{cm}^2}$; 2.2 μJ (*red*) $\Rightarrow \approx 2.1 \cdot 10^{14} \frac{\text{W}}{\text{cm}^2}$. This is consistent with the thumb formula $I \left[10^{14} \frac{\text{W}}{\text{cm}^2} \right] \approx W_{probe}[\mu\text{J}]$.
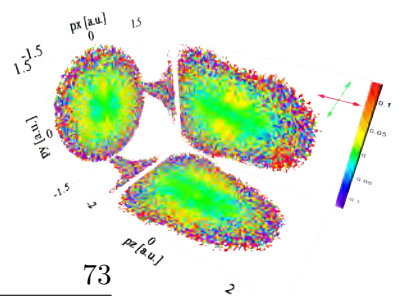
Method	Experiment A	Experiment B
Thumb Rule	$3.0 \cdot 10^{14} \frac{\text{W}}{\text{cm}^2}$	$1.3 \cdot 10^{14} \frac{\text{W}}{\text{cm}^2}$
$H+$ TOF Spectrum	$3 \cdot 10^{14} \frac{\text{W}}{\text{cm}^2}$	$< 1.5 \cdot 10^{14} \frac{\text{W}}{\text{cm}^2}$
$2U_P$ Knee in Electron Rate	$3 \cdot 10^{14} \frac{\text{W}}{\text{cm}^2}$	$1.1 \cdot 10^{14} \frac{\text{W}}{\text{cm}^2}$
$10U_P$ Cutoff in Electron Rate	$2.8 \cdot 10^{14} \frac{\text{W}}{\text{cm}^2}$	$1.4 \cdot 10^{14} \frac{\text{W}}{\text{cm}^2}$
Width of Ar^+ $p_\parallel$ Distribution	$3.3 \cdot 10^{14} \frac{\text{W}}{\text{cm}^2}$	n/a
Assumed "Real" Intensity	$3.0 \cdot 10^{14} \frac{\text{W}}{\text{cm}^2}$	$1.3 \cdot 10^{14} \frac{\text{W}}{\text{cm}^2}$

Table 4.1.: Values for the probe pulse's peak intensity I, obtained via different methods. See text.

equals the energy of probe pulses in μJ. This thumb formula is confirmed by the H^+ method.

- Direct electrons are more abundant than re-scattered ones. Since direct electrons can reach only a maximum kinetic energy of $2U_P$. Electron energy spectra show drop in rate at this value and then show a plateau. We searched for this change in rate in spectra of electron momenta along the probe polarization (p_z).

- Re-scattered electrons can reach a maximum energy of $\approx 10U_P$ [26]. This cutoff can be used, too. We accessed it in the same spectra as the $2U_P$ drop.

- We can fit a Gaussian curve through Ar^+ ion momentum distributions in the direction along the probing laser field ($p_\parallel$). The obtained standard deviation relates to intensity via ADK-based theory (equation (2.6)).

Values obtained with these methods are summarized in table 4.1. None of these values is more reliable than within $\pm 0.5 \cdot 10^{14} \frac{\text{W}}{\text{cm}^2}$.

For experiment A, we assume a peak intensity of $I = 3.0 \cdot 10^{14} \frac{\text{W}}{\text{cm}^2}$ and $I = 1.3 \cdot 10^{14} \frac{\text{W}}{\text{cm}^2}$ in case of experiment B.

4.2.2. Pump Pulse Intensity

The intensity of pump pulses was estimated according to the focus calculation in chapter 3.3.2. In the case of experiment A, we obtain $I_{pump} \approx 0.2 \cdot 10^{14} \frac{\text{W}}{\text{cm}^2}$, while $I_{pump} \approx 0.5 \cdot 10^{14} \frac{\text{W}}{\text{cm}^2}$ for experiment B.

4.2.3. Translation Stage

We set the translation stage's zero position by using second harmonics (blue light) generation in a photonic crystal (BBO).

First, we adjusted the splitting ratio in the interferometer such that each pulse alone was too weak to generate a visible amount of blue light, but close to this
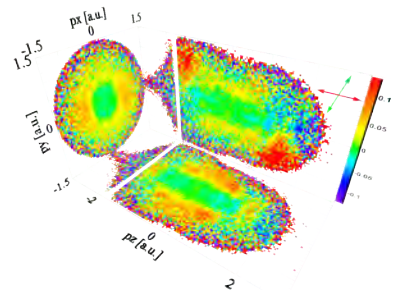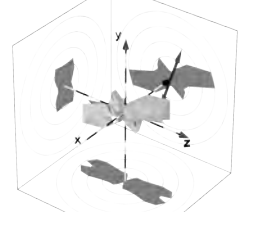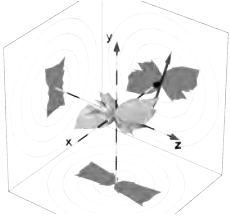
threshold. Second harmonics generation is a non-linear process. Hence, small changes in intensity led to large changes in the yield of harmonics. We moved the translation stage until we saw maximum generation of blue light in the crystal. The stage controller's zero position was then reset.

4.2.4. Rotation Stage

For experiment B, we also had to adjust the zero position of the rotation stage, corresponding to both the aligning and the ionizing pulse polarization being along the z direction. This was done in the analysis after the experiment.

In case of the N_2 measurement, we could simply fit a cosine through the ion rate's dependence on the alignment angle ϕ_{al}. N_2 is most easily ionized if aligned along the probing electric field, which is most likely at an alignment angle of 0°. Hence, the stage angle leading to maximum ionization rate was set to 0°. The behavior of fragment distributions was consistent with our expectations after this simple method of calibration.

The ionization rate based method did not work in case of the O_2 measurement. Instead, we had to rely on the angular distributions of $O^+ + O^+$ fragments. We shifted ϕ_{al} such that we got maximum population along $\varphi_{yx} = 0$ at $\phi_{al} = 90^o$ (pump polarization along y) and isotropic φ_{yx}-dependent distributions at $\phi_{al} = 0, 180^o$.

4.3. Special Definitions used in the Analysis

We are going to use some definitions in the results chapter which shall be explained here.

4.3.1. Normalized Differences

During the analysis of alignment-dependent momentum distributions, it turned out that absolute count rates are sometimes not very insightful, as they span many orders of magnitude. Compare, for example, those displayed in figure 5.4. Instead, a method is needed to show the differences between spectra on some sort of a percentage scale.

Be $\bar{a}$ and $\bar{b}$ histograms of arbitrary dimension to be compared. Operations on histograms are defined on an element-by-element basis, e.g.

$$(\bar{a} + \bar{b})_{i,j} = a_{i,j} + b_{i,j}$$

for two-dimensional histograms. Now, we define the distribution of *normalized differences* as

$$\bar{nd}(\bar{a}, \bar{b}) = \frac{\bar{a} - \bar{b}}{\bar{a} + \bar{b}}. \tag{4.3}$$
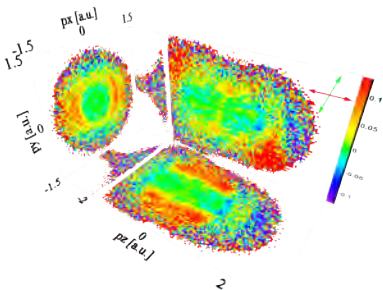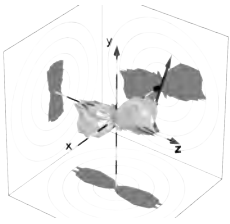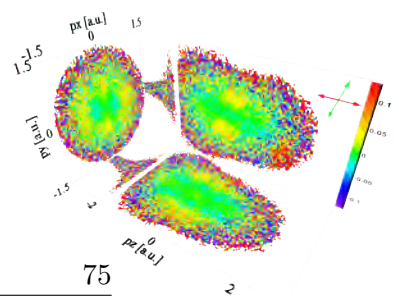
The normalized difference in some specific point is the difference of countrates, given as a fraction of the total countrate. It is also known as "asymmetry parameter" or "contrast function". The ratio a/b related to normalized differences via

$$\frac{a}{b} = \frac{nd+1}{1-nd}.$$

We sometimes have to scale histograms (i.e. multiply their contents) by factors f_a and f_b. The resulting distribution of normalized differences is

$$\bar{nd}(f_a\bar{a}, f_b\bar{b}) = \frac{f_a\bar{a} - f_b\bar{b}}{f_a\bar{a} + f_b\bar{b}}.$$

The statistical uncertainty of a bin containing n counts is

$$\Delta n = \sqrt{n}.$$

For normalized differences, using Gauss's error propagation law, this leads to an uncertainty of

$$\Delta\bar{nd}(f_a\bar{a}, f_b\bar{b}) = 2f_a f_b \sqrt{\bar{a}\bar{b}} \frac{\sqrt{\bar{a}+\bar{b}}}{(f_a\bar{a} + f_b\bar{b})^2}$$

for rescaled histograms and

$$\Delta\bar{nd}(\bar{a}, \bar{b}) = 2\sqrt{\frac{\bar{a}\bar{b}}{(\bar{a}+\bar{b})^3}}$$

if $f_a = f_b = 1$, i.e. $\bar{a}$ and $\bar{b}$ contain absolute numbers of counts.

If we have only a small number of counts in both the signal and the reference, we obtain a large statistical error. This leads to blurring of the normalized difference in regions where our absolute distributions are only sparsely populated. We suppress this noise by plotting the normalized difference only for bins where both the signal and the reference spectrum contains a number of counts that is above a set lower limit.

4.3.2. Column and Row-Wise Normalization

It also turned out that various kinds of normalization can be applied in order to gain insight. We will be using "column-wise" and "row-wise" normalization of a two-dimensional histogram. We define the *column-wise normalization* of a 2D histogram $\bar{a}$ as

$$a_{colnorm_{i,j}} = a_{i,j} \cdot f_i$$

with the scaling factors being the contents of an array (1D histogram) $\bar{f}$ where

$$f_i = \frac{1}{\sum_j a_{i,j}}.$$

(a) Absolute Spectrum   (b) Column-wise normalized   (c) Row-wise normalized
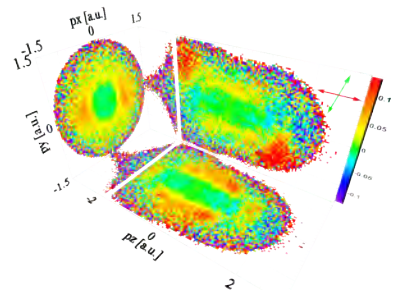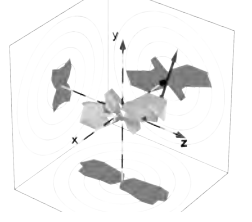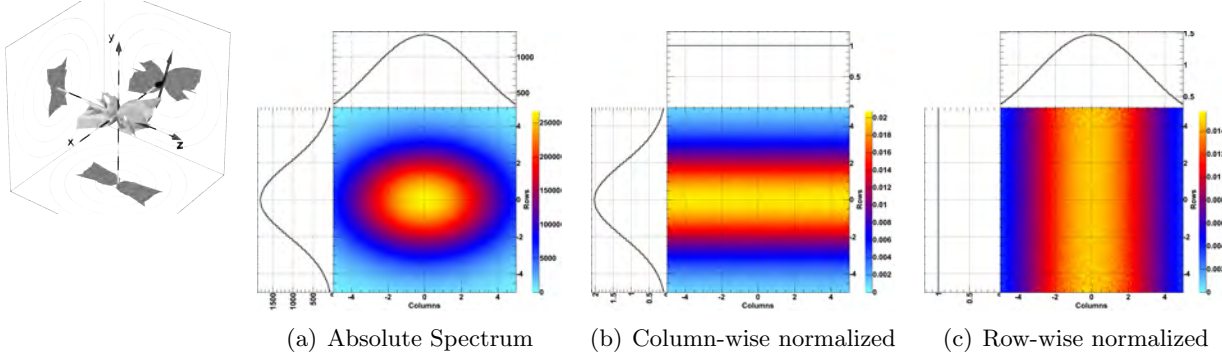
Figure 4.9.: Illustration of (b) column- and (c) row-wise normalization. Each inset above a color plot shows the x projection of the latter with the y direction integrated over. Insets on the left of a color plot show its y projection.

In words, we divide each bin content in a column by the sum of all bin contents in that column. Along this line we define *row-wise normalization* as

$$a_{rownorm_{i,j}} = a_{i,j} \cdot f_j$$

with

$$f_j = \frac{1}{\sum_i a_{i,j}}.$$

These types of normalization are illustrated in figure 4.9.

4.3.3. Spherical Coordinates and Solid Angle

We are going to plot some distributions in spherical coordinates around the z axis, i.e. depending on the angles ϑ_z and φ_{yx}. A peculiarity of spherical coordinates is the non-constant solid angle element

$$d\Omega(\vartheta_z) = \sin\vartheta_z d\varphi_{yx} d\vartheta_z.$$

We are generally interested in rates without a bias by the size of the solid angle element. As our bin size is usually fixed and constant across a histogram, we have to divide each bin by the corresponding value of $\sin\vartheta_z$.

4.3.4. Three-Dimensional Representations of Angular Distributions

The three-dimensional angular distributions used in various parts of this work (such as the flip-book feature) are in spherical coordinates around the z axis, depending on φ_{yx} and ϑ_z. The solid angle element is normalized out where appropriate (i.e. wherever we show experimental data). The shadows on the coordinate planes are really just shadows of the three-dimensional distributions rather than real integrations over an angle.
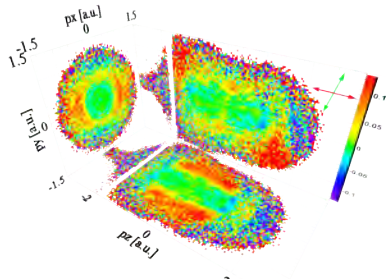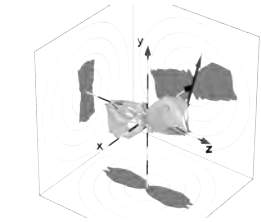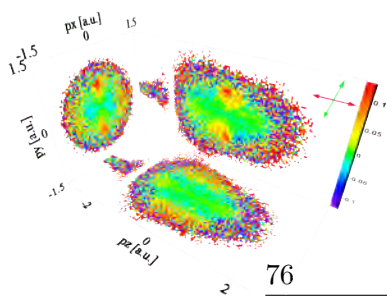
We do not have data for the "poles" in the coordinate system, i.e. for $\vartheta_z = 0$ and $\vartheta_z = 180^o$. We set these points to the average value of the respective neighboring bins.

Around the "poles", the statistical error of our bin contents diverges due to the normalization of the solid angle element, leading to large fluctuations. This is why the implemented cutoff at a maximum radius value is visible around the poles.
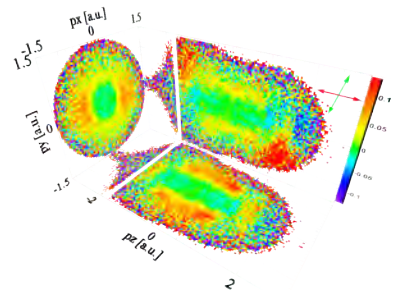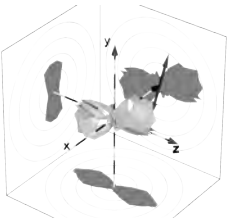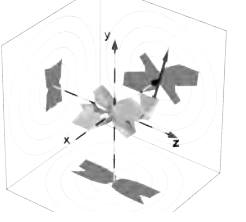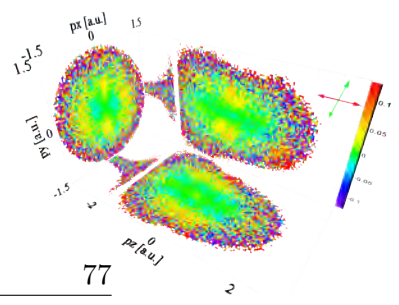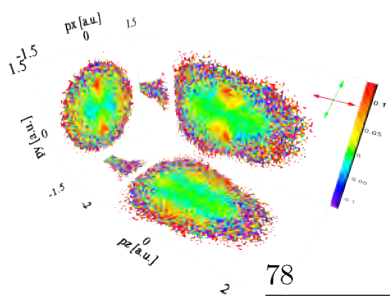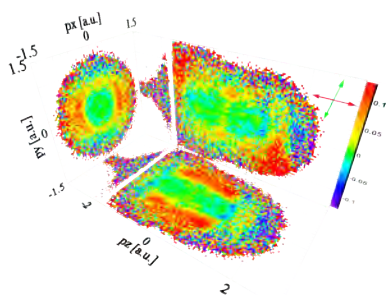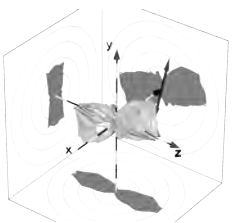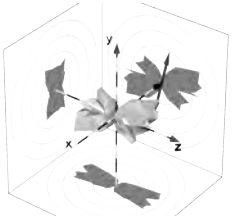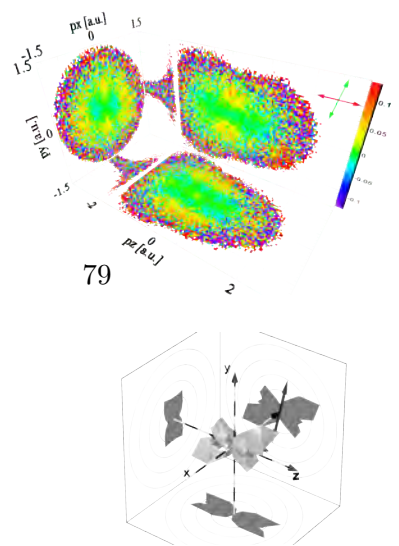
5. Data and Results

> If your experiment needs
> statistics, you ought to have
> done a better experiment.
>
> *(Ernest Rutherford)*

We performed two main experiments, which are called "experiment A" and "experiment B" in this work. In experiment A, we were able to achieve two different distributions of molecular axes prior to ionization. In experiment B, we rotated such a distribution step by step.

Parameters were changed between experiment A and B. Care was taken to keep them constant during each of them, though.

Results from experiment A will be presented in section 5.1, followed by those of experiment B in section 5.2. Many plots and findings which did not fit into this chapter can be found in appendices A and B.
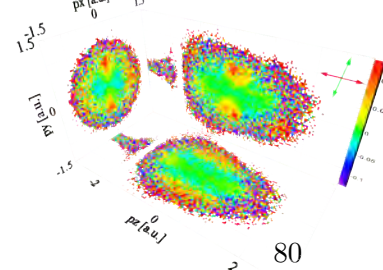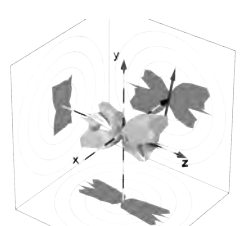
5.1. Experiment A: Aligned / Anti-Aligned

Experiment A is a pump-probe alignment experiment as outlined before. We measured the electron and ion momentum distributions from aligned and anti-aligned nitrogen and oxygen molecules, as well as argon atoms.

Our jet target was composed of all target particles, plus helium for cooling purposes and traces of xenon. Approximate abundances are given in table 5.1. A spectrum of the measured ion mass/charge ratios is shown in figure 5.1 up to $m/q = 50$. All the mentioned atomic and molecular species were literally in the same gas bottle. Hence, data for all processes, alignments and species discussed in the following sections were recorded virtually simultaneously and under identical conditions. They were sorted out in a post-experiment analysis.

Due to the fact that N_2 and O_2 have different moments of inertia, we had to use different pump-probe delays to align them. In order to rule out possible effects by any (unobserved) drift in the laser system, we changed the the delay between the aligning pump and the ionizing probe pulse between the values for aligning N_2, anti-aligning N_2, aligning O_2 and anti-aligning O_2 after every ten seconds at one position.
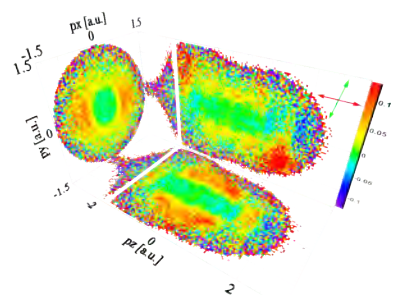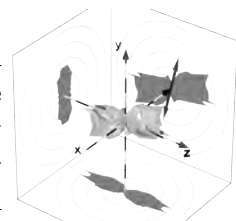
Gas	Pressure reading [PSI]	Abundance [%]
Xe	0	< 0.25
O_2	36	8.8
N_2	120	21.3
Ar	140	13.8
He	400	86.3

Table 5.1.: Composition of the target gas mixture in experiment A. A gas bottle was filled with the given species up to the respective total pressure specified above. These readings are all excess pressures over the atmosphere, which was accounted for in the calculation of approximate abundances. The assumed upper limit for Xe corresponds to a pressure of one atmosphere.

The most relevant experimental parameters are summarized in table 5.2. It is important to note that the polarizations of pump and probe pulses were always perpendicular with respect to each other in this experiment: The aligning pump along the y- and the ionizing probe pulses along the z-axis.

The set of raw data underlying this section led to results published in [11] and the respective "supplementary online material" (SOM) [75]. Most of the graphs shown here are based on a re-evaluation of the dataset, though. Deviations of the calibration from the one used in the paper are minor and do not affect the results[1]. The interpretations of the data and predicted implications are published in [11], too.

5.1.1. Coulomb Exploded Fragments / Alignment Distributions

For further analysis we would like to estimate the angular distribution of molecules $P_{al}(\vartheta_y)$ prior to ionization. A standard technique to measure such a distribution is Coulomb explosion imaging (CEI) [54]. Usually, circularly polarized laser pulses are used to make the molecules explode. The fragments then fly apart back to back, with their momentum vectors pointing along the former molecular axis. As energetic as possible fragments are used to minimize the errors induced by rotations of the molecules and the lifetimes of intermediate states.

5.1.1.1. Conditions

During our experiment, at a certain rate, molecules were doubly ionized and Coulomb exploded:

$$N_2 \rightarrow N^+ + N^+ + 2e^-$$
$$O_2 \rightarrow O^+ + O^+ + 2e^-.$$

---
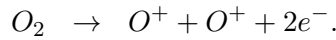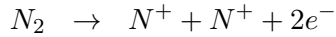
[1]In the paper, we assumed a probe intensity of $I = 2.5 \cdot 10^{14} \frac{\text{W}}{\text{cm}^2}$ while here, we estimate $3.0 \cdot 10^{14} \frac{\text{W}}{\text{cm}^2}$. This deviation is within the error margin. We confirmed all parameters of the diffraction analysis (section 5.1.2.2) remain the same within rounding errors for both intensities.
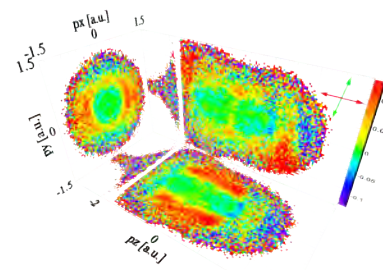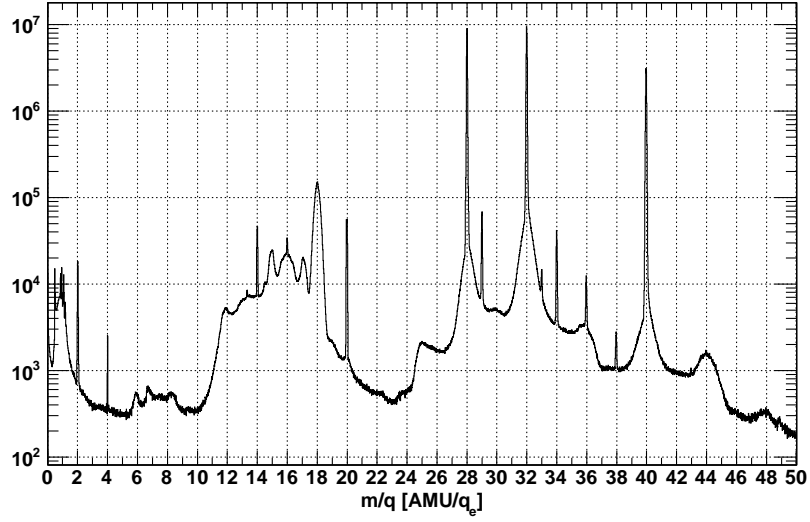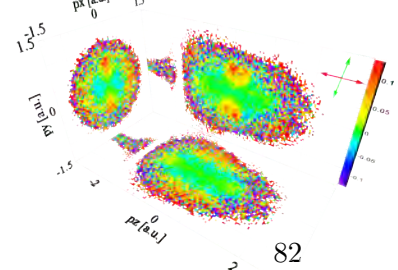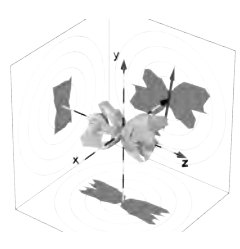
Figure 5.1.: Distribution of ion mass/charge ratios in experiment A. m/q was calculated for each ion from its time of flight according to equation (4.1), assuming zero initial velocity. The highest peaks originate from $^{14}N_2^+$ ($m/q = 28$), $^{16}O_2^+$ ($m/q = 32$) and $^{40}Ar^+$. Several less abundant isotopes can be found as well. These will not be further analyzed. Narrow peaks from the double ions corresponding to the mentioned species are visible at the expected positions (14, 16, 20). The broad pedestal roughly extending between calculated mass/charge ratios from 10 to 20 is caused by a mixture of dissociated and exploded molecules ($N^+ + N$, $N^+ + N^+$ and the same from oxygen accordingly). A conventional time of flight (TOF) spectrum can be found in the appendix, figure A.1.

Optics	Laser	wavelength:	$\lambda = 800$ nm
		repetition rate:	$f = 30$ kHz
	Ionizing pulse	polarization:	linear along z-axis
		energy:	$W_{Ionize} = 3.0\ \mu$J
		intensity:	$I_{Ionize} = 3.0 \cdot 10^{14}\ \frac{\text{W}}{\text{cm}^2}$
			$\Rightarrow U_P = 14.9$ eV
			$\Rightarrow v_{osc} = 1.5$ a.u.
		length:	$\tau_{Ionize} \approx 40$ fs
	Aligning pulse	polarization:	linear along y-axis
		energy:	$W_{Align} = 1.2\ \mu$J
		intensity:	$I_{Align} \sim 10^{13}\ \frac{\text{W}}{\text{cm}^2}$
		length:	$\tau_{Align} \sim 60$ fs
		shape:	clipped & chirped
	Pump-probe delays	N_2 aligned:	3.856 ps
		N_2 anti-aligned:	4.490 ps
		O_2 aligned:	2.949 ps
		O_2 anti-aligned:	8.759 ps
	Focusing mirror	type:	parabolic, on-axis
		focal length:	$f = 50$ mm
Jet	Gas	mixture:	$N_2, O_2, Ar, He, (Xe)$
		pressure	1.4 bar
	Nozzle	diameter:	10 μm
		temperature:	110 K
	Skimmer	hole diameter:	0.3 mm
		nozzle-distance:	8 mm
Spectrometer	Length of electron	extraction:	$l_{extr,elec} = 68.5$ mm
		drift:	$l_{drift,elec} = 151.5$ mm
	Length of ion	extraction:	$l_{extr,ion} = 148$ mm
		drift:	$l_{drift,ion} = 0$ mm
	Magnetic field	strength:	$B = 13.7$ Gauss
		orientation:	along z-axis, homogeneous
	Electric field	strength:	$E = 2910\ \frac{\text{V}}{\text{m}}$
		orientation:	along z-axis, homogeneous
	4π solid angle	$N^+ + N^+$ (ions)	$p_{max,i} \leq 106$ a.u.
		$O^+ + O^+$ (ions)	$p_{max,i} \leq 113.5$ a.u.
	Electron momentum	Cutoff:	$|p_{\parallel,e}| < 4.0$ a.u.
			$p_{\perp,e} < 1.6$ a.u.
Misc.	Data taking	Start:	2005-08-22 06:10 EST
		Stop:	2005-08-23 14:00 EST
	Analysis Version	Run7-2.1_N2O2ArXe_2.2.0	
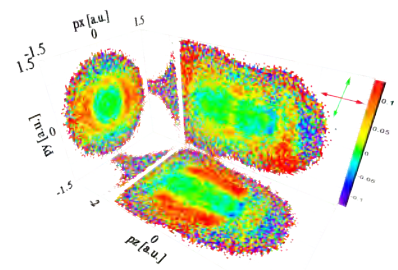
Table 5.2.: Parameters of experiment A (aligned / anti-aligned).

Species	$p_{cms,Max}$[a.u.]	KER_{Min}[eV]	KER_{Max}[eV]
$N^+ + N^+$	8	4.9	12.0
$O^+ + O^+$	8	4.2	12.0

Table 5.3.: Conditions an explosion event has to fulfill to be further analyzed: The kinetic energy release of the ionic fragments (KER) has to be in a windows between KER_{Min} and KER_{Max} and the center of mass momentum shall not exceed $p_{cms,Max}$. KER_{Max} was chosen as a cutoff such that our spectrometer detects ions with 4π solid angle.

We distinguish correlated fragments by Coulomb explosions from background by exploiting momentum conservation. Given the electron momentum is negligible, the ion center of mass momentum would ideally be zero. We plot only events where the maximum center of mass momentum $p_{cms,Max}$ specified in table 5.3 is not exceeded and the kinetic energy release KER is within the given range. This method also enables us to distinguish between N^+, O^+ and the respective molecular double ions.

5.1.1.2. Angular Fragment Distributions

The angular distributions of such correlated fragments are shown in figure 5.2 for both species at the two measured alignments. Ideally aligned molecules would be oriented along the aligning pulse polarization, i.e., along the y (vertical) axis. Perfectly anti-aligned ones would lie in the plane perpendicular to the pump polarization, that is, in the $z - x$ plane. However, the observed distributions show interesting structures in the $z - y$ plane as well. This coincides with the ionizing laser pulses being linearly polarized along z. Each event is used twice for angle-dependent spectra: Once we fill them with $\vec{p}$ and another time with $-\vec{p}$. This is justified by the fact that the momentum vector of the ion reaching the detector second is anti-parallel to the first ion's.

5.1.1.3. Alignment Distributions

What we are observing is a convolution of two angular dependencies. The probe pulse is "offered" an angular distribution of neutral molecules

$$P_{al}(\vartheta_y)$$

caused by our attempt to align. Here ϑ_y is the angle of a molecular axis with the aligning laser polarization. This is the distribution we are interested in. Each molecule is ionized and exploded with a probability depending on the angle between the probe polarization and the molecular axis $\vec{d}$:

$$P_{Explode}[\angle(\vec{d}, \vec{\epsilon}_{probe})].$$
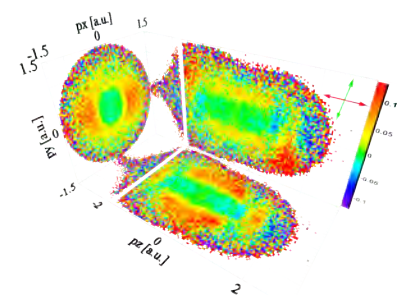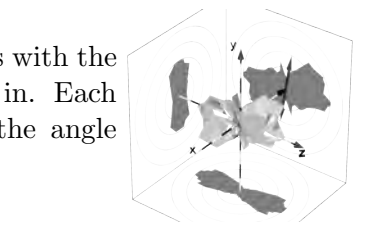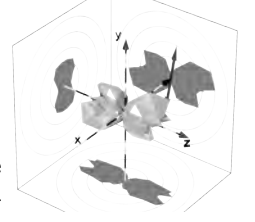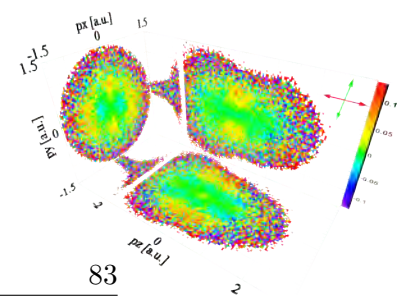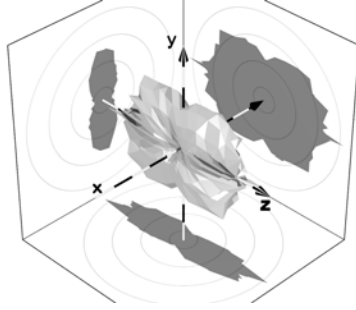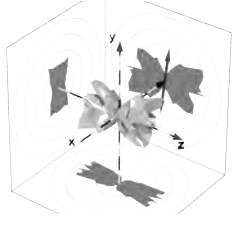
(a) $N^+ + N^+$ from Aligned N_2
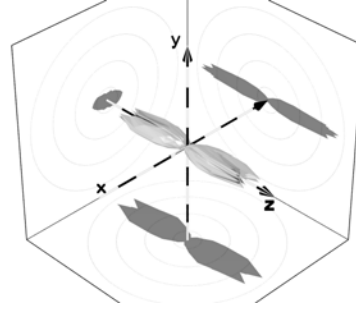
(b) $N^+ + N^+$ from Anti-Aligned N_2
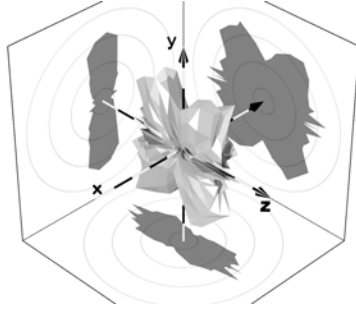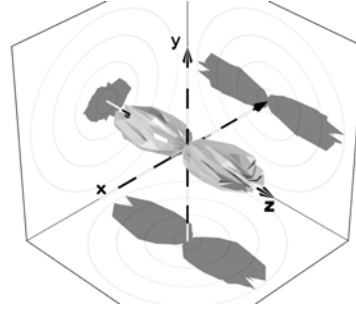
(c) $O^+ + O^+$ from Aligned O_2

(d) $O^+ + O^+$ from Anti-Aligned O_2
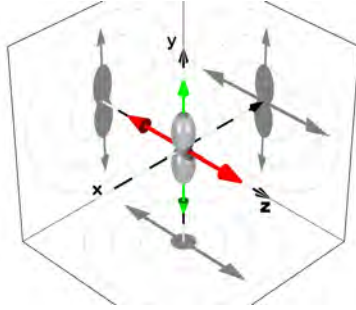
(e) Sketch: Aligned Distribution
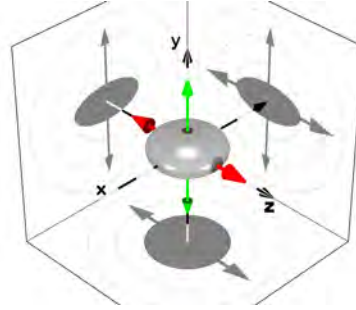
(f) Sketch: Anti-Aligned Distribution

Figure 5.2.: (a) to (d): Measured three-dimensional distributions of singly charged fragments from Coulomb explosions. The applied conditions are summarized in table 5.3. The expected shape of an aligned distribution is sketched in (e) and the one of an anti-aligned distribution in (f). The direction of the aligning pulse polarization (y) is denoted by a *green* and the ionizing polarization (along z) by a *red* double arrow in the latter two panels. The experimentally observed patterns resemble the expected alignment distributions only in the direction perpendicular to the probe polarization ($x-y$ plane). This is because the fragment rates depend on the angle between the molecular axes and the probing electric field. See section 5.1.1.4 for a discussion. Two-dimensional color plots with the same content are given in the appendix, figure A.6.
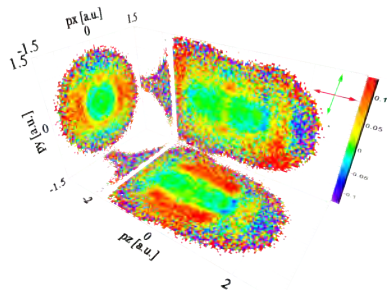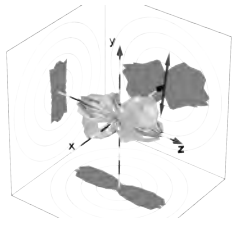
	N_2	O_2	Ideal
Aligned	0.69	0.71	1
Anti-Aligned	0.40	0.44	0

Table 5.4.: Values of the alignment parameter $< \cos^2 \varphi_{yx} >$ for the cases used in the experiment. These were extracted from the revival structure given in the appendix, figure A.5. The values $< \cos^2 \varphi_{yx} >$ would take in case of ideal alignment / anti-alignment are stated in the column on the very right.

Our ionization signal $S_{Explode}$ is determined by the product of the explained angle-dependent probabilities:

$$S_{Explode} = P_{al} \cdot P_{Explode}.$$

Nevertheless, in the direction perpendicular to the probing laser polarization, i.e. in the $x - y$ plane, we can assume the laser field will not cause a bias. That is, $P_{Explode}$ does not depend on the angle φ_{yx} in our laboratory coordinate system. Hence, the distribution of fragments with respect to the angle φ_{yx} approximately reflects the distribution $P_{al}(\vartheta_y)$ of neutral molecules.[2] The angular distributions of fragments in the direction perpendicular to the probe polarization are shown in figure 5.3. We give the corresponding values of the alignment parameter $< \cos^2 \varphi_{yx} >$ in table 5.4. The revival structure, i.e. the dependence of the alignment parameter on the pump-probe delay τ can be found in the appendix, figure A.5.

We conclude that the experimentally achieved degree of alignment is significant, though far from being perfect.

5.1.1.4. Angle-Dependent Ionization Probabilities

We will now briefly discuss the three-dimensional fragment distributions with respect to the angle-dependent single ionization probabilities of the measured species. It has been previously established that the tunneling (single ionization) step dominates the rate of Coulomb explosions [72].

All experimental distributions in figure 5.2 show a suppression of rates if the fragments explode in the $x - y$ direction, having only a small component along z. The ion detector is oriented within this plane. The detector deadtime significantly reduces detection efficiency for molecules exploding within the $x - y$

---

[2]Three remarks have to be made regarding this interpretation: 1) The lifetime of any possible intermediate states multiplied by the angular frequency of a spinning molecule is assumed to be negligible. 2) We also assume that the probe pulse does not rotate the molecular axes. The effect of such a rotation would be weakest in our plane of observation, though. 3) The dominant process for double ionization in our intensity regime is inelastic electron re-scattering. We assume that $P_{Explode}[\angle(\vec{d}, \vec{\epsilon}_{probe})]$ is dominated by the angular-dependent tunneling probability. Any angle-dependence in the probability of inelastic re-scattering which might also affect φ_{yx} is ignored. The assumptions 1) and 3) are supported by [72].
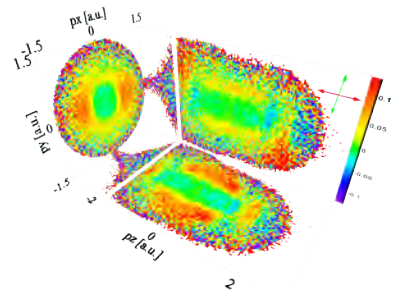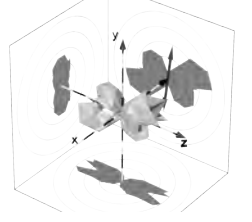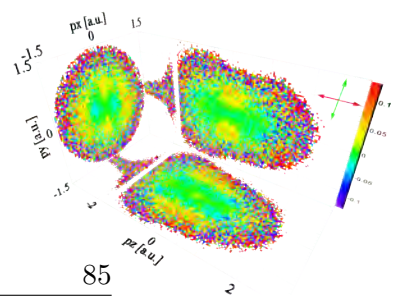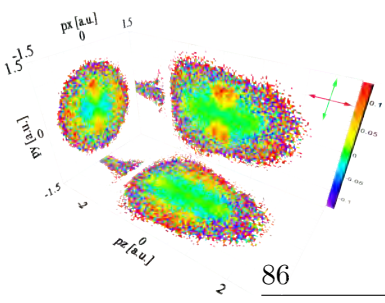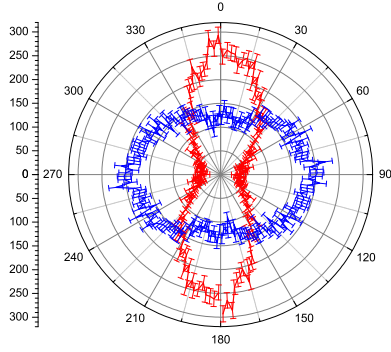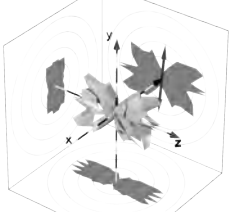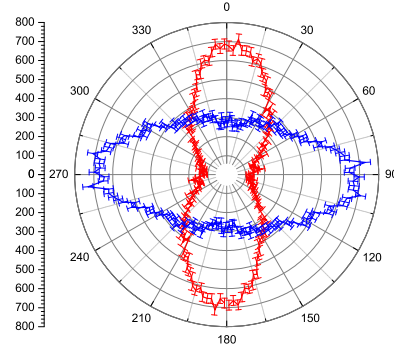
(a) $O^+ + O^+$ (b) $N^+ + N^+$

Figure 5.3.: Angular distributions of correlated ionic fragments in the plane perpendicular to the probe polarization. (a): $O^+ + O^+$; (b): $N^+ + N^+$. Red lines: Pump-probe delays adjusted for alignment; blue lines: Anti-alignment. The aligning pulse polarization (i.e. alignment direction) is vertical. These fragment distributions should reflect the angular distributions of the aligned / anti-aligned molecular ensembles at the instant of ionization. Perfect alignment would have yielded a narrow line along the vertical axis whereas perfect anti-alignment would have led to a horizontal line. Error bars are statistical.
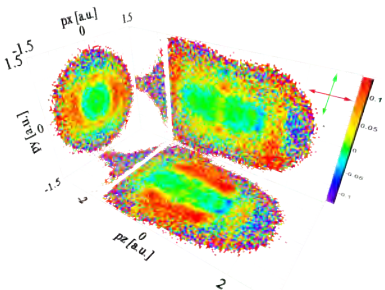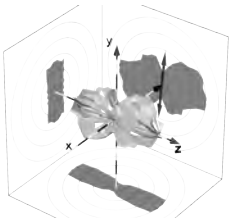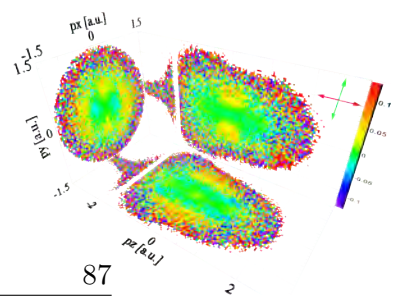
plane, successively arriving withing a very short time interval. This leads to a minimum in all of the angular distributions shown.

First, we analyze the distributions from *aligned* molecules. As sketched in figure 5.2(e), we are expecting the ensemble of molecules prior to ionization to be mostly along the aligning pulse polarization (y axis).
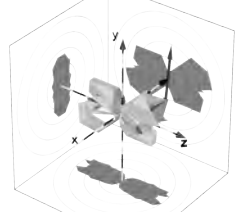
However, the ion distribution from aligned O_2 molecules (figure 5.2(c)) shows a characteristic, butterfly-like shape in the the $z - y$ plane. This is composed of a significant suppression of molecules exploding along the alignment direction (y axis), suppression along the probe polarization (z) and an enhancement at an angle of $\approx 45^o$ withing the $z - y$ plane. The suppression at 90° can be only partly caused by the detector deadtime, as it is observed remarkably stronger for O_2 than for N_2. The suppression coincides with the tunneling probability from O_2 minimizing at 0° and 90° and maximizing at an angle of $\approx 45^o$ between the ionizing electric field and the molecular axis (cf. chapter 2.2.9 / figure 2.4). Obviously, the preference of oxygen to ionize at 45° is so strong the relatively small fraction of all molecules pointing in this direction due to imperfections in the achieved alignment are enough to shape the fragment distribution. We can directly see the effect of our alignment technique only in the direction perpendicular to the probe polarization.

In case of aligned N_2 (fig. 5.2(a)), the minimum along y is weaker than in case of O_2 while the one along z into a maximum. While the minimum along the y axis can be explained by the detector deadtime, the maximum along the probe polarization is in agreement with the ionization probability of N_2 being maximum in a parallel and minimum in a perpendicular geometry.

In case of *anti-alignment*, we expect the molecular axes to be randomly oriented within the $z - x$ plane (perpendicular to the aligning pulse); see sketch in figure 5.2(e).

The fragment distribution from anti-aligned N_2 (fig. 5.2(b)) is strongly enhanced along the probing laser field. This is the orientation of preference for tunneling. We see that the the distribution is squeezed together in the y direction, which is an effect of the anti-alignment.

The fragments from anti-aligned O_2 (fig. 5.2(d)) explode preferentially along the probe polarization, too, although their distribution is not as narrow as in N_2. Since we are expecting O_2 to ionize most likely at 45° with the z axis, this is unexpected. It becomes even more surprising if we realize that the maximum of the ionization probability at 45° prevailed in case of alignment, where this angle was suppressed in the distribution "offered" to the ionizing pulse. In the occasion of anti-alignment, all angles between the laser polarization and a molecular axis are equally populated. This shall be assessed no further here, though.
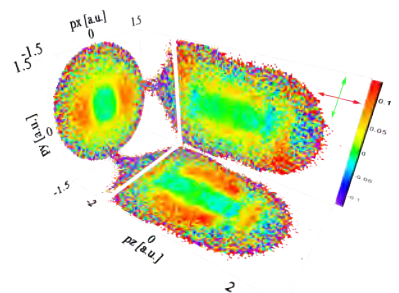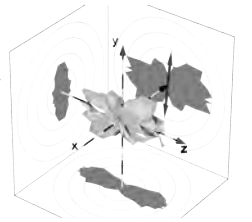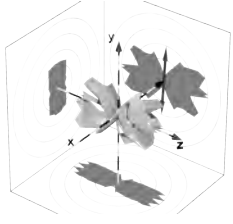
Ion Species	$p_{cms,x}$[a.u.]	$p_{cms,y}$[a.u.]	$p_{cms,z}$[a.u.]
N_2^+	10	10	0.5
O_2^+	10	10	0.6

Table 5.5.: Cutoff values for center of mass momenta as defined in equation 5.1. Only events with values lower than the ones given above in each direction were counted as valid.

5.1.2. Electron Momentum Distributions from Single Ionization

Our main interest was aimed at the single ionization of aligned molecules, i.e. the channels

$$N_2 \quad \rightarrow \quad N_2^+ + e^- \qquad \text{and}$$
$$O_2 \quad \rightarrow \quad O_2^+ + e^-$$
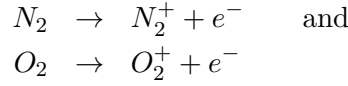
where stable molecular single ions emerge. In this case, momentum should be conserved between the electron and the ion:

$$\vec{p}_{cms} = \vec{p}_{elec} + \vec{p}_{ion} = \vec{0}. \tag{5.1}$$

Both particles therefore carry a copy of the same piece of information. Our resolution for electron momenta was better than the one for ions in the range of interest, so we will further analyze electrons rather than ions. For each electron, the correlated ion was still detected and its momentum calculated, though. Only events where the center of mass momentum was below the respective cutoff value given in table 5.5 for each direction were considered as valid. This condition also provided for the assignment of a detected ion to a species, as wrong assignments lead to large calculated center of mass momenta in the z direction.

The distributions of electron momenta from aligned and anti-aligned N_2 and O_2 are shown as a pseudo-3D representation in figure 5.4. The three-dimensional density distributions were projected onto each coordinate plane by integrating over the respective third dimension.[3]

The greater spread of electrons along the z axis as compared to the x and y direction is immediately obvious. This is no surprise as it coincides with the direction of the driving electric field of the ionizing pulse "streaking" the electron (cf. chapter 2.3.1). A "tail" at $p_x = p_y = 0$, $p_z < -2$ a.u. is visible only in the distribution from oxygen molecules. However, as this should be symmetric along the z axis but is not, it can be identified as an artifact (of unknown origin). Apart from this, we do not see any significant structure or difference between neither the species nor the alignments. The most prominent feature of the spectra is a dynamic range spanning more than five orders of magnitude and making the full-range color scale too coarse to reveal detailed structure.

---

[3]The same projections with the respective third dimension being restricted to ±0.1 a.u. can be found in the appendix, chapter A.4.

(a) N_2 Aligned

(b) N_2 Anti-Aligned

(c) O_2 Aligned

(d) O_2 Anti-Aligned
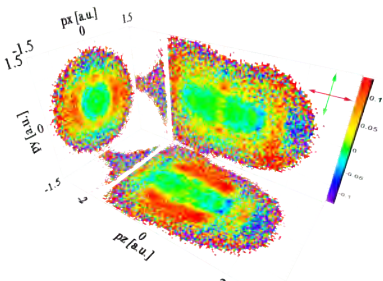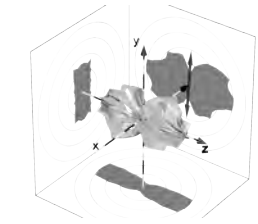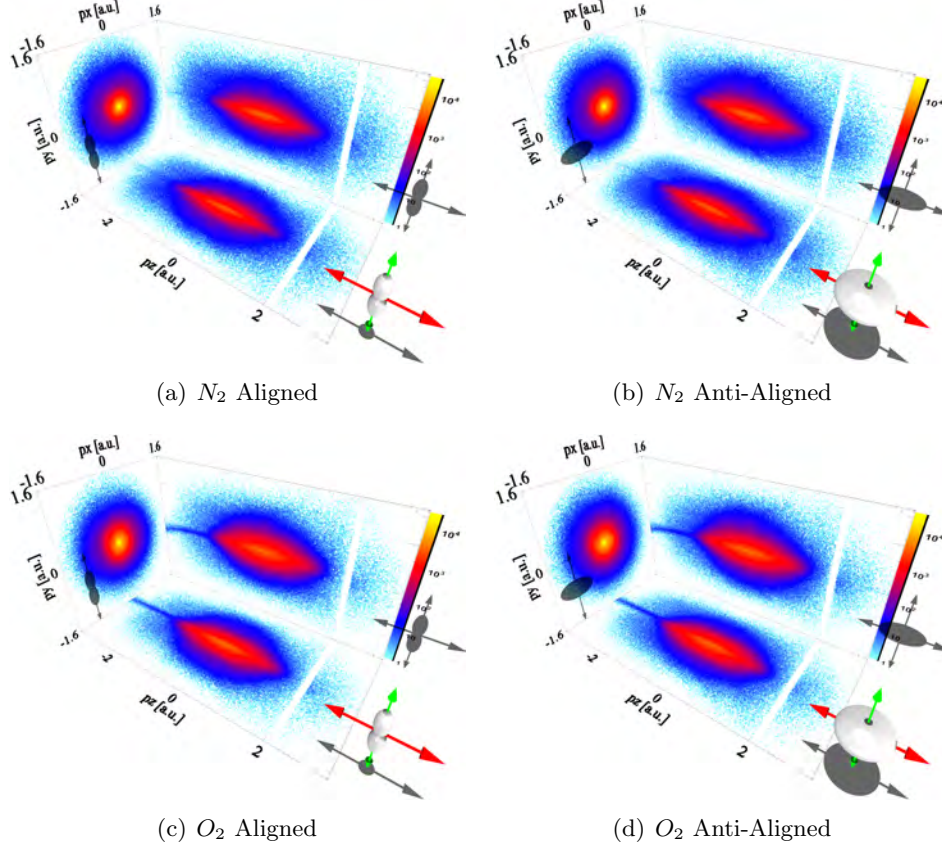
Figure 5.4.: Distributions of electron momenta in a pseudo-3D representation. For each projection in a plot the respective third dimension was integrated over. Only electrons correlated with either stable N_2^+ (*top*) or O_2^+ (*bottom* row) ions are shown. The molecules were aligned (*left*) or anti-aligned (column on the *right*) prior to ionization. The sketches in the foreground illustrate the angular distributions of molecular axes prior to ionization. The aligning pulse polarization was along the y axis (*green* double arrow), whereas ionizing pulses were polarized along z (*red* arrow). Electrons are spread out more along the ionizing electric field direction than perpendicular to it. The features visible as white stripes around $p_z = -2$ a.u. are artifacts ("wiggles"). The origin of the blue tails visible almost exclusively in the O_2 spectra at $p_x = p_y = 0$, $p_z < 2$ a.u. is not clear. Nevertheless, these must be an artifact, as they do not appear at $p_z > +2$ a.u. despite physics being symmetric along the z-axis. No further striking difference between either the species or the alignments is visible to the plain eye. Everything we see is a dynamic range spanning five orders of magnitude. The graphs are reproduced without the 3D effect in the appendix, figures A.8 to A.11.
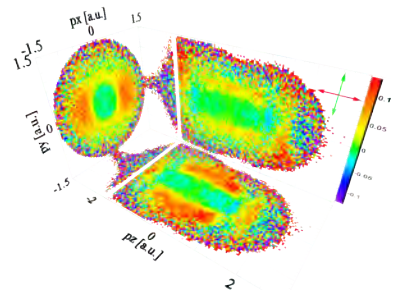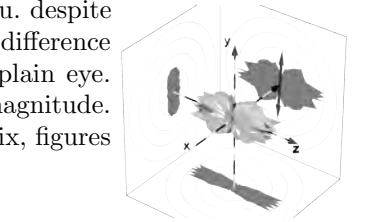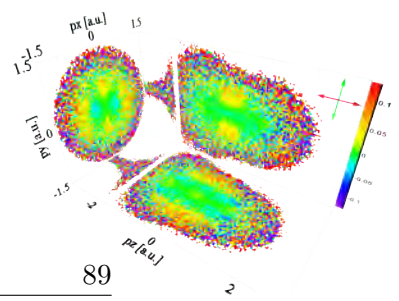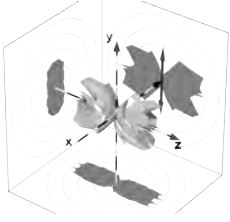
In order to make alignment-dependent modulations visible, we calculate the "normalized differences" between the electron momentum distributions from aligned and anti-aligned molecules according to equation (4.3). These are displayed in figure 5.5.

The patterns suggest a distinction between two regions in momentum space:

- Up to $p_\perp = \sqrt{p_x^2 + p_y^2} \approx 0.5$ a.u., $|p_\parallel| = |p_z| \approx 1.5$ a.u., the structures in all projections differ substantially between N_2 and O_2. We will show that these reflect the symmetry of the tunneled wavepacket and therefore the ionized molecular orbital in section 5.1.2.1.

- At higher momenta, there are no significant differences between N_2 and O_2 at first impression. This regime will be further analyzed in section 5.1.2.2.

5.1.2.1. Low-Momentum Structures

As explained in chapter 2.3.1, p_{osc} is the maximum momentum an electron can gain from "streaking" by the oscillating electric field by the intense light without re-scattering. The peak intensity of the ionizing pulse in the experiment corresponds to an oscillation momentum of $p_{osc} \approx 1.5$ a.u., coinciding with the width of the low-momentum structures along the z axis (probe polarization direction). This suggests that the pattern is caused by direct, non-rescattered electrons which can be expected to dominate the spectra in the mentioned regions.

From equation (2.9) we learn that the distribution of electrons in the directions perpendicular to the driving laser polarization is essentially a projection of the ionized molecular orbital (pre-exponential factor), "filtered" by the tunnel. The exponential factor is the Gaussian filter function. It shall be noted that the latter does not explicitly depend on the orientation of the molecular axis.

By calculating normalized differences for experimental electron momentum distributions from different alignments, we therefore divide the exponential factor out. The molecular orbital is locked to the molecular frame, though, making the pre-exponential factor alignment-dependent. Hence, the low-momentum structures of the $x - y$ projection in figure 5.5 can be explained as being caused by projections of the ionized orbitals.

It can be argued that the electric field at the time of tunneling E is still contained in the exponential factor. It depends on the tunneling phase φ_i which, according to equation (2.12), relates to momentum along the ionizing pulse polarization (z direction) via

$$p_z(\varphi_i) \approx p_{osc} \sin \varphi_i.$$

The $x - y$ projection in figure 5.5 was made by integrating over p_z, that is, over all occurring values of E. In figure 5.6, we compare reproductions of these integrated-over distributions to ones where the momentum along the laser field was restricted to an interval of $|p_z| < 0.1$ a.u. This condition relates to allowing
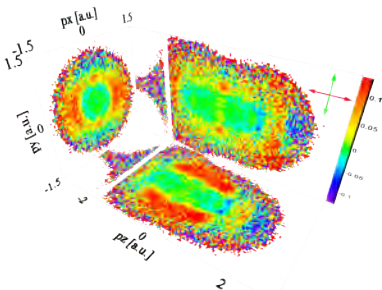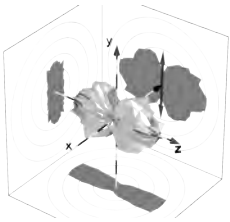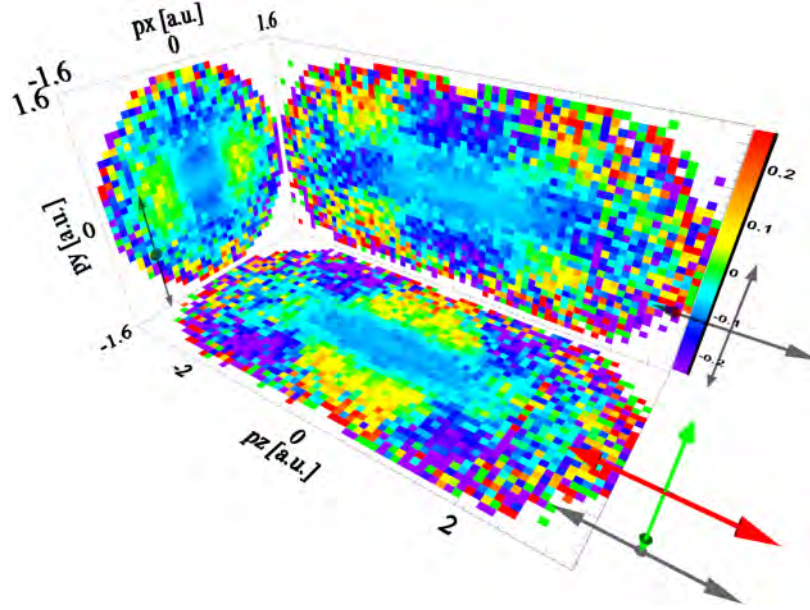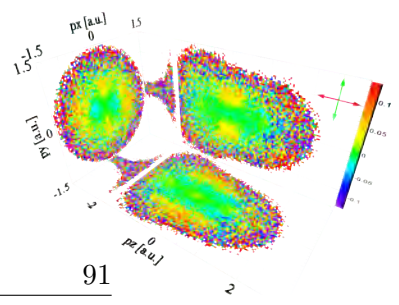
(a) Electrons correlated with N_2^+ ions
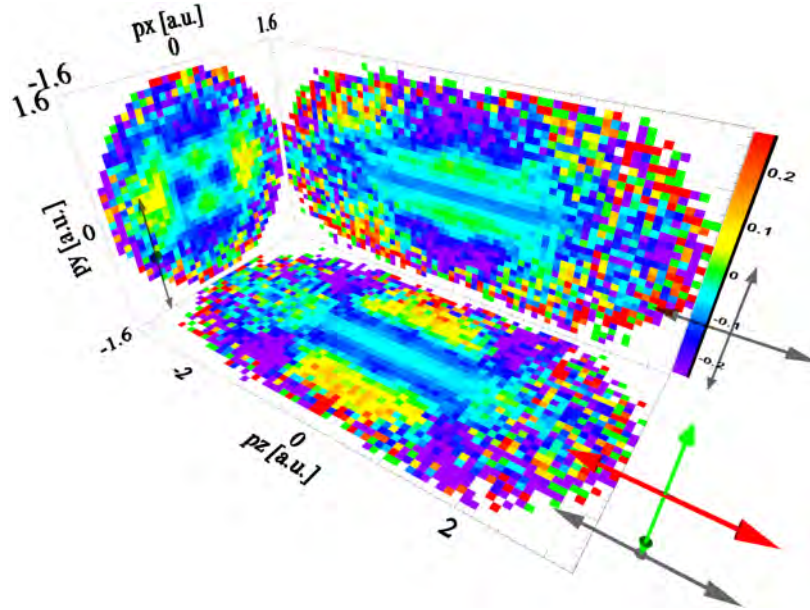
(b) Electrons correlated with O_2^+ ions

Figure 5.5.: Normalized differences of the electron momentum distributions from aligned and anti-aligned molecules as shown in figure 5.4. (a): Electrons emerged in the single ionization of Nitrogen; (b): Same for Oxygen. The green double arrow denotes the aligning while the red one shows the direction of the ionizing pulse polarization. See text for discussion. Normalized differences were calculated according to equation (4.3). The projections are reproduced without the 3D effect in figures A.12 and A.13.

(a) Oxygen - $|p_z| < 4$ a.u.   (b) Nitrogen - $|p_z| < 4$ a.u.

(c) Oxygen - $|p_z| < 0.1$ a.u.   (d) Nitrogen - $|p_z| < 0.1$ a.u.
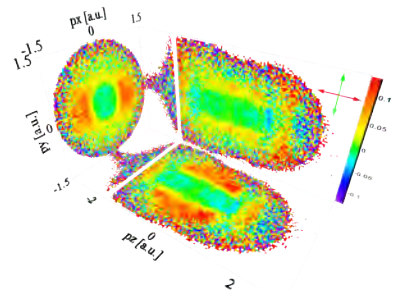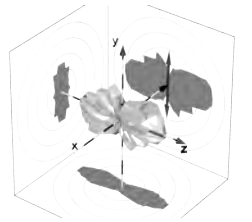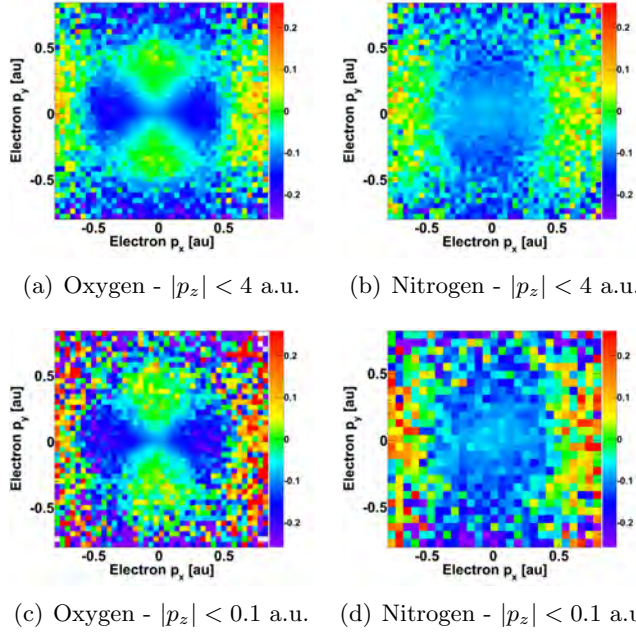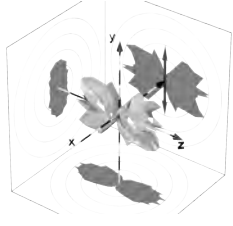
Figure 5.6.: Normalized difference distributions of electrons in the directions perpen-
dicular to the ionizing laser field. *Top* row: No significant restriction
of the out-of-plane momentum. *Bottom* row: Out-of-plane momentum
restricted to $|p_z| < 0.1$ a.u., corresponding to an electric field upon tun-
neling between $\hat{E}$ and $0.997\hat{E}$. There is no systematic difference between
the patterns with and without the out-of-plane momentum (i.e. tunneling
field) restriction. *Left* (*right*) -hand column: Electrons correlated with O_2^+
(N_2^+). The structures are caused by the ionized highest molecular orbital
(HOMO), differing substantially between O_2 and N_2.

only a tunneling phase of $|\varphi_i| < 4^o$ and an electric field E at the instant of
tunneling between its peak value in the pulse $\hat{E}$ and $0.997\hat{E}$. The normalized
difference distributions with and without the said restriction of E do not show
any systematic difference in structure. We conclude that, within our method of
analysis, E does not change the final patterns we are looking at. The normal-
ized difference distributions carry the fingerprint of the ionized orbital, with the
exponential factor caused by tunneling being normalized out.

In order to further underpin this interpretation, David Villeneuve of NRC and
Daniel Comtois of INRS-EMT jointly performed a simulation based on the above-
mentioned tunneling formula (equation (2.9)), assuming that only the highest
occupied molecular orbital (HOMO) is ionized. Numerical representations of the
ionized orbitals were obtained using the quantum chemistry package GAMESS.
The simulation averaged over the experimental alignment distributions and took
the lateral contraction of the electron distribution by interaction with the parent
ion's Coulomb potential ("Coulomb focusing" [76]) into account. Details are
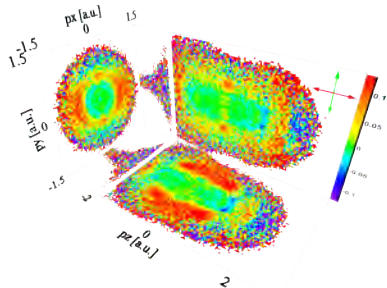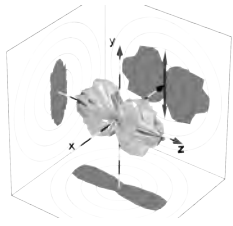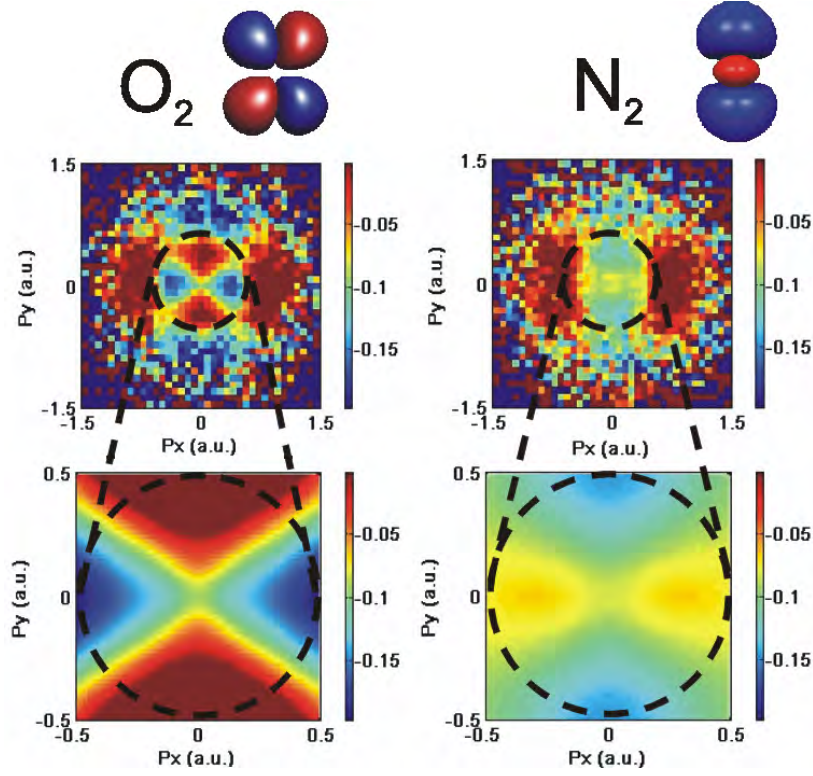
Figure 5.7.: Normalized differences in the x-y plane. The ionizing electric field points out of the paper plane while the aligning pulse polarization is along the vertical axis. *Left* (*right*) column: Data for oxygen (nitrogen). The sketches in the *top* row illustrate the highest occupied molecular orbital (HOMO) of the respective species. The *middle* row shows experimental normalized differences in the x-y direction as in figure 5.5. Results of the simulation as described in the text and in [75] are shown in the *bottom* row. Published in [11]; exact calibration described there.

given in [75]. The results are compared to our experimental findings in figure 5.7. Agreement is good and confirms the given understanding.

Hence, tunneling ionization of aligned molecules gives us direct access to the ionized molecular orbital.

5.1.2.2. High-Momentum Structures

Electrons with a measured momentum of $|p| > p_{osc} \approx 1.5$ a.u. in figure 5.5 must have re-scattered. By analyzing only electrons that are correlated with a stable molecular single ion, we mostly discriminate against inelastic re-scattering.[4]

---

[4]Conceivable inelastic re-scattering leading to non-dissociative excitation of the molecular ion cannot be discriminated against. We assume this effect does not play a significant role, though.
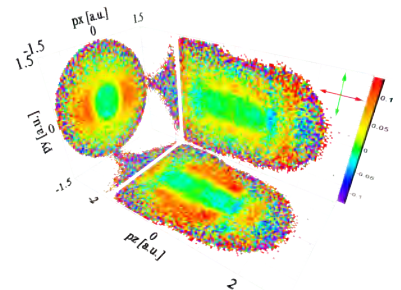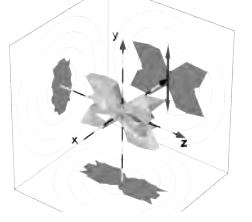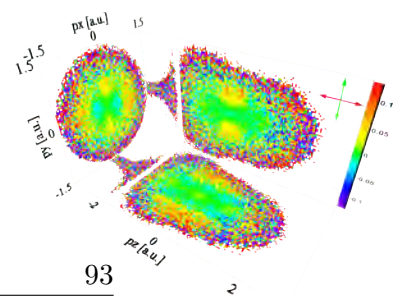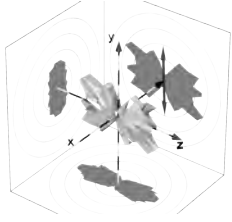
p_{rec} [a.u.]	p_{streak} [a.u.]	λ_{DB}[a.u.]	λ_{DB}[Å]	Line color in fig. 5.9
1.0 ± 0.1	-0.95	6.3	3.3	Black
1.2 ± 0.1	-1.11	5.2	2.8	Red
1.4 ± 0.1	-1.26	4.5	2.4	Blue

Table 5.6.: Parameters of "diffraction spheres": p_{rec} is the re-collision momentum, i.e. the radius of the sphere and p_{streak} its offset along the z direction. The values are for "long" trajectories. In order to gain statistics, we integrated over ranges of $p_{rec} \pm 0.1$ a.u. and an opening angle of $\theta_{x_{circ}} < 45^o$. λ_{DB} is the DeBroglie wavelength associated relating to p_{rec}.

Accordingly, we can expect to see effects of elastic scattering of the re-colliding electron at its parent ion, such as double-slit diffraction (LIED) as described in chapter 2.5.3.

Data Analysis   Equation (2.18) implies that any possible diffraction pattern will appear on a sphere in momentum space that is shifted along the z axis. The radius of this sphere is the re-collision momentum $p_r = p(t_i, t_r)$, relating to the electron's DeBroglie wavelength. The shift is due to and by the streaking momentum $p_{streak}(t_r)$.

Besides laser parameters, both p_r and p_{streak} only depend on the time of tunneling t_i; see section 2.3[5]. A given re-collision momentum can result from two different ionization times, leading to the "long" and the "short" trajectory of the electron. These result in different streaking. Simulation showed that only the "long" trajectories contribute significantly to our distributions [77], so we will neglect the "short" ones. This makes the the interdependence between re-collision- and streaking momentum unambiguous. The streaking momenta corresponding to the re-collision momenta to be considered are summarized in table 5.6[6].

We will analyze our data within a spherical shell, having a radius of $p_r \pm 0.1$ a.u. and being cut by two cones. That is, we first transform the measured momentum vector $\vec{p}$ into a spherical coordinate system whose origin is offset by p_{streak}:

$$\rho = \sqrt{p_x^2 + p_y^2 + (p_z - p_{streak})^2}$$

$$\theta_x = \arccos\left(\frac{p_x}{\rho}\right)$$

$$\varphi_{zy} = \arctan\left(\frac{p_y}{p_z - p_{streak}}\right)$$

---
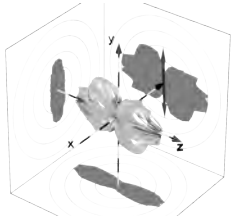
[5]This is because $t_r = t_r(t_i)$.

[6]The relationship between all possible re-collision and streaking momenta is graphed in figure 2.6.
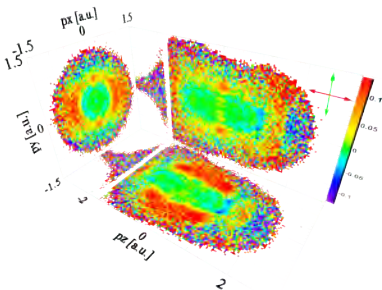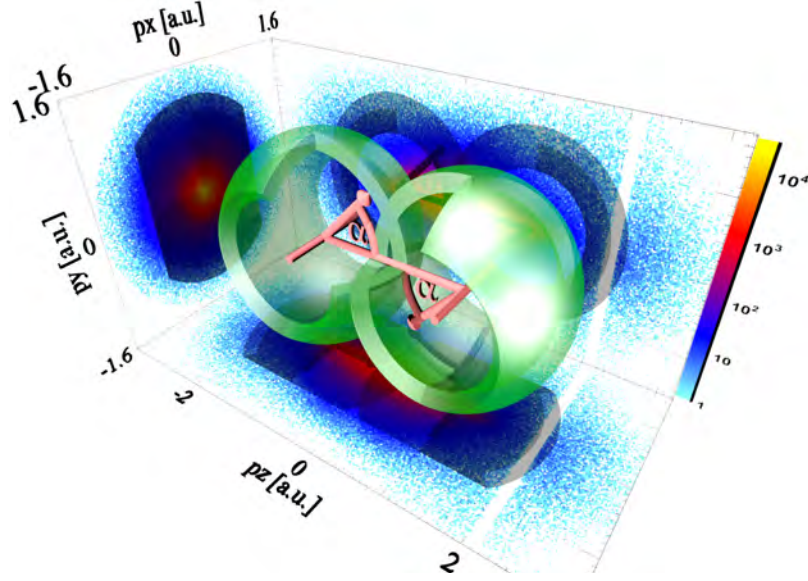
Figure 5.8.: Illustration of "diffraction spheres" (green): These spherical shells in momentum space have a radius of $p_{rec} \pm 0.1$ a.u. and are offset along the z axis by $\pm p_{streak}$. Additionally, they are cut by two cones along the x axis with an opening angle of 45°. We cut them open in the illustration in the upper central part to make the definition of the scattering angle α better visible. In reality, the latter cut does not exist. We analyze the dependence of the electron population within these bodies on the angle α.

We then select only events fulfilling the conditions

$$\rho = p_r \pm 0.1 \text{ a.u.} \quad \text{and}$$
$$\theta_x = 90^o \pm 45^o.$$

The scattering angle now is

$$\alpha = \varphi_{zy} + 180^o.$$

A sketch of such a diffraction sphere, including the scattering angle α, is shown in figure 5.8. Due to symmetry there are two such spheres with the same radius and opposite offsets along the z axis: One at p_{streak} and another at $-p_{streak}$. With the coordinates adapted accordingly, we analyze the α-dependence of count rates for both and add them up for improved statistics. We then calculate normalized differences between the distributions from aligned and anti-aligned molecules. These are plotted as points in the left-hand column of figure 5.9. The same is repeated accordingly with the scattering angle lying in the $z - x$ instead of the $z - y$ plane and restricting the angle θ_y; results are in the column on the right in figure 5.9.
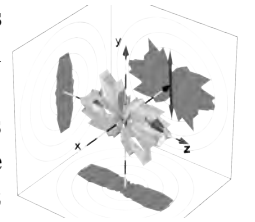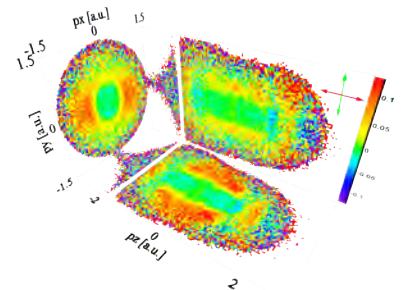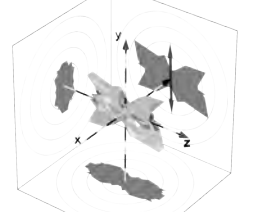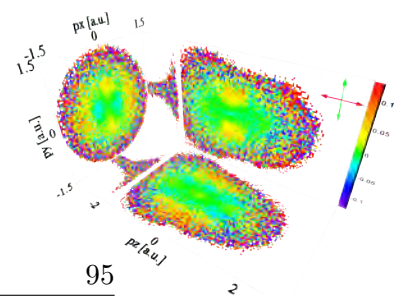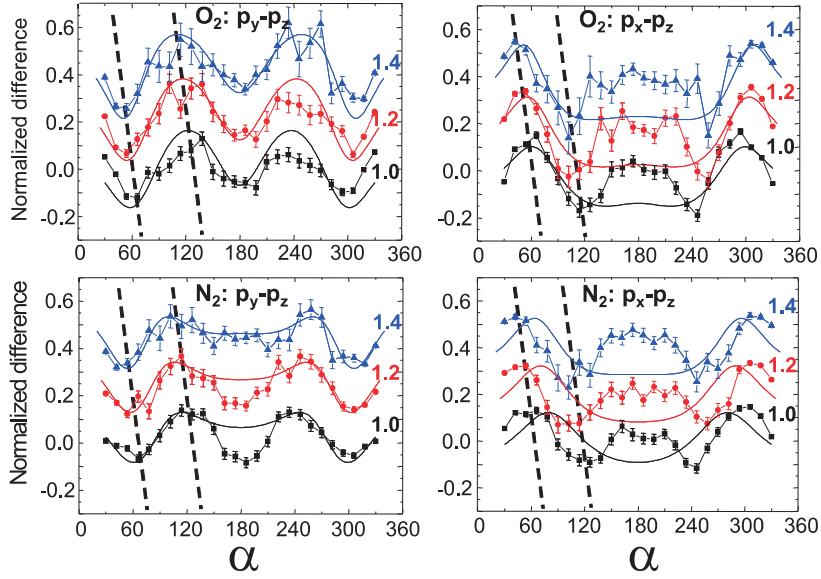
Figure 5.9.: Normalized differences between supposable diffraction data from aligned
and anti-aligned ensembles of molecules. The data were analyzed within
diffraction spheres as illustrated in figure 5.8; see text for details. α (de-
noted by the *horizontal* axis) is the scattering angle of the re-collided
electron. *Top* row: Electrons correlated with O_2^+; *bottom*: Electrons cor-
related with N_2^+. *Left* column: $z - y$ plane; *right*: $z - x$ plane. The *blue*
points (offset along the vertical axis by 0.4 for clarity) correspond to a re-
collision momentum of $p_{rec} = 1.4$ a.u., leading to an electron wavelength
of $\lambda_{DB} = 4.5$ a.u.. *Red* (offset by 0.2): $p_{rec} = 1.2$ a.u.; $\lambda_{DB} = 5.2$ a.u..
Black points: $p_{rec} = 1.0$ a.u.; $\lambda_{DB} = 6.3$ a.u.. Error bars are purely
statistical. The parameters of the respective diffraction spheres are given
in table 5.6. The smooth lines are simulated data; see section 5.1.2.2 for
details. Published in [11]; exact calibration described there.
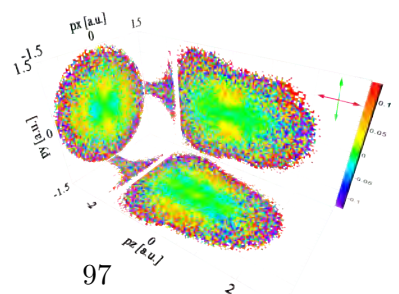
Simulation: LIED The smooth curves in figure 5.9 are from a simulation by Daniel Comtois of INRS-EMT [11, 75]. For a given re-collision momentum, this simulation proceeds via the following steps:
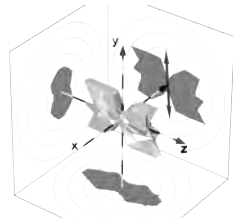
1. Calculate the angular distribution of axes of molecules contributing to the ionization signal in three dimensions. This was assumed to be the alignment distribution of molecules prior to ionization as experimentally determined in section 5.1.1.3, convoluted with the respective MO-ADK ionization rate.

2. Calculate double-slit diffraction amplitudes for each molecular orientation. The re-collision energy relating to the diffracting DeBroglie wavelength was increased by the ionization potential of the molecular species as suggested in [10].

3. Do an average over all diffraction amplitudes weighted by the distribution of ionized molecules from step 1.

4. Normalize the resulting distributions and calculate normalized differences.

The model systematically overestimates the scattering angle in case of N_2 in the $z - x$ plane. It is not clear why. Otherwise agreement between the model and experiment is reasonable. This is despite the fact that pure double-slit diffraction is an over-simplification in our range or re-collision electron energies. See appendix C for a discussion of double-slit diffraction versus exact potential scattering. Apparently our technique of comparing data from different alignment distributions removes a great deal of the complexity usually seen in low-energy electron-molecule scattering.

5.1.3. Implications

Experiment A has two important implications.

5.1.3.1. Probing the Orbital

The findings presented in section 5.1.2.1 allow us to sample molecular orbitals by tunneling. Up to now, we have basically seen the symmetry of the HOMO of the molecules we ionized. However, the technique relates to a scanning tip microscope (STM): Population tunnels from the molecule only in the direction of the probing field. The tunnel is a strong-field analog of the tip in an STM. Nevertheless, rather than just measuring the tunneling current, we measure momentum distributions. These contain more information than an integral rate (current).[7]

---
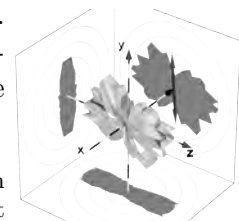
[7]The idea of tracing out orbitals only with the tunneling current (angle-dependent ionization rate) is prone to the criticism by *Murray* et al. that ionization may not necessarily be most likely in the direction of highest electron density in the orbital [21]; cf. chapter 2.2.8. We do
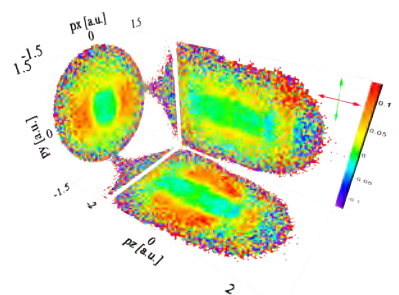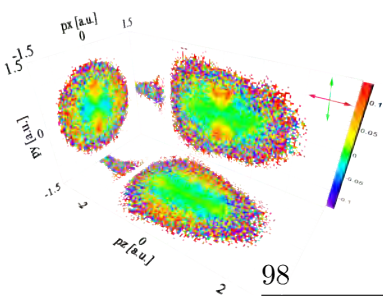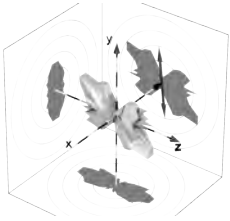
What remains to be done to make the STM analogy perfect is scanning. This can be accomplished by rotating the molecule relative to the ionizing pulse's polarization. The aforementioned idea is what initially inspired experiment B, presented in section 5.2.

5.1.3.2. Electron Diffraction

The second important finding is that there actually is some sort of diffraction of the re-scattering electron wave at its parent ion. The simple diffraction model coinciding with the experiment basically proves the concept of LIED, as proposed in [9, 10]. This is a major finding, as this concept is hoped to open a route towards high-resolution structure determination with a time resolution of just a single laser cycle. The re-collision energy of the electrons in our experiment was too low to achieve a useful image, though.

---
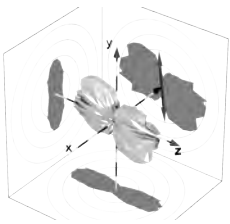
not rely on the integral ionization rate (current) but on the lateral distributions of electron momenta, though.
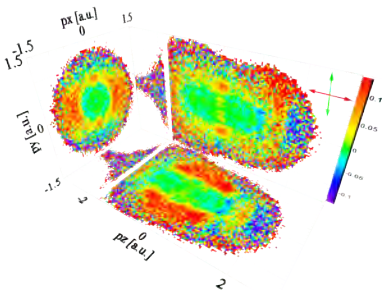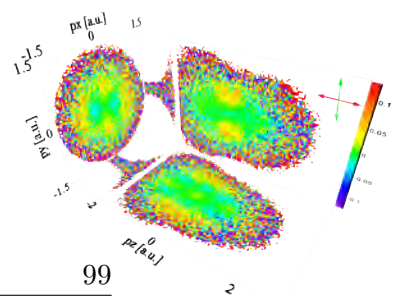
5.2. Experiment B: Rotating Alignment

We carried out a second set of measurements that is similar to experiment A and now called "experiment B". It was initially inspired by the prospect of scanning molecular orbitals, as outlined in section 5.1.3.1. We wanted to rotate the target molecules step by step with respect to the ionizing pulse's polarization.

In contrast to experiment A, the beam combiner in the interferometer was now non-polarizing to allow for the desired rotation of the alignment direction. This came at the cost of significantly reducing our probe intensity.

We changed the "*alignment angle*" ϕ_{al} between the aligning and the ionizing pulse polarization (probe frozen along z) in the $z - y$ plane in increments of 2° after every three seconds. The pump-probe delay now remained at a constant value corresponding to "alignment". We measured nitrogen and oxygen molecules successively instead of using a gas mixture. And finally, TDC readout was now triggered by the electron detector. This allowed us to drop the requirement of having detected an ion in addition to the electron of interest, improving statistics. The most relevant parameters of experiment B are summarized in table 5.7.

Count rates are given in table 5.8. Although the rates of electrons generated by the pump pulse seem negligible at first impression, they may be causing a bias in a specific region of electron momentum normalized difference distributions. Potential problems are analyzed in chapter 6.2.3.
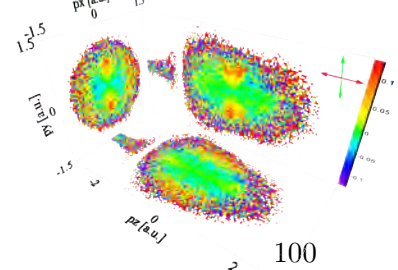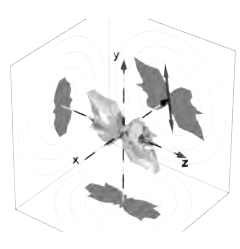
In the discussion we will follow the lines of experiment A. A distribution of ion mass / charge ratios calculated from the measured spectrum of ion times of flight is shown in figure 5.10 for both the N_2 and the O_2 measurement. From this we learn that the contamination of the experiments with foreign species is negligible. In particular, we do not sense any cross-contamination between the N_2 and the O_2 runs. Nevertheless, there is some background by clusters and, in case of O_2, traces of argon. It is obvious that we acquired much better statistics in the nitrogen measurement than we have for oxygen. The statistics problem with O_2 was worsened by an issue the alignment pulse polarization making it impossible to use the range of alignment angles from 0° to 180° (see section 6.3). This issue was not present in the N_2 measurement, enabling us to add up the ranges of ϕ_{al} from 0° to 180° and 180° to 360°.

We will first analyze data taken under three prominent alignment angles: $\phi_{al} \approx 0^o$, $\approx 45^o$ and $\approx 90^o$. Spectra for all alignment angles are shown as a flipbook in the corners of odd-numbered pages; see section 5.2.3 for an explanation.

5.2.1. Alignment Distributions

As in the case of experiment A, we would like to estimate the angular distribution of molecular axes prior to ionization. We again make use of the fragments from Coulomb exploded double ions recorded during the measurements. The applied conditions are summarized in table 5.9. Angular fragment distributions

Optics	Laser	wavelength:	$\lambda = 800$ nm
		repetition rate:	$f = 30$ kHz
	Ionizing pulse	polarization:	linear along z-axis
		energy:	$W_{Ionize} = 1.3\ \mu$J
		intensity:	$I_{Ionize} = 1.3 \cdot 10^{14}\ \frac{\text{W}}{\text{cm}^2}$
			$\Rightarrow U_{P_{Ionize}} = 7.8$ eV
			$\Rightarrow v_{osc} = 1.1$ a.u.
		length:	$\tau_{Ionize} \approx 40$ fs
	Aligning pulse	polarization:	rotating in z-y plane
			increment: 2° every 3 sec.
		energy:	$W_{Align} = 0.7\ \mu$J
		intensity:	$I_{Align} \sim 10^{13}\ \frac{\text{W}}{\text{cm}^2}$
		length:	$\tau_{Align} \approx 60$ fs
		shape:	chirped
	Pump-probe delay	N_2:	3.883 ps
		O_2:	2.929 ps
	Focusing mirror	type:	parabolic, on-axis
		focal length:	$f = 50$ mm
Jet	Gas	either	N_2 (pure)
		or	O_2 (pure)
	Pressure	N_2:	7.2 bar
		O_2:	2.2 bar
	Nozzle	diameter:	10 μm
		temperature:	110 K
	Skimmer	hole diameter:	0.3 mm
		nozzle-distance:	8 mm
Spectrometer	Length of electron	extraction:	$l_{extr,elec} = 70.0$ mm
		drift:	$l_{drift,elec} = 155.0$ mm
	Length of ion	extraction:	$l_{extr,ion} = 162.4$ mm
		drift:	$l_{drift,ion} = 0$ mm
	Magnetic field	strength:	$B = -18.4$ Gauss
		orientation:	along z-axis, homogeneous
	Electric field	strength:	$E = 3390.4\ \frac{\text{V}}{\text{m}}$
		orientation:	along z-axis, homogeneous
	4π solid angle	$N^+ + N^+$ (ions)	$p_{max} \leq 103$ a.u.
		$O^+ + O^+$ (ions)	$p_{max} \leq 115$ a.u.
	Electron momentum	Cutoff:	$\|p_\|\| < 4.0$ a.u.
			$p_\perp < 1.5$ a.u.
Misc.	Data taking	Start N_2:	2008-08-15 12:23 EST
		Stop N_2:	2008-08-17 11:54 EST
		Start O_2:	2008-08-13 16:24 EST
		Stop O_2:	2008-08-14 13:13 EST
	Analysis Version	N_2:	STM_N2_2.8.0
		O_2:	STM_O2-try4_2.8.0
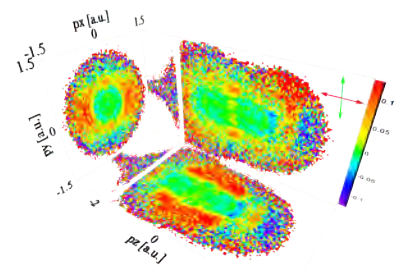
Table 5.7.: Parameters of experiment B (rotating alignment).
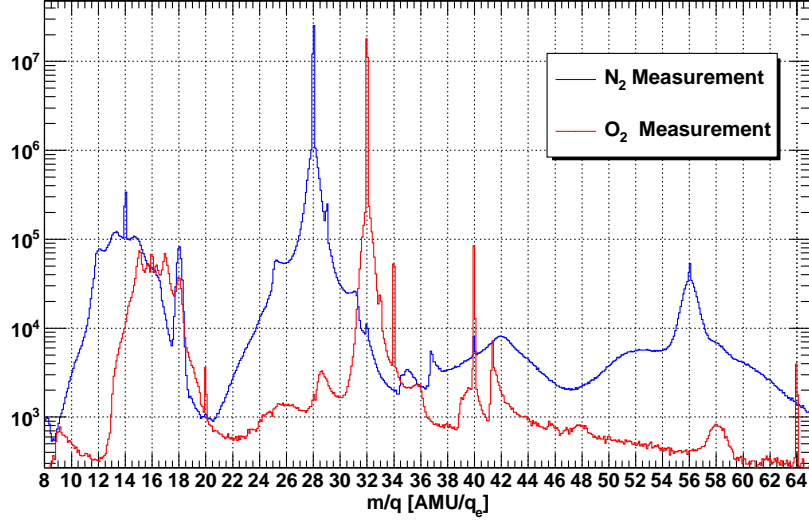
Figure 5.10.: Distribution of ion mass / charge ratios, calculated from TOFs according to equation (4.1), assuming negligible initial velocities. *Blue* curve: N_2 measurement. The largest peak is at $m/q = 28$, i.e. $^{14}N_2^+$. It is surrounded by a pedestal probably caused by dissociated clusters. The smaller spike at $m/q = 14$ results from stable $^{14}N_2^{2+}$ ions and is surrounded by a broad distribution of dissociated $N^+ + N^+$. H_2O^+ from warm background gas causes the maximum at $m/q = 18$. At $m/q = 56$, we see a small amount of singly ionized $(N_2)_2^+$ dimers surrounded by fragments of larger clusters. *Red* curve: O_2 measurement. Once again, the highest peak is caused by singly ionized molecules, i.e. $^{16}O_2$ with $m/q = 32$. The sharp spike at $m/q = 16$ is caused by the molecular double ion $^{16}O_2^{2+}$ and surrounded by fragments from dissociations or explosions of O_2. Again, we see a background water peak at $m/q = 18$. In addition, the O_2 data show traces of singly and doubly charged argon ions ($m/q = 40$ and $m/q = 20$). Only the first ion of each event was evaluated here. The time of flight spectrum corresponding to this m/q distribution can be found in the appendix, figure B.1.
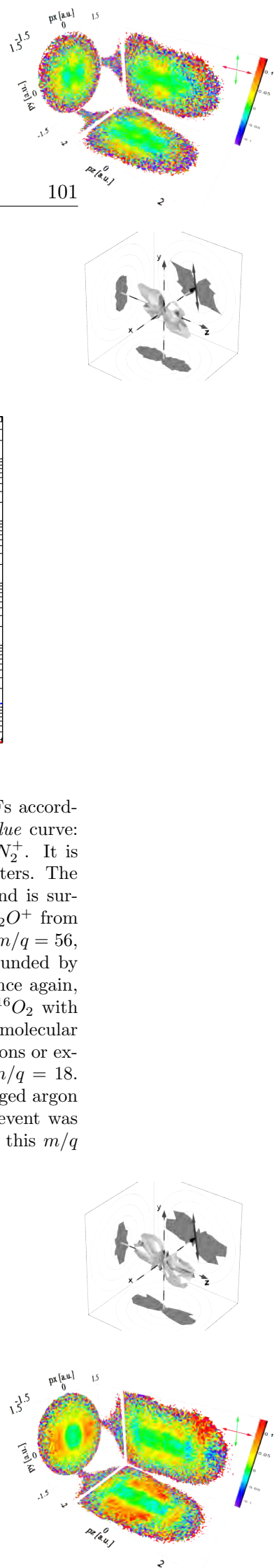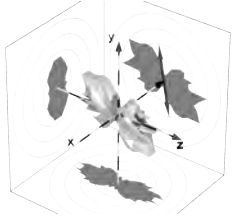
	N_2 Measurement		O_2 Measurement	
Laser	Electrons [Hz]	Ions [Hz]	Electrons [Hz]	Ions [Hz]
Dark	210	15	210	20
Pump Only	230	15	530	35
Probe Only	6,600	400	13,500	700

Table 5.8.: Total count rates of electrons and ions in Hz, measured as detector MCP signals with a rate meter at the beginning of each measurement. Rates are given for no light being fed into the chamber (detector dark counts), only the pump and only the probe beam enabled. The ion detector had to be operated at a reduced voltage, curtailing its detection efficiency. However, the measured ion MCP trigger rate underestimates the rate of detected ions, as the respective analog signal was weak and noisy. After hit reconstruction, we obtained at least one ion in $\approx 13\%$ of all events containing at least one electron.

Species	$p_{cms,Max}$[a.u.]	KER_{Min}[eV]	KER_{Max}[eV]
$N^+ + N^+$	5	3.8	11.3
$O^+ + O^+$	6	3.4	12.3

Table 5.9.: Conditions a Coulomb explosion event had to fulfill in experiment B to be further analyzed. The KER had to be in a window between KER_{Min} and KER_{Max} and the ion center of mass momentum was allowed be no greater than $p_{cms,Max}$.

are shown as three-dimensional plots in figure 5.11.

It becomes clear that both in the case of N_2 and O_2 our alignment pulse had some effect on the distribution of molecules. N_2 behaves as one would expect: The fragment distribution follows the aligning pulse polarization but always shows a preference along the probing field. The latter is due to the angle-dependence in the tunneling probability of N_2. Our statistics for O_2 are poor, forcing us to use a relatively large bin size and sum over several alignment angles. In the $x - y$ direction, effects of alignment are visible.

Just like in section 5.1.1.3, we have to integrate over the direction of the probe laser polarization to minimize bias by the ionizing electric field. Molecules are to be aligned perpendicular to this direction to reveal their distribution in the projection. Hence, the fragment distributions to look at are those in the $x - y$ plane, recorded at an alignment angle of 90°. These are shown in figure 5.12. Perfectly aligned molecules would be oriented vertically in this representation.

We assume this fragment distribution approximately represents the distribution of neutral molecules at the instant before the probe pulse is shone in. See section 5.1.1.3 for a discussion of the assumption. We also suppose this initial distribution rotates with the aligning pulse polarization.[8] The degree of

---

[8]When summing over alignment angles, one has to add three-dimensional alignment distributions rotated by the respective alignment angle. Please note this is not the same as

(a) $N^+ + N^+$ with $\phi_{al} = 1^o \pm 3^o$

(b) $O^+ + O^+$ with $\phi_{al} = 1^o \pm 5^o$

(c) $N^+ + N^+$ with $\phi_{al} = 45^o \pm 3^o$

(d) $O^+ + O^+$ with $\phi_{al} = 45^o \pm 5^o$

(e) $N^+ + N^+$ with $\phi_{al} = 89^o \pm 3^o$

(f) $O^+ + O^+$ with $\phi_{al} = 89^o \pm 5^o$
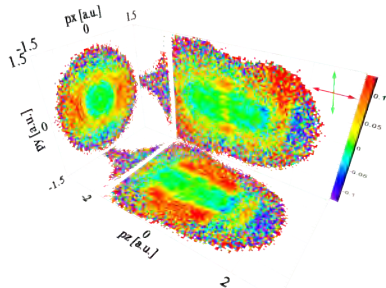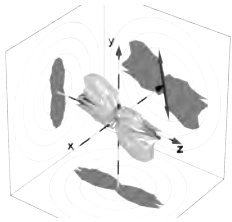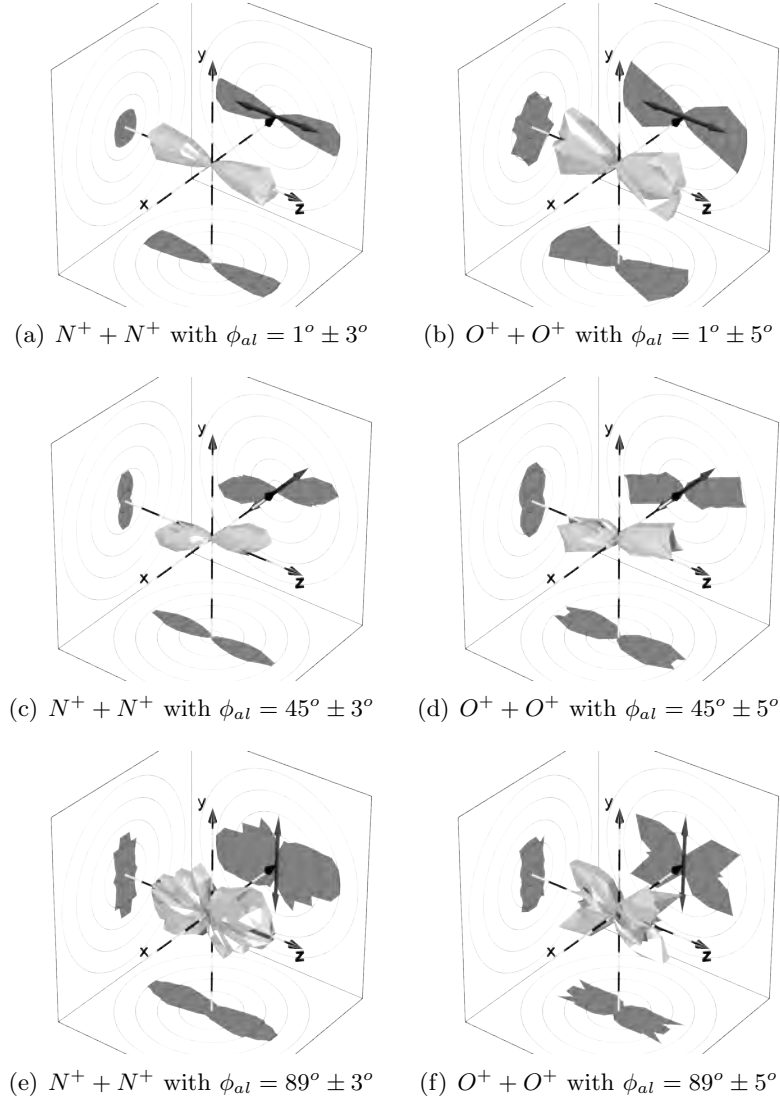
Figure 5.11.: Angular distributions of correlated fragments at different alignment angles ϕ_{al}. An arrow in the $z - y$ plane depicts the direction of the aligning pulse polarization. In all cases the probe polarization was along the z axis. Column on the *left*: $N^+ + N^+$; *right*: $O^+ + O^+$. All distributions are symmetrized (inversion and azimuth). A measure of alignment can be seen in the shadow on the $x - y$ plane. In the $z - y$ direction we see that the fragment distributions follow the aligning field but still show a remarkable preference to stay along the z axis.
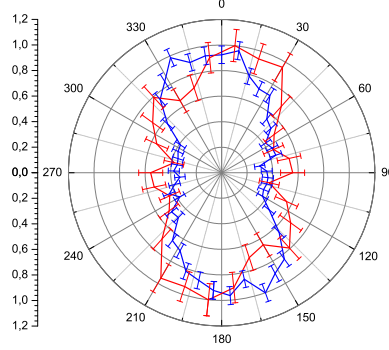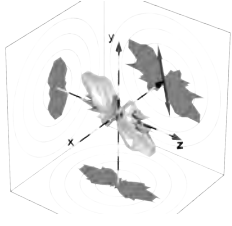
Figure 5.12.: One-dimensional angular distributions of energetic fragments. *Blue* curve: Correlated $N^+ + N^+$ with an alignment angle of $\phi_{al} = 90^o \pm 2^o$; *red* curve: $O^+ + O^+$ with $\phi_{al} = 90^o \pm 4^o$. The aligning pulse polarization is vertical while the probe polarization points out of the paper plane. The distributions therefore should not be biased by the probe polarization, giving an estimate of the aligned ensembles of molecules "offered" to the ionizing laser pulse. Rotating them around the vertical axis (aligning polarization) should give the three-dimensional molecular distributions. The datasets were normalized to the same maximum value. The curves approximately correspond to the shadows on the $x-y$ planes of the three-dimensional fragment distributions in figure 5.11(e) and (f), respectively. Error bars are statistical.

alignment achieved for N_2 ($< \cos^2 \varphi_{yx} > \approx 0.64$) is better than the one for O_2 ($< \cos^2 \varphi_{yx} > \approx 0.59$).

5.2.2. Electron Momentum Distributions from Single Ionization

In this section, we will analyze the distributions of electrons emerging in the single ionization of N_2 and O_2. Nevertheless, in contrast to experiment A, we did not necessarily detect the ion. Unless stated otherwise, we will use electrons without an ion condition, assuming the majority of all electrons is correlated with an N_2^+ or an O_2^+ ion, respectively, be it detected or not. This greatly improves statistics and prevents problems on the ion detector from propagating into electron distributions. It makes us vulnerable to background, though.
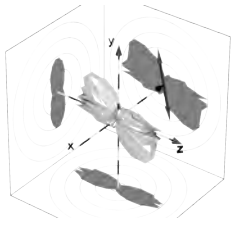
5.2.2.1. Absoulte Electron Spectra

We now briefly discuss the distributions of electron momenta without any normalization. As in experiment A, we do not see any alignment-dependencies with the plain eye. We therefore present pseudo three-dimensional representations

---

integrating over fragment distributions recorded under these alignment angles.

(a) N_2 - 3rd direction integrated over.

(b) O_2 - 3rd direction integrated over.

(c) N_2 - Out-of-plane momentum < 0.1 a.u.

(d) O_2 - Out-of-plane momentum < 0.1 a.u.

(e) N_2 - Out-of-plane angle $< 10^o$.

(f) O_2 - Out-of-plane angle $< 10^o$.
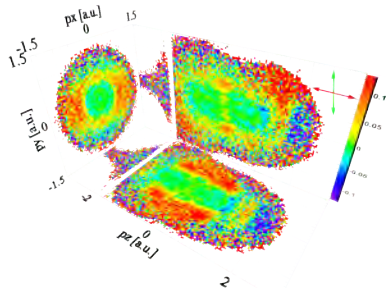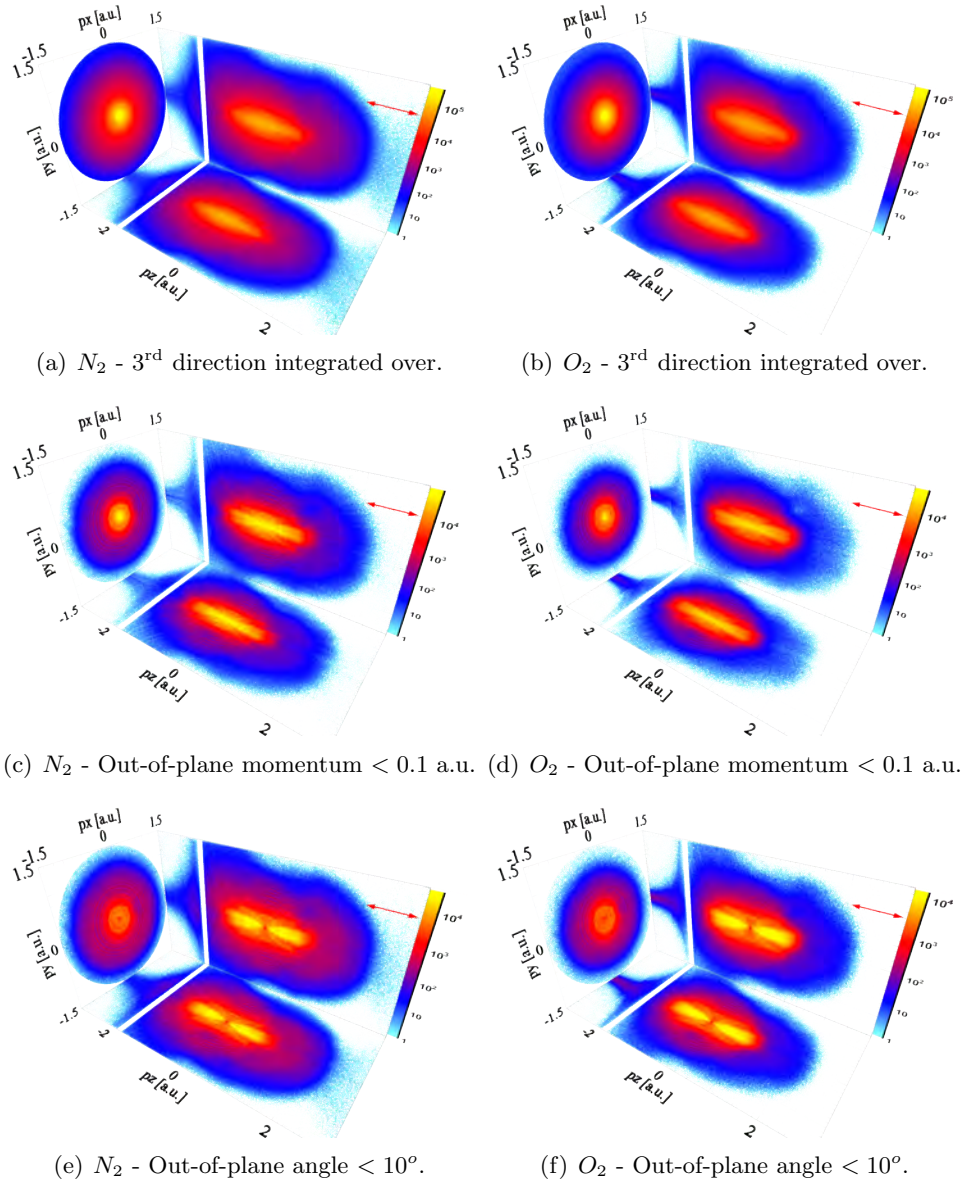
Figure 5.13.: Electron momentum distributions in a pseudo-3D representation. We assume that the majority of these electrons is correlated with either N_2^+ (column on the *left*) or O_2^+ ions (*right*). No condition on alignment angles. *Top* row: Projections made by integrating over the respective third dimension. Row in the *middle*: Out-of-plane momenta restricted to ± 0.1 a.u. *Bottom*: Out-of-plane angles restricted to $\pm 10^o$. The direction of the ionizing pulse polarization is denoted by the red arrow. The white stripes around $p_z = -2$ a.u. are "wiggles" (artifacts). There is a great deal of similarity between spectra for the two species. The restricted spectra (5.13(c) through 5.13(f)) reveal circular / spherical structures interpreted as ATI peaks and interesting low-momentum patterns. See text for interpretations. The color plots are given without the 3D effect in the appendix, section B.2.
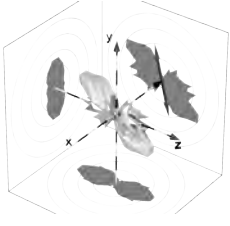
of such distributions with all measured alignment angles summed up. [9] These graphs are shown in figure 5.13.

The projections onto the coordinate planes in figure 5.13(a) and (b) were made by integrating over the respective out-of-plane momentum. The results are very similar between the species and to their counterparts from experiment A (cf. fig. 5.4).

A restriction of the out-of-plane momentum to ± 0.1 a.u. (fig. 5.13(c) and (d)) makes circular structures visible in the projections at higher lateral momenta. These relate to spheres in momentum space. The energy difference between two consecutive spheres corresponds to our photon energy of 1.55 eV. We interpret them as a manifestation of ATI.

Furthermore, we obtain interesting patterns which are partly parallel to the probing laser polarization at low lateral momenta ($p_x, p_y < 0.4$ a.u.). These can be seen most clearly if we restrict the out-of-plane angle of the momentum vectors, as done in figure 5.13(e) and (f).

The observation of similar structures at low lateral momenta has been reported very recently by *Huismans* et al. [78] (spectrum reproduced in figure 5.14(a)). They used $\lambda = 7$ μm, $I = 7.1 \cdot 10^{11} \frac{W}{cm^2}$ light from a free electron laser to ionize metastable xenon atoms. The "side lobes that extend from low to high momentum and run parallel to the laser polarization axis for high momenta" are interpreted as a "holographic" interference between direct and re-scattered electrons, following the predictions in [3].

Our spectra are compared to [78] in figure 5.14. The low lateral momentum structures up to $p_z \approx 1$ a.u. in our data qualitatively resemble those in the distribution by Huismans up to a longitudinal momentum of $p \approx 0.3$ a.u. This indicates our low lateral momentum structures are the onset of "holography". The fact we do not see them extend nearly as far as in [78] is most likely owing to our experimental conditions, which are very different.

5.2.2.2. Reference Distribution for Normalized Differences

In order to make differences in the electron distributions recorded under different alignment angles visible we apply normalized differences. In the analysis of experiment A, we used anti-alignment as reference. Anti-alignment meant an isotropic distribution of molecular axes lying in the $z-x$ plane. We did not record any data for anti-alignment in experiment B. Instead, our reference distribution is the sum of electrons recorded under all alignment angles. The supposed angular distribution of molecules leading to this electron distribution is illustrated in figure 5.15. The alignment pulse was rotated in the $z - y$ plane. Hence, the distribution of molecules leading to our new reference is similar to anti-alignment, but lies in the $z - y$ plane.[10]

---

[9] Some distributions with restricted alignment angles can be found in the appendix, figure B.4.

[10] Please note once more that the distribution of molecules actually contributing to the ionization signal is not isotropic in any plane, neither in experiment A nor B. Only the angular
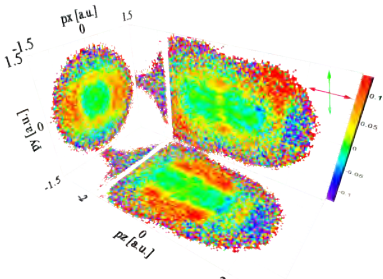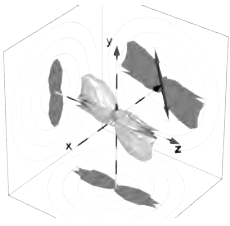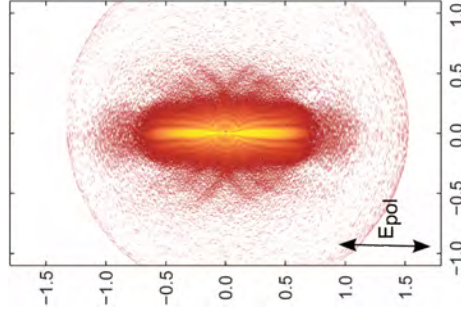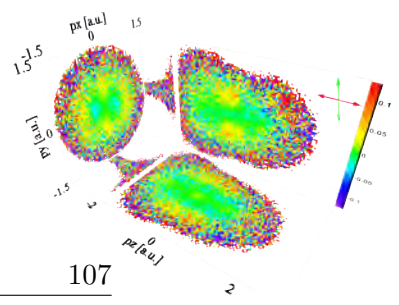
(a) Results by *Huismans* et al. [78].
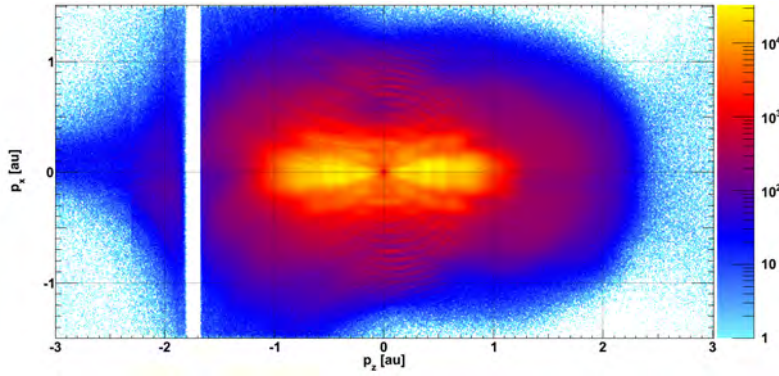
(b) Experiment B: N_2 - Out-of-plane angle $< 10^o$.
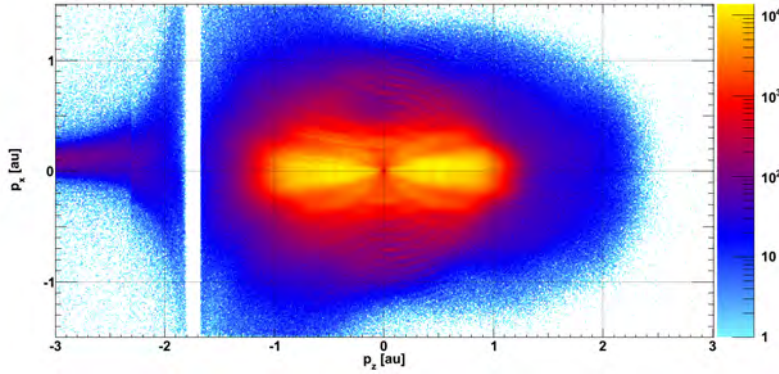
(c) Experiment B: O_2 - Out-of-plane angle $< 10^o$.

Figure 5.14.: Electron momentum distributions. In all cases, the ionizing pulse polarization is along the *horizontal* axis. (a): Electrons from the ionization of metastable Xe atoms by $\lambda = 7$ μm, $I = 7.1 \cdot 10^{11} \frac{\text{W}}{\text{cm}^2}$ light by *Huismans* et al. [78]. Momenta are given in a.u. (b) and (c): Distributions from experiment B in the $z - x$ direction with the out-of-plane angle restricted to $\pm 10^o$ (alignment angle integrated over). The structures in (b) and (c) seemingly starting at zero momentum and extending to $p_z \approx 1$ a.u., $p_x \approx 0.35$ a.u. resemble the onset of the horizontal lobes in (a). This suggests a similar origin of the structures, which are interpreted as "holography" in [78].

(a) Alignment angle rotated in 20° steps.   (b) "Tilted" anti-alignment.
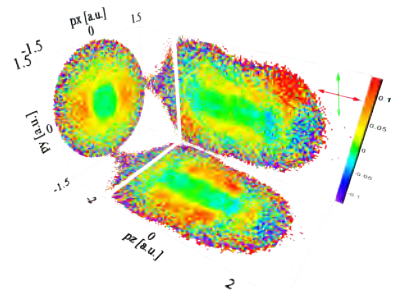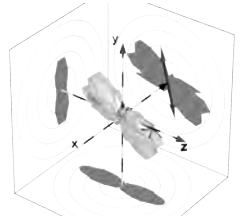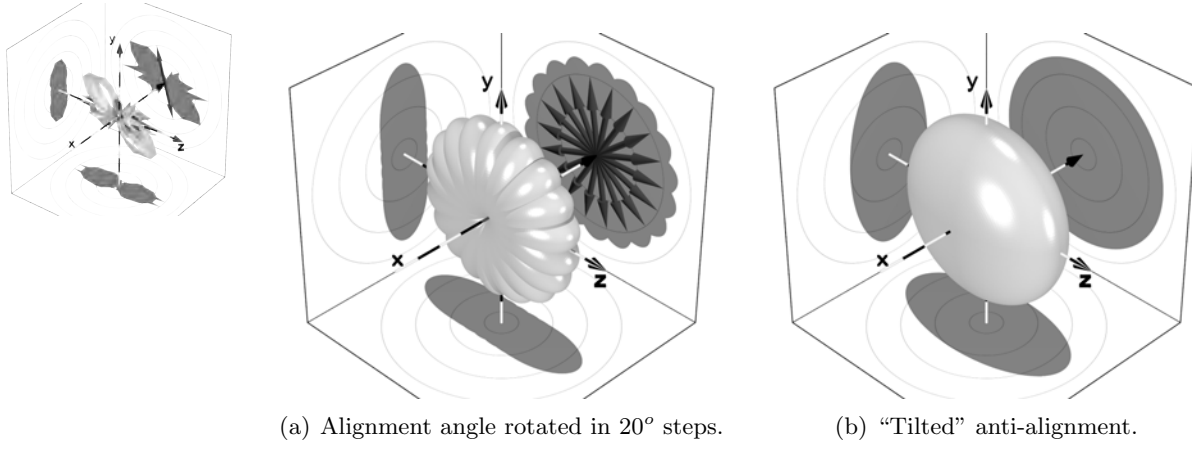
Figure 5.15.: Sketches of the distribution of molecular axes leading to the reference electron distribution in experiment B. (a): The aligning pulse is rotated in the $z-y$ plane in steps of 20°. In the experiment, we used $\Delta\phi_{al} = 2^o$, leading to a smoother expected alignment distribution. The increased increment in the sketch was chosen for visual clarity. (b): "Tilted" anti-alignment. This is the same as the reference distribution used in experiment A but rotated around the z axis by 90°. (*Note*: The distribution sketches for the individual alignments intersect in the picture (a) for technical reasons. In reality, these distributions add up, leading to more population close to the x-axis.)

5.2.2.3. Normalized Differences

The normalized differences for electrons from N_2 and O_2 are shown in figure 5.16 for signal distributions recorded at $\phi_{al} \approx 0^o$, $\approx 45^o$ and $\approx 90^o$. For each projection, the third dimension was integrated over. The same set of distributions with the third dimension restricted to ± 0.1 a.u. is shown in figure 5.17. Here we had to sum over an increased range of alignment angles ($\pm 11^o$) to compensate for the lost statistics.

The latter distributions are quite similar to the former ones. They show most low-momentum features with an increased contrast, though. Some low-momentum features, visible particularly well in the $z-y$ plane, seem to be along the pump polarization regardless of the alignment angle. We analyze the potential influence of electrons ionized by the pump pulse on the normalized difference spectra in chapter 6.2.3. In the N_2 data it is possible and in O_2 it is likely these structures are biased by such unwanted electrons.

We notice that in the case where aligning and ionizing pulses are parallel to each other (fig. 5.17(a) and (b)), there is a large degree of similarity to the respective normalized difference graphs from experiment A (fig. 5.5) if we rotate them by 90° around the z axis. This can be explained with the similarity of our

---

distribution of molecular axes "offered" to the probe laser is. The probe pulse "picks" molecules at the angle-dependent probability of ionization.
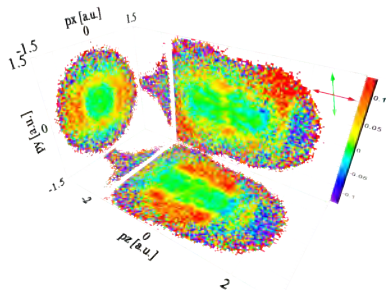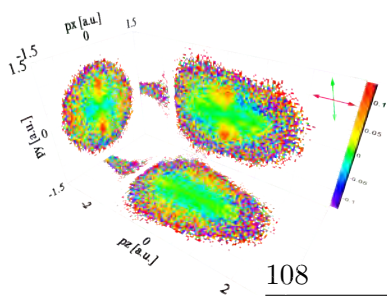
new reference distributions to "tilted" anti-alignment discussed above (cf. figure 5.15). The structures are not completely identical because our signal ("aligned") molecules are not perpendicular to the anti-alignment plane here. A similar argument holds for alignment angles of 90° (fig. 5.17(e) and (f)): The plots are similar to those from experiment A but not identical because this time, although the alignment direction coincides with experiment A, the reference is still tilted.
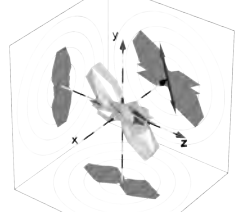
5.2.2.4. Low-Momentum Structures

Regarding experiment A, we interpreted low-momentum ($p_\perp < 0.5$ a.u.) structures in the normalized differences of electron momentum distributions in the directions perpendicular to the ionizing laser field as the fingerprint of the ionized orbital; cf. section 5.1.2.1. We compare spectra from experiment B recorded under an alignment angle of $\phi_{al} \approx 90^o$ to those from experiment A in figure 5.18.

Oxygen In the case of oxygen (right-hand column in figure 5.18), the pattern seen in experiment A is reproduced by experiment B. This is the case regardless whether we integrate over the out-of-plane momentum (figure 5.18(d)) or restrict it to ± 0.1 a.u. (fig. 5.18(f)). In these plots, the maxima at $p_x \approx 0$, $p_y \approx 0.5$ extend to larger values of p_y than in the case of experiment A. This may either be due to the different reference distributions or due to pollution with electrons generated by the pump pulse; cf. chapter 6.2.3.

Nitrogen For N_2 (column on the left in figure 5.18), we see ring-like sub structures in the data from experiment B, which were not present in experiment A. It is possible this is an ATI effect. The spacing between adjacent rings does not match our photon energy of 1.55 eV, though. This shall be investigated no further here.

In figure 5.18(c), where we integrated over p_z, a decrease of normalized differences with increasing p_y as in experiment A can be sensed. However, this is not the case if we apply the condition $|p_z| < 0.1$ a.u.. The resulting graph is shown in figure 5.18(e). It does not appear to reproduce the feature seen in experiment A.

There are two possible explanations why N_2 does not show the expected pattern in experiment B, while O_2 does.

Tunneling versus Multiphoton Ionization On the one hand, the peak intensity of the ionizing laser pulse was substantially reduced to $I \approx 1.3 \cdot 10^{14} \frac{W}{cm^2}$ in experiment B, from $I \approx 3 \cdot 10^{14} \frac{W}{cm^2}$ in experiment A. The respective values of the Keldysh parameter γ for the ionized species are summarized in table 5.10.

Strictly speaking, the tunneling picture is only appropriate for $\gamma \ll 1$. There is little doubt experiment A took place in the tunneling regime. There, we saw only
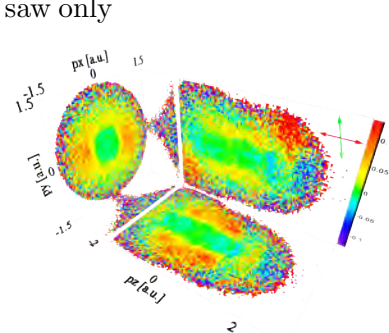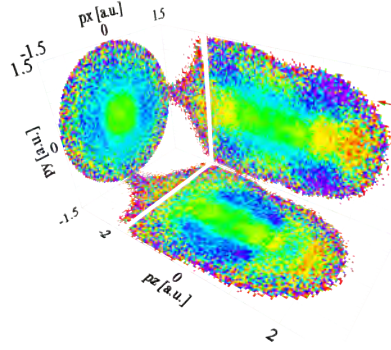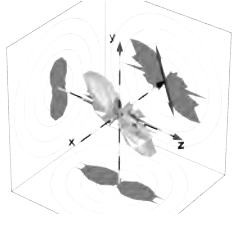
(a) N_2 with $\phi_{al} = 1^o \pm 3^o$
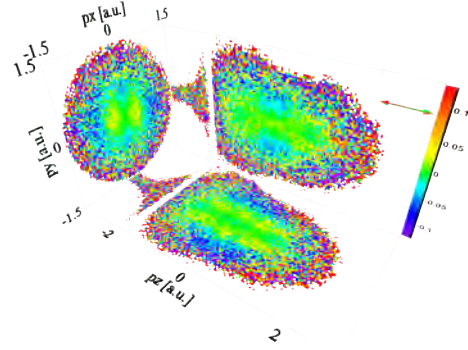
(b) O_2 with $\phi_{al} = 1^o \pm 5^o$
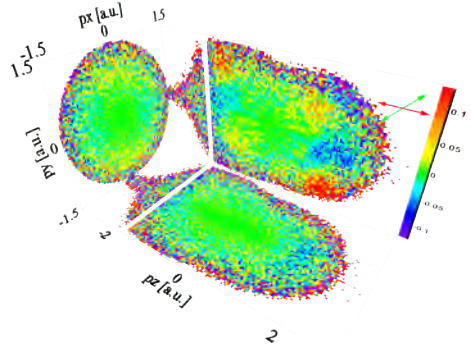
(c) N_2 with $\phi_{al} = 45^o \pm 3^o$
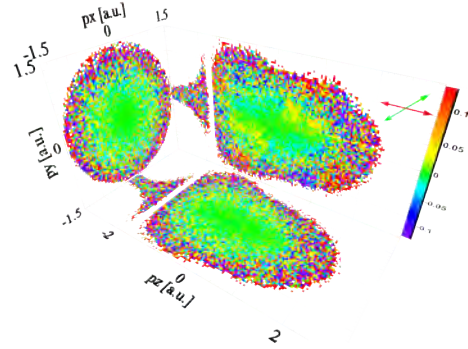
(d) O_2 with $\phi_{al} = 45^o \pm 5^o$
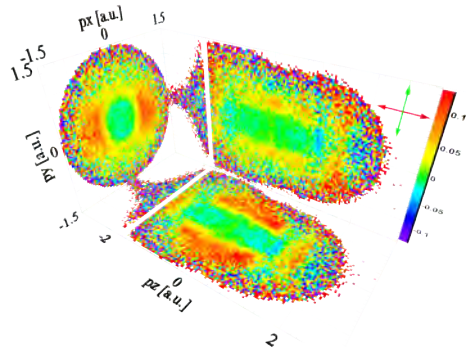
(e) N_2 with $\phi_{al} = 89^o \pm 3^o$
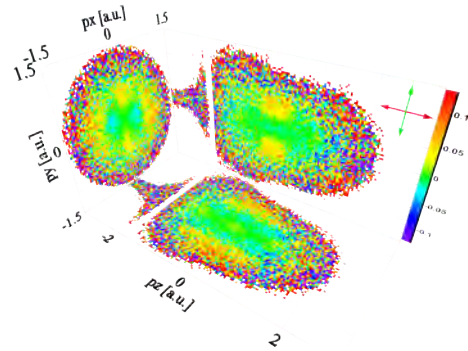
(f) O_2 with $\phi_{al} = 89^o \pm 5^o$

Figure 5.16.: Normalized differences of the electron momentum distributions recorded at the specified alignment angle ϕ_{al} (signal) and the integral over all alignment angles (reference). Projections were made by integrating over the third dimension. Column on the *left*: Electrons from the nitrogen measurement; *right*: Oxygen measurement. The green double arrows denote the aligning while the red ones show the direction of the ionizing pulse polarization. See text for discussion. Please refer to chapter 6.2.3 to judge the reliability of these distributions with respect to pollution by electrons generated by the pump pulse. The projections are reproduced without the 3D effect in appendix B.2.1, figures B.6 to B.12.

(a) N_2 with $\phi_{al} = 1^o \pm 11^o$

(b) O_2 with $\phi_{al} = 1^o \pm 11^o$

(c) N_2 with $\phi_{al} = 45^o \pm 11^o$

(d) O_2 with $\phi_{al} = 45^o \pm 11^o$

(e) N_2 with $\phi_{al} = 89^o \pm 11^o$

(f) O_2 with $\phi_{al} = 89^o \pm 11^o$
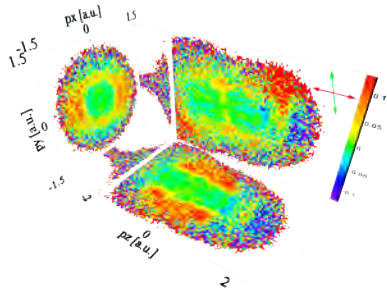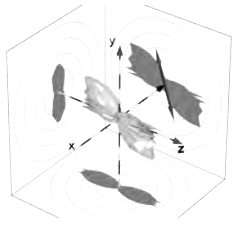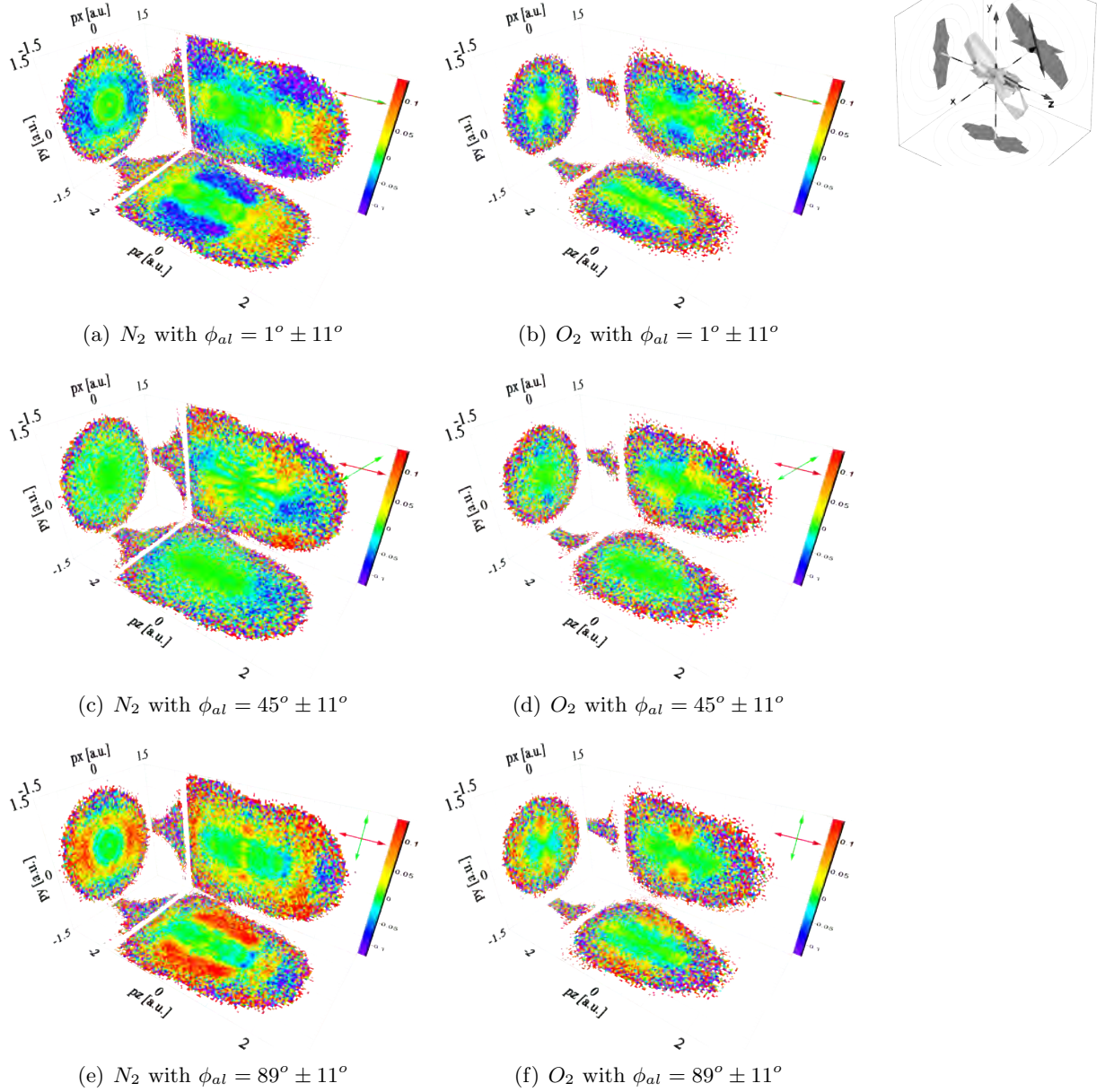
Figure 5.17.: Same as figure 5.16 but projections were made by restricting the respective third dimension to ± 0.1 a.u. (for both signal and reference). Normalized differences of the electron momentum distributions recorded at the specified increased range of alignment angles ϕ_{al} (signal) and the integral over all alignment angles (reference). Column on the *left*: Electrons from the nitrogen measurement; *right*: Oxygen measurement. The green double arrows denote the aligning while the red ones show the direction of the ionizing pulse polarization. See text for discussion. Please refer to chapter 6.2.3 to judge the reliability of these distributions with respect to pollution by electrons generated by the pump pulse.
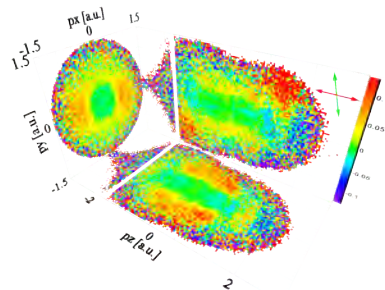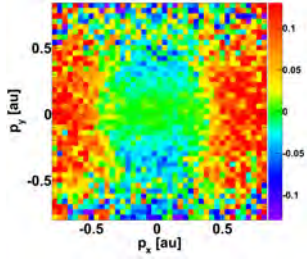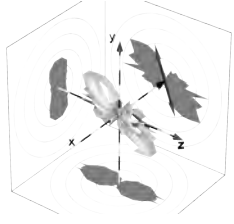
(a) Ex. A: N_2, $|p_z| < 4$ a.u..
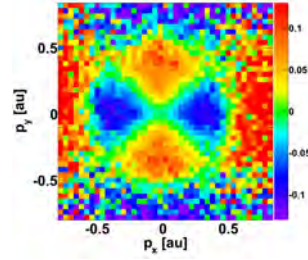
(b) Ex. A: O_2, $|p_z| < 4$ a.u..
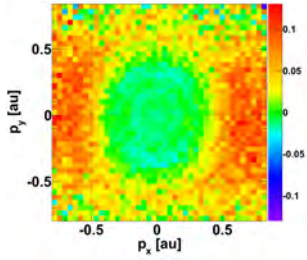
(c) Ex. B: N_2, $|p_z| < 4$ a.u., $\phi_{al} = 89^o \pm 3^o$ (d) Ex. B: O_2, $|p_z| < 4$ a.u., $\phi_{al} = 89^o \pm 5^o$
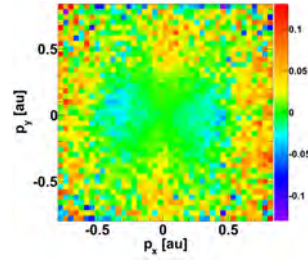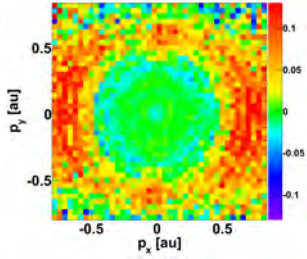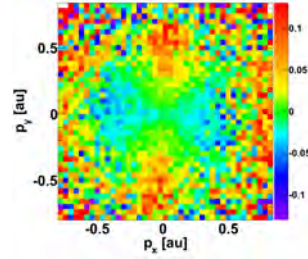
(e) Ex. B: N_2, $|p_z| < 0.1$ a.u., $\phi_{al} = 89^o \pm 11^o$ (f) Ex. B: O_2, $|p_z| < 0.1$ a.u., $\phi_{al} = 89^o \pm 11^o$

Figure 5.18.: Comparison of normalized difference distributions in the direction per-
pendicular to the probing laser polarization between experiment A (*top*)
and B (*middle* row with the out-of-plane momentum integrated over and
bottom row with p_z restricted to ± 0.1 a.u.). In all cases the aligning
pulse polarization of the "signal" distribution is along the vertical axis
and the probe out of the paper plane. In the plots from experiment A,
we compare to anti-alignment, i.e. molecular axes lying in a plane along
the horizontal axis pointing out of the paper plane. In experiment B,
our reference is the sum over all alignment angles, i.e. a distribution in
a plane spanned by the y axis and the normal of the paper. In order
to facilitate the comparison we normalized the absolute momentum dis-
tributions before calculating normalized differences also for experiment
A and matched color scales. Contrast is significantly weakened in ex-
periment B as compared to A. For oxygen, the patterns in the spectra
from experiment B reproduce those of experiment A. In the case of the
nitrogen measurement of experiment B, we see circular structures which
were absent in experiment A. If we restrict the out-of-plane momentum
as done in (e), these structures become clearer. We do not see the pattern
found in experiment A.
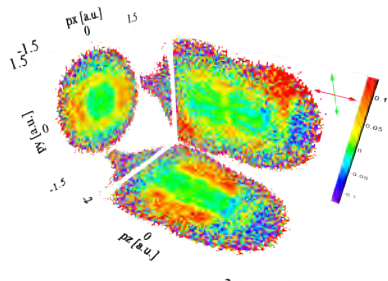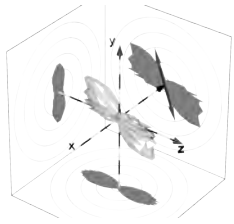
	Experiment A	Experiment B
N_2	0.66	1.00
O_2	0.58	0.88

Table 5.10.: Values of the Keldysh parameter γ according to equation (2.3) for the two experiments and species. In experiment A, we used a probe intensity of $I \approx 3 \cdot 10^{14}\ \frac{\mathrm{W}}{\mathrm{cm}^2}$ while $I \approx 1.3 \cdot 10^{14}\ \frac{\mathrm{W}}{\mathrm{cm}^2}$ in experiment B. We conclude that experiment B was more "multiphotonish", while experiment A took place in the tunneling regime.

very weak signs of ATI, which is a multiphoton effect. However, in experiment B, we see clear ATI structures (cf. figure 5.13(c) through (f)). Nitrogen with $\gamma = 1$ is in "no man's land". Due to the lower ionization potential of oxygen, the Keldysh parameter for this species is still lower than the one for nitrogen, leaving O_2 a little closer to the tunneling limit. This may explain why the pattern observed in experiment A re-appears in the oxygen but not in the nitrogen measurement of experiment B. We interpreted it as a tunneling effect and the tunneling picture may be breaking down for the N_2 measurement in experiment B.

Reference Distributions Another difference between the experiments is the reference distribution. In experiment A, we compared electron momentum distributions from aligned and anti-aligned molecules. The alignment direction was perpendicular to the plane of anti-alignment. However, in experiment B, our reference is similar to anti-alignment rotated by 90° (cf. section 5.2.2.2 / figure 5.15). As a result, the alignment direction now is within this synthetic anti-alignment plane. This reduces our contrast between the signal and reference. It is not obvious why the pattern from O_2 survives while the one from N_2 vanishes, though.

Conclusion Hence, it is not clear how successful our attempt of sampling the orbital from different directions actually was. The intention was to provide an analogue of scanning in a scanning tip microscope (cf. section 5.1.3.1). This should allow for a tomography-type reconstruction of the three-dimensional orbital electron density, similar to [38][11].

Work in this direction is currently under way [79]. The method being pursued has been previously described with a slightly different purpose in mind in [80]. Preliminary results of an electron density reconstruction from our N_2 data look more similar to the expected HOMO than the same for oxygen, although one would expect the opposite from figure 5.18.

---

[11]In comparison to [38] where high harmonic radiation was used as a probe, we are lacking information, though. There, the extra piece of information needed to reconstruct the full bound-state electron wavefunction including the sign came from the polarization of the photons. We only have electron momentum rates, corresponding to high harmonic spectra. This will allow for the reconstruction of electron densities but not wavefunctions.
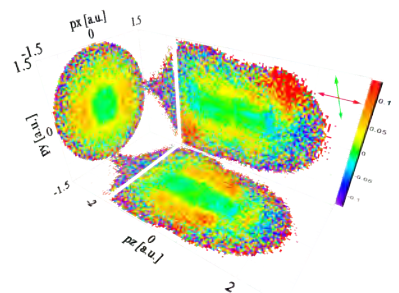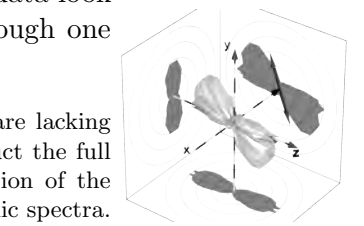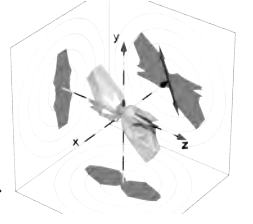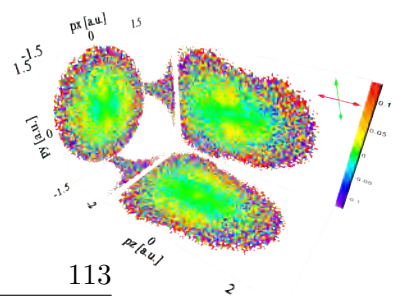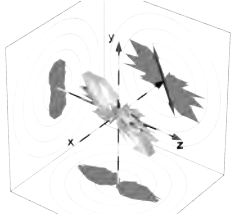
p_{rec} [a.u.]	p_{streak} [a.u.]	λ_{DB}[a.u.]	λ_{DB}[Å]	Color in fig. 5.19
0.86 ± 0.1	0.79	7.3	3.9	black
1.01 ± 0.1	0.92	6.2	3.3	red
1.15 ± 0.1	1.01	5.5	2.9	blue

Table 5.11.: Parameters of "diffraction spheres" for experiment B: p_{rec} is the re-collision momentum, i.e. radius of the sphere and p_{streak} its offset along the z direction. The values are for "long" trajectories. In order to gain statistics, cuts were applied with a radius of $p_{rec} \pm 0.1$ a.u. and an opening angle of $\vartheta_{x_{circ}} < 45^o$. λ_{DB} is the DeBroglie wavelength of an electron of momentum p_{rec}. These spheres are illustrated in figure 5.19 with the color-coding given in the last column.

In addition to experimental problems, the non-isotropic ionization probability of our molecules is adding complexity. If we rotate the aligning polarization, we rotate the distribution of molecules the probe pulse is going to interact with. But the angle-dependence of the ionization probability imprints itself on top of this distribution, making the real change of the ionized distribution more complicated.[12] The effect is expected to be particularly pronounced in the case of O_2 (cf. chapter 2.2.9). Pollution by re-scattered electrons at higher lateral momentum may be causing another obstacle to be dealt with.

5.2.2.5. High-Momentum Structures

Like in experiment A, we will now analyze the structures at higher electron momenta ($|\vec{p}| > 1$ a.u.) with respect to double-slit diffraction.

Data Analysis We use "diffraction spheres" again, as explained in section 5.1.2.2 and illustrated by figure 5.8. Parameters of the different spheres used are given in table 5.11. These are shown as circles in figure 5.19. As before, we restrict the angle $\vartheta_{x_{circ}}$ to $90^o \pm 45^o$.

To make alignment dependencies of the diffraction circle data easily visible in a graph, we will normalize our histograms. This is shown step-by-step in figure 5.20. The horizontal axes plot the alignment angle while the vertical ones account for the scattering angle α_{zy} (for $p_{rec} = 1.01$ a.u. in this example). Count rates are color-coded. As can be seen in the non-normalized spectrum in figure 5.20(a), significant maxima occur at scattering angles around $\alpha = 0^o, 360^o$. This is where the spheres cut through the electron distribution at close to zero momentum. In that region, direct electrons are highly abundant and expected to vastly outnumber re-scattered ones. If we take a closer view on a range of scattering angles less prone do direct electrons (fig. 5.20(b)), we see some structures, including a weak diagonal line. By normalizing column-wise (cf.

---
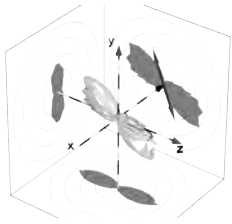
[12]Nota bene: Orbital tomography based on high harmonics generation (HHG) [38] should have the same problem.
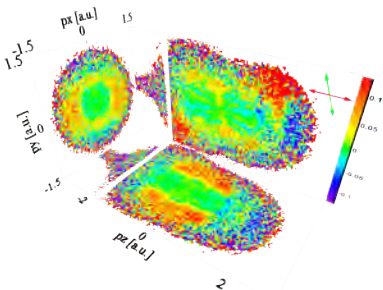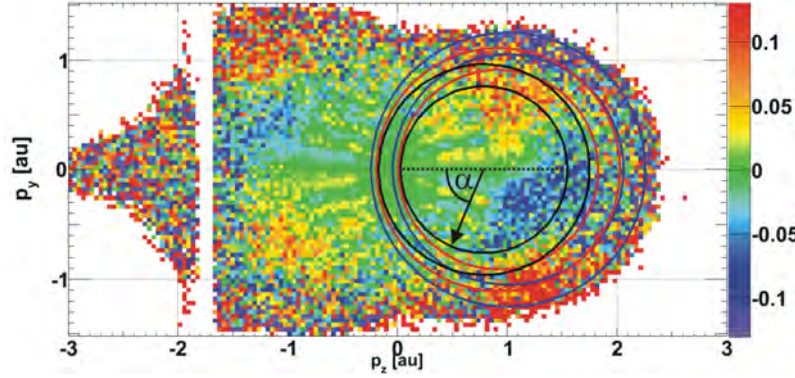
Figure 5.19.: Illustration of a cut through diffraction spheres. The region between two rings of the same color belongs to the same sphere. Parameters are given in table 5.11. The spectrum in the background shows normalized differences for N_2 with $\phi_{al} = 45^o \pm 11^o$ and $|p_z| < 0.1$ a.u. Its maximum around $(p_z, p_y) \approx (1.3, -1)$ a.u. relates to $\alpha \approx 100^o$ and moves with the alignment angle, causing the diagonal lines in the spectra shown in figures 5.22 and 5.23.

chapter 4.3.2), we remove the alignment-dependent ionization probability. This is because, due to their large number, we actually normalize to the rate of close to zero momentum direct electrons. The result is shown in figure 5.20(c). Now the diagonal has become much more prominent. We continue by applying normalized differences column-wise. The integral over all alignment angles (y projection of the distribution) is used as reference. Each column serves as signal. The result is shown in figure 5.20(d). This allows us to explore the full range of scattering angles in a single graph. However, the physical motivation of diffraction spheres holds only for re-scattered electrons.

Double-Slit Model In order to model the high-momentum structures we once again assume a plane electron wave being scattered by a double-slit. The phase difference between partial waves originating from the two slits, separated by a distance vector $\vec{d}$ is according to equation (2.21)

$$\Delta\varphi = \frac{1}{\hbar}\vec{d} \cdot (\vec{p}_s - \vec{p}_{rec})$$

with $\vec{p}_{rec}$ being the momentum of the incident (re-scattering) electron and $\vec{p}_s$ the momentum of the scattered one. $\vec{d}$ is the distance vector of the two slits. As the bond lengths of ground-state N_2 and O_2 are almost identical within the accuracy of the whole model (1.1 Å and 1.2 Å, respectively) we will run the simulation for the former value only. We comment that the scattering factor f as discussed in chapter 2.4 is divided out when calculating normalized differences.

At an alignment angle of 0°, molecules are preferentially aligned along the z

(a) No normalization. Logarithmic scale.

(b) No normalization. Zoomed in.

(c) Column-wise normalized. Zoomed.

(d) Normalized differences of (c).
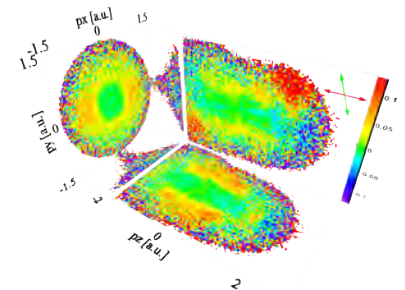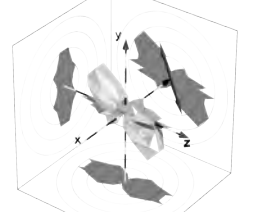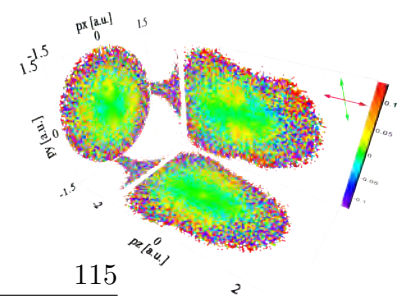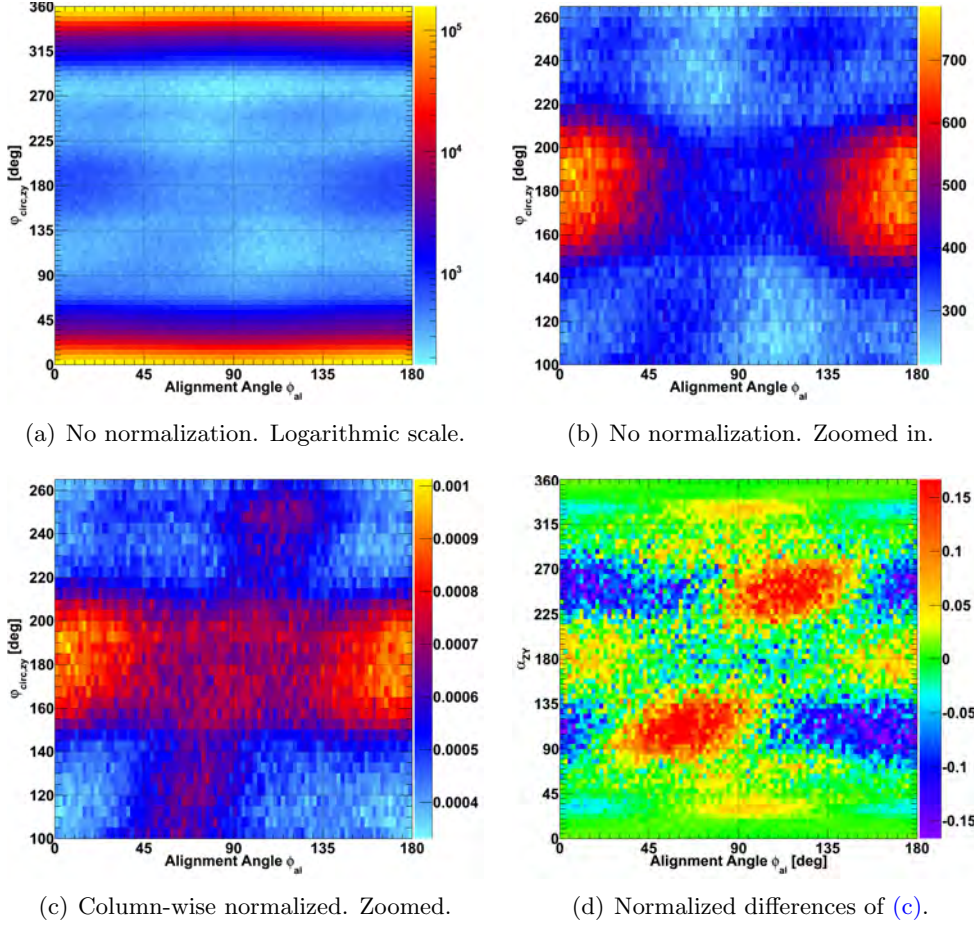
Figure 5.20.: Normalization of data from a diffraction sphere (nitrogen measurement, $p_{rec} = 1.01$ a.u., $z - y$ plane) step-by-step. All images show histograms of the alignment angle (*horizontal* axis) versus the electron scattering angle α (*vertical* axis). (a): Count rates without normalization. The large values around $\alpha = 0, 360^o$ are caused by direct electrons. (b): Same graph as (a) with the vertical axis zoomed in order to mask the direct electrons. Besides the two blobs at $\alpha = 180^o$, a weak diagonal line can be seen. (c): Histogram (a) column-wise normalized and zoomed in. Due to the fact that the majority of all counts are from direct electrons at $\alpha = 0, 360^o$, column-wise normalization removes the dependence of the tunneling rate on the alignment angle. The diagonal line that could only be guessed in (b) now becomes prominent. (d): Normalized differences. Each column in (c) served as signal. The reference used is the sum over all columns (i.e. alignment angles). The last step enables us to explore regions of φ having had out-of-range count rates before.
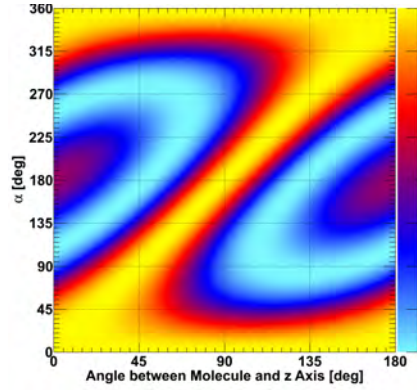
Figure 5.21.: Diffraction pattern by a double-slit spaced by the bondlength of N_2 (1.1Å) and an electron scattering elastically with a momentum of 1.15 a.u.. The *horizontal* axis denotes the angle between the incident electron and the slit while the scattering angle is plotted along the *vertical* axis. The diffraction amplitude is color-coded. It shall be pointed out that the diffraction maximum at $\alpha = 0, 360^o$ coincides with the experiment (fig. 5.20(a)) only incidentally. In the experiment, maxima in these regions are caused by non-re-scattered electrons, which are not treated by the simulation. A comparison with experimental data is given in figure 5.22.

axis, so the initial geometry is defined by

$$\vec{d} = \begin{pmatrix} 0 \\ 0 \\ 1.1 \text{ Å} \end{pmatrix} \quad \text{and} \quad \vec{p}_{rec} = \begin{pmatrix} 0 \\ 0 \\ p_{rec} \end{pmatrix}.$$

We rotate $\vec{d}$ step-by-step to mimic the changing alignment angle. We do not average over any distributions of molecular axes. $\vec{p}_{rec}$ remains frozen along the negative z direction. The scattering angle α is the angle between the incident and the outgoing electron vector, i.e.

$$\alpha = \angle(\vec{p}_{rec}, \vec{p}_s),$$

as defined before. Technically, we convert the above-mentioned phase difference to diffraction amplitude by filling a complex-valued histogram twice: Once with a (unit) amplitude and zero phase for a partial wave coming from one atom and another time with (unit) amplitude and the phase $\varphi = \Delta\varphi$ for the second atom. We then calculate the absolute square of the complex histogram.

The result for a re-collision momentum of $p_{rec} = 1.15$ a.u. is shown in figure 5.21. Its companions for the other momenta of interest look similar. However, the diffraction maxima at $\alpha = 0, 360^o$ coincide with those in the experiment (fig. 5.20(a)) purely incidentally. There are no direct electrons in the simulation.

In figure 5.22, we compare the simulation to column-wise normalized experimental data. If we take the reduced statistics of the O_2 measurement into
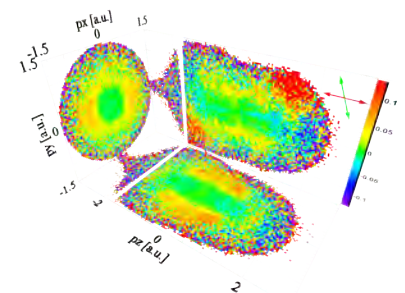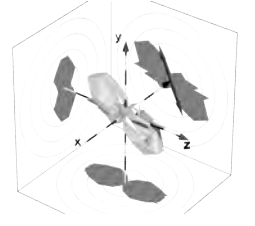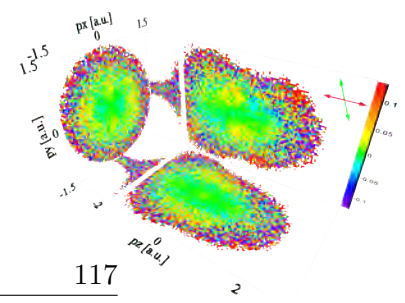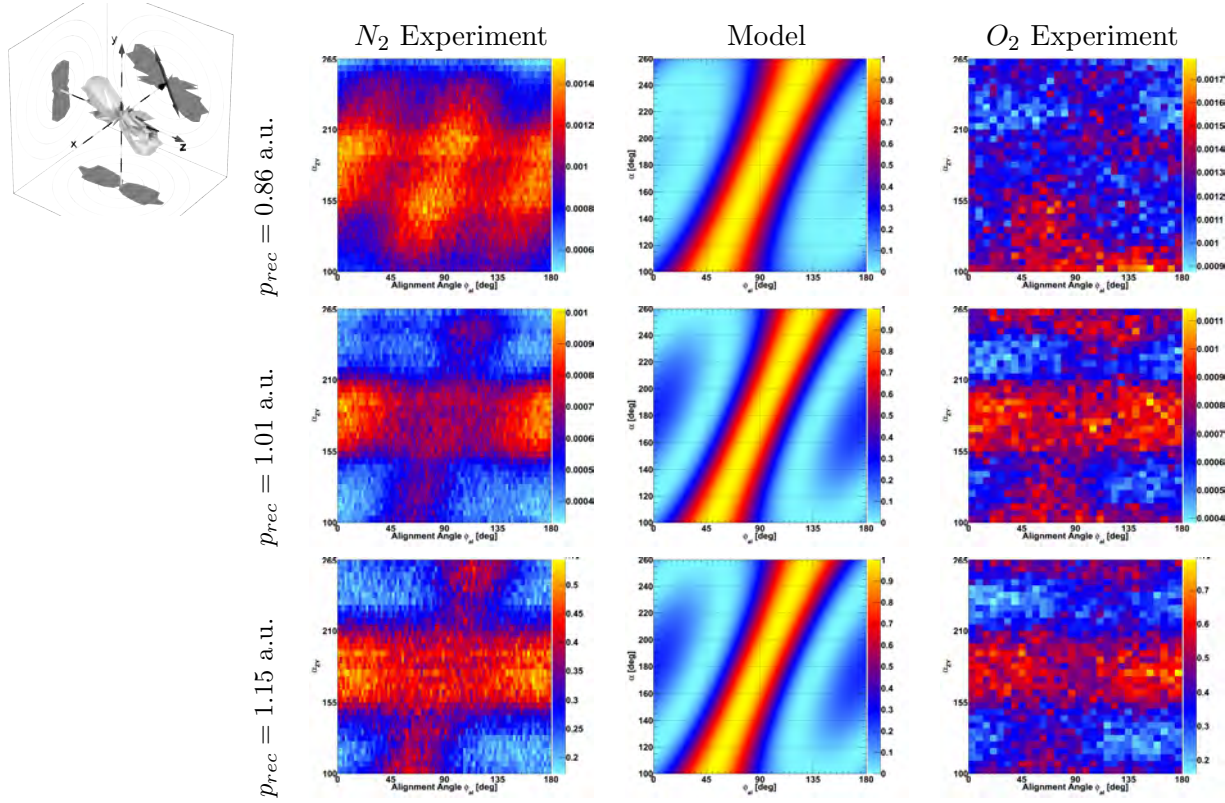
Figure 5.22.: Comparison of a simple diffraction model (*center*; see text for details) with experimental diffraction spheres in in the $z - y$ direction for three re-collision momenta p_{rec}. *Left*: N_2, *right*: O_2. Experimental histograms are column-wise normalized. The alignment angle ϕ_{al} is plotted by the *horizontal* and the scattering angle α withing the diffraction sphere denoted by the *vertical* axes. Both the simulated and the experimental data are shown only in the region of α where re-scattered electrons can be expected to make a significant contribution. The diagonal line clearly visible in N_2 and less clearly in O_2 is well reproduced by the model. However, this is not the case for the horizontal line around $\alpha = 180^o$, corresponding to exact backscattering without lateral deflection.

account, experimental data for the two species look very similar. The diagonal lines seen in the experiment are reproduced by the model. These represent the zeroth order diffraction maximum. Nevertheless, the simulation is not able to reproduce the horizontal line the experimental data show around $\alpha = 180^o$. In order to remove potential atomic effects, we calculate normalized differences with the integral over all alignment angles as reference. Results are shown in figure 5.23. Many features of the experiment are qualitatively reproduced by the model. The case $\alpha \approx 180^o$ (backscattering) remains problematic, in particular at an alignment angle of $\phi_{al} \approx 90^o$ remains problematic.
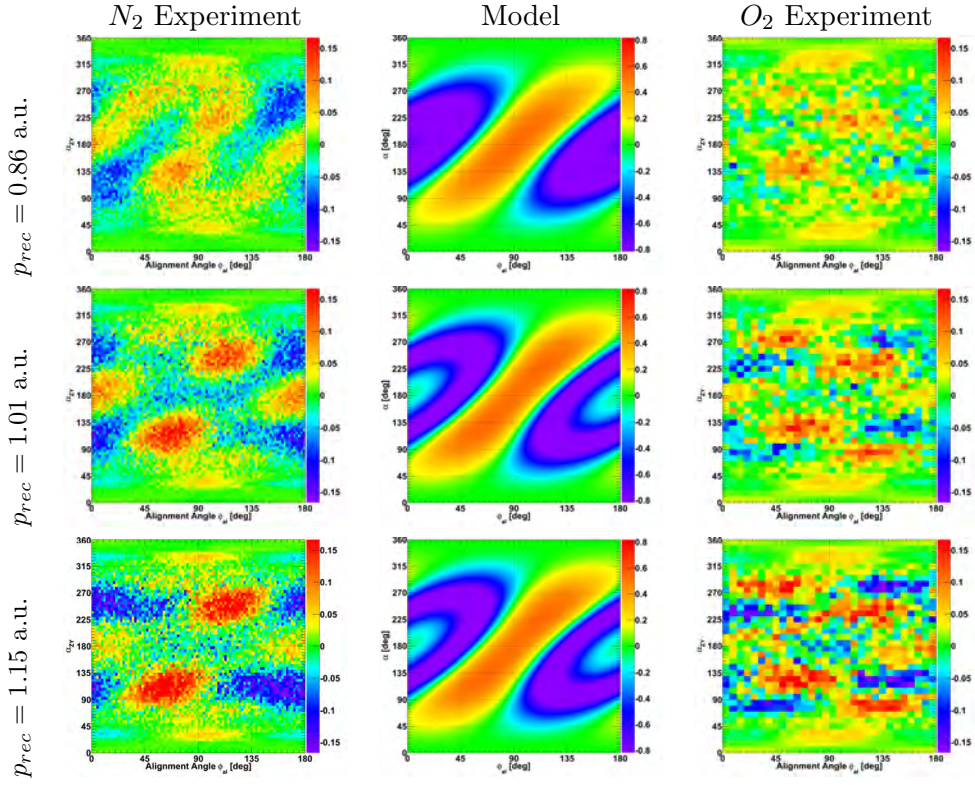
Figure 5.23.: Normalized Differences: Comparison of a simple diffraction simulation (*center*; see text for details) with experimental diffraction spheres in the $z - y$ direction for three re-collision momenta p_{rec}. *Left*: N$_2$, *right*: O$_2$. Experimental histograms were first column-wise normalized (cf. fig. 5.22). We then calculated the normalized differences with the integral over all alignment angles. The latter was also done with the results of the model calculation.
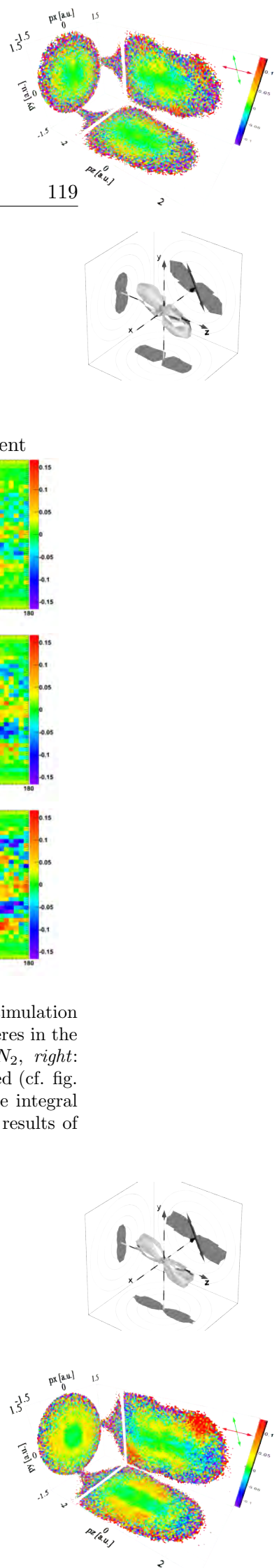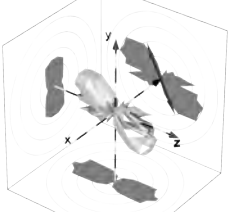
Conclusion   Our simple double-slit model can be criticized with several good arguments.

- First and foremost, it is quite primitive. By assuming pure double-slit diffraction, we are ignoring any interference effects by the non-slit shapes of the molecular potential and interaction between the re-scattering electron and the molecular ion's electron cloud. Within the static independent atom model (IAM), normalized differences remove the atomic scattering factors. Nevertheless, at first impression, the static IAM appears to be a rather problematic approximation given our re-scattering electron energies are way below 100 eV; cf. chapter 2.4.

- Additionally, the simulation is for a perfectly aligned double-slit. This is definitely not what we had in the experiment; see section 5.2.1.

- In the experiment, we analyzed data within spherical shells that are cut by cones (cf. fig. 5.8). The cones leave an opening angle of $\pm 45^o$, and we integrate this over. The simulation by contrast is two-dimensional, corresponding to the opening angle being 0°.

- A fourth potential issue is the assumption of only long electron trajectories playing a role. This assumption may be breaking down under certain conditions.

Seen in this light, the agreement between the experiment and our model is surprisingly good.

5.2.3. All Alignment Angles: The Flip-Book

Up to now, we mostly restricted our presentation to distributions recorded under three different alignment angles ϕ_{al}. In the experiment, we rotated the pump polarization by 180°, though. Spectra for all alignment angles are presented in the form of a flip-book throughout this work, with ϕ_{al} being varied over "time", i.e. page number. Actually, there are eight such flip-books: For

- N_2 (bottom) and

- O_2 (top of pages), we show

- normalized differences of electron momentum distributions (color plots) and

- angular distributions of correlated fragments (3D angle plots).

The fragment distributions are either for $N^+ + N^+$ or for $O^+ + O^+$. Conditions are given in table 5.9. The normalized differences are from electron momentum distributions recorded under an alignment angle relating to the page number (see below) as signal and the integral over all alignment angles as reference (cf.
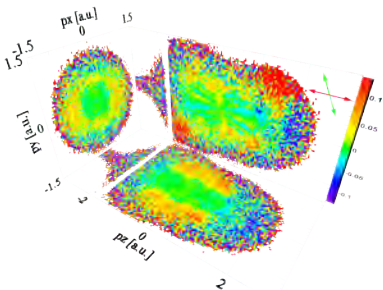
section 5.2.2.2). The red double arrow in the top right part of each such graph denotes the polarization direction of ionizing probe- and the green arrow the direction of aligning pump pulses.

Be n the page number.

- On odd-numbered pages (right-hand part of the double page),

  – the alignment angle in degrees is $\phi_{al} = n-2$ and summed over a range of $\pm 3^o$ for N_2 and $\pm 5^o$ in case of O_2.

  – the projections onto the coordinate planes leading to the electron normalized difference distributions were made by integrating over the respective third direction.

- On even-numbered pages (left-hand part of the double page),

  – the alignment angle in degrees is $\phi_{al} = n - 1$. It is summed over a range of $\pm 11^o$ for both N_2 and O_2.

  – the electron normalized difference distributions were made by restricting the respective third direction to ± 0.1 a.u..

Hence, we show distributions for the same average alignment angle throughout a double page.
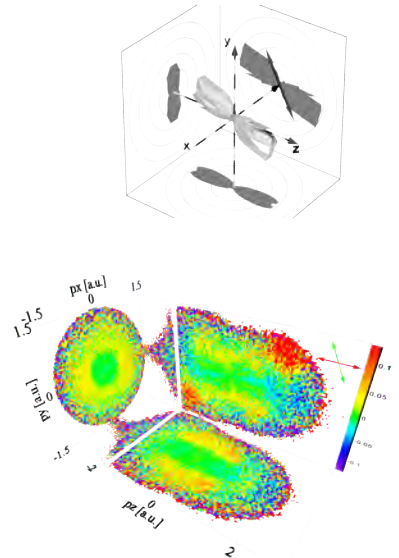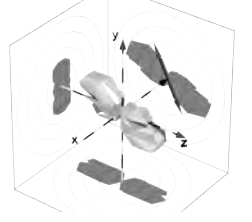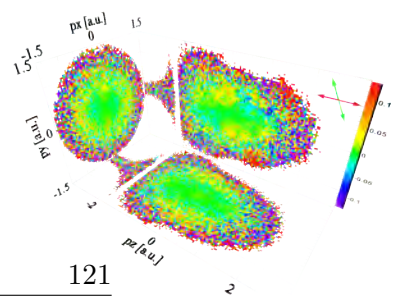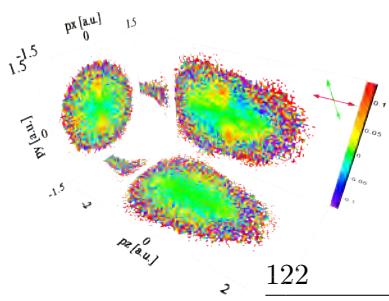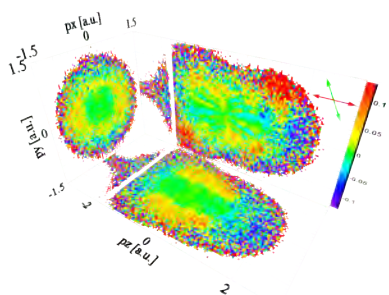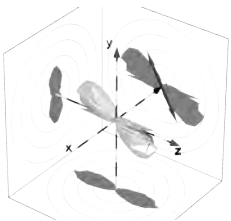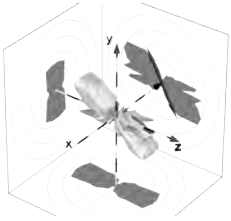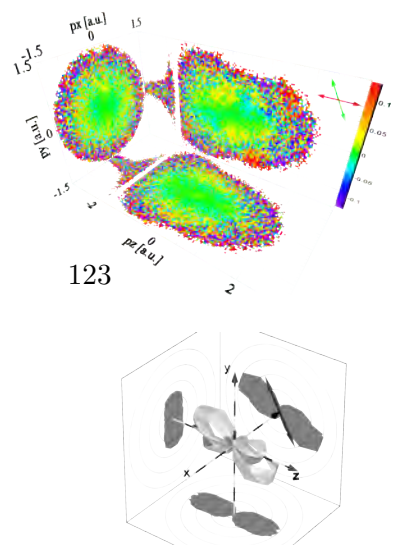
6. Resolution and Flaws

Nothing is perfect.

(Anonymous)

In order to judge the quality of the data we have to estimate the systematic errors of all measured parameters. These will given as full width at half maximum (FWHM) values. In addition, the data are subject to some flaws, which will be discussed.

6.1. Resolution

Resolution defines the smallest possible change of a measured quantity that can still be distinguished.

6.1.1. Detector Coordinates

For experiment A, we assume the following uncertainties of both electron and ion detector coordinates:

$$
\begin{aligned}
\Delta x &= 0.7 \text{ mm} \\
\Delta y &= 0.7 \text{ mm} \\
\Delta TOF &= 0.7 \text{ ns.}
\end{aligned}
$$

In the case of experiment B,

$$
\begin{aligned}
\Delta x &= 0.3 \text{ mm} \\
\Delta y &= 0.3 \text{ mm} \\
\Delta TOF &= 0.5 \text{ ns}
\end{aligned}
$$

appear to be appropriate due to the improved electronics. Here the spatial resolution is limited by the 0.26 mm width of the mesh in front of the detectors. The performance of the detectors by themselves after the electronics upgrade is so much better that we resolve the mesh very well; see figure 6.1.
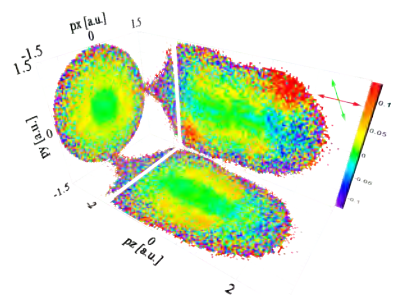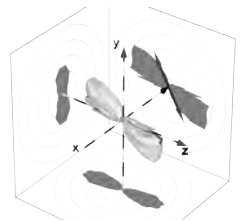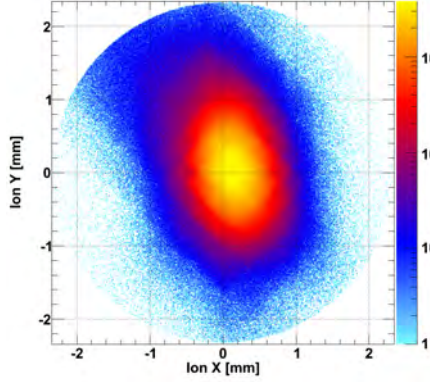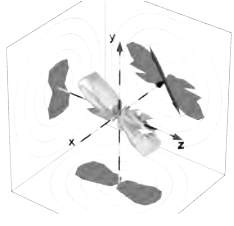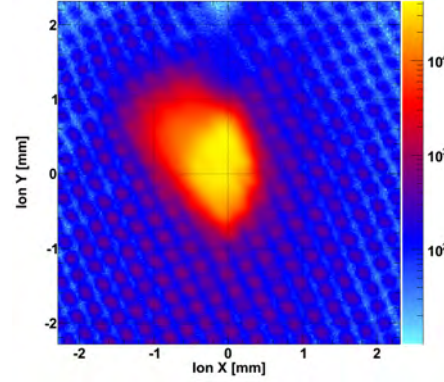
(a) Experiment A   (b) Experiment B

Figure 6.1.: Distribution of N_2^+ ions on the detector. (a): Experiment A. The mesh is
not visible in the image. (b): Experiment B, after the electronics upgrade.
We clearly see the mesh in front of the detector, having a width of $\approx$
0.26 mm. The maxima in the origin are caused by the desired cold ions,
while the background is from warm molecules.

6.1.2. Ion Momenta

In an electron-ion coincidence experiment, two different approaches can be used
to obtain the systematic errors of measured momenta. On the one hand, one
can calculate them from detector resolutions. On the other hand, if we observe
a single ionization channel, the center of mass momentum $\vec{p}_{CMS} = \vec{p}_{ion} + \vec{p}_{elec}$
should be zero for each event. The real-world width of the $\vec{p}_{CMS}$ distribution is
a measure of the combined errors caused by both of the detectors and the finite
jet temperature. Our ion detector was tuned to capture energetic fragments
rather than low-energy stable molecular ions. Additionally, the momentum error
imposed to electrons by thermal motion is negligible, while ions do suffer from
it. Hence, the center of mass momentum distribution is dominated by the errors
of ion momenta, giving a measure only of the latter. These distributions are
plotted for N_2^+ and O_2^+ in figure 6.2. The respective widths of the distributions
are given in table 6.1.
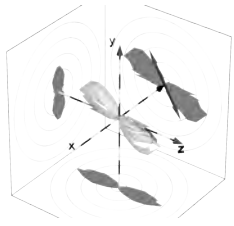
6.1.3. Electron Momenta

While our ion detection was tuned to catch energetic fragments we wanted to
measure relatively small momenta (less than 3.5 a.u. in any case and direction)
on the electron side. We calculate their uncertainty from the resolution of the
electron detector.

(a) Experiment A: $N_2^+ + e^-$

(b) Experiment A: $O_2^+ + e^-$

(c) Experiment B: $N_2^+ + e^-$
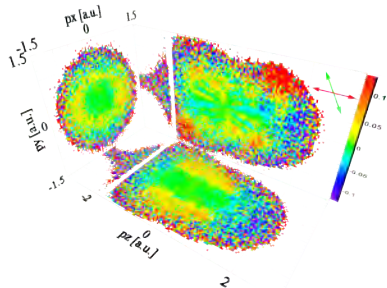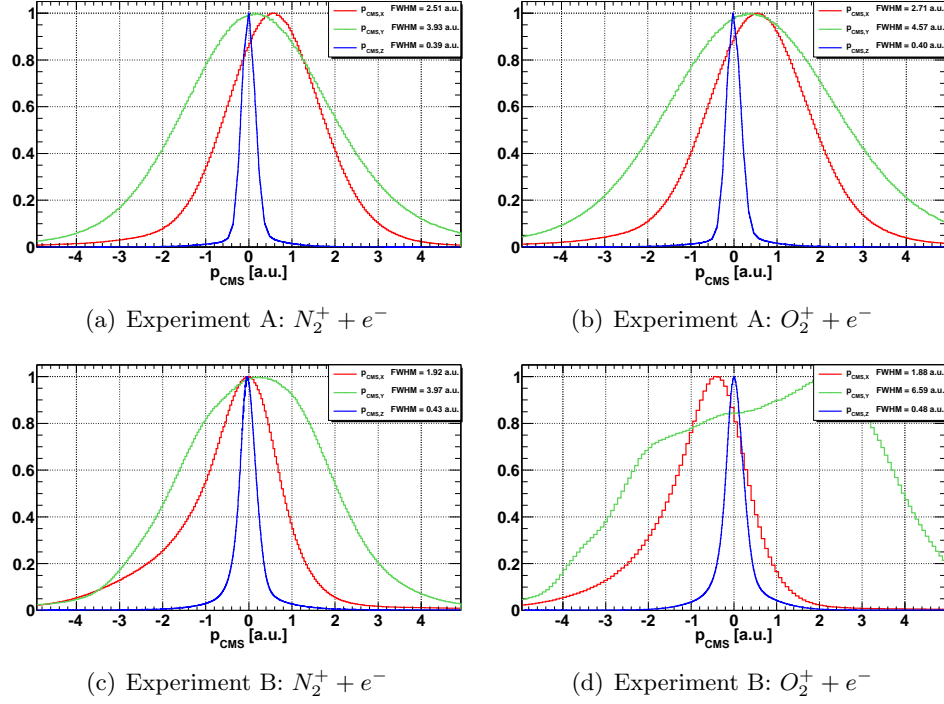
(d) Experiment B: $O_2^+ + e^-$

Figure 6.2.: Center of mass momentum distributions of single ions and their correlated electrons in the x- (*red*), y- (*green*) and z-direction (*blue* curve). *Upper* row: Experiment a; *lower* row: Experiment B. The distributions for singly ionized nitrogen are shown on the *left* and the ones for oxygen on the *right*-hand side. For each curve, the full width at half maximum, giving a measure mostly of our resolution for ion momenta, is denoted in the legend and repeated in table 6.1.

Direction	Exp. A: N_2^+	Exp. A: O_2^+	Exp. B: N_2^+	Exp. B: O_2^+
x	2.5 a.u.	2.7 a.u.	1.9 a.u.	1.9 a.u.
y	3.9 a.u.	4.6 a.u.	4.0 a.u.	6.6 a.u.
z	0.4 a.u.	0.4 a.u.	0.4 a.u.	0.5 a.u.

Table 6.1.: Full widths at half maximum of the center of mass distributions shown in figure 6.2 for the experiments and ions (+ electrons) specified in the table headline. These values give a measure of the combined resolution of detectors and the jet target temperature. They are dominated by the errors of ion momenta. The y direction is worst because this is the jet propagation direction. Along x and y, the skimmer provides geometric cooling.
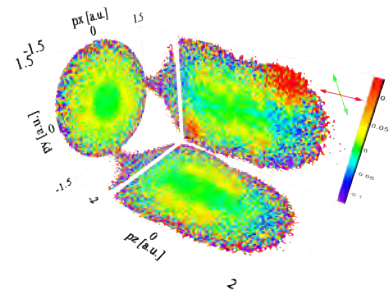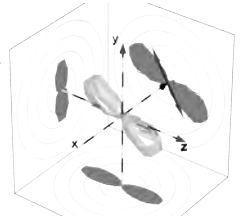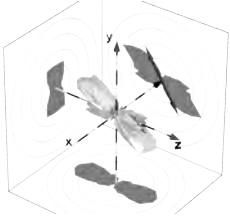
6.1.3.1. Spatial Directions

In the spatial directions, i.e. in the detector plane, we do this by means of Gaussian error propagation. The formulae used to calculate electron momenta p_x and p_y from x, y and the time of flight are given in equation (3.13). We combine them to yield the momentum magnitude in the spatial directions (i.e. perpendicular to the spectrometer axis)

$$p_\perp = \sqrt{p_x^2 + p_y^2} = r \cdot \frac{m_e \omega_{gyr}}{2} \sqrt{\frac{1}{\xi^2} + 1}.$$

Here, $r = \sqrt{x^2 + y^2}$ is the radius of the electron's impact position from the origin of the detector and

$$\xi = \tan\left(\frac{1}{2}\omega_{gyr}TOF\right).$$

Using the Gaussian error propagation law we obtain the error

$$
\begin{aligned}
\Delta p_\perp &= \sqrt{\left(\Delta r \frac{\partial p_\perp}{\partial r}\right)^2 + \left(\Delta TOF \frac{\partial p_\perp}{\partial TOF}\right)^2} \\
&= \frac{m_e \omega_{gyr}}{2}\sqrt{\Delta r^2 \left(\frac{1}{\xi^2} + 1\right) + \Delta TOF^2 \left(r\omega_{gyr}\frac{1+\xi^2}{\xi^3\sqrt{1/\xi^2+1}}\right)^2}.
\end{aligned}
\quad (6.1)
$$

The resulting distributions of expected inaccuracies are shown in figure 6.3 for each experiment (A and B). From these we conclude that the assumption of $\Delta p_\perp = 0.15$ a.u. should be a reasonable and safe assumption outside the regions subject to wiggles for both experiment A and B.

6.1.3.2. Time of Flight Direction

In the time of flight direction, we estimate the error Δp_z by comparing values for p_z within a range of times of flight. The sought-after error is

$$\Delta p_z = \max[|p_z(TOF + \Delta t) - p_z(TOF)|] \quad (6.2)$$

with the local time of flight error $\Delta t \in [-\Delta TOF, \Delta TOF]$ being iterated. The resulting dependence of errors on p_z is graphed for both experiments in figure 6.4.
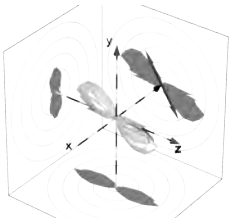
6.2. Flaws

In addition to the resolution problem inherent in experimental physics, our data show two sets of flaws: Inhomogeneities of detection efficiencies and issues related to the fields in the spectrometer.

(a) Experiment A   (b) Experiment B
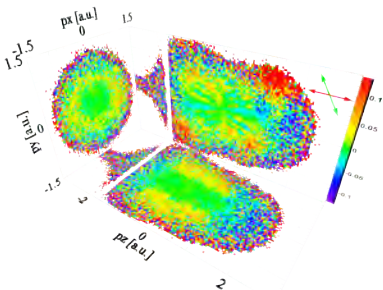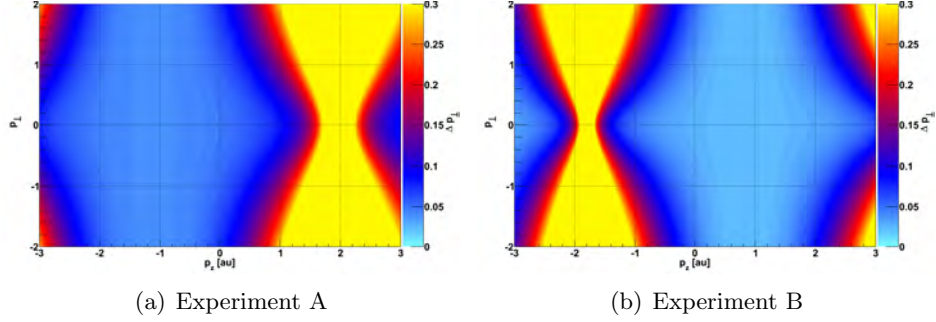
Figure 6.3.: Resolution of electron momenta in the detector plane $\Delta p_\perp$ (*color*-coded), depending on momentum in that plane ($p_\perp$, *vertical*) and along the time of flight direction (p_z, *horizontal* axis). $\Delta p_\perp$ was calculated using equation 6.1 and the respective detector resolutions given in section 6.1.1. In case of experiment A, a wiggle appears nearby $p_z \approx 2$ a.u., making resolution deteriorate around this value. The same is observed in the vicinity of $p_z \approx -1.8$ a.u. for experiment B. Outside these regions, assuming an error of $\Delta p_\perp = 0.15$ a.u. appears to be cautious. (N.b.: $p_\perp$ as defined here is always positive. Negative values appear in the above plots for technical reasons.)

(a) Experiment A   (b) Experiment B
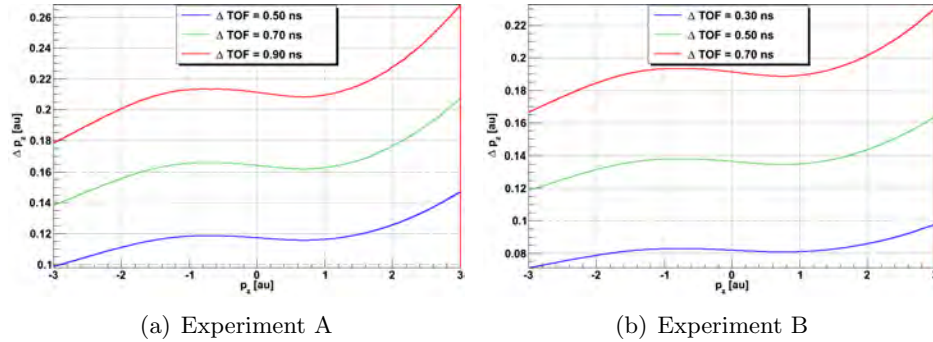
Figure 6.4.: Resolution of electron momenta in the time of flight direction (z), as it depends on the momentum in that direction. Calculated according to equation (6.4). Different curves are for different errors ΔTOF of the times of flight. For both experiments, the green curves show the respective case assumed in the text, whereas the blue ones are for a more optimistic and the red ones for a more pessimistic scenario. Within the assumed TOF error, $\Delta p_z < 0.21$ a.u. in case of experiment A and $\Delta p_z < 0.17$ a.u. for experiment B.

(a) Experiment A   (b) Experiment B (N_2)
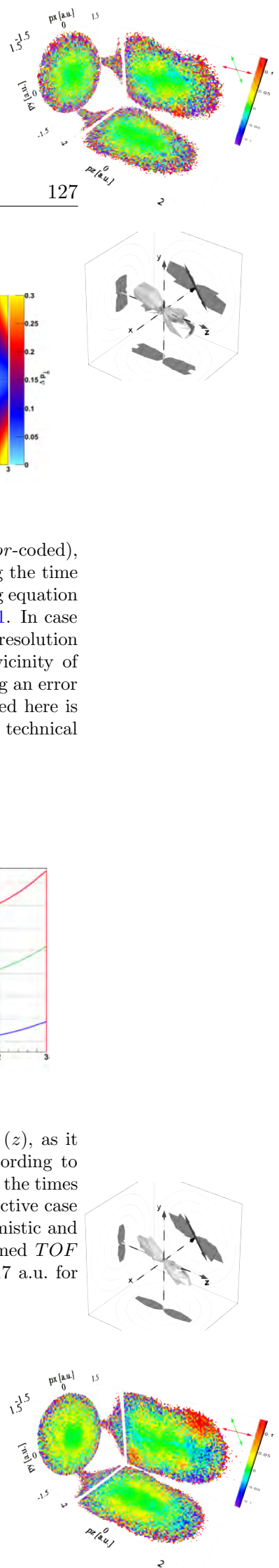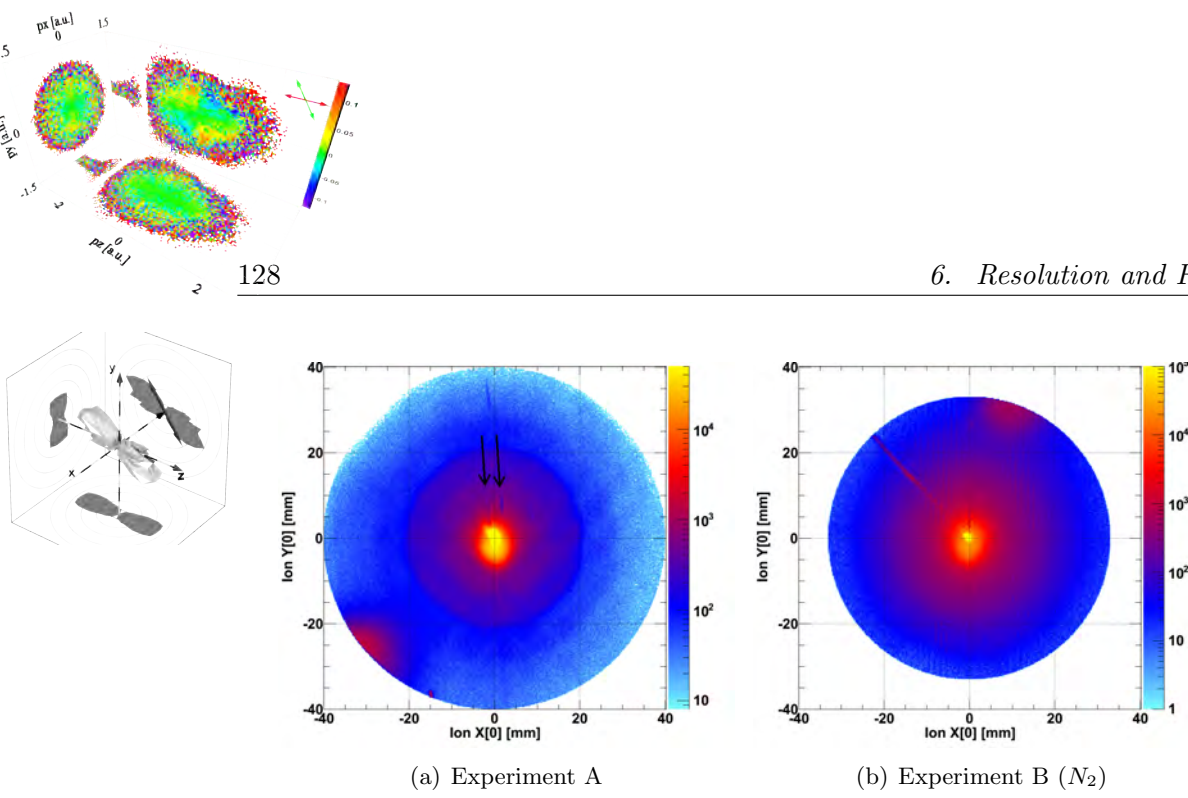
Figure 6.5.: Spatial distribution on the ion detector. (a): Experiment A. Two regions of strongly reduced detection efficiency are marked by arrows. (b): N_2 measurement of experiment B. The oscillations are most likely a Moiré pattern caused by an interference between the mesh (cf. figure 6.1(b)) and the binning of the histogram. The "beam" departing at the center towards the top left is probably caused by an electronics problem. It does not appear in ion-specific spectra. The jet velocity (along the y axis) is removed from ions before the images are made. This extends the "holes" in subfigure 6.5(a) in the vertical direction as compared to the detector surface. Both distributions are restricted to the region used for the analysis.

6.2.1. Detector Issues

The MCPs of our detectors were not new. In particular the ion MCP had dead spots from previous experiments. These are marked by arrows in figure 6.5. In addition, the mesh imprinted its structure on ion distributions, which is visible only in the improved setup used for experiment B (see figure 6.1). This sub-structure is below our assumed resolution but causes a prominent Moiré pattern in the detector image (fig. 6.5(b)). This covers the scars on the MCPs in the image, which were the same as used in experiment A.

On the electron side we had two spots with reduced detection efficiency in experiment A (see arrows in figure 6.6(a). However, it is possible these are caused by electron-ion correlation. Due to the fact that only events containing at least one ion were saved in experiment A, dead spots on the ion detector propagated into electron distributions. We avoided this in experiment B by storing events if they contained an electron without requiring an ion.

6.2.2. Field Inhomogeneities

In chapter 4.1.3.2 (calibration), we observed that the origin on the electron detector is not constant but changes, depending on the electron's time of flight. In

(a) Experiment A (b) Experiment B
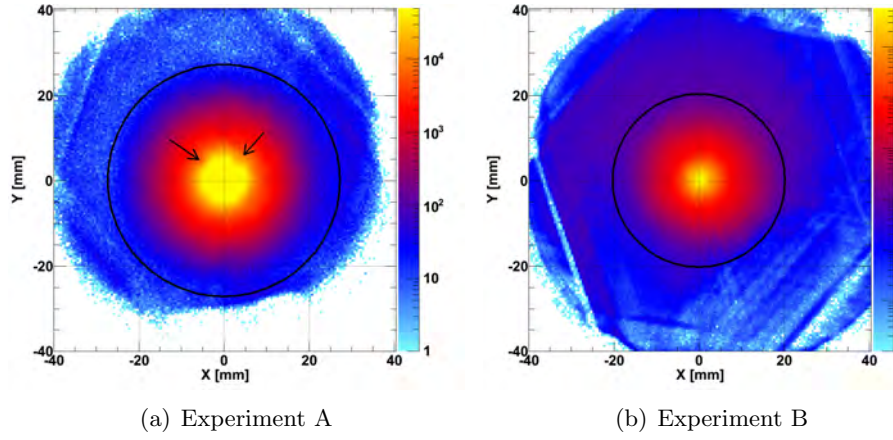
Figure 6.6.: Electron detector images. (a): Experiment A. Two regions of reduced detection efficiency are marked by arrows. (b): N_2 measurement of experiment B. The stripes along the delayline layers are caused by an electronics problem (crosstalk). We can clearly see the regions of coverage by the three layers of the hexagonal detector. The circles denote the maximum radius of $p_\perp = 1.6$ a.u. / $p_\perp = 1.5$ a.u. electrons (experiment A / B, respectively).

addition, the electron time of flight offset turned out to depend on the electric field applied to the spectrometer, which should not be the case either.

As briefly discussed before, the most likely explanation is that the focusing mirror in the spectrometer caused an inhomogeneity in the electric field. The mirror and its holder are conductive and therefore constitute an equipotential surface. Due to its focal length of $f = 50$ mm, it had to be effectively moved into the spectrometer. The latter had an inner radius of slightly more than 40 mm. The focus was supposed to be at its center. Six spectrometer plates had cutouts to provide room for the mirror; see figure 6.7. This gave way for a penetration of field lines into the spectrometer.

As a result, $\vec{E}$ and $\vec{B}$ were not aligned with each other everywhere in the spectrometer, causing complicated interdependencies between the initial momentum vector of an electron, its final time of flight and impact position on the detector.

We tried to rectify the problem by applying correction functions forcing the spatial distributions to peak at zero in a rather brute force way. This made it possible to to analyze the data, but it did not completely solve the issue. In experiment B, we can see clear ATI structures if we cut through momentum space rather than integrating. These are bent in unphysical ways; see figure 6.8. We did not manage to remove these effects by means of calibration.

In principle, the whole concern could have been avoided by using a mirror with a larger focal length that can be kept outside the spectrometer, and cutting a smaller hole into the spectrometer. However, we were always at the lower limit of acceptable focal intensity. Hence, in practice, using a larger focal length
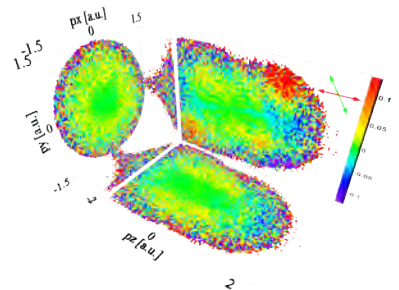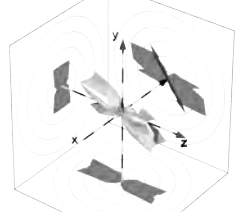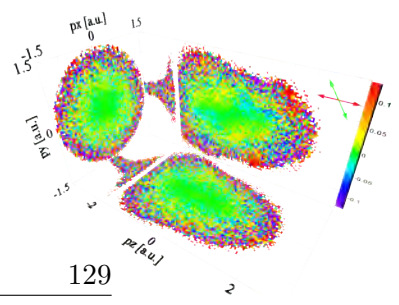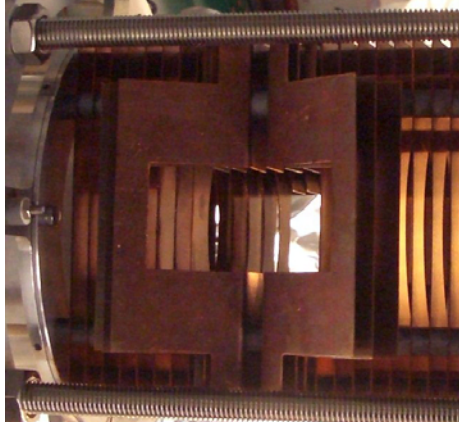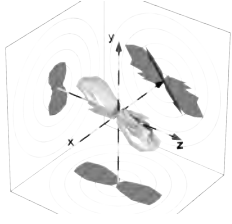
(a) Cut-out part of the spectrometer   (b) Inside the chamber with mirror
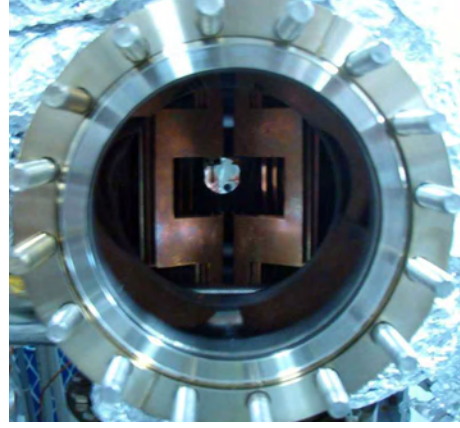
Figure 6.7.: Part of the spectrometer housing the focusing mirror, outside (a) and inside the chamber (b). Six spectrometer plates are cut to make room for the mirror on the one and the incident light beam on the other side. This allowed for the use of an $f = 50$ mm mirror achieving tight focusing but led to electric field inhomogeneities in the spectrometer.

leading to less tight focusing with the given laser system was not an option for the experiments reported here.

6.2.3. Ionization by the Pump Pulse in Experiment B

We did not intend to ionize with the pump pulse. This did happen at a low rate in experiment B, though, see table 5.8. In the electron normalized difference spectra in figure 5.16, in particular in the $\phi_{al} \approx 90^o$ case, we see a low-momentum structure apparently following the aligning pulse polarization in the $z - y$ plane directly. If ionization by the pump was significant, the generated electrons would be most abundant along the pump polarization, possibly causing a structure like the one observed.

6.2.3.1. Tunneling Model

In order to confirm whether or not ionization by the alignment pulse could play a role, we perform a simulation. We employ the atomic tunneling theory by using equation (2.6), assuming a static electric field corresponding to peak intensity. For each species, we calculate two distributions of electron momenta. The first is for the probe pulse, being polarized along the z axis and having an intensity of $I_{probe} = 1.3 \cdot 10^{14} \; \frac{\text{W}}{\text{cm}^2}$. The second is for the pump pulse, which we assume to be polarized along the y axis and have an intensity of $I_{pump} = 0.5 \cdot 10^{14} \; \frac{\text{W}}{\text{cm}^2}$. We then normalize these spectra according to the respective ratio of detected count rates of the pump- and the probe pulse (the latter minus dark counts).
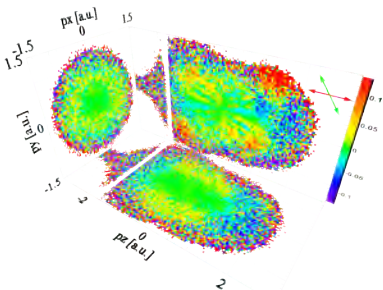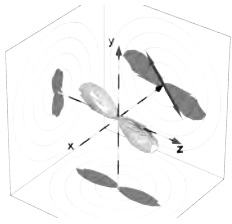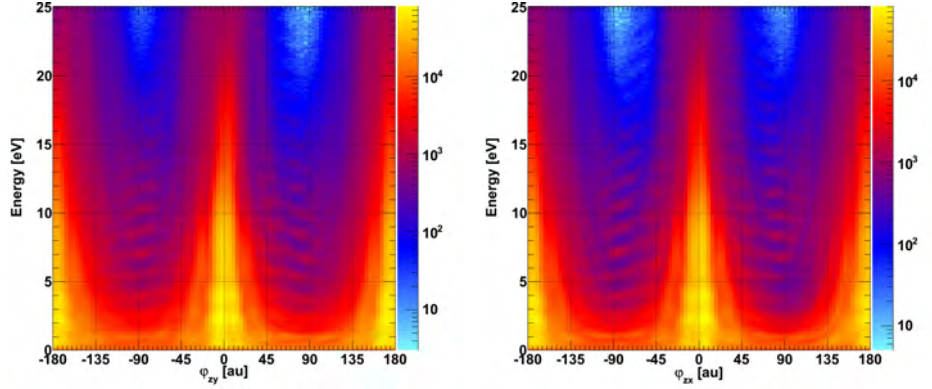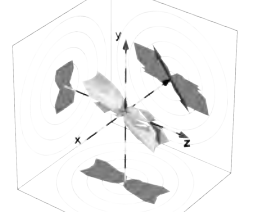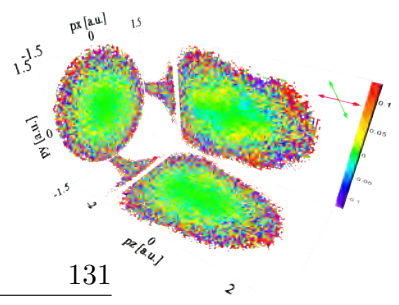
(a) Angle in $z - y$ plane. $\vartheta_x = 90^o \pm 10^o$

(b) Angle in $z - x$ plane. $\vartheta_y = 90^o \pm 10^o$
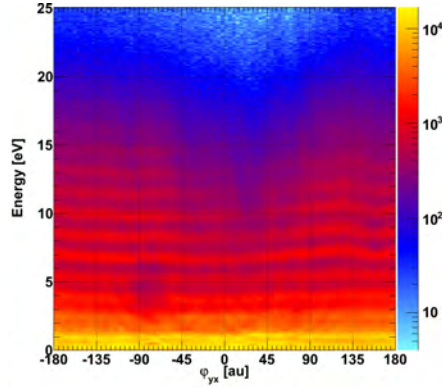
(c) Angle in $x - y$ plane. $\vartheta_z = 90^o \pm 10^o$

Figure 6.8.: From experiment B (N_2 measurement): Electron angle (*horizontal* axes) vs. kinetic energy (*vertical* axes). The angles are within the planes specified in the respective figure subscripts. We set conditions restricting the out-of-plane momenta. The maxima, showing up as horizontal lines in the spectra, are ATI peaks. These lines should be straight. Their bends are artifacts probably caused by field inhomogeneities within the spectrometer. All efforts to straighten them (e.g. by adjusting fields, spectrometer lengths, etc.) failed.
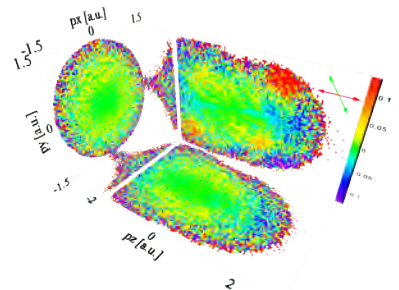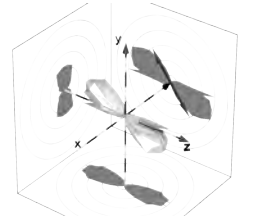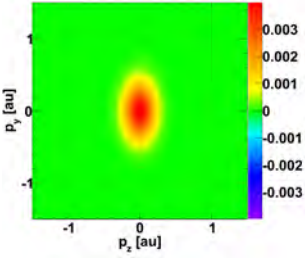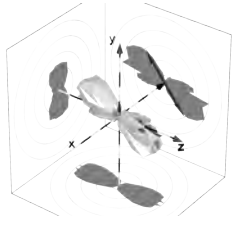
(a) N_2: Zoomed Color Bar.   (b) N_2: Like Experiment.   (c) N_2: Experiment.
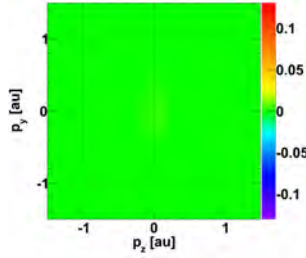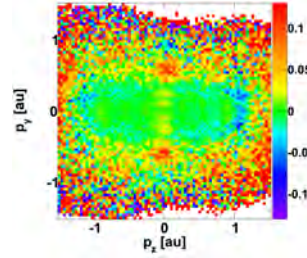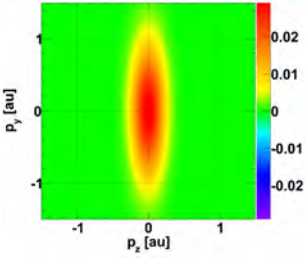
(d) O_2: Zoomed Color Bar.   (e) O_2: Like Experiment.   (f) O_2: Experiment.
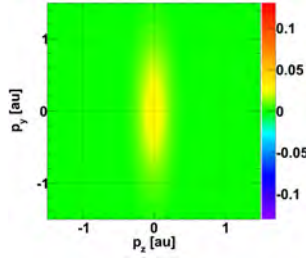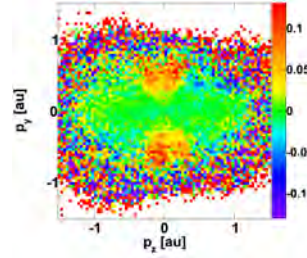
Figure 6.9.: Analysis of ionization by the pump pulse with respect to our normalized difference distributions in the $z - y$ plane. The pump is polarized along the vertical and the probe along the horizontal axis. This is the geometry where the problem - if any - will be most severe. Column on the *left*: Simulation as described in the text. The color scales are adapted to make the central structure visible. The latter is caused by electrons generated by the pump pulse. Column in the *middle*: Same with color scale as used in the experiment. *Right*: Experimental distributions, with out-of-plane momentum restricted to $|p_x| < 0.1$ a.u. and $\phi_{al} = 89^o \pm 11^o$. Nitrogen data are shown in the *top* row. Although we do not see an effect when using the same color scale as in the experiment 6.9(b) within the pure tunneling model, Coulomb focusing reduces the safety margin. See text. *Bottom*: Oxygen, where an effect should be visible, even without Coulomb focusing.

Finally we apply normalized differences. The signal is the electron momentum distribution obtained for the probe plus the one for the pump pulse. The distribution for the probe alone serves as reference. The resulting normalized difference distributions are shown in figure 6.9.
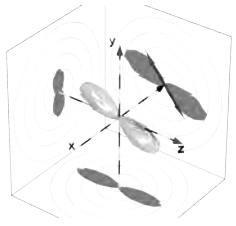
6.2.3.2. Coulomb Focusing

So far, we have not taken Coulomb focusing [76] into account. This effect can be expected to reduce the spread of pump-generated electrons along the z and concentrate them more along the y axis. Moreover, Coulomb focusing of the electrons generated by the probe pulse will reduce their spread along y. Both focusing effects make the relative abundance of the unwanted pump electrons in-

(a) N_2 (b) O_2
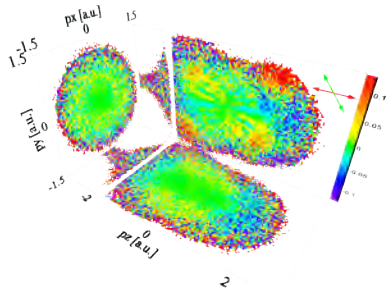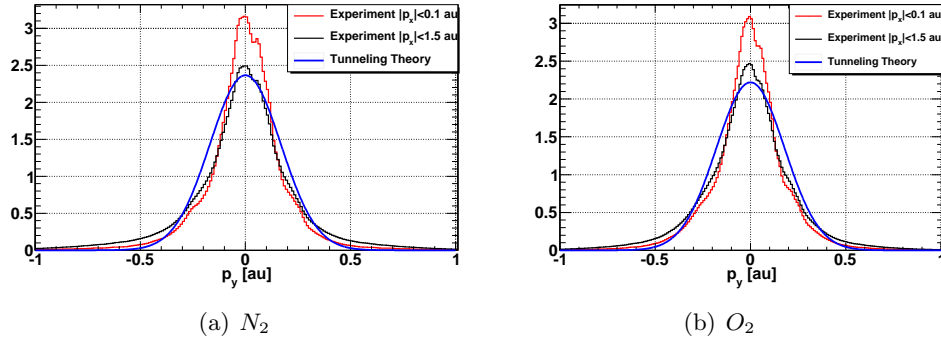
Figure 6.10.: Influence of Coulomb focusing on the lateral distributions of electrons. *Blue* curves: Electron momentum distributions calculated according to atomic tunneling theory ($p_\perp$-dependent component of equation (2.6) with $\Gamma_0 = const.$ and E according to an intensity of $I = 1.3 \cdot 10^{14} \frac{\mathrm{W}}{\mathrm{cm}^2}$). *Black* curves: Experimental distributions in one direction perpendicular to the laser polarization, with the other directions integrated over. *Red* curve: Same as black curves but momentum in the second direction restricted to ± 0.1 a.u.. All curves are normalized to an integral value of one. Comparison between the experimental and calculated plots yields that Coulomb focusing can have increased the maximum value of the measured distributions by no more than a factor of 1.5.

crease with p_y around $p_z \approx 0$ beyond the simulation. To estimate the magnitude of the effect we compare measured (and therefore Coulomb focused) absolute electron momentum distributions to tunneling theory in figure 6.10. The measured electrons were generated almost solely by the probe pulse. The calculated curves are for the respective (static) electric field. All curves are normalized to an integral value of one.

We conclude that Coulomb focusing increases the maxima of electron momentum distributions generated by the probe pulse by no more than a factor of 1.5 over tunneling. We assume the same is the case for electrons ionized by the pump. Hence, Coulomb focusing can increase the fraction of unwanted electrons by a factor of $1.5^2 = 2.25$ in the worst case.

6.2.3.3. Nitrogen Measurement

For the nitrogen measurement, the calculated spectrum in figure 6.9 does not show any visible structure if we use the same color scale as in the experiment. The normalized differences reach a maximum value of $nd \approx 0.004$. That is, the pump-generated electrons reach a maximum of up to 0.8% of the abundance of probe-generated ones. The color scale used for the experimental data does not allow us to see an effect below $nd = 0.015$, relating to 3% pump electrons. If we factor in our worst-case estimate of the contribution by Coulomb focusing, we obtain a maximum of 1.8% unwanted pump electrons, which should not
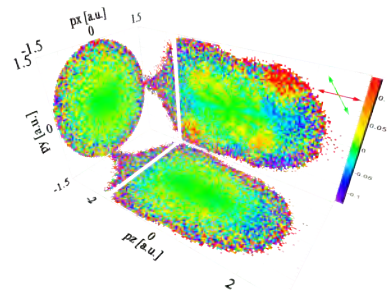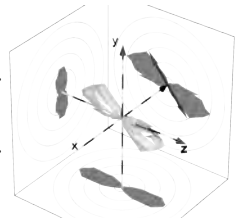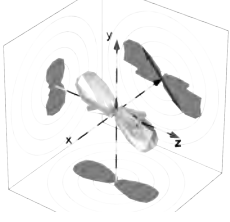
be visible. However, within the worst-case scenario developed here, the safety margin seems quite low. This is particularly worrisome with respect to the rather coarse initial value of ionization rate by the pump (20 Hz). Therefore we cannot rule out the presence of a small effect with final reliability.

6.2.3.4. Oxygen Measurement

Regarding the oxygen measurement, the situation is even less favorable. The pattern in our simulated normalized difference distribution reaches a maximum value of $nd \approx 0.03$, relating to a signal:reference ratio of $1.22 : 1$. This should clearly be visible, even without taking Coulomb focusing into account. Hence, we cannot rule out the structure staying parallel to the aligning pulse polarization and extending up to a momentum of ≈ 0.8 a.u. is a result of ionization by the pump pulse in the oxygen measurement.

6.2.3.5. Conclusion

Hence, we have to conclude that small structures along the pump polarization at low momenta cannot be trusted without further investigation. This is particularly bad in the case of oxygen.

For the above analysis we chose projections such that the relative abundance of the unwanted electrons was maximum. That is, we considered the $z - y$ plane with the x direction being restricted to ± 0.1 a.u.. If we integrate over p_x rather than cutting, pollution will be diluted. In the $x - y$ and $z - x$ direction, another effect reduces the problem. The further the alignment angle ϕ_{al} deviates from 90°, the more pump-generated electrons will have momenta out of these planes. When restricting out-of-plane momenta, the unwanted electrons in these spectra will be attenuated, the more the higher the in-plane momentum and the more ϕ_{al} differs from 90°.

We note that experiment A is not prone to this problem. There, the pump and the probe polarization were frozen at all times. Even if the pump had generated some electrons, their distribution would have had no dependence on the pump-probe delay used to generate the distributions to be compared. Therefore, the contribution by these electrons would have been the same to the aligned and the anti-aligned distribution and removed by the normalized differences.

6.3. Waveplate Problems
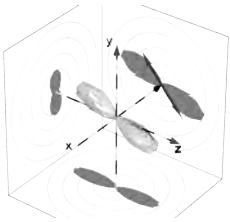
In experiment B, we rotated the polarization of aligning pulses from $\phi_{al} = 0$ to $\phi_{al} = 360^o$. All effects occurring between 0 and 180° should repeat between 180° and 360° accordingly. We were expecting maximum alignment in the detector plane at angles of $\phi_{al} = 90^o$ and $\phi_{al} = 270^o$.

But in the case of the O_2 measurement, we observed something different. Within the region between 0 and 180°, the polarization seemed to follow the
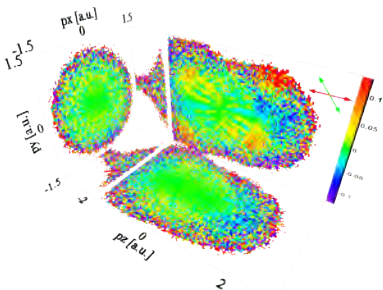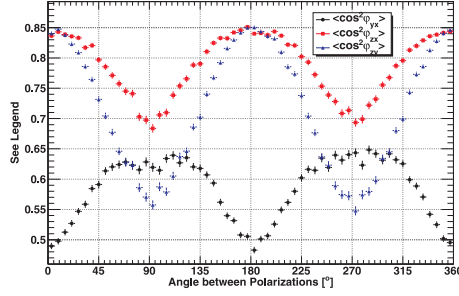
(a) N_2 Measurement: As expected.   (b) O_2 Measurement: Flawed from 0 to 180°.
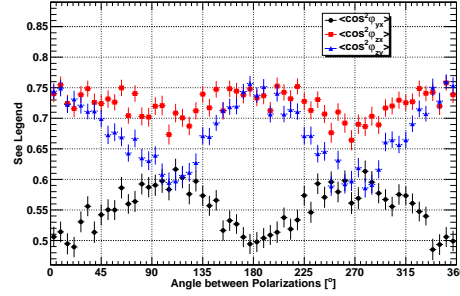
Figure 6.11.: Distributions of average cosine squares of various angles for $N^+ + N^+$ (a) and $O^+ + O^+$ explosions (b) (*vertical* axis), depending on the desired value of the alignment angle (*horizontal* axis). The distributions from nitrogen behave as expected. In the case of oxygen, apart from showing a generally poor degree of alignment, the maximum of $< \cos^2 \varphi_{yx} >$ (*black* circles) is found at an alignment angle of $\approx 110^o$, though. It should occur at 90°. Electron spectra proved being consistent with this finding. We discarded the original range of angles from 0 to 180° in our O_2 data and shifted the remains down.

waveplate in a nonlinear and asymmetric way; see figure 6.11(b). The problem was also clearly visible in the electron normalized difference distributions. We discarded data taken under the said range of alignment angles and used the remaining second region (shifted to start at 0°).

Potential phase shifts of beam components at mirrors or the beam combiner cannot explain the phenomenon, as these would not have violated our symmetry expectations. A possible explanation might be a wedge in the waveplate. If the latter was not hit centrally by the beam, a non-planar wave plate would have an angle-dependent thickness, leading to effects not necessarily periodic by 180° alignment / 90° waveplate angle. Interestingly, this problem did not re-occur in the N_2 measurement. We may have replaced the waveplate or re-aligned the beam between the measurements.
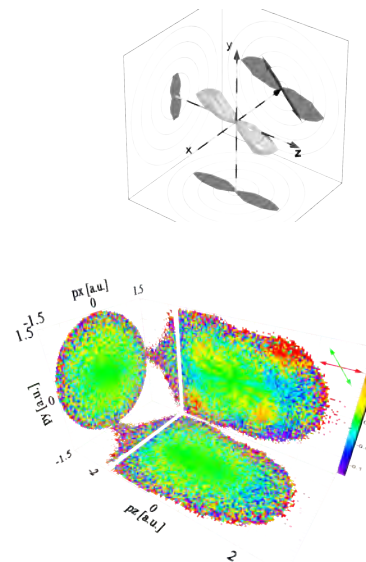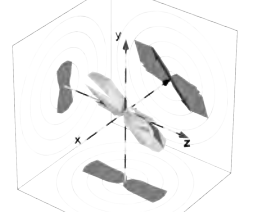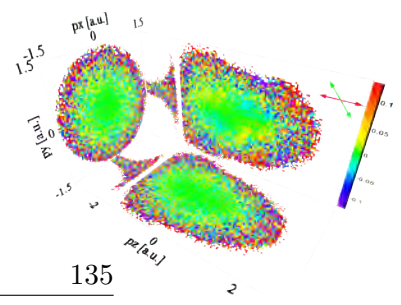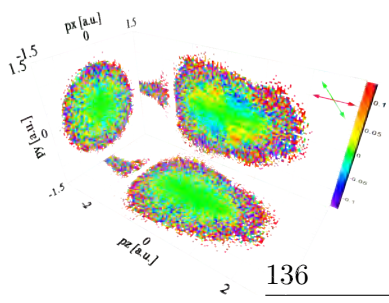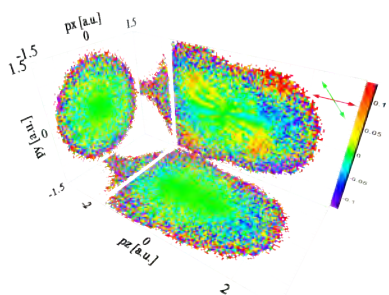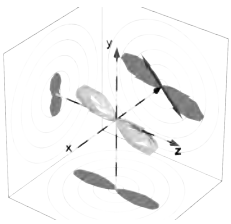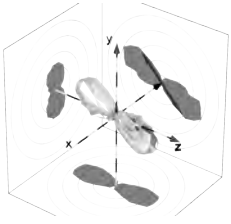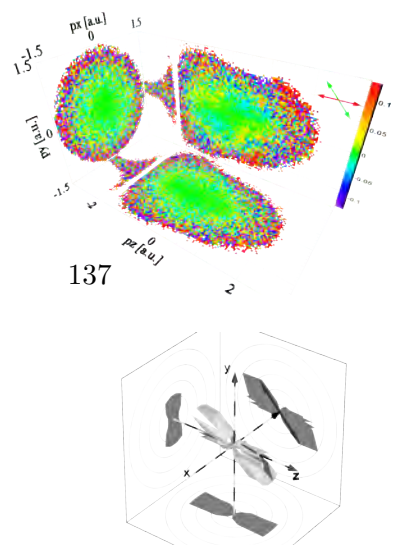
7. Conclusion and Outlook

Begin thus from the first act,
and proceed; and, in
conclusion, at the ill which
thou hast done, be troubled,
and rejoice for the good.

(Pythagoras)

We found two interesting and important effects in experiment A: Laser-induced electron tunneling and diffraction. Both may become useful to gain information about a molecule.

Tunneling from aligned molecules is a probe for the highest occupied molecular orbital. We intended to probe the orbitals of N_2 and O_2 from many different directions in experiment B. The idea was to perform a tomography-type reconstruction of the electron density in the orbital. It is not yet clear if we succeeded, as the data from N_2 do not look the way we expected. The intensity of ionizing probe pulses may have been too low for the tunneling picture to come into effect. However, we prove the basic concept in experiment A. There is hope it will be possible to observe the rearrangement of the electron cloud during a chemical reaction in real time in the future, using laser-induced electron tunneling.

Elastically re-scattered electrons carry an imprint of the ion's potential. In our experiments, simple double-slit models were sufficient to explain the basic structures in the electron distributions. It may be possible to refine the technique such that "real" elastic electron-ion scattering cross sections can be retrieved.

An important detail to be improved if structure should be probed is the kinetic energy of the electron upon re-scattering. The DeBroglie wavelength of our re-colliding electrons was way too long to retrieve high-resolution images.

The energy of re-colliding electrons increases linearly with the intensity I and proportional to the square of the wavelength λ of the ionizing radiation. However, the former is only true up to a saturation intensity. As soon as all electron population has ionized, the electric field in a laser pulse may well continue to rise - this does no more lead to an increased re-scattering momentum. Hence, increasing I will only allow for a limited improvement.

The second tunable parameter is λ. It is possible to convert the standard 800 nm wavelength of a titanium sapphire laser system down to a few μm by us-

ing an optical parametric amplifier (OPA). However, in a longer-wavelength electric field, the electron wavepacket will spend more time in the continuum before re-scattering. This gives it more time to expand laterally, leading to depletion of the part actually re-encountering with the ion. The reduced re-scattering probability will be an experimental challenge with the detection technique we used. Spectrometers designed to mask unwanted low-energy electrons will alleviate this drawback.
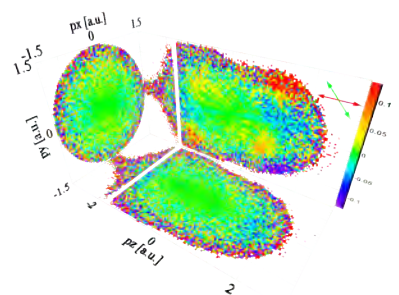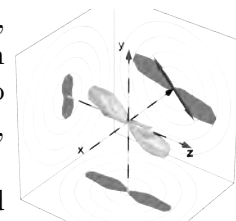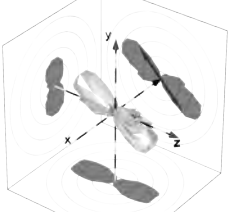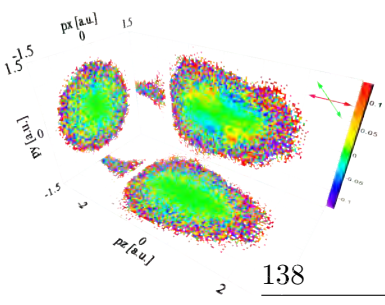
The temporal resolution of both tunneling and re-scattering / diffraction is solely defined by the ionizing laser radiation. Hence, it will automatically benefit from all progress in the generation of ever-shorter laser pulses.

We prove two concepts for a new kind of ultrafast spectroscopy. The future will show whether they will find a place in the real world.
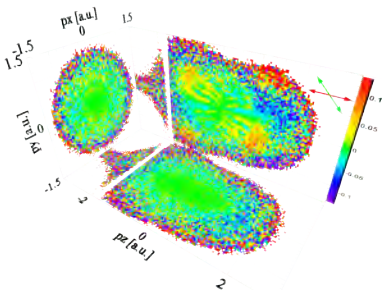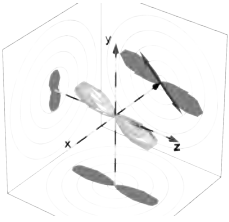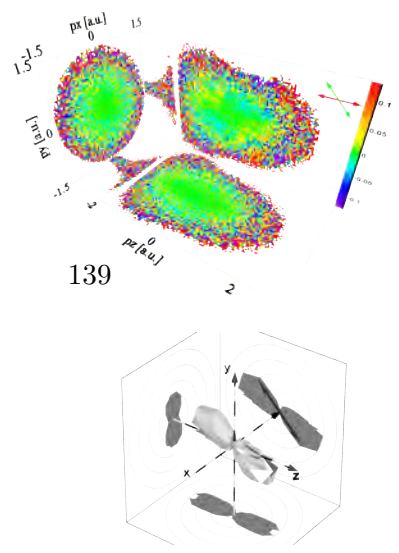
A. Experiment A: Miscellaneous

A.1. Calibration Spectra

A.1.1. Ion Time of Flight
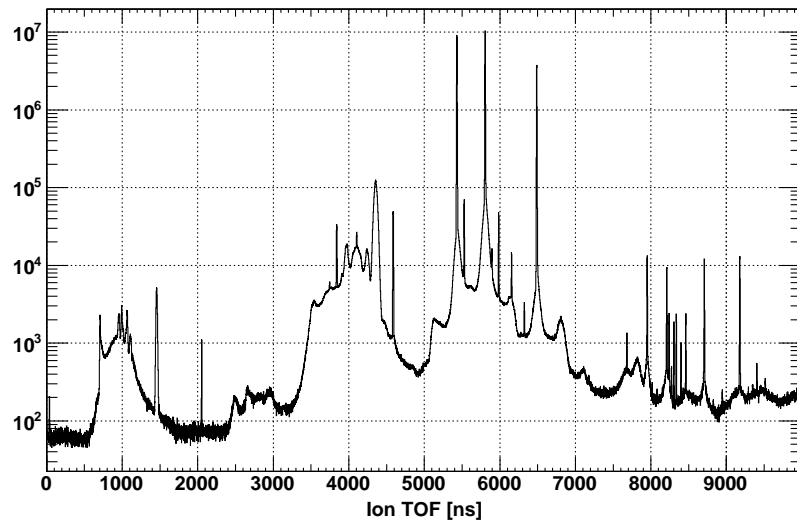
Figure A.1.: Experiment A: Ion time of flight (TOF) distribution. Only the first detected ion is plotted. A version of this spectrum with the TOF axis converted to mass / charge ratios is shown in figure 5.1.
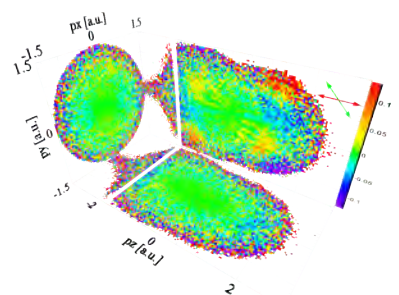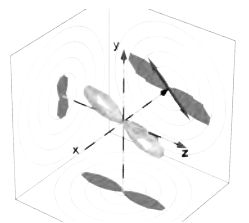
A.1.2. Photoion-Photoion Coincidence
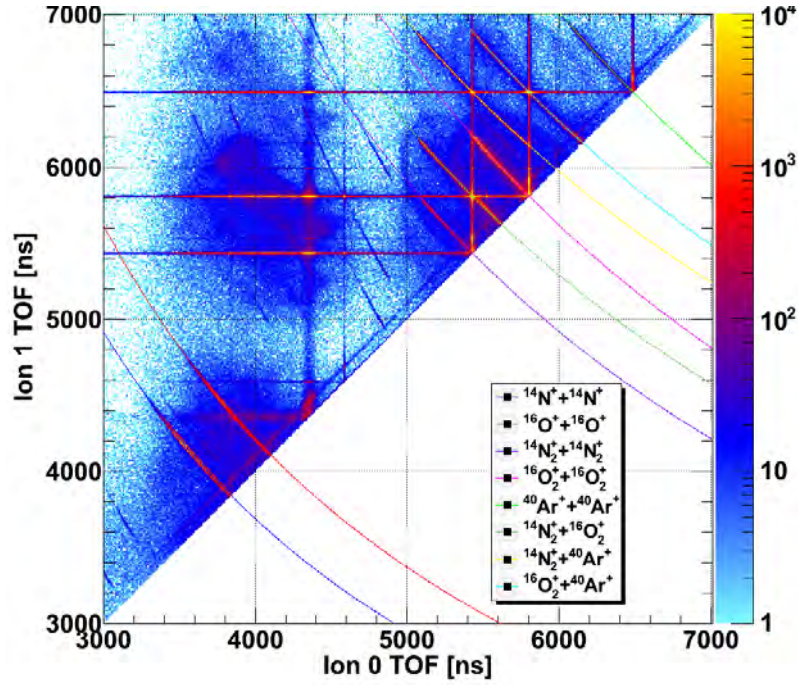
Figure A.2.: Experiment A: Photoion-photoion coincidence (PIPICO) spectrum. The time of flight of the ion reaching the detector first (*horizontal*) is plotted versus the TOF of the second (*vertical* axis). Correlated fragments lead to bent lines. Calculated values for the combinations of ions given in the legend are plotted as thin lines. Traces of various further species and breakup channels are visible. A version of this spectrum with the axes converted to mass / charge ratios is shown in figure A.3.
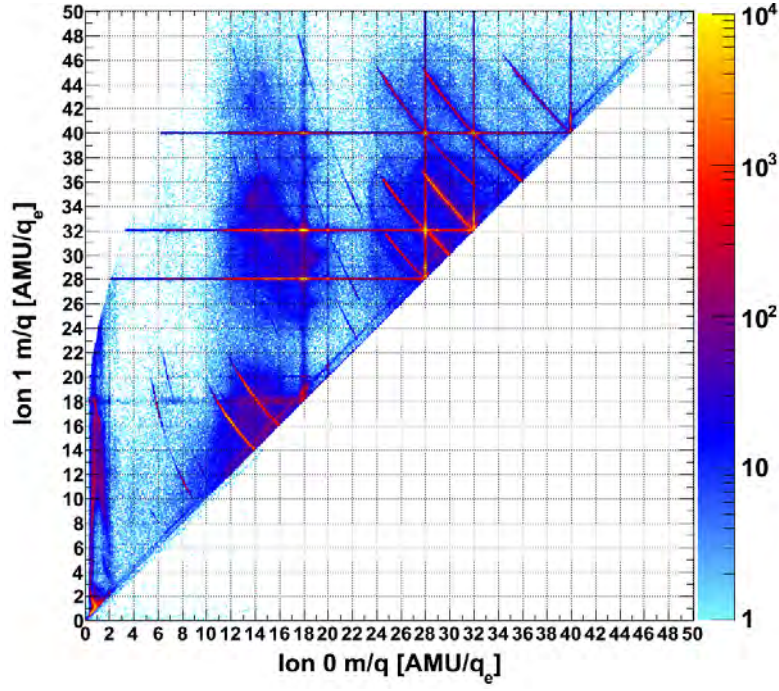
Figure A.3.: Experiment A: The photoion-photoion coincidence spectrum in figure A.2, converted to mass / charge ratios. The values are valid as such only for ions starting with zero velocity in the time of flight direction. This is the case for PIPICO lines extending to the diagonal cutoff, in the point where the cutoff is reached.

(a) $N^+ + N^+$

(b) $O^+ + O^+$
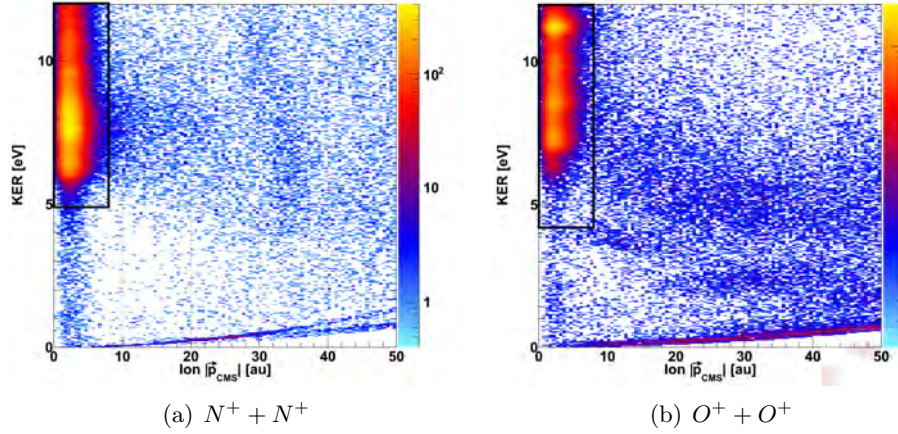
Figure A.4.: Experiment A, Coulomb exploded fragments: The ion center of mass momentum $|\vec{p}_{CMS}| = |\vec{p}_{ion1} + \vec{p}_{ion2}|$ (*horizontal* axis) is plotted versus the kinetic energy release (KER, *vertical* axis) of the breakup. Only events lying within the regions enclosed by the black boxes are selected for further analysis. This is a sufficient condition to identify the species.

A.2. Revival Structure
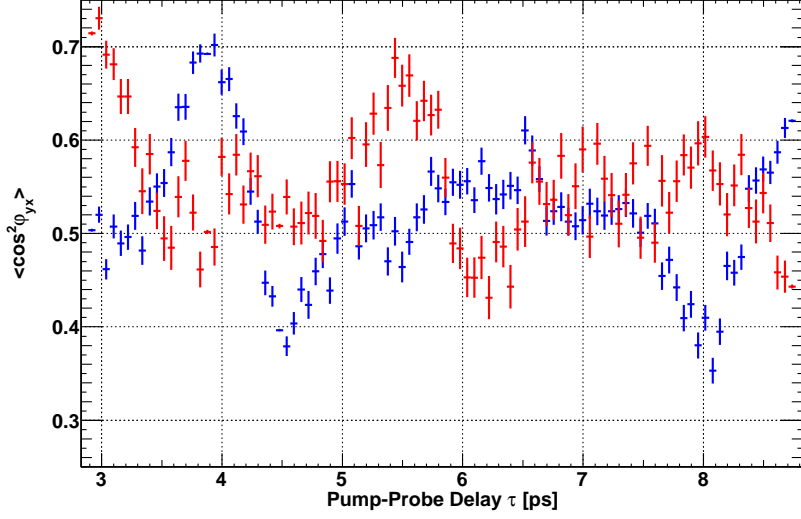
Figure A.5.: Experiment A: Dependence of the alignment parameter ($< \cos^2 \varphi_{yx} >$, *vertical*) on the delay τ between the aligning and ionizing pulse (*horizontal* axis). *Blue* data points: $N^+ + N^+$, *red*: $O^+ + O^+$ fragments. Error bars are statistical. Perfect alignment would correspond to $< \cos^2 \varphi_{yx} >= 1$, anti-alignment to $< \cos^2 \varphi_{yx} >= 0$ and a random distribution leads to $< \cos^2 \varphi_{yx} >= 0.5$. Data were recorded during the main experiment. The delays used are: 2.949 ps (O_2 aligned), 3.856 ps (N_2 aligned), 4.490 ps (N_2 anti-aligned) and 8.759 ps (O_2 anti-aligned). The respective data points have minimum error bars due to improved statistics. All other delays only occurred while the translation stage was traveling, leading to relatively large statistical errors.

A.3. Two-Dimensional Spectra Behind 3D Plots

From time to time, two-dimensional plots with a color-coded third axis can give a more exact picture than pseudo three-dimensional representations. This is why, for each three-dimensional plot in chapter 5.1, the corresponding color plots are given here.

A.3.1. Correlated Ionic Fragments

(a) $N^+ + N^+$ from Aligned N_2

(b) $N^+ + N^+$ from Anti-Aligned N_2

(c) $O^+ + O^+$ from Aligned O_2

(d) $O^+ + O^+$ from Anti-Aligned O_2
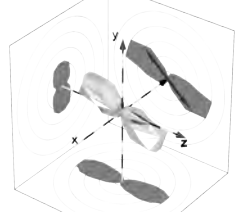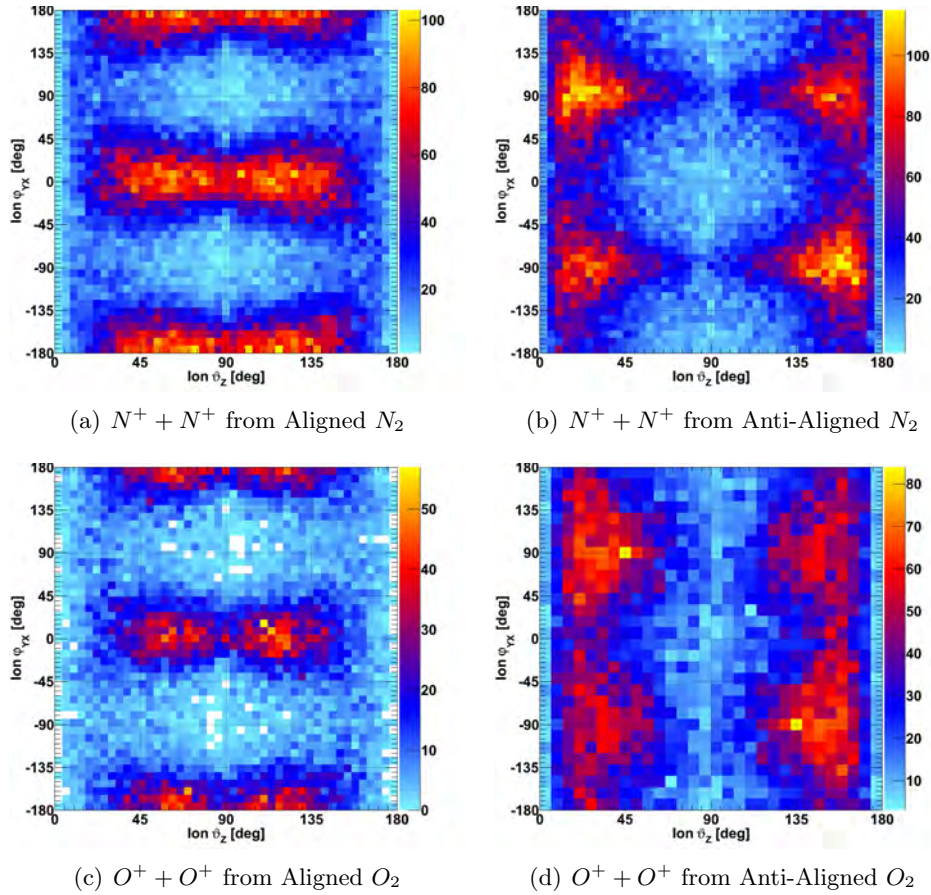
Figure A.6.: Experiment A: Distributions of correlated ionic fragments as specified in the figure subscripts in spherical coordinates. Solid angle is not normalized (for this, see figure A.7). Three-dimensional representations are given in figure 5.2. The conditions applied are summarized in table 5.3. The probe polarization is along $\vartheta_z = 0^o$, while aligning pulses are polarized along $\vartheta_z = 90^o, \varphi_{yx} = 0^o$.
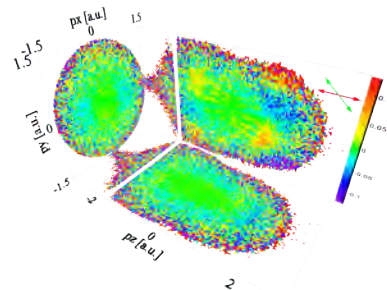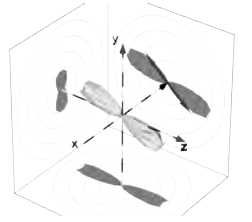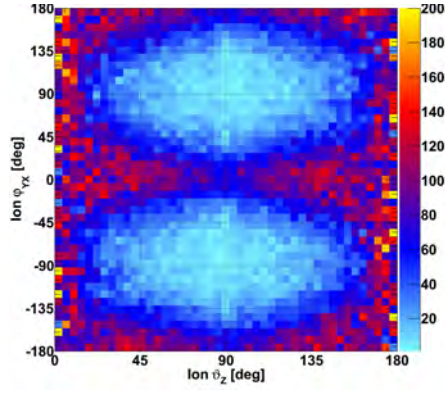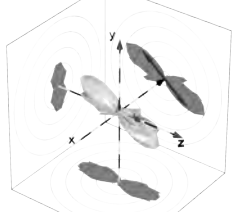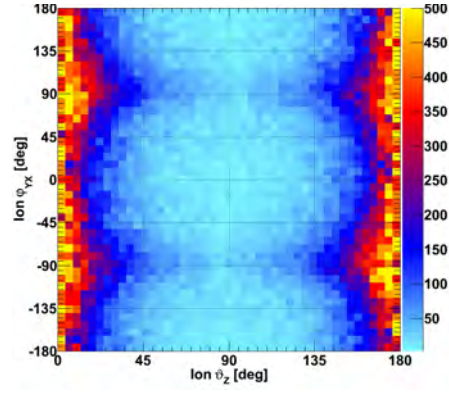
(a) $N^+ + N^+$ from Aligned N_2

(b) $N^+ + N^+$ from Anti-Aligned N_2
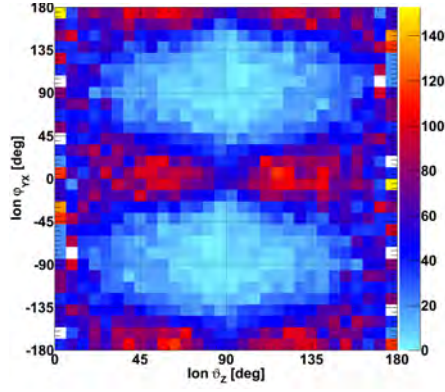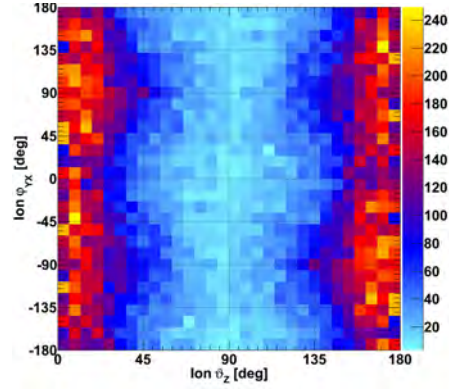
(c) $O^+ + O^+$ from Aligned O_2

(d) $O^+ + O^+$ from Anti-Aligned O_2

Figure A.7.: Experiment A: Same fragment distributions in spherical coordinates as in figure A.6 but the solid angle element is normalized out (cf. chapter 4.3.3).
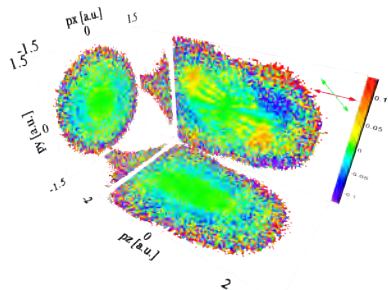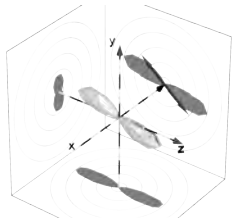
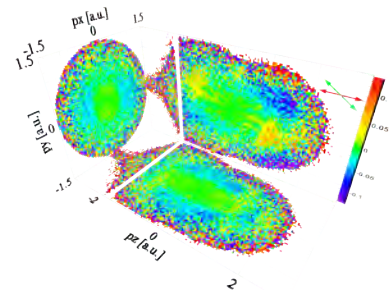## A.3.2. Electrons Correlated with Molecular Single Ions
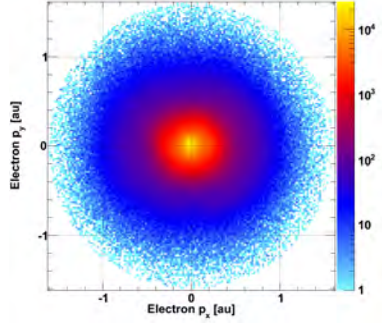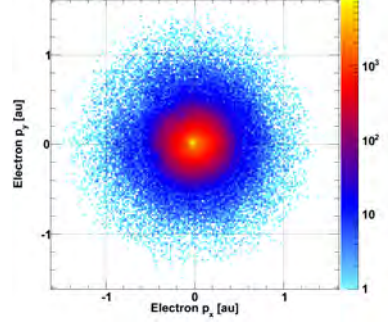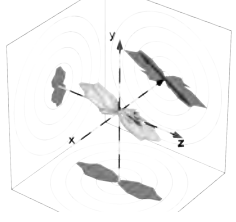

(a) N_2 Aligned $x - y$ Projection
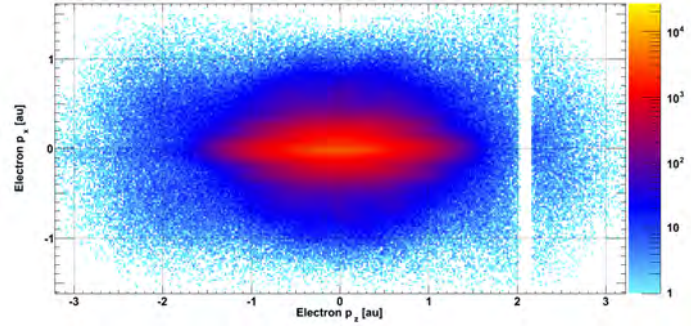
(b) N_2 Aligned $z - x$ Projection
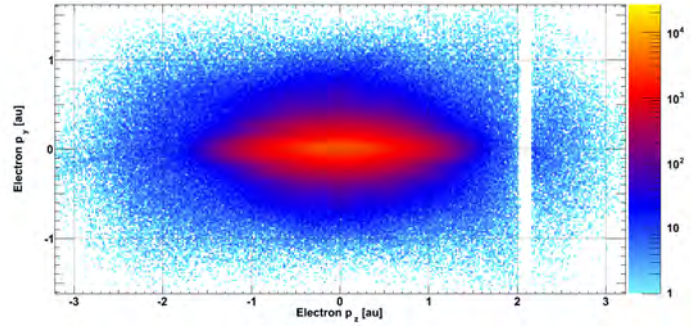
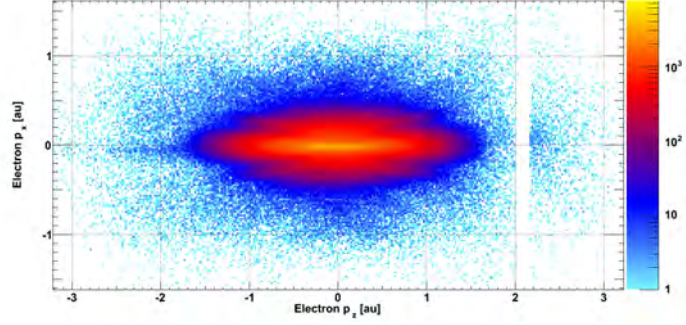(c) N_2 Aligned $z - y$ Projection

Figure A.8.: Experiment A: Momentum distributions of electrons correlated with N_2^+ ions. Aligned case. Projections were made with the respective third dimension being integrated over. Probe pulses are polarized along the z axis while the polarization of aligning pulses is along y. Reproduction of projections in figure 5.4(a).
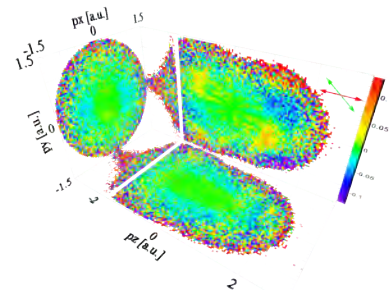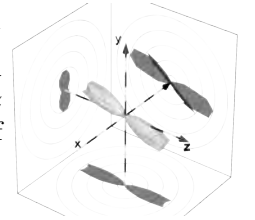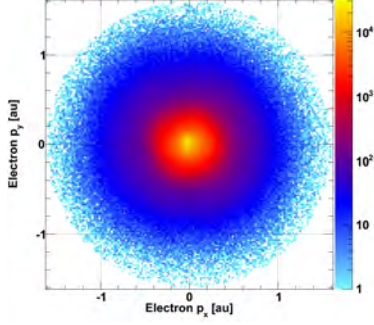
(a) N_2 Anti-Aligned $x - y$ Projection
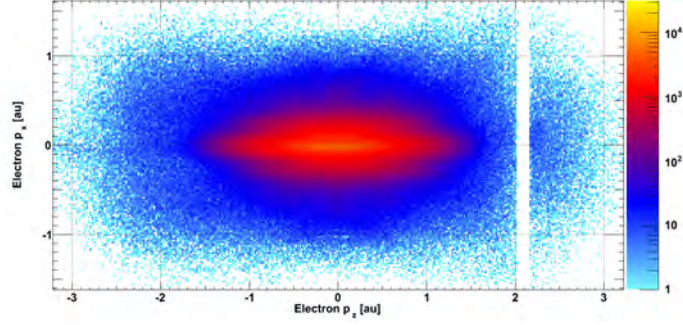
(b) N_2 Anti-Aligned $z - x$ Projection
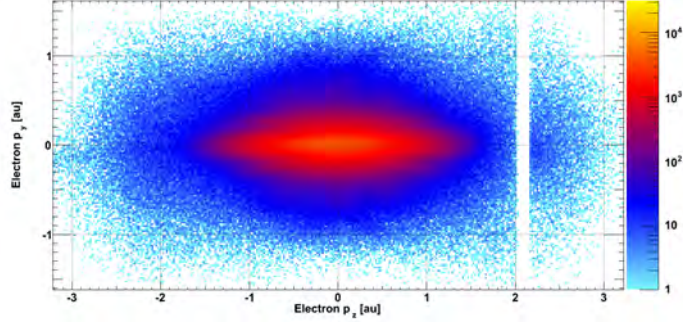
(c) N_2 Anti-Aligned $z - y$ Projection

Figure A.9.: Experiment A: Momentum distributions of electrons correlated with N_2^+ ions. Anti-Aligned case. Projections were made with the respective third dimension being integrated over. Probe pulses are polarized along the z axis while the polarization of aligning pulses is along y. Reproduction of projections in figure 5.4(b).
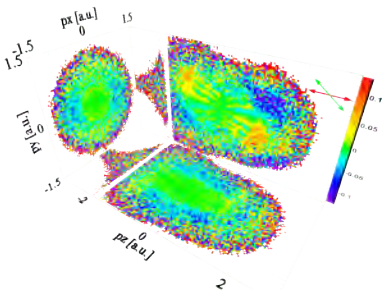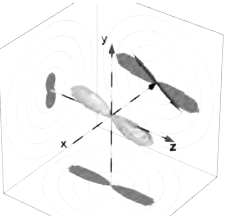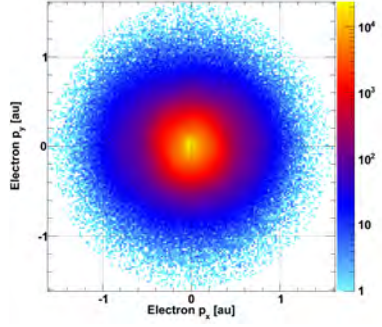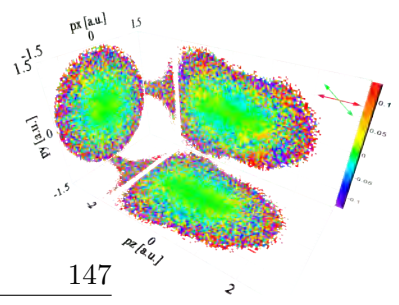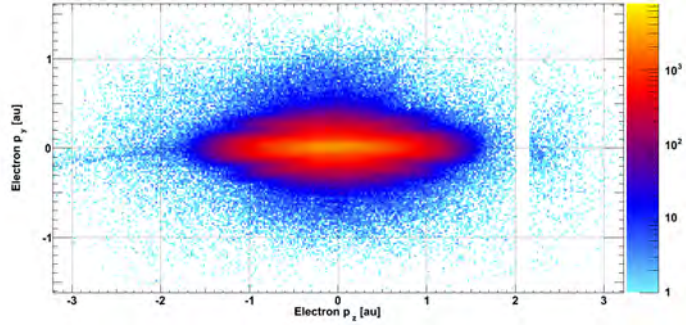
(a) O_2 Aligned $x - y$ Projection
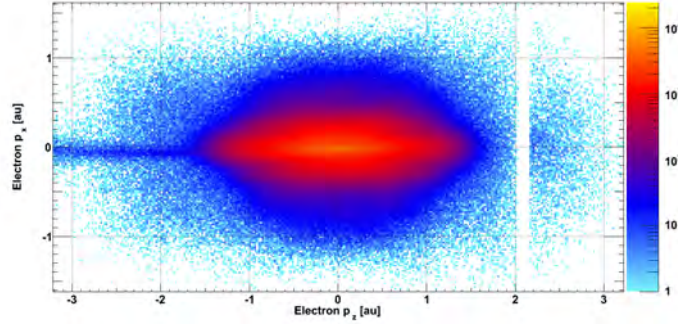
(b) O_2 Aligned $z - x$ Projection
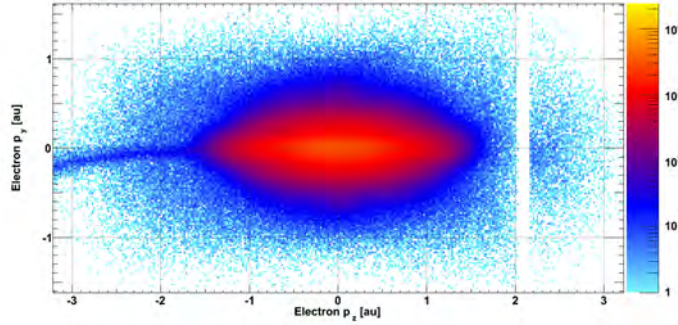
(c) O_2 Aligned $z - y$ Projection

Figure A.10.: Experiment A: Momentum distributions of electrons correlated with O_2^+ ions. Aligned case. Projections were made with the respective third dimension being integrated over. Probe pulses are polarized along the z axis while the polarization of aligning pulses is along y. Reproduction of projections in figure 5.4(c).
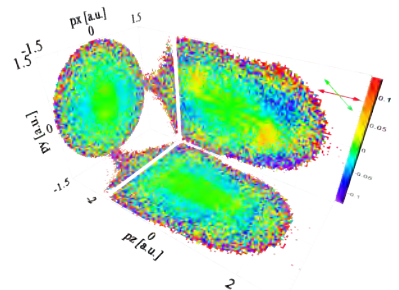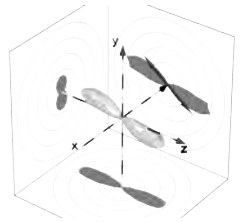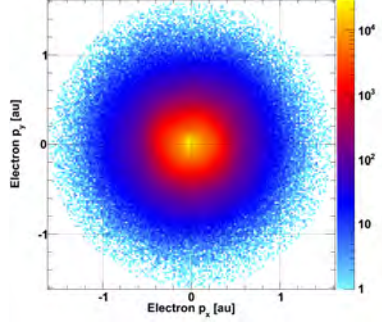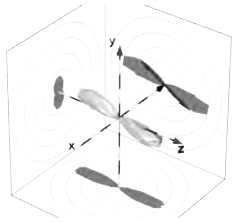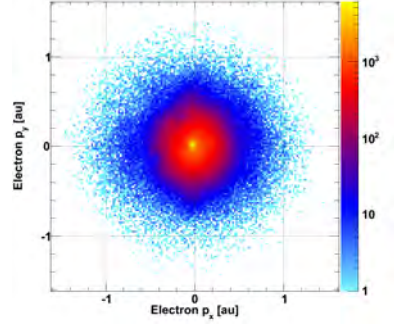
(a) O_2 Anti-Aligned $x - y$ Projection
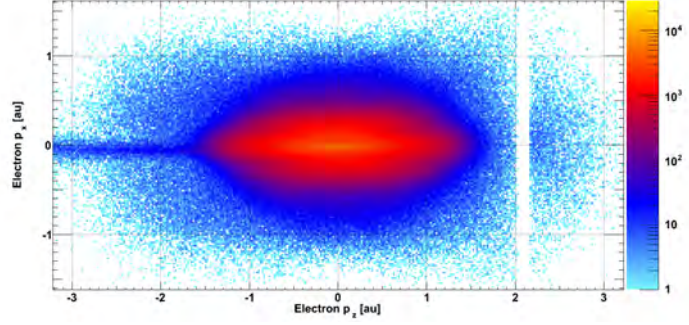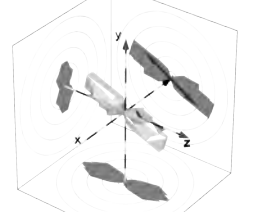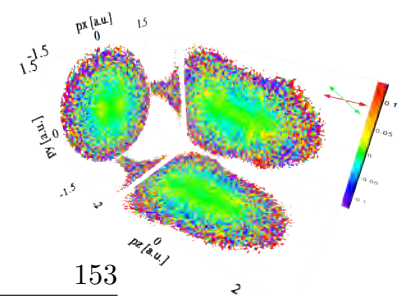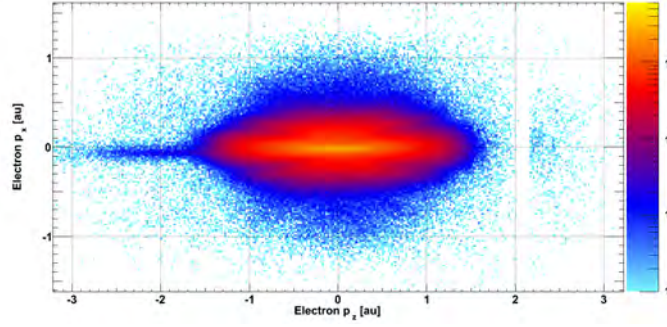

(b) O_2 Anti-Aligned $z - x$ Projection
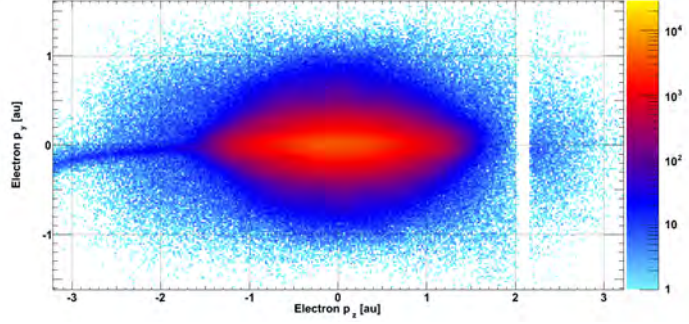
(c) O_2 Anti-Aligned $z - y$ Projection

Figure A.11.: Experiment A: Momentum distributions of electrons correlated with O_2^+ ions. Anti-Aligned case. Projections were made with the respective third dimension being integrated over. Probe pulses are polarized along the z axis while the polarization of aligning pulses is along y. Reproduction of projections in figure 5.4(d).
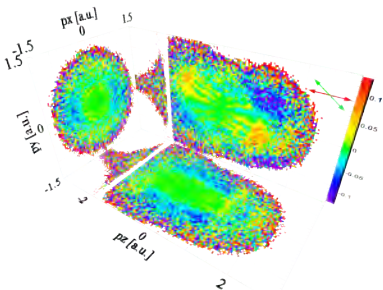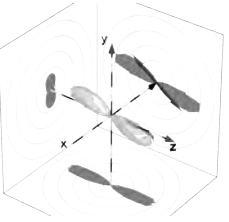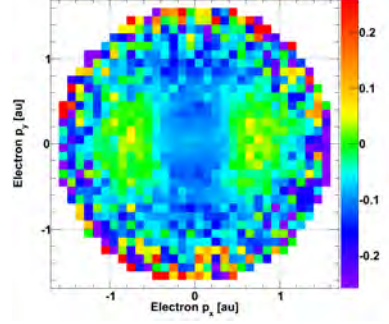
(a) N_2 Normalized Differences $x - y$ Projection
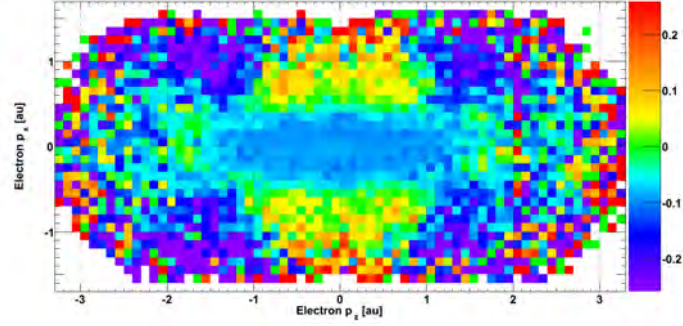
(b) N_2 Normalized Differences $z - x$ Projection
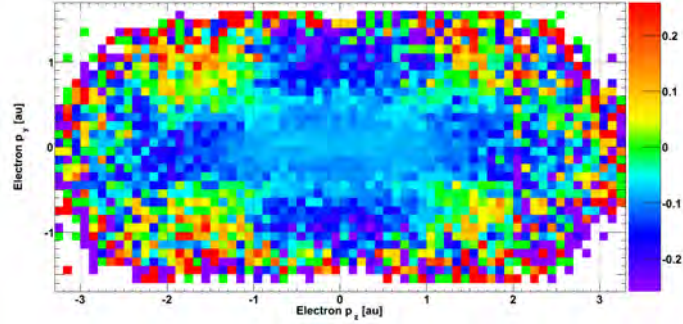
(c) N_2 Normalized Differences $z - y$ Projection

Figure A.12.: Experiment A: Normalized differences of the electron momentum distributions in figures A.8 and A.9. Electrons are correlated with N_2^+. Projections were made with the respective third dimension being integrated over before calculating normalized differences. Probe pulses are polarized along the z axis while the polarization of aligning pulses is along y. Reproduction of projections in figure 5.5(a).
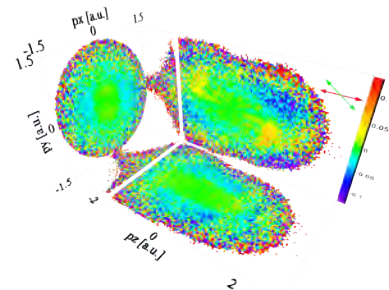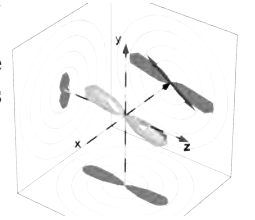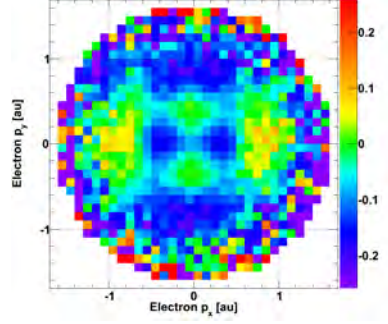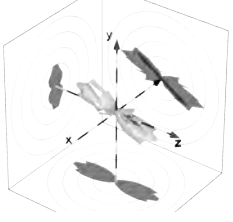
(a) O_2 Normalized Differences $x - y$ Projection
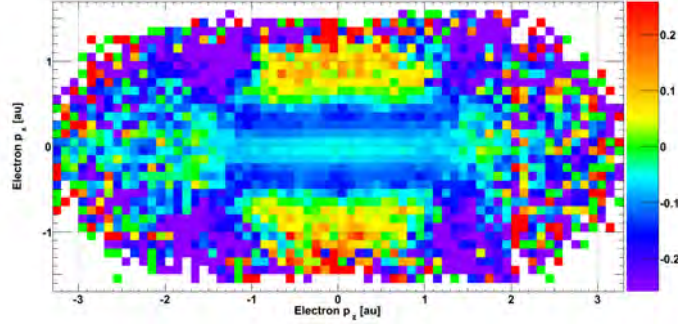
(b) O_2 Normalized Differences $z - x$ Projection
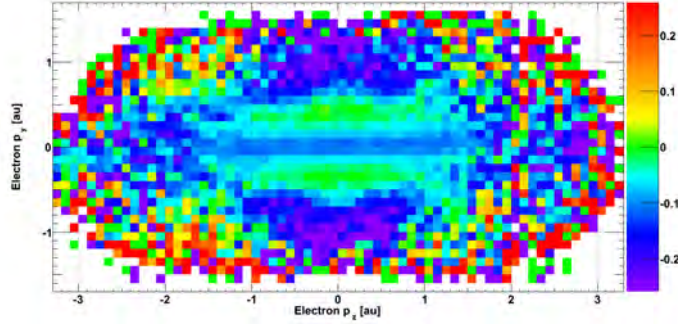
(c) O_2 Normalized Differences $z - y$ Projection

Figure A.13.: Experiment A: Normalized differences of the electron momentum distributions in figures A.10 and A.11. Electrons are correlated with O_2^+. Projections were made with the respective third dimension being integrated over before calculating normalized differences. Probe pulses are polarized along the z axis while the polarization of aligning pulses is along y. Reproduction of projections in figure 5.5(b).
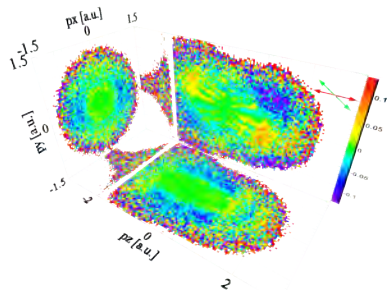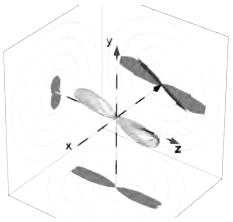
A.4. Spectra of Electrons from Single Ionization: Cut
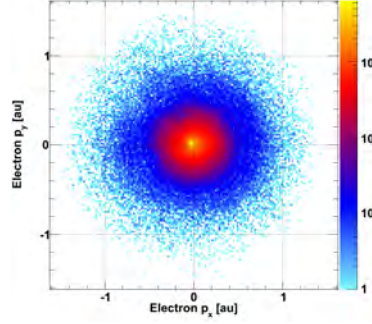
(a) N_2 Aligned $x - y$ Projection. $|p_z| < 0.1$ a.u.
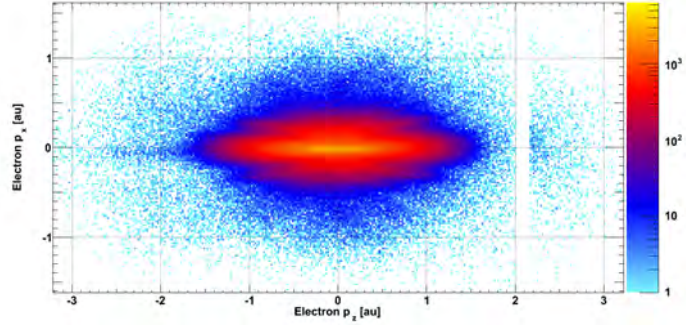
(b) N_2 Aligned $z - x$ Projection. $|p_y| < 0.1$ a.u.
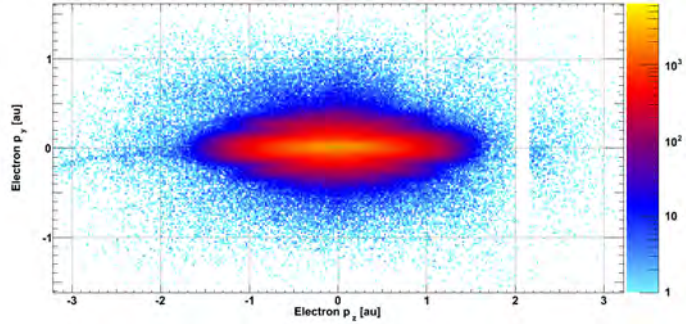
(c) N_2 Aligned $z - y$ Projection. $|p_x| < 0.1$ a.u.

Figure A.14.: Experiment A: Momentum distributions of electrons correlated with N_2^+ ions. Aligned case. Projections were made with the respective third dimension being restricted to ± 0.1 a.u.. Probe pulses are polarized along the z axis while the polarization of aligning pulses is along y.
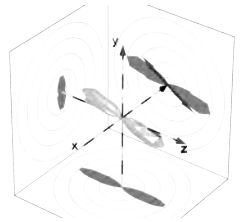
(a) N_2 Anti-Aligned $x - y$ Projection. $|p_z| < 0.1$ a.u.

(b) N_2 Anti-Aligned $z - x$ Projection. $|p_y| < 0.1$ a.u.

(c) N_2 Anti-Aligned $z - y$ Projection. $|p_x| < 0.1$ a.u.

Figure A.15.: Experiment A: Momentum distributions of electrons correlated with N_2^+ ions. Anti-Aligned case. Projections were made with the respective third dimension being restricted to ± 0.1 a.u.. Probe pulses are polarized along the z axis while the polarization of aligning pulses is along y.
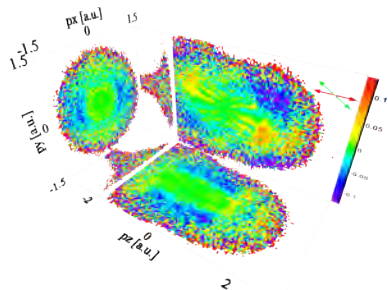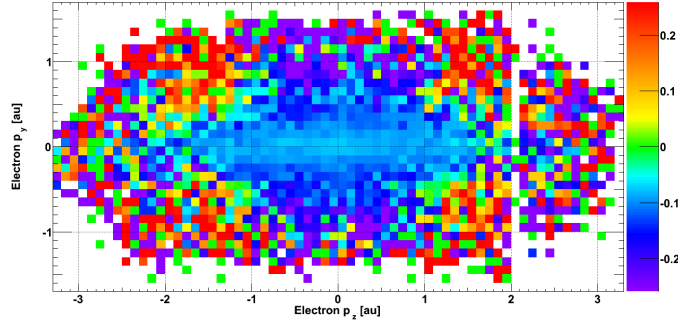
(a) O_2 Aligned $x - y$ Projection. $|p_z| < 0.1$ a.u.

(b) O_2 Aligned $z - x$ Projection. $|p_y| < 0.1$ a.u.
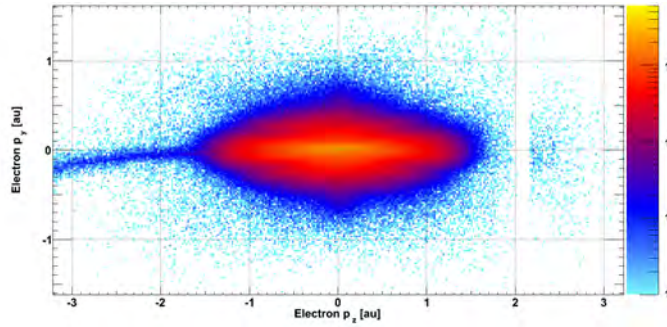
(c) O_2 Aligned $z - y$ Projection. $|p_x| < 0.1$ a.u.

Figure A.16.: Experiment A: Momentum distributions of electrons correlated with O_2^+ ions. Aligned case. Projections were made with the respective third dimension being restricted to ± 0.1 a.u.. Probe pulses are polarized along the z axis while the polarization of aligning pulses is along y.
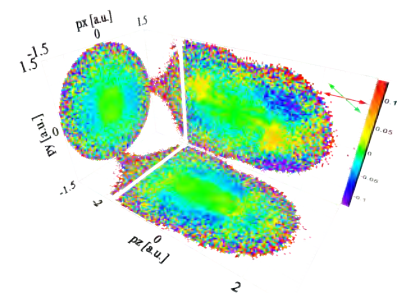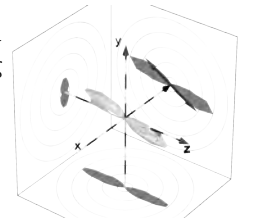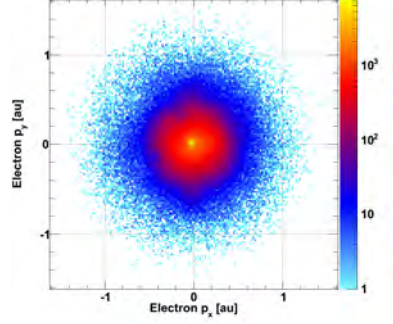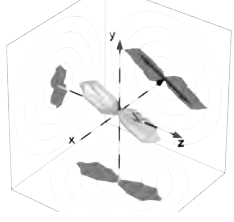
(a) O_2 Anti-Aligned $x - y$ Projection. $|p_z| < 0.1$ a.u.
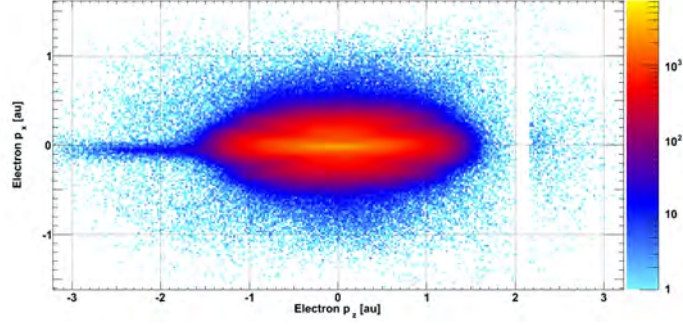
(b) O_2 Anti-Aligned $z - x$ Projection. $|p_y| < 0.1$ a.u.
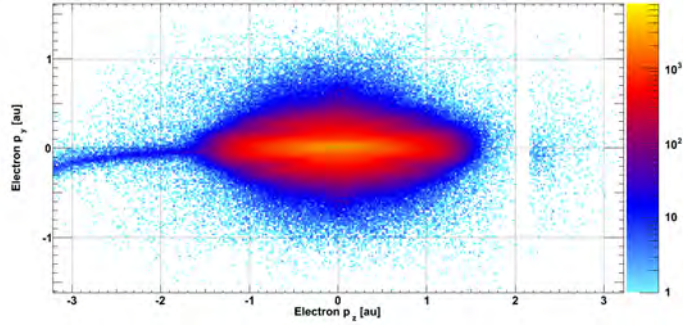
(c) O_2 Anti-Aligned $z - y$ Projection. $|p_x| < 0.1$ a.u.

Figure A.17.: Experiment A: Momentum distributions of electrons correlated with O_2^+ ions. Anti-Aligned case. Projections were made with the respective third dimension being restricted to ± 0.1 a.u.. Probe pulses are polarized along the z axis while the polarization of aligning pulses is along y.
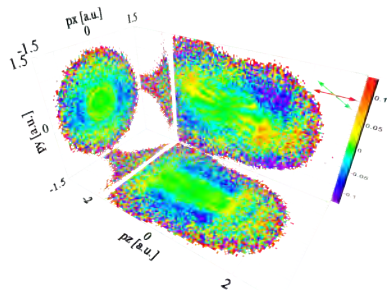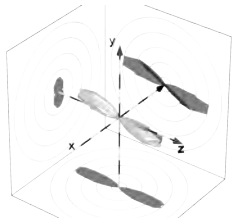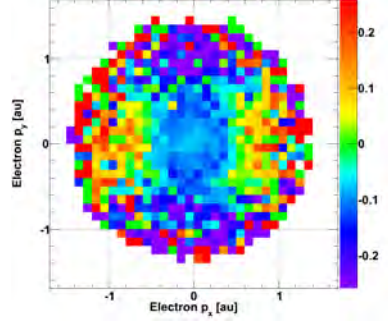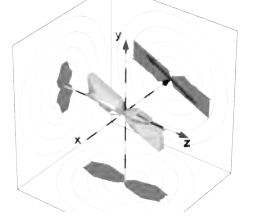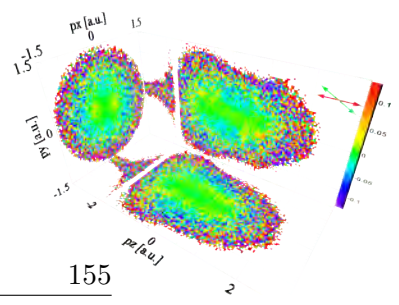
(a) N_2 Normalized Differences: $x - y$ Projection. $|p_z| < 0.1$ a.u.
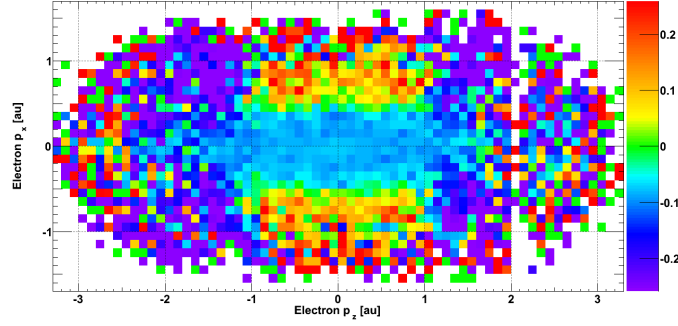
(b) N_2 Normalized Differences: $z - x$ Projection. $|p_y| < 0.1$ a.u.

(c) N_2 Normalized Differences: $z - y$ Projection. $|p_x| < 0.1$ a.u.

Figure A.18.: Experiment A: Normalized differences of the electron momentum distributions in figures A.14 and A.15. Electrons are correlated with N_2^+. Projections were made by restricting the respective third dimension to ± 0.1 a.u. before calculating normalized differences. Probe pulses are polarized along the z axis while the polarization of aligning pulses is along y.
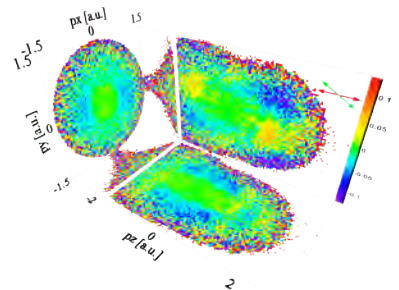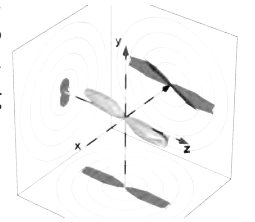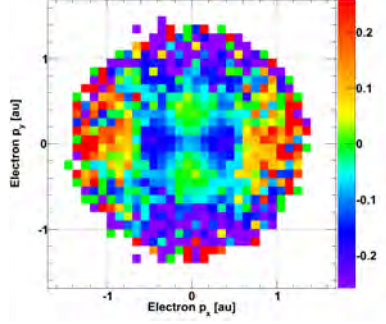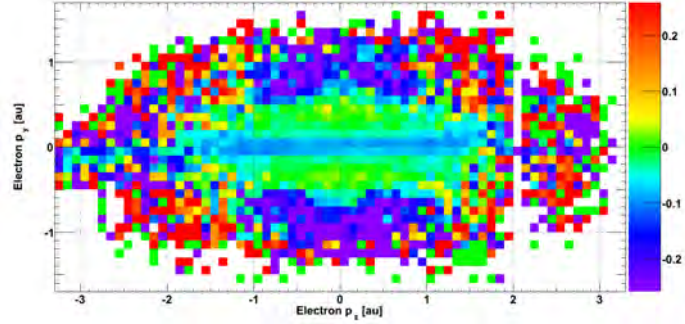
(a) O_2 Normalized Differences $x - y$ Projection- $|p_z| < 0.1$ a.u.
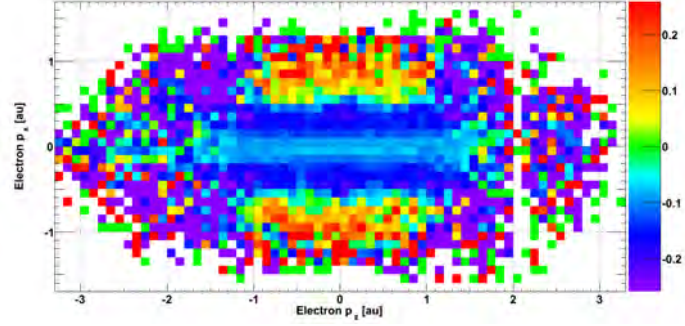
(b) O_2 Normalized Differences $z - x$ Projection. $|p_y| < 0.1$ a.u.

(c) O_2 Normalized Differences $z - y$ Projection. $|p_x| < 0.1$ a.u.

Figure A.19.: Experiment A: Normalized differences of the electron momentum distributions in figures A.16 and A.17. Electrons are correlated with O_2^+. Projections were made by restricting the respective third dimension to ± 0.1 a.u. before calculating normalized differences. Probe pulses are polarized along the z axis while the polarization of aligning pulses is along y.
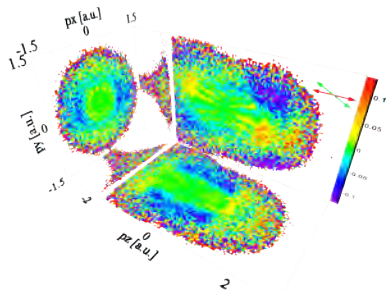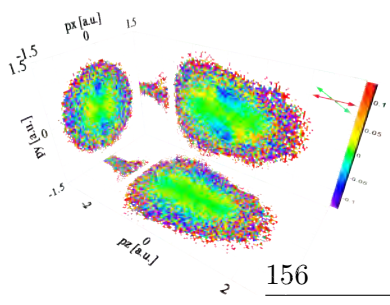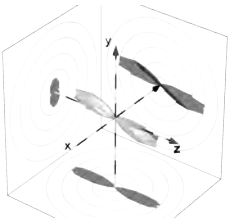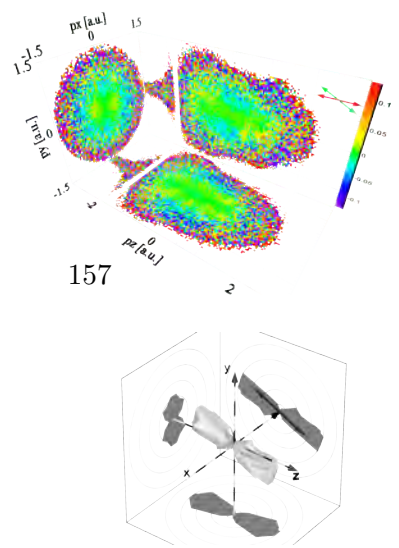
B. Experiment B: Miscellaneous

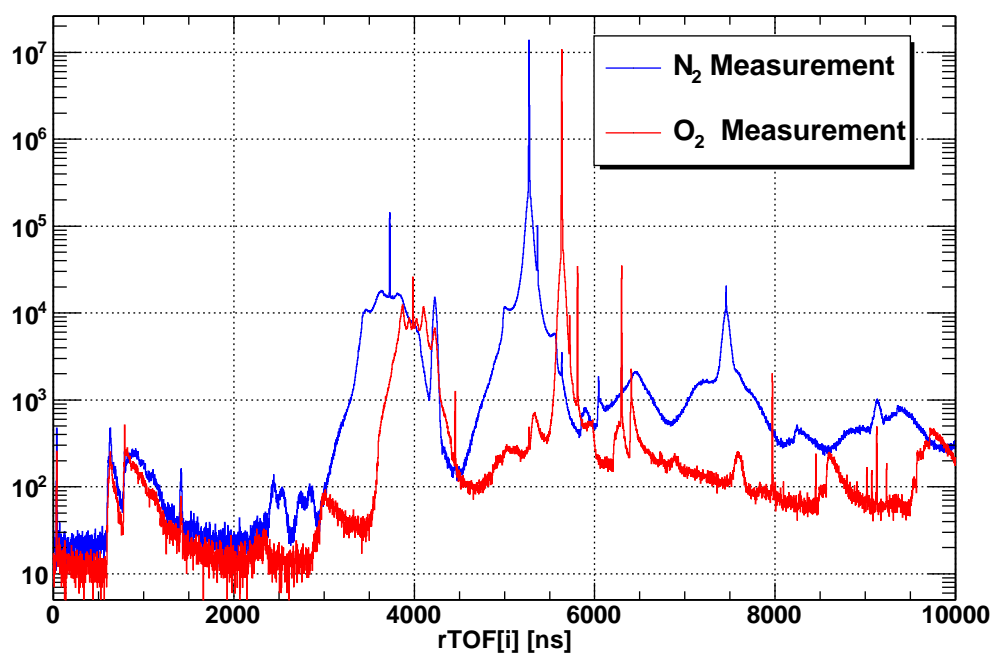## B.1. Calibration Spectra
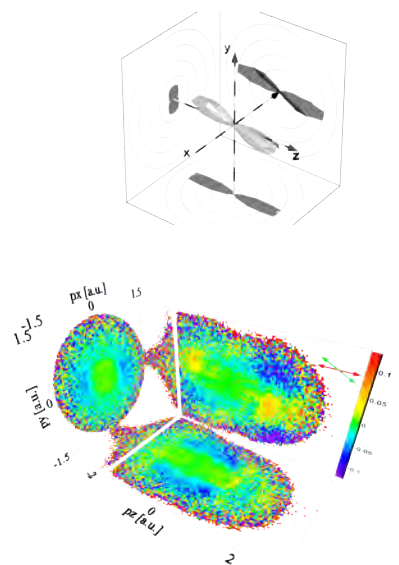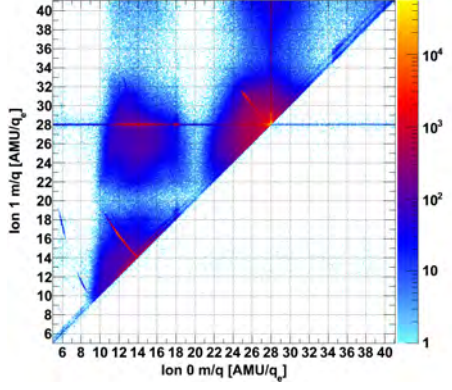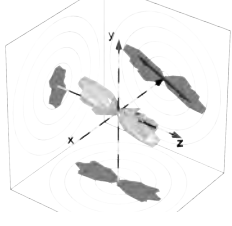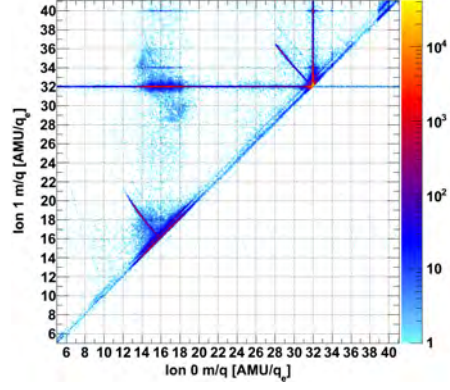
B.1.1. Ion Time of Flight

Figure B.1.: Experiment B: Time of flight (TOF) distribution of ions. The same is shown in figure 5.10 with the horizontal axis converted to mass/charge ratios.

B.1.2. Photoion-Photoion Coincidence

(a) Nitrogen Measurement

(b) Oxygen Measurement

Figure B.2.: Experiment B: Photoion-photoion coincidence spectra: Mass-charge ratio calculated according to equation (4.1) of first (*horizontal*) versus second detected ion (*vertical* axis).
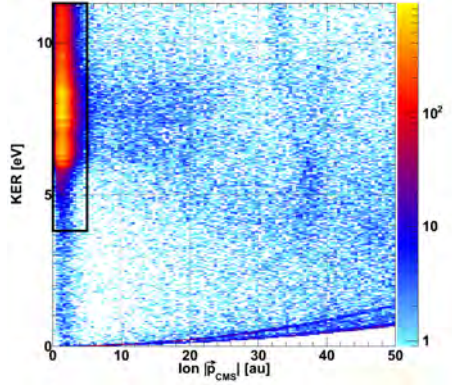

(a) $N^+ + N^+$
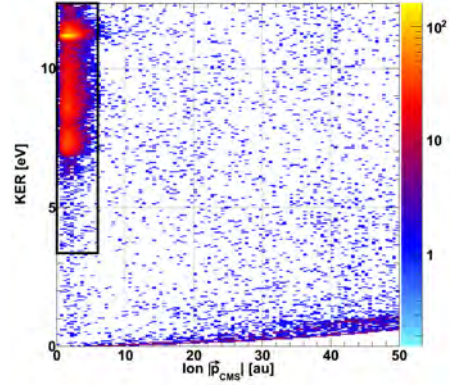
(b) $O^+ + O^+$

Figure B.3.: Distributions of ion center of mass momentum magnitude (horizontal) versus kinetic energy release (vertical axis). (a): N_2 measurement. Calculations are based on the assumption that every ion is N^+. Same for the O_2 measurement in figure (b) accordingly. Only events lying within the regions inside the black boxes are accepted as coincident.
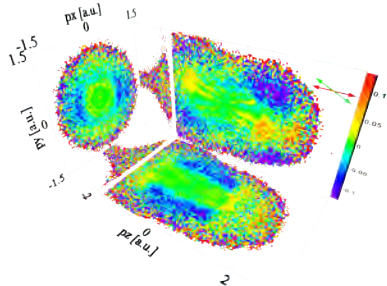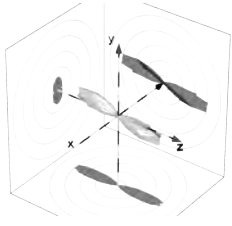
B.2. Electrons Spectra

B.2.1. Cartesian Coordinates - Third Dimension Integrated Over
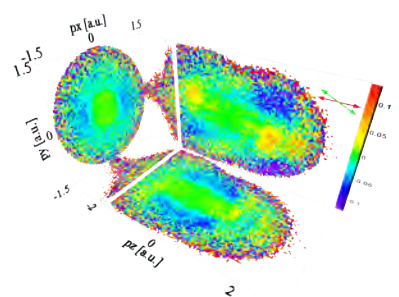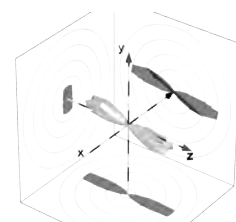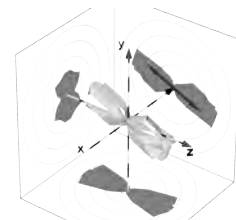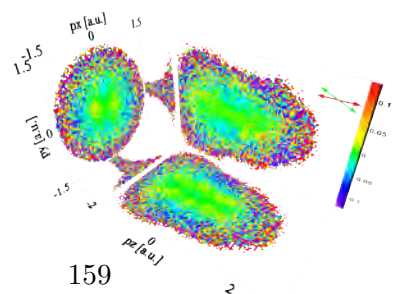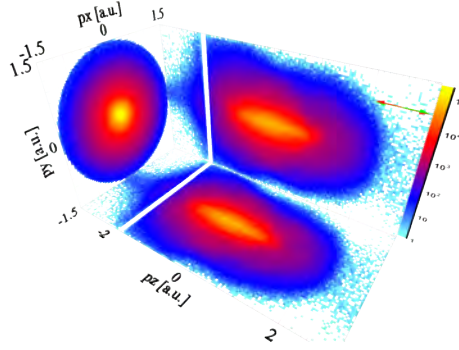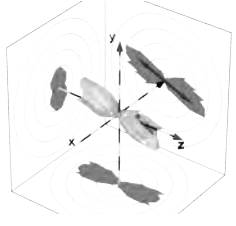
(a) N_2 with $\phi_{al} = 1^o \pm 3^o$
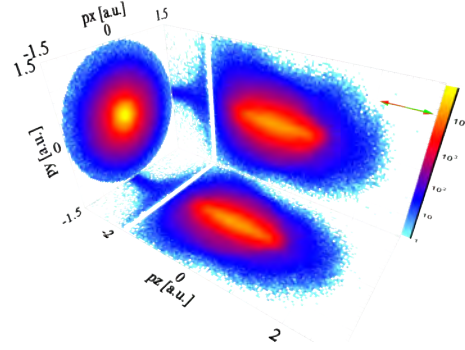
(b) O_2 with $\phi_{al} = 1^o \pm 5^o$
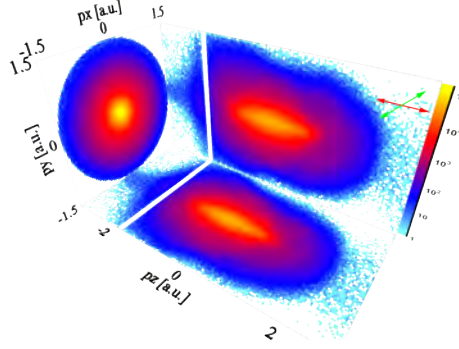
(c) N_2 with $\phi_{al} = 45^o \pm 3^o$
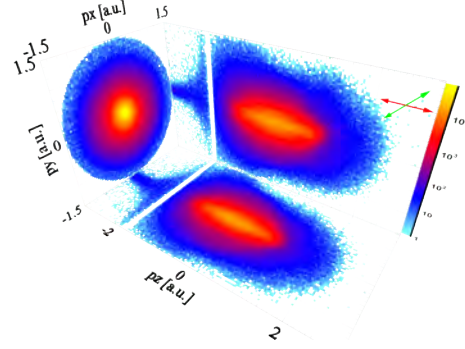
(d) O_2 with $\phi_{al} = 45^o \pm 5^o$
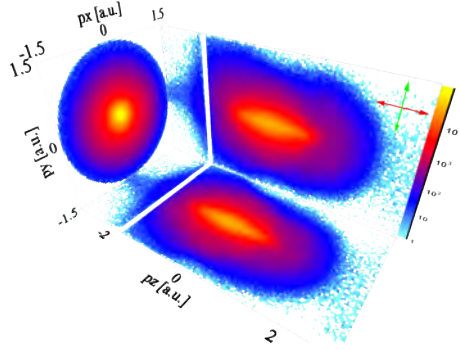
(e) N_2 with $\phi_{al} = 89^o \pm 3^o$
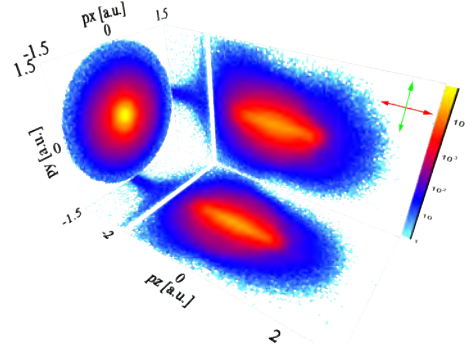
(f) O_2 with $\phi_{al} = 89^o \pm 5^o$

Figure B.4.: Electron momentum distributions in a pseudo-3D representation. We assume that the majority of these electrons is correlated with either N_2^+ (column on the *left*) or O_2^+ ions (*right*). Alignment angles were added over a range of $\pm 3^o$ (N_2) or $\pm 5^o$ (O_2), respectively. For each projection in a plot the respective third dimension was integrated over. The direction of the aligning pulse polarization is denoted by the green arrow while the red arrow is along the probe polarization. The white stripes around $p_z = -2$ a.u. are "wiggles" (artifacts). All histograms show a great deal of similarity with each other and with their counterparts from experiment A, shown in figure 5.4.
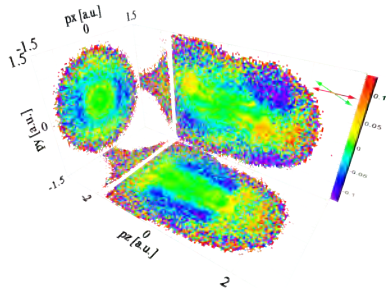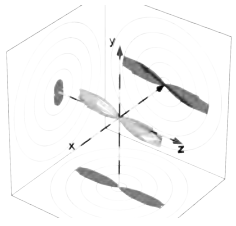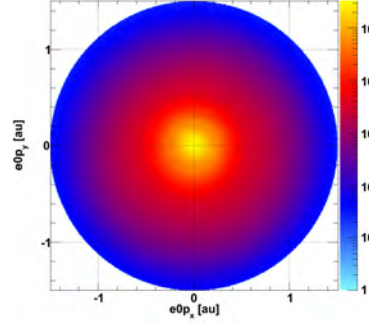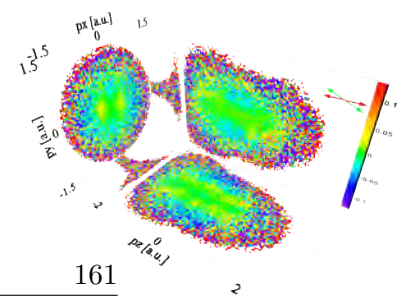
(a) N_2: $x - y$ - $|p_z| < 4$ a.u.

(b) N_2: $z - x$ - $|p_y| < 1.5$ a.u.

(c) N_2: $z - y$ - $|p_x| < 1.5$ a.u.

Figure B.5.: Experiment B, N_2 measurement: Electron momentum distributions. Out-of-plane momenta were integrated over within the full available ranges. Sum over all alignment angles without normalization. These are the two-dimensional components of figure 5.13(a). With a different pixel size, similar distributions were used as reference for the normalized differences with unrestricted out-of-plane momenta, such as the N_2 spectra in figure 5.16 and the flip-book on odd-numbered pages. Probe pulses are polarized along the z axis while the polarization of aligning pulses is rotated in the $z - y$ plane.
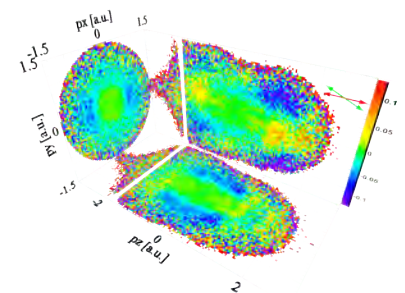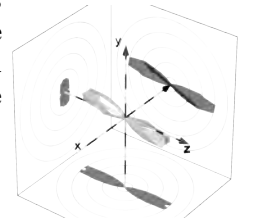
(a) N_2 with $\phi_{al} = 1^o \pm 3^o$: $x - y$ Projection.
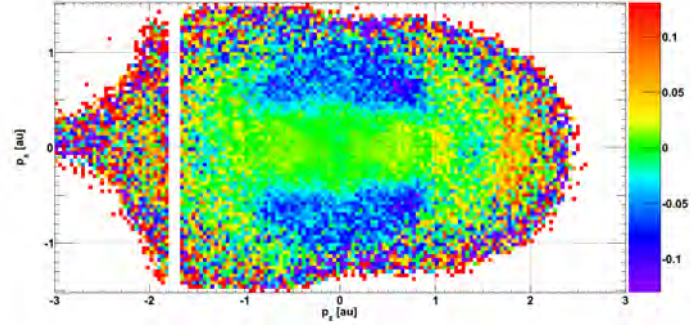
(b) N_2 with $\phi_{al} = 1^o \pm 3^o$: $z - x$ Projection.
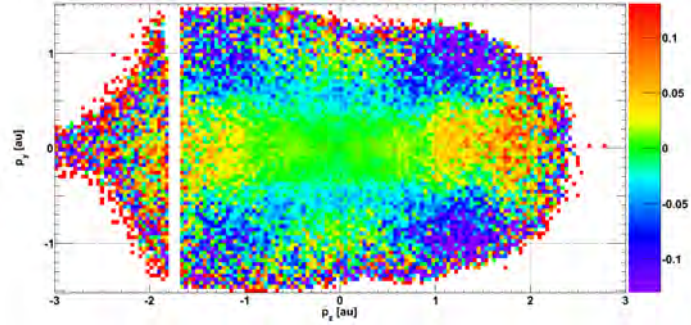
(c) N_2 with $\phi_{al} = 1^o \pm 3^o$: $z - y$ Projection.

Figure B.6.: Experiment B, N_2 measurement: Normalized differences of electrons recorded under an alignment angle of $\phi_{al} = 1^o \pm 3^o$ and the reference shown in figure B.5. This is a reproduction of figure 5.17(a). Both pump and probe pulses are polarized along the z axis. Projections were made with the respective third dimension being integrated over.
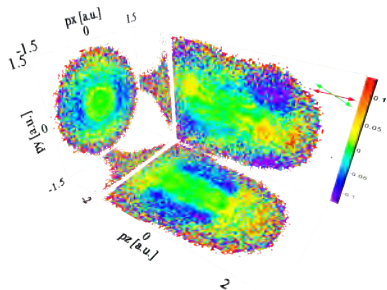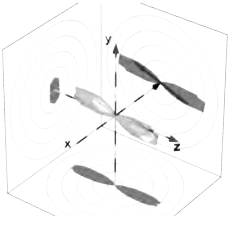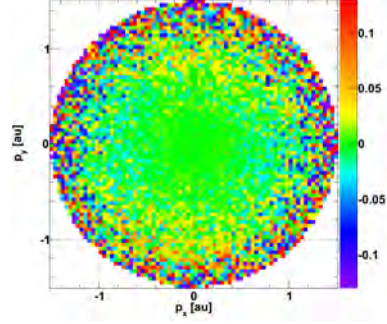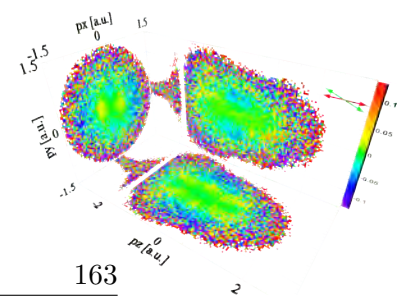
(a) N_2 with $\phi_{al} = 45^o \pm 3^o$: $x - y$ Projection.
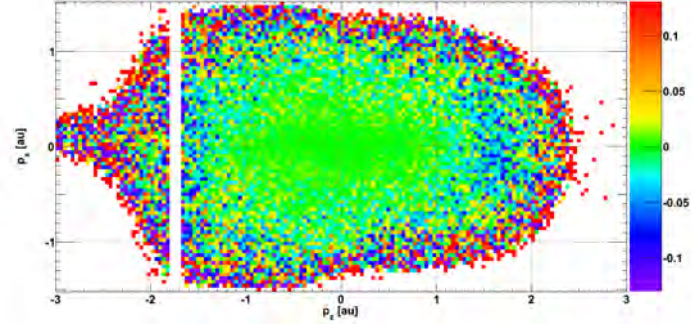
(b) N_2 with $\phi_{al} = 45^o \pm 3^o$: $z - x$ Projection.
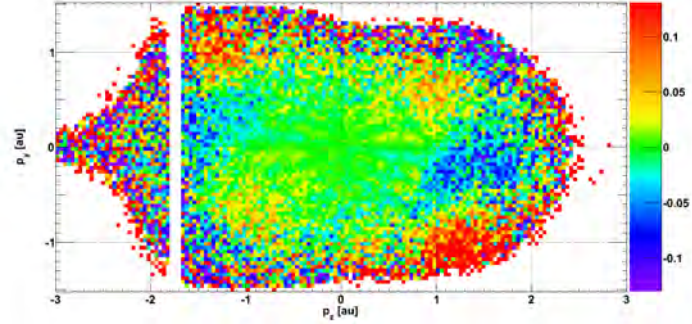
(c) N_2 with $\phi_{al} = 45^o \pm 3^o$: $z - y$ Projection.

Figure B.7.: Experiment B, N_2 measurement: Normalized differences of electrons recorded under an alignment angle of $\phi_{al} = 45^o \pm 3^o$ and the reference shown in figure B.5. This is a reproduction of figure 5.17(c). Probe pulses are polarized along the z axis. The alignment angle ϕ_{al} is the angle of the pump polarization with the z-axis in the $x - y$ plane. Projections were made with the respective third dimension being integrated over.
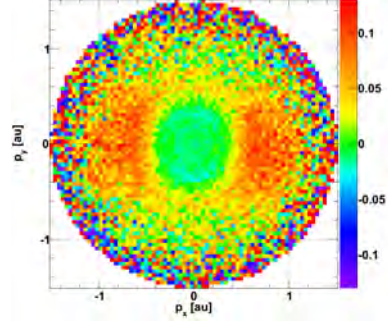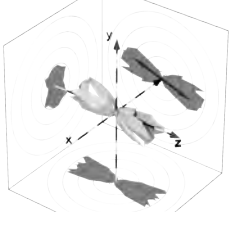
(a) N_2 with $\phi_{al} = 89^o \pm 3^o$: $x - y$ Projection.
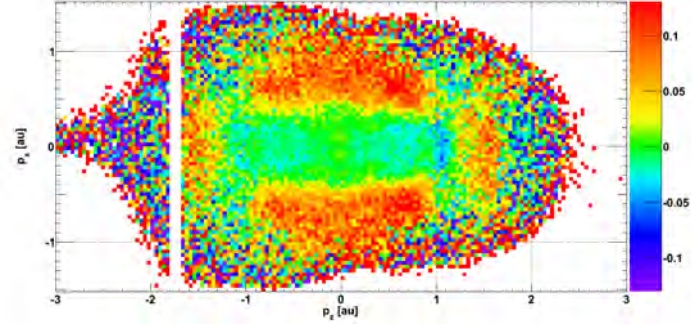
(b) N_2 with $\phi_{al} = 89^o \pm 3^o$: $z - x$ Projection.
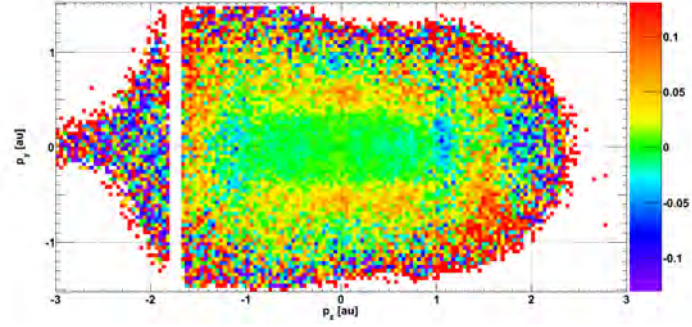
(c) N_2 with $\phi_{al} = 89^o \pm 3^o$: $z - y$ Projection.

Figure B.8.: Experiment B, N_2 measurement: Normalized differences of electrons recorded under an alignment angle of $\phi_{al} = 89^o \pm 3^o$ and the reference shown in figure B.5. This is a reproduction of figure 5.17(e). Probe pulses are polarized along the z axis, while the pump is along the y-axis. Projections were made with the respective third dimension being integrated over.
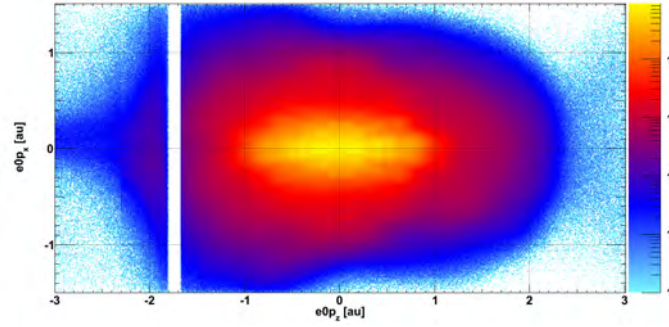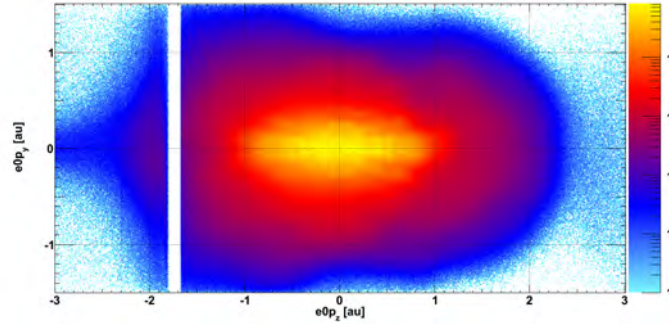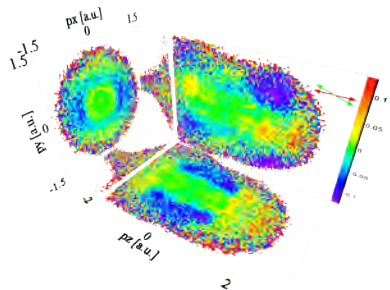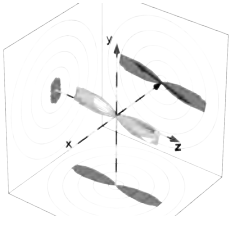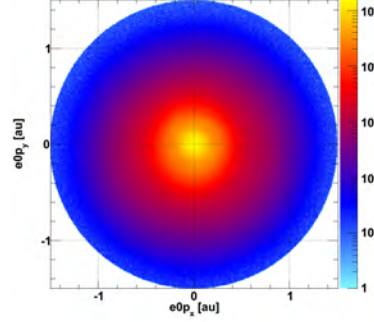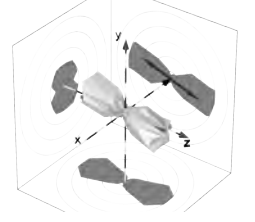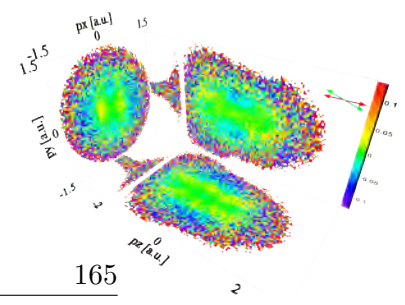
(a) O_2: $x - y$ - $|p_z| < 4$ a.u.

(b) O_2: $z - x$ - $|p_y| < 1.5$ a.u.
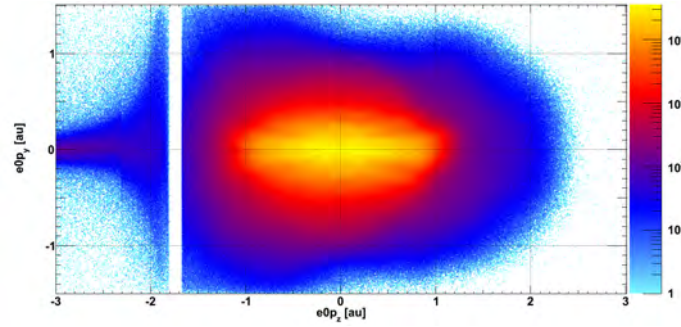
(c) O_2: $z - y$ - $|p_x| < 1.5$ a.u.

Figure B.9.: Experiment B, O_2 measurement: Electron momentum distributions. Out-of-plane momenta were integrated over within the full available ranges. Sum over all alignment angles without normalization. These are the two-dimensional components of figure 5.13(b). With a different pixel size, similar distributions were used as reference for the normalized differences with unrestricted out-of-plane momenta, such as the O_2 spectra in figure 5.16 and the flip-book on odd-numbered pages. Probe pulses are polarized along the z axis while the polarization of aligning pulses is rotated in the $z - y$ plane.
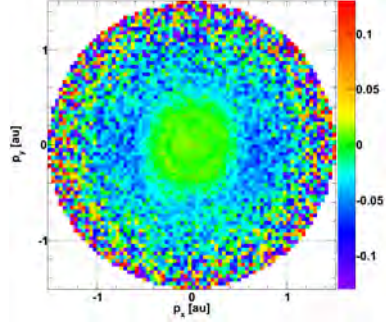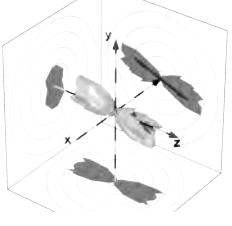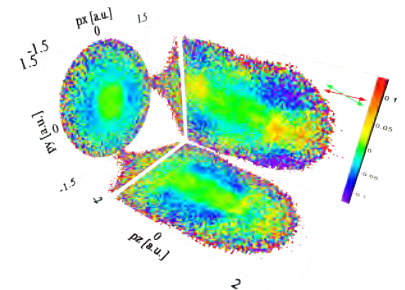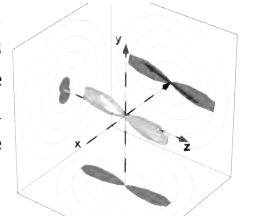
(a) O_2 with $\phi_{al} = 1^o \pm 5^o$: $x - y$ Projection.

(b) O_2 with $\phi_{al} = 1^o \pm 5^o$: $z - x$ Projection.

(c) O_2 with $\phi_{al} = 1^o \pm 5^o$: $z - y$ Projection.

Figure B.10.: Experiment B, O_2 measurement: Normalized differences of electrons recorded under an alignment angle of $\phi_{al} = 1^o \pm 5^o$ and the reference shown in figure B.9. This is a reproduction of figure 5.16(b). Both pump and probe pulses are polarized along the z axis. Projections were made with the respective third dimension being integrated over.
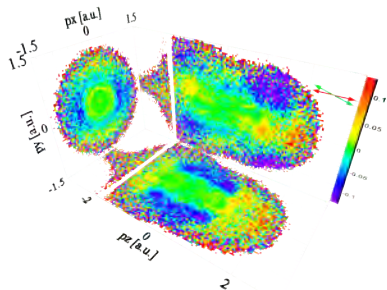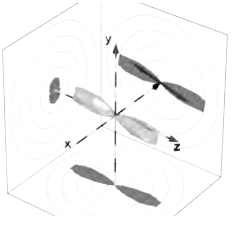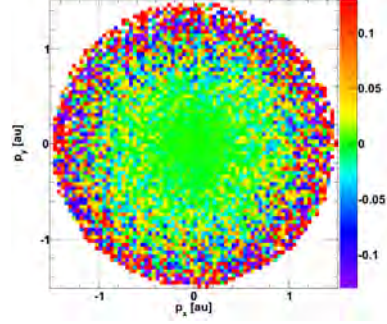
(a) O_2 with $\phi_{al} = 45^o \pm 5^o$: $x - y$ Projection.

(b) O_2 with $\phi_{al} = 45^o \pm 5^o$: $z - x$ Projection.
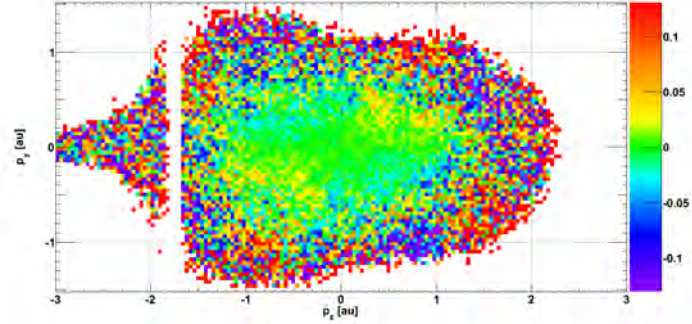
(c) O_2 with $\phi_{al} = 45^o \pm 5^o$: $z - y$ Projection.

Figure B.11.: Experiment B, O_2 measurement: Normalized differences of electrons recorded under an alignment angle of $\phi_{al} = 45^o \pm 5^o$ and the reference shown in figure B.9. This is a reproduction of figure 5.16(d). Probe pulses are polarized along the z axis. The alignment angle ϕ_{al} is the angle of the pump polarization with the z-axis in the $x - y$ plane. Projections were made with the respective third dimension being integrated over.
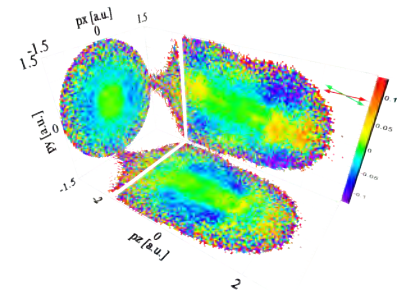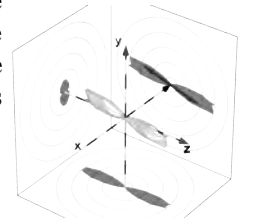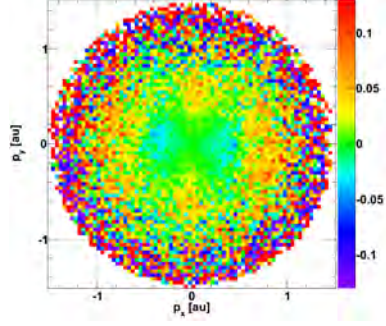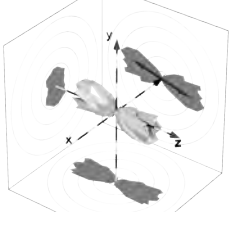
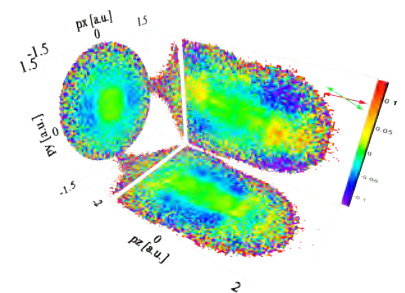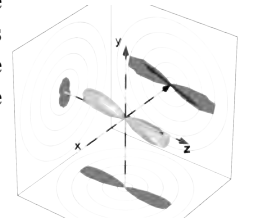(a) O_2 with $\phi_{al} = 89^o \pm 5^o$: $x - y$ Projection.
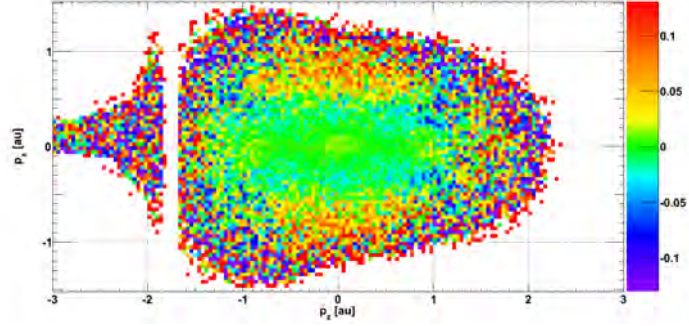
(b) O_2 with $\phi_{al} = 89^o \pm 5^o$: $z - x$ Projection.
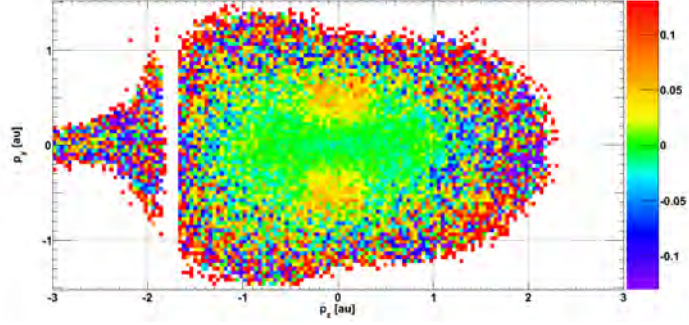
(c) O_2 with $\phi_{al} = 89^o \pm 5^o$: $z - y$ Projection.

Figure B.12.: Experiment B, O_2 measurement: Normalized differences of electrons recorded under an alignment angle of $\phi_{al} = 89^o \pm 5^o$ and the reference shown in figure B.9. This is a reproduction of figure 5.16(f). Probe pulses are polarized along the z axis, while the pump is along the y-axis. Projections were made with the respective third dimension being integrated over.
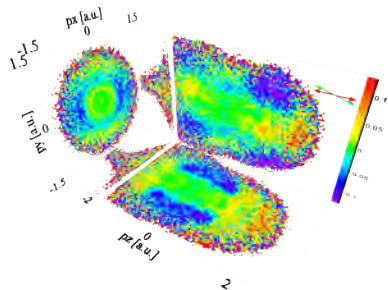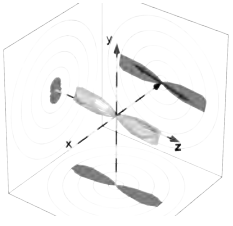
B.2.2. Cartesian Coordinates - Out of Plane Momentum Restricted
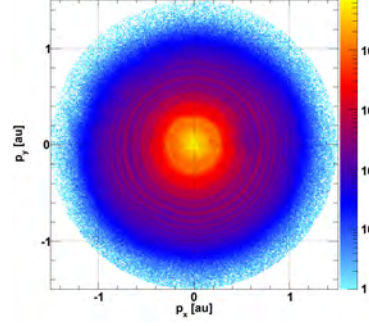
(a) N_2: $x - y$ - $|p_z| < 0.1$ a.u.
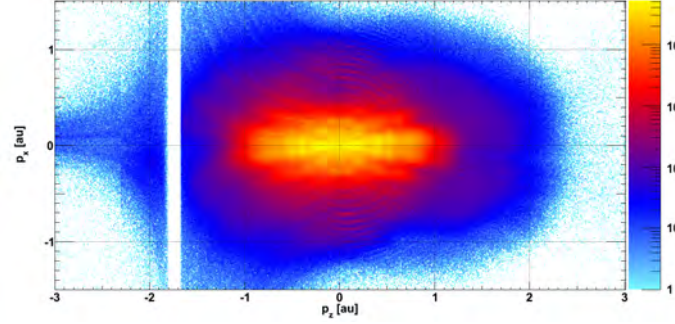
(b) N_2: $z - x$ - $|p_y| < 0.1$ a.u.
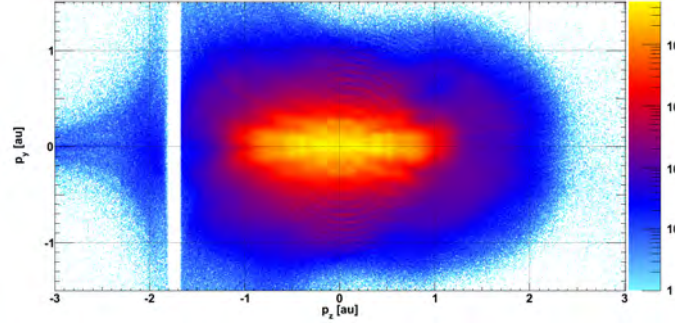
(c) N_2: $z - y$ - $|p_x| < 0.1$ a.u.

Figure B.13.: Experiment B, N_2 measurement: Electron momentum distributions. Out-of-plane momenta were restricted to ± 0.1 a.u.. Sum over all alignment angles without normalization. These are the two-dimensional components of figure 5.13(c). With a different pixel size, similar distributions were used as reference for the normalized differences with restricted out-of-plane momenta, such as the N_2 spectra in figure 5.17, the flip-book on even-numbered pages and section B.2.2. Probe pulses are polarized along the z axis while the polarization of aligning pulses is rotated in the $z - y$ plane.
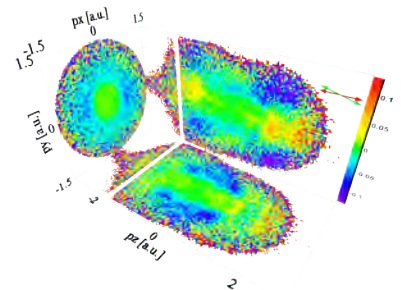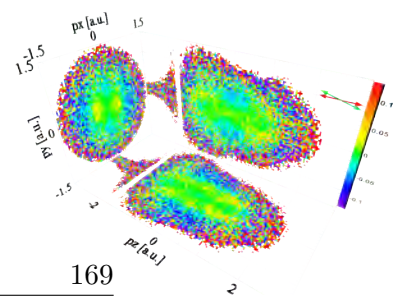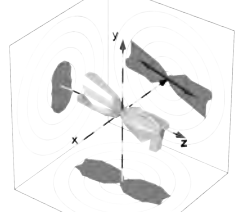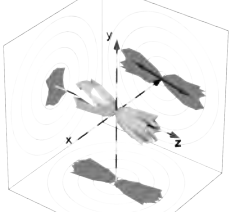
(a) N_2 with $\phi_{al} = 1^o \pm 11^o$: $x - y$ Projection.
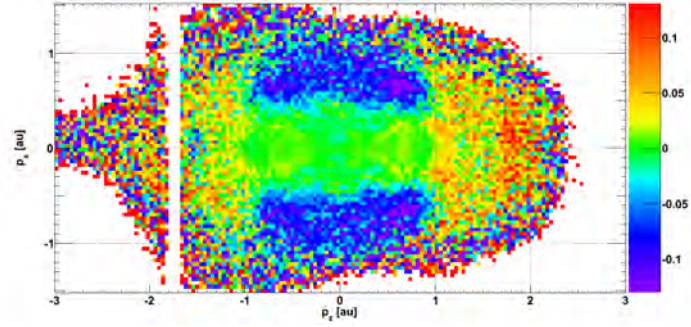
(b) N_2 with $\phi_{al} = 1^o \pm 11^o$: $z - x$ Projection.
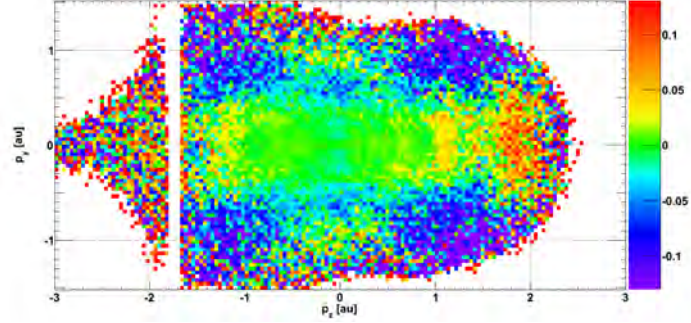
(c) N_2 with $\phi_{al} = 1^o \pm 11^o$: $z - y$ Projection.

Figure B.14.: Experiment B, N_2 measurement: Normalized differences of electrons recorded under an alignment angle of $\phi_{al} = 1^o \pm 11^o$ and the reference shown in figure B.13. Both pump and probe pulses are polarized along the z axis. Projections were made with the respective third dimension being restricted to ± 0.1 a.u..
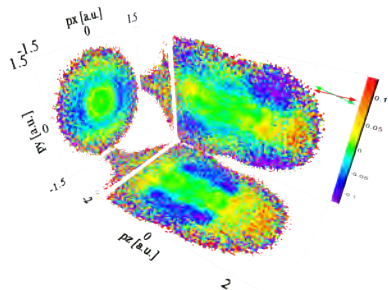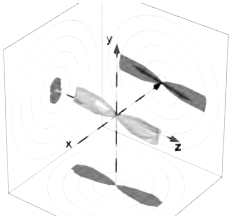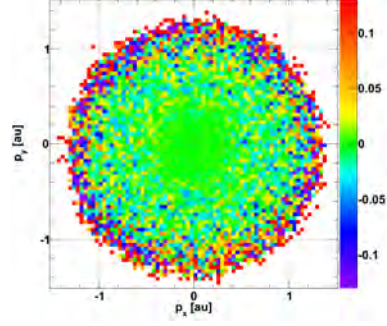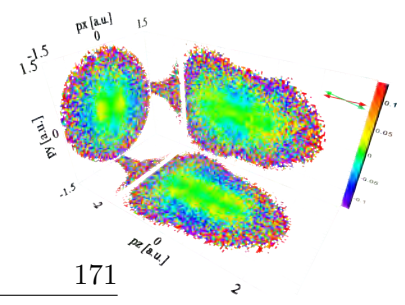
(a) N_2 with $\phi_{al} = 45^o \pm 11^o$: $x - y$ Projection.
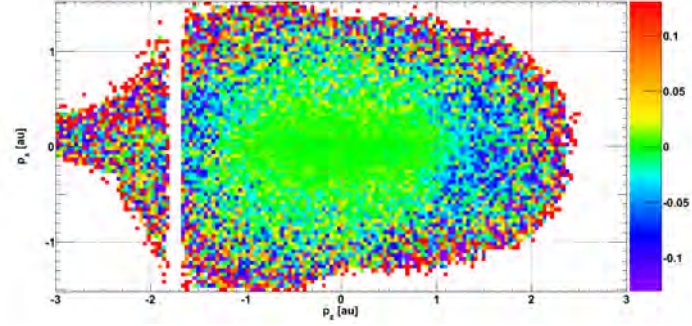
(b) N_2 with $\phi_{al} = 45^o \pm 11^o$: $z - x$ Projection.
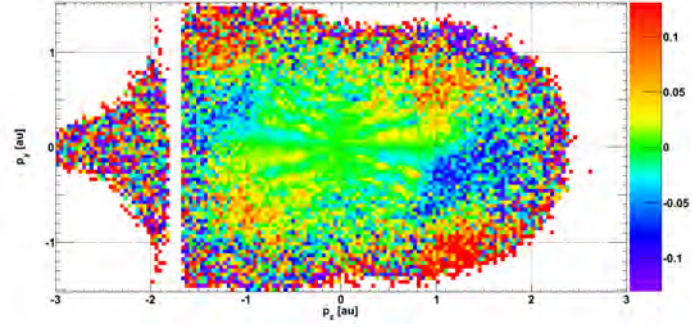
(c) N_2 with $\phi_{al} = 45^o \pm 11^o$: $z - y$ Projection.

Figure B.15.: Experiment B, N_2 measurement: Normalized differences of electrons recorded under an alignment angle of $\phi_{al} = 45^o \pm 11^o$ and the reference shown in figure B.13. Probe pulses are polarized along the z axis. The alignment angle ϕ_{al} is the angle of the pump polarization with the z-axis in the $x - y$ plane. Projections were made with the respective third dimension being restricted to ± 0.1 a.u..
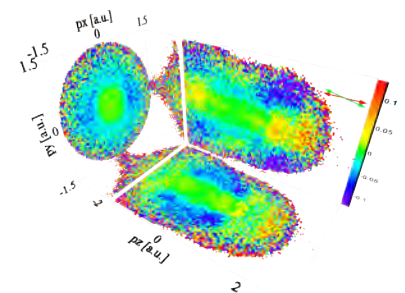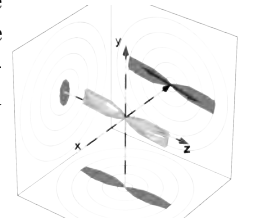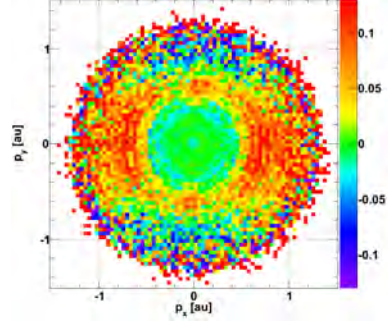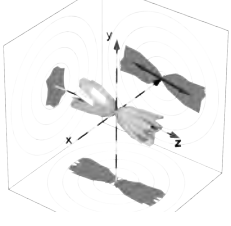
(a) N_2 with $\phi_{al} = 89^o \pm 11^o$: $x - y$ Projection.
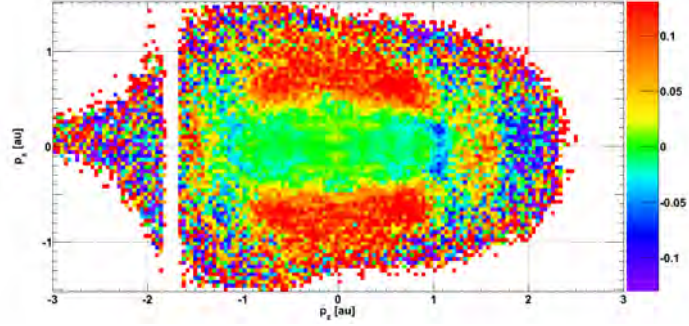
(b) N_2 with $\phi_{al} = 89^o \pm 11^o$: $z - x$ Projection.
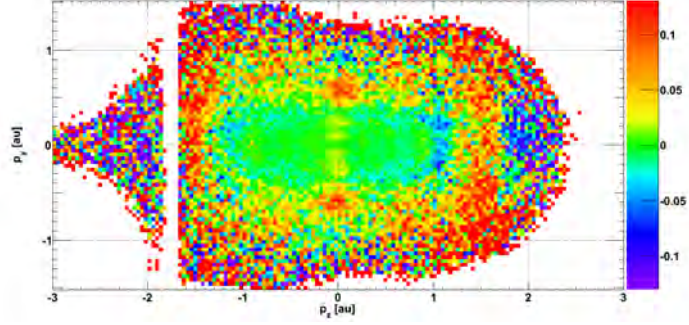
(c) N_2 with $\phi_{al} = 89^o \pm 11^o$: $z - y$ Projection.

Figure B.16.: Experiment B, N_2 measurement: Normalized differences of electrons recorded under an alignment angle of $\phi_{al} = 89^o \pm 11^o$ and the reference shown in figure B.13. Probe pulses are polarized along the z axis. The alignment angle ϕ_{al} is the angle of the pump polarization with the z-axis in the $x - y$ plane. Projections were made with the respective third dimension being restricted to ± 0.1 a.u..
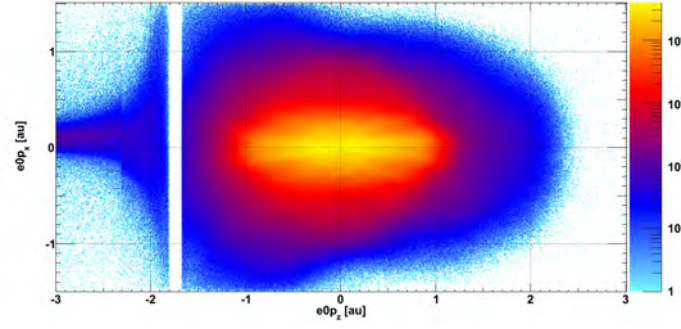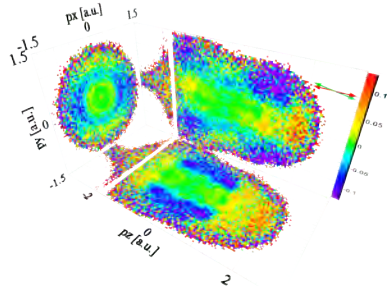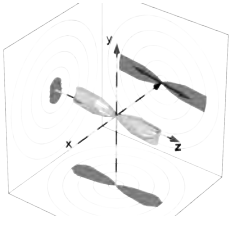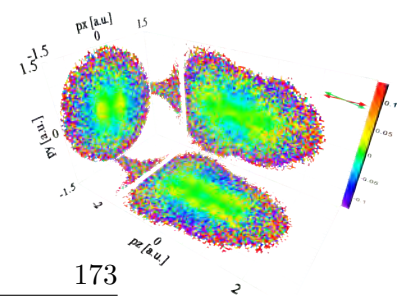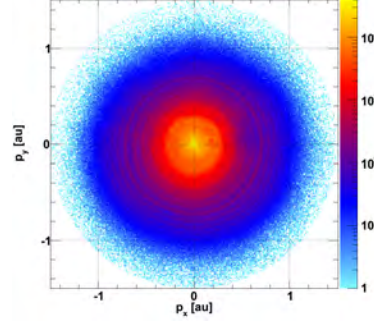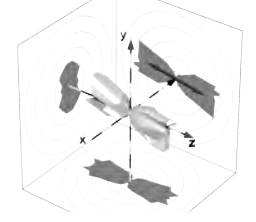
(a) O_2: $x - y$ - $|p_z| < 0.1$ a.u.
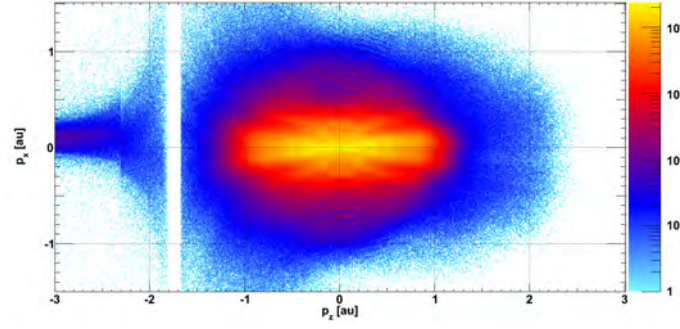
(b) O_2: $z - x$ - $|p_y| < 0.1$ a.u.
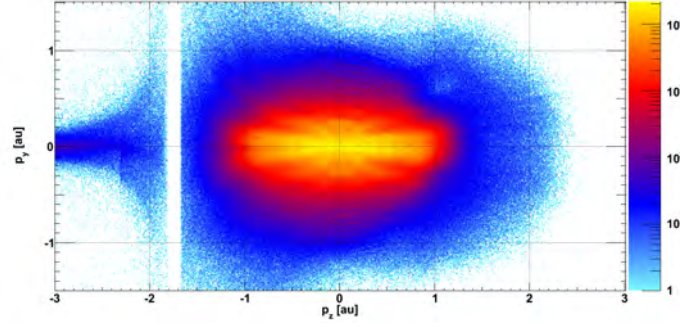
(c) O_2: $z - y$ - $|p_x| < 0.1$ a.u.

Figure B.17.: Experiment B, O_2 measurement: Electron momentum distributions. Out-of-plane momenta were restricted to ± 0.1 a.u.. Sum over all alignment angles without normalization. These are the two-dimensional components of figure 5.13(d). With a different pixel size, similar distributions were used as reference for the normalized differences with restricted out-of-plane momenta, such as the O_2 spectra in figure 5.17, the flip-book on even-numbered pages and section B.2.2. Probe pulses are polarized along the z axis while the polarization of aligning pulses is rotated in the $z - y$ plane.
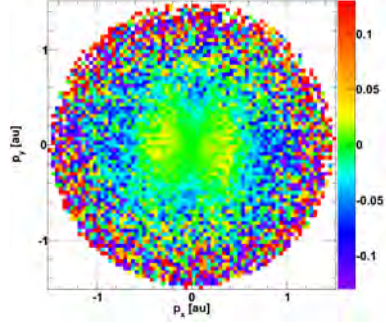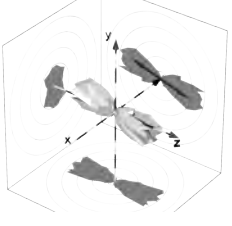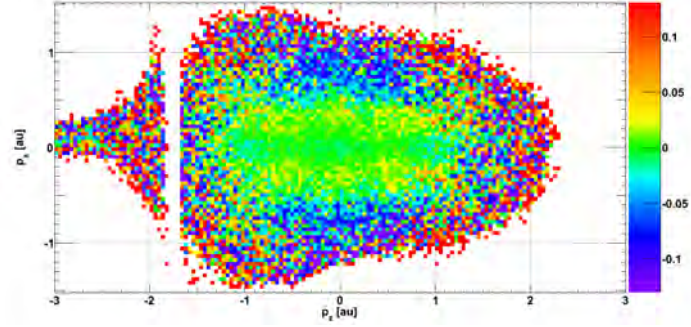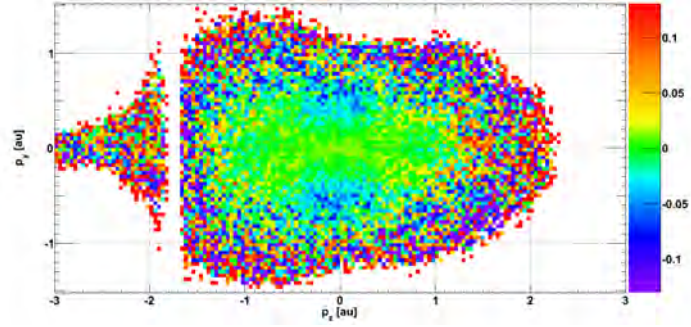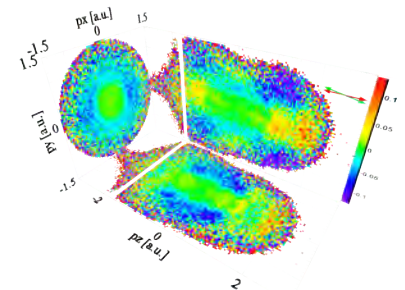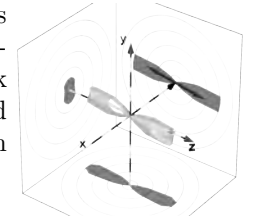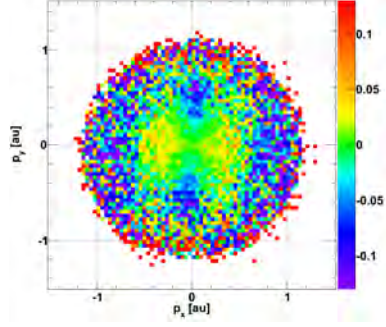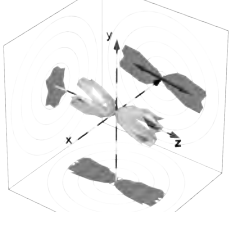
(a) O_2 with $\phi_{al} = 1^o \pm 11^o$: $x - y$ Projection.
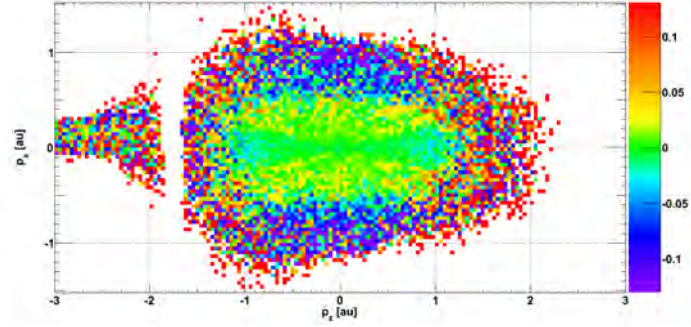
(b) O_2 with $\phi_{al} = 1^o \pm 11^o$: $z - x$ Projection.
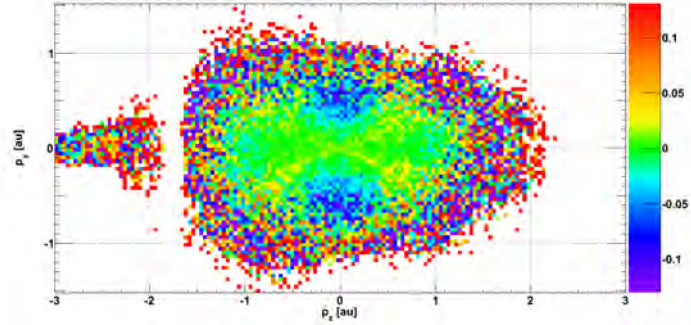
(c) O_2 with $\phi_{al} = 1^o \pm 11^o$: $z - y$ Projection.

Figure B.18.: Experiment B, O_2 measurement: Normalized differences of electrons recorded under an alignment angle of $\phi_{al} = 1^o \pm 11^o$ and the reference shown in figure B.17. Both pump and probe pulses are polarized along the z axis. Projections were made with the respective third dimension being restricted to ± 0.1 a.u..
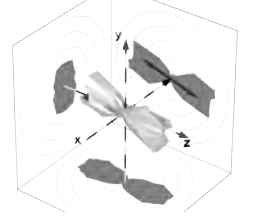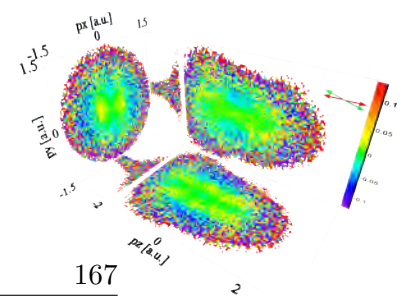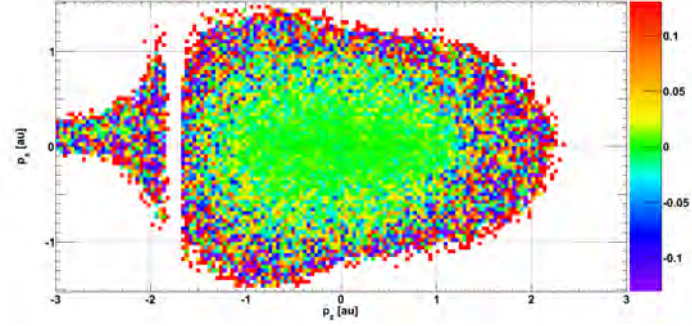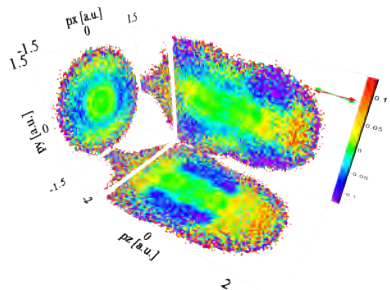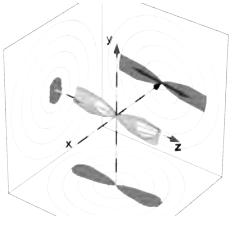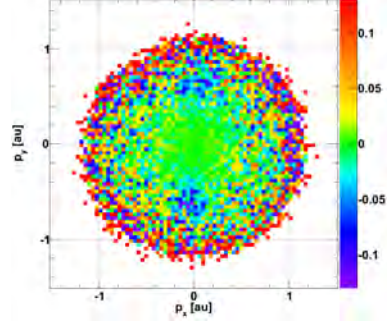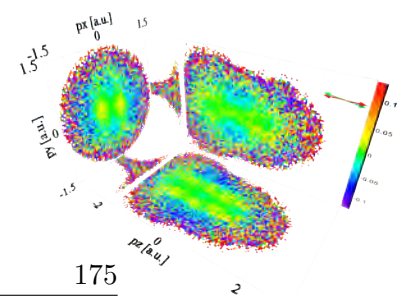
(a) O_2 with $\phi_{al} = 45^o \pm 11^o$: $x - y$ Projection.
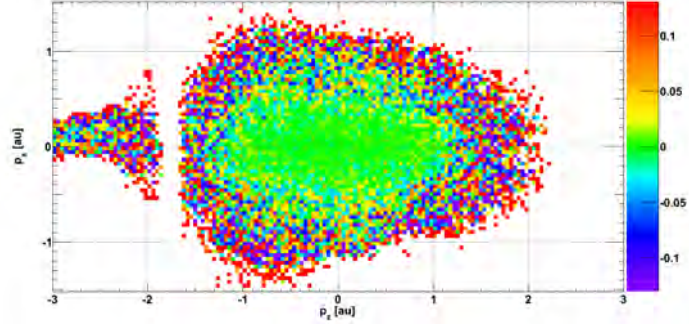
(b) O_2 with $\phi_{al} = 45^o \pm 11^o$: $z - x$ Projection.
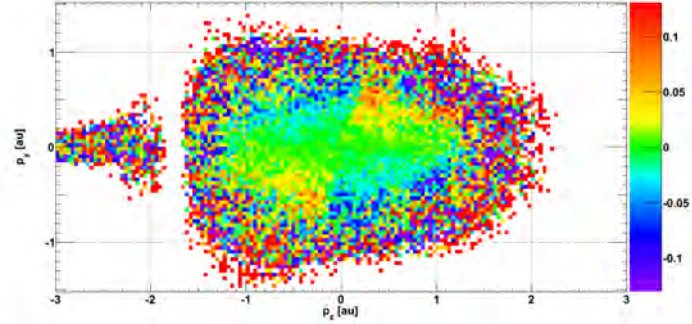
(c) O_2 with $\phi_{al} = 45^o \pm 11^o$: $z - y$ Projection.

Figure B.19.: Experiment B, O_2 measurement: Normalized differences of electrons recorded under an alignment angle of $\phi_{al} = 45^o \pm 11^o$ and the reference shown in figure B.17. Probe pulses are polarized along the z axis. The alignment angle ϕ_{al} is the angle of the pump polarization with the z-axis in the $x - y$ plane. Projections were made with the respective third dimension being restricted to ± 0.1 a.u..
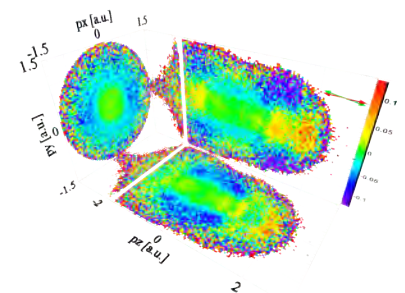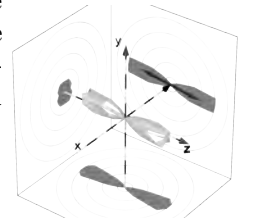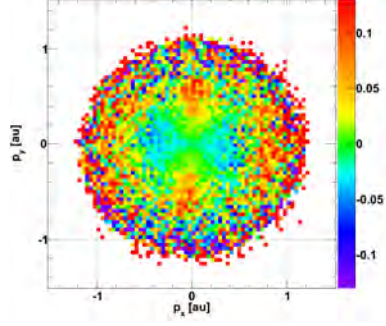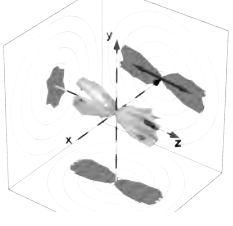
(a) O_2 with $\phi_{al} = 89^o \pm 11^o$: $x - y$ Projection.
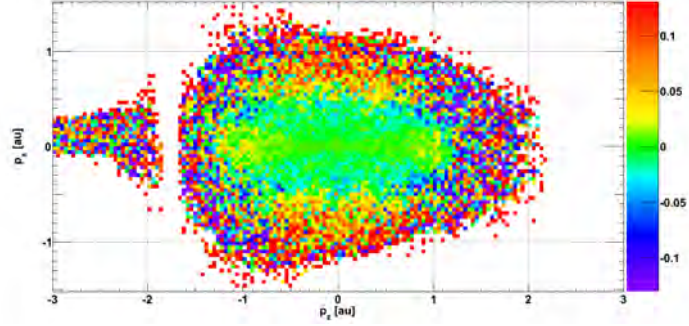
(b) O_2 with $\phi_{al} = 89^o \pm 11^o$: $z - x$ Projection.
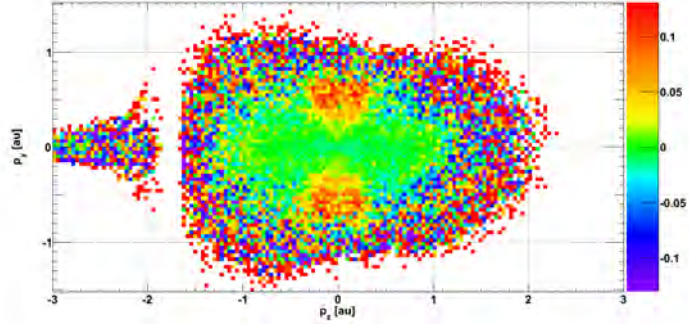
(c) O_2 with $\phi_{al} = 89^o \pm 11^o$: $z - y$ Projection.

Figure B.20.: Experiment B, O_2 measurement: Normalized differences of electrons recorded under an alignment angle of $\phi_{al} = 89^o \pm 11^o$ and the reference shown in figure B.17. Probe pulses are polarized along the z axis. The alignment angle ϕ_{al} is the angle of the pump polarization with the z-axis in the $x - y$ plane. Projections were made with the respective third dimension being restricted to ± 0.1 a.u..
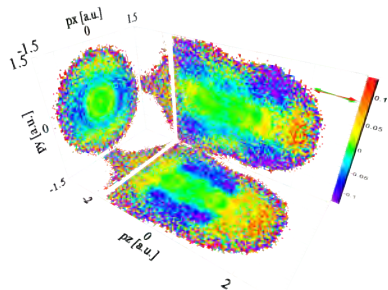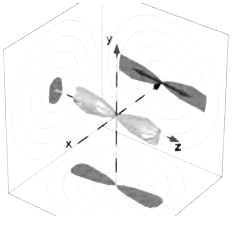
B.2.3. Cartesian Coordinates - Out of Plane Angle Restricted

(a) N_2: $x - y$ - $\vartheta_z = 90^o \pm 10^o$

(b) N_2: $z - x$ - $\vartheta_y = 90^o \pm 10^o$

(c) N_2: $z - y$ - $\vartheta_x = 90^o \pm 10^o$
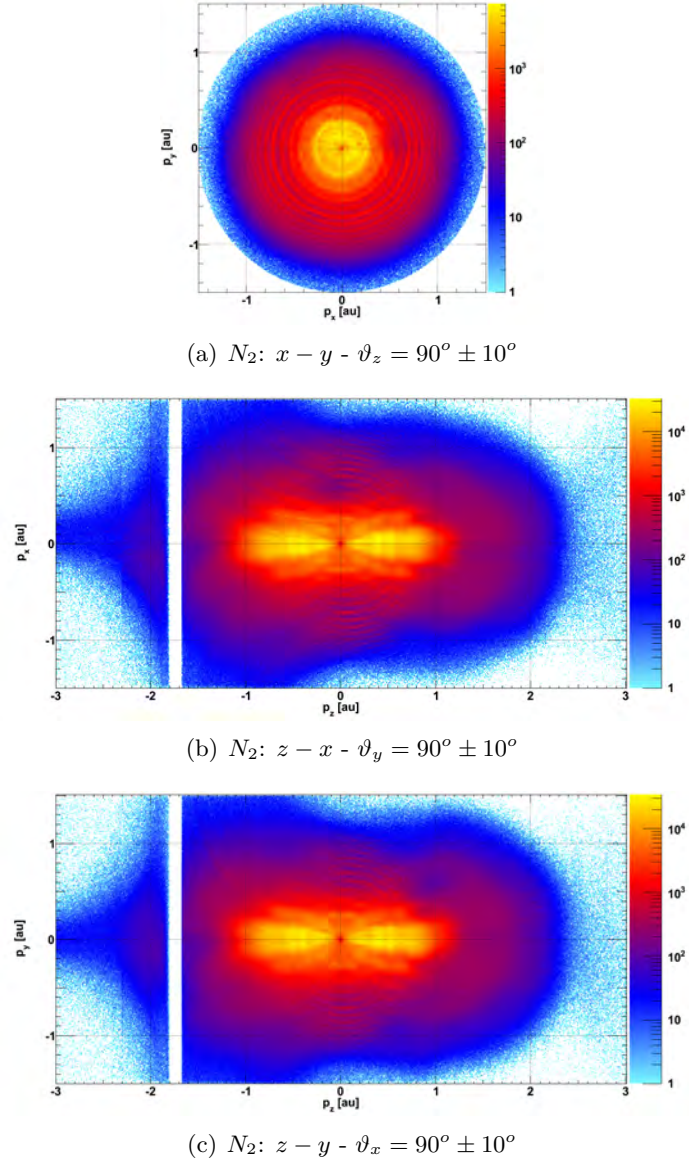
Figure B.21.: Experiment B, N_2 measurement: Electron momentum distributions. Out-of-plane angles were restricted to $\pm 10^o$. Sum over all alignment angles without normalization. These are the two-dimensional components of figure 5.13(e). Probe pulses are polarized along the z axis while the polarization of aligning pulses is rotated in the $z - y$ plane.

(a) O_2: $x - y$ - $\vartheta_z = 90^o \pm 10^o$

(b) O_2: $z - x$ - $\vartheta_y = 90^o \pm 10^o$

(c) O_2: $z - y$ - $\vartheta_x = 90^o \pm 10^o$
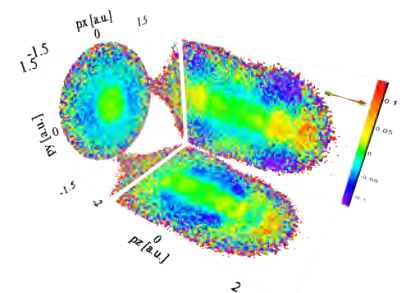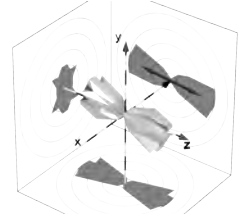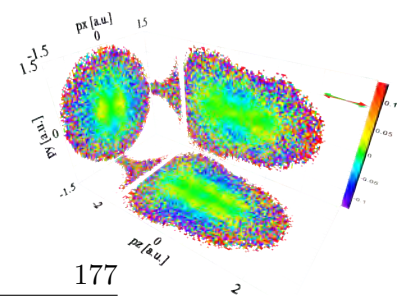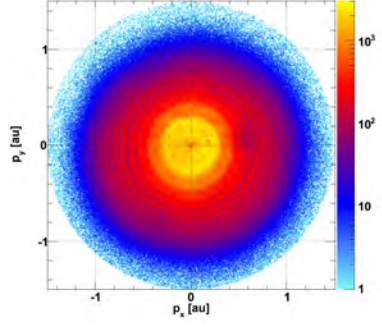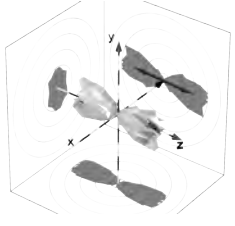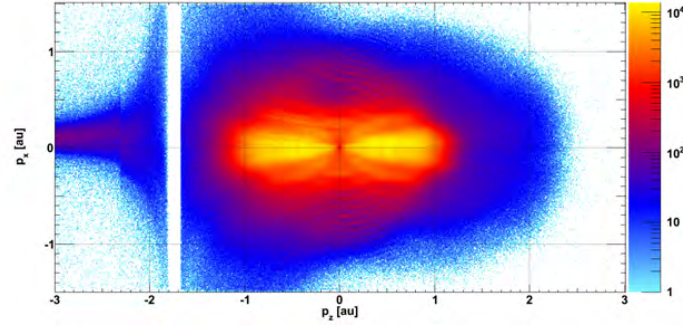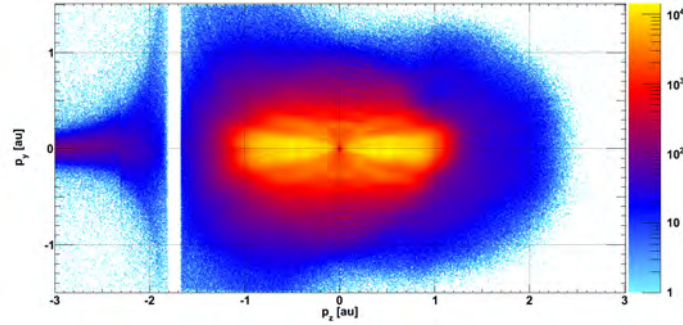
Figure B.22.: Experiment B, O_2 measurement: Electron momentum distributions. Out-of-plane angles were restricted to $\pm 10^o$. Sum over all alignment angles without normalization. These are the two-dimensional components of figure 5.13(f). Probe pulses are polarized along the z axis while the polarization of aligning pulses is rotated in the $z - y$ plane.
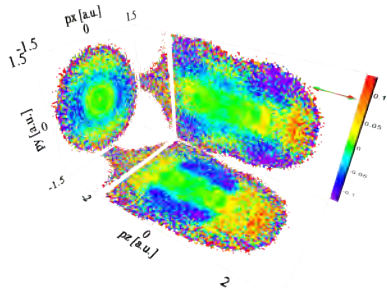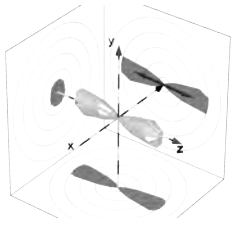
B.2.4. Non-Cartesian Coordinates
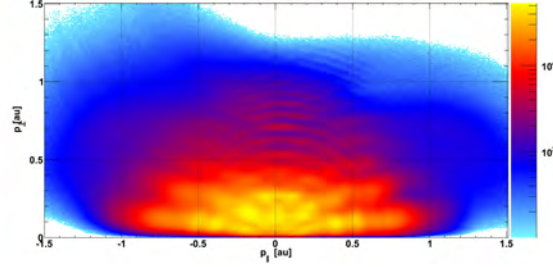
(a) N_2 Measurement - Logarithmic Scale
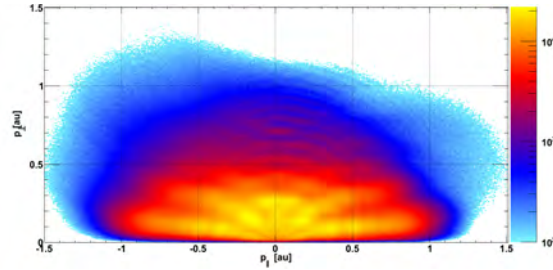
(b) O_2 Measurement - Logarithmic Scale
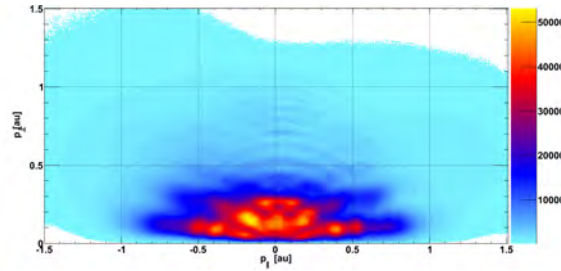
(c) N_2 Measurement - Linear Scale
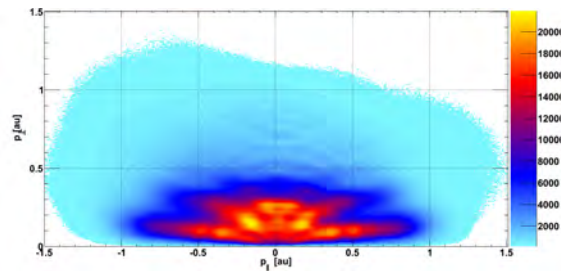
(d) O_2 Measurement - Linear Scale

Figure B.23.: Experiment B: Spectra of electron momentum along the probe polarization ($p_\parallel = p_z$, *horizontal* axis) vs. momentum perpendicular to the probe ($p_\perp = \sqrt{p_x^2 + p_y^2}$, *vertical*). Sum over all alignment angles. (a) and (c): Nitrogen measurement; (b) and (d): Oxygen measurement.
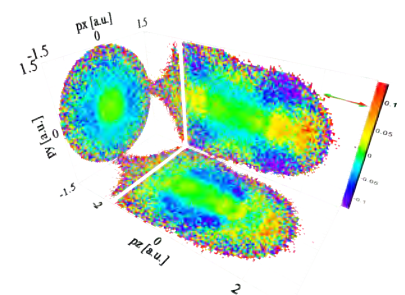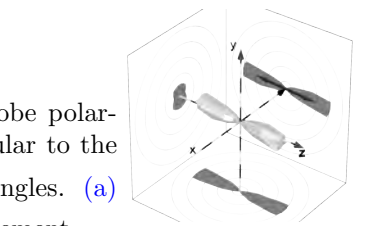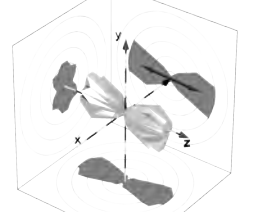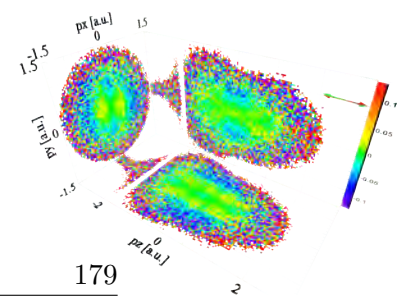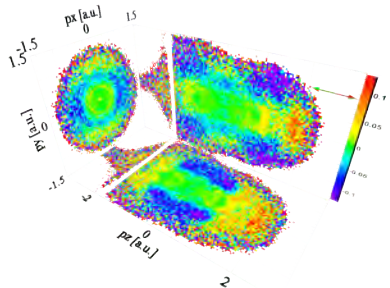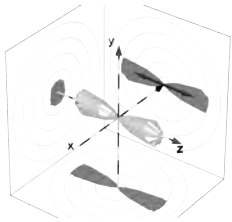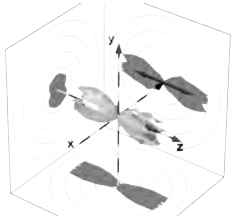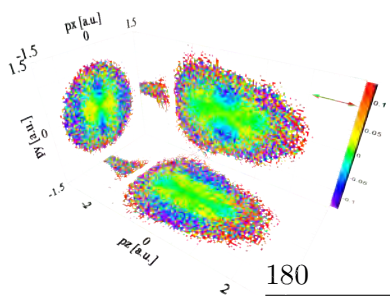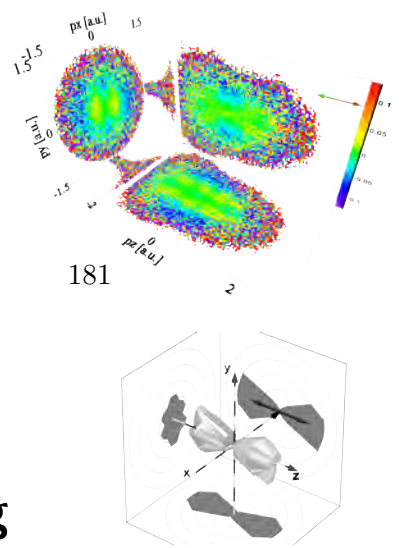
C. Comparison: Electron Scattering and Double-Slit Diffraction

The description of elastic low-energy electron scattering at a diatomic molecular ion by simple double-slit diffraction as in chapters 5.1.2.2 and 5.2.2.5 can be criticized as being too simplistic. It misses, for instance, the phase shifts the ion's potential induces between different electron trajectories. This effect can be expected to become even more significant if the electron wave penetrates through the electron clouds shielding the electrostatic potentials of the molecule's nuclei.

However, for the case of electron re-scattering at H_2^{2+}, it has been found by means of simulation that the effect of the ion's potential can be approximately accounted for by assuming that it merely accelerates the electron [10]. The DeBroglie wavelength causing the resulting pattern corresponds to the electron's re-collision energy plus the ionization potential that needed to be overcome to free the electron in the first place.

C.1. Models: Hydrogen Molecules

Whereas this might work if the electron wave is scattered by two bare protons, it remains to be shown that a simple diffraction model still works for more complex molecules. As a first step of complication, we compare exact elastic cross sections of electrons at H_2^+ ions to simple double-slit diffraction in figure C.1. The exact cross sections were calculated by Tom Rescigno and Ann Orel, using the "complex Kohn variational method" [81, 82, 83]. Simple double-slit diffraction was calculated by using equation (2.21). In both cases, the molecular axis (double-slit) was fixed at $\vartheta = 90^o$, $\varphi = 0^o$. Incident electrons are at $\vartheta = 0^o$, $\varphi = 0^o$.

We find good qualitative agreement between the models, even without adding the ionization potential. Regarding the position of the first-order minimum, the exact simulation's result is between the double-slit with and without the augmentation of the electron energy by the ionization potential.

C.2. Models: Molecular Single Ions of Nitrogen

In figures C.2 to C.5, simple diffraction patterns are compared to exact elastic electron-N_2^+ ion scattering cross sections by Orel and Rescigno [82, 83]. Geometries are as in the context of H_2^+. The exact simulations show significantly

(a) Exact Cross Sections, 65.8 eV.

(b) Double-Slit Diffraction, 65.9 eV.

(c) Double-Slit Diffraction, 81.3 eV
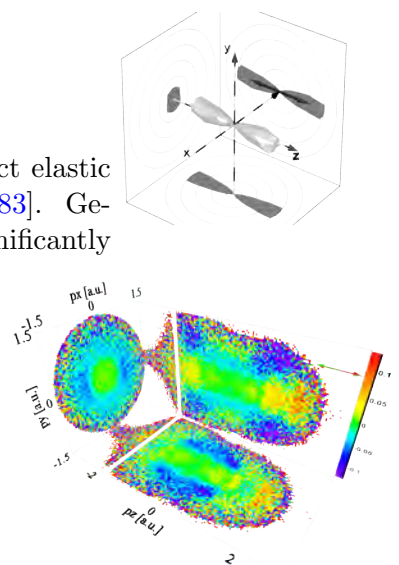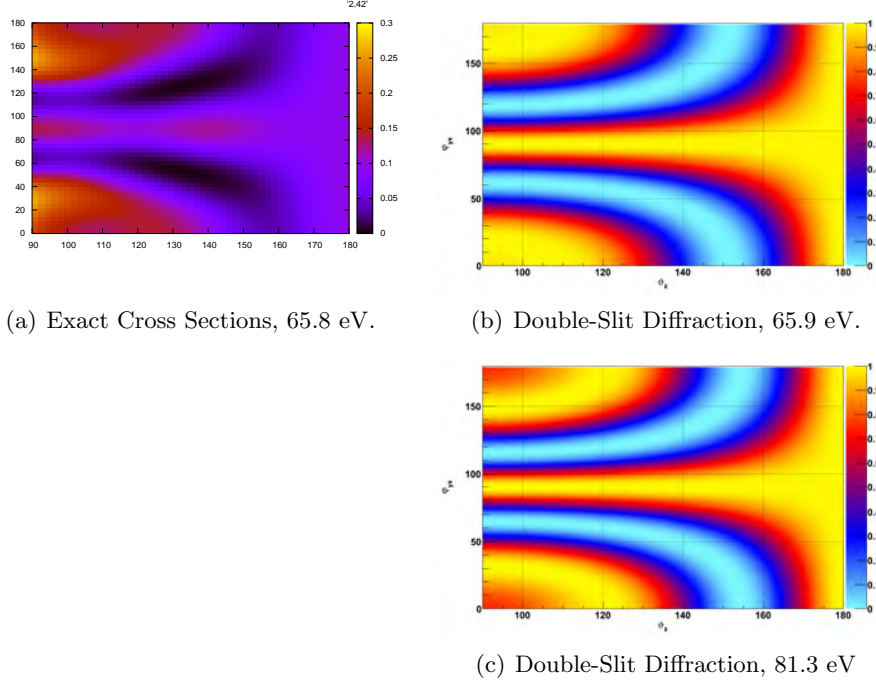
Figure C.1.: Electron scattering in spherical coordinates. ϑ is plotted along the *horizontal*, while φ is along the *vertical* axis and scattering amplitude is color-coded. The molecular axis is fixed at $\vartheta = 90^o$, $\varphi = 0^o$. (a): Precisely simulated doubly differential cross sections for elastically scattering 65.8 eV electrons at H_2^+ ions with a bondlength of 3 a.u. [82, 83]. (b): Simple double-slit electron diffraction, at the same electron energy, geometry and internuclear distance as the exact case. (c): Same as (b) but the ionization potential of H_2 (15.4 eV) is added to the electron's kinetic energy. Agreement between the exact cross sections and simple diffraction is good in both cases. Only the modulation on the zeroth-order maximum ($\varphi = 90^o$) in the exact spectrum is not reproduced by the simple model.

(a) Exact Cross Sections, 7 eV.

(b) Double-Slit Diffraction, 7 eV

(c) Double-Slit Diffraction: 22.6 eV
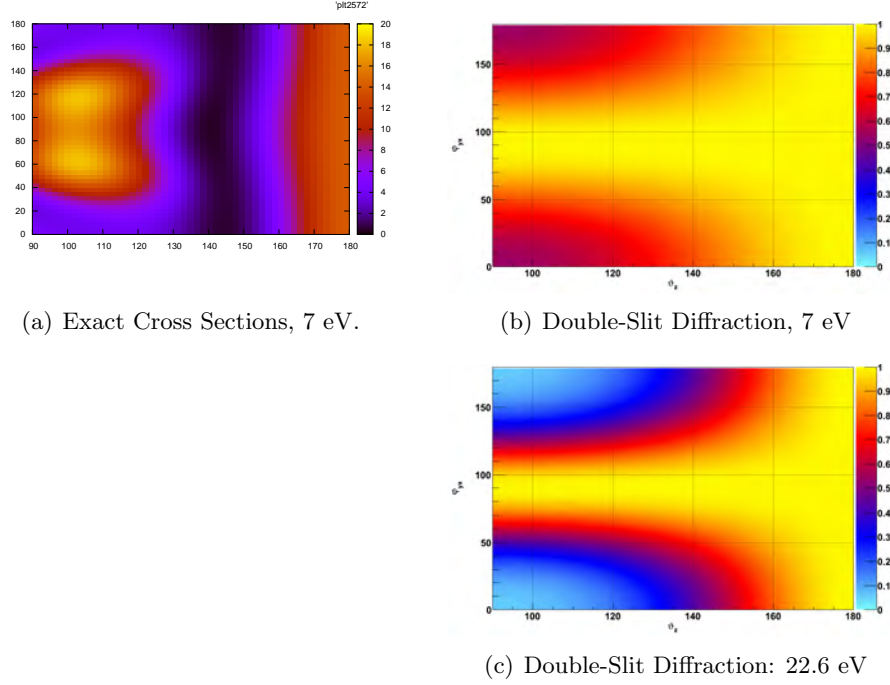
Figure C.2.: Electron scattering in spherical coordinates. ϑ is plotted along the *horizontal*, while φ is along the *vertical* axis and scattering amplitude is color-coded. The molecular axis is fixed at $\vartheta = 90^o$, $\varphi = 0^o$.(a): Exact differential cross sections for elastically scattering 7 eV electrons at N_2^+ ions [82, 83]. The molecular axis is fixed at $\vartheta = 90^o$, $\varphi = 0^o$. (b): Simple double-slit diffraction of electrons with the same energy as in the exact case. (c): Same as (b) but the ionization potential of N_2 (15.4 eV) is added to the electron's kinetic energy. Agreement between the exact cross sections and diffraction is rather poor due to the prominent scattering minimum around $\vartheta = 145^o$ not reproduced by simple diffraction.

more intricate structure than simple diffraction. In particular, the spectrum for 7 eV in figure C.2(a) exhibits a broad, φ-independent minimum around $\vartheta \approx 145^o$ not appearing in double-slit diffraction. It moves towards higher values of ϑ for increasing electron energy but changes its shape and is broken by a structure resembling the zeroth order diffraction maximum; see figures C.3 to C.5. Furthermore, additional maxima ("wings", see the said figures and figure subscripts) become visible beyond 7 eV. Nevertheless, in particular for higher electron energies, the basic diffraction structure becomes visible besides the fringes caused by the extra complexity of N_2^+ over H_2^+ and the simple double-slit. In order to reach some level of agreement, the energy of the scattering electron has to be augmented for the diffraction as compared to the scattering calculation.

(a) Exact Cross Sections: 14 eV.

(b) Double-Slit Diffraction: 14 eV.

(c) Double-Slit Diffraction: 29.6 eV.

(d) Double-Slit Diffraction: 50 eV.
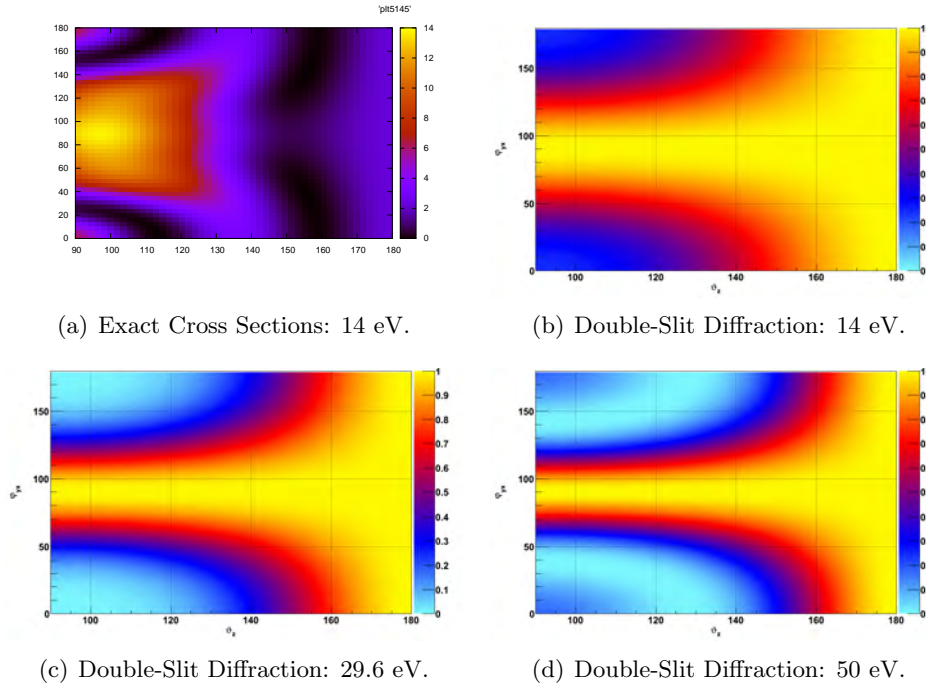
Figure C.3.: (a) to (c): Same as in figure C.2 with the basic electron energy increased to 14 eV. In the exact calculation (a), the non-diffraction minimum at $\vartheta \approx 145^o$ is now broken by a weak structure at $\varphi = 0^o$ resembling the zeroth order diffraction maximum. At $\vartheta = 90^o$, $\varphi = 0^o/180^o$, a new maximum becomes visible that is neither present in the 14 eV (b) nor in the 14 eV$+I_P$ diffraction structure (c). However, a similar maximum emerges if we further increase the electron energy; see (d) for the case of 50 eV. In the exact spectrum, the (supposed) zeroth order maximum shows a structured broadening in the φ-direction at $100^o < \vartheta < 140^o$ with increasing ϑ that is not observed in the diffraction patterns.

(a) Exact Cross Sections: 18 eV.

(b) Double-Slit Diffraction: 18 eV.

(c) Double-Slit Diffraction: 33.6 eV.

(d) Double-Slit Diffraction: 50 eV.
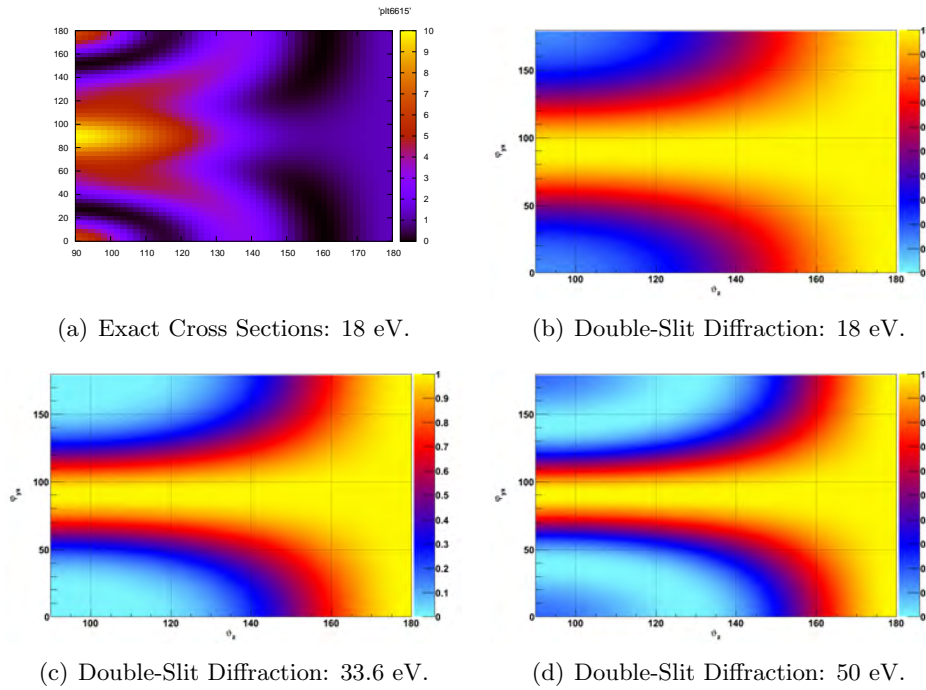
Figure C.4.: (a) to (d): Same as in figures C.2 and C.3 with the basic electron energy increased to 18 eV. The (supposed) zeroth-order maximum at $\varphi = 90^o$ in (a) is less suppressed than in the 14 eV case (fig. C.3(a)) by the non-diffraction minimum now around $\vartheta \approx 150^o$. It is becoming distinguishable from the now parabola-shaped non-diffraction maxima ("wings") connecting the end points $\vartheta = 90^o$, $\varphi = 120^o$ and $\vartheta = 140^o$, $\varphi = 180^o$.

(a) Exact Cross Sections: 22 eV.

(b) Double-Slit Diffraction: 22 eV.

(c) Double-Slit Diffraction: 37.6 eV

(d) Double-Slit Diffraction: 50 eV
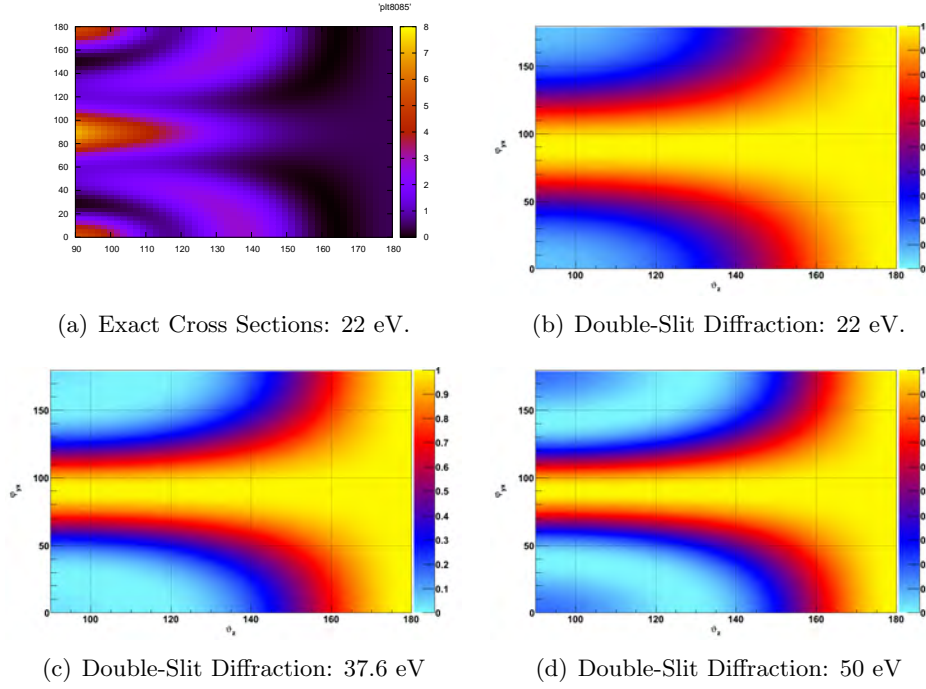
Figure C.5.: (a) to (d): Same as in figure C.2 to C.4 with the basic electron energy increased to 22 eV. The structure at $\varphi = 90^o$ in (a) now clearly resembles a zeroth-order diffraction maximum. It is separated from the non-diffraction "wings" spanning from $\vartheta = 90^o$, $\varphi = 120^o$ to $\vartheta = 140^o$, $\varphi = 180^o$ by an extension of the non-diffraction minimum still located around $\vartheta \approx 150^o$ in the 18 eV case (fig. C.4(a)).

C.3. Experiment: N_2^+ and O_2^+

In figures C.6 to C.9, we show experimental electron distributions within diffraction spheres (cf. chapter 5.1.2.2 / figure 5.8) for the re-collision energies used for the models discussed above. In contrast to chapter 5.1.2.2 we now use spherical coordinates.

ϑ is the angle between the incident and the outgoing (scattered) electron. $\vartheta = 0^o$ corresponds to forward scattering. This region is polluted by direct, non re-scattered electrons and therefore unfit for an analysis with respect to diffraction. At $\vartheta = 180^o$, electrons were back-scattered. $\varphi_{yx} = 0$ relates to the scattered electron leaving along the y axis, which is the alignment axis. The axes of "aligned" molecules are preferentially oriented along $\varphi_{yx} = 0^o$, $\vartheta = 90^o$. Anti-aligned ones are distributed around $\varphi_{yx} = 90^o$, with ϑ taking all possible values.

All spectra should show a 180° symmetry within φ_{yx}. Deviations from this are mostly due to inhomogeneities in the detection efficiencies of our MCPs. This is alleviated by the normalized differences between electron distributions from aligned and anti-aligned molecules, as detection efficiency divides out.

At first impression, the "aligned" case in the experiment should show the same scattering geometry as the simulations presented above. Nevertheless, we do not see anything close to the intricate fringes found in the exact electron-N_2^+ scattering cross sections by Orel and Rescigno. (Please note the different axis ranges between theory and experiment!) There are various possible reasons.

First of all, our alignment distributions were imperfect (cf. chapter 5.1.1.3). The distributions of molecules contributing to the electron spectra are further biased by the angle-dependent ionization probabilities of N_2 and O_2. Hence, the real scattering geometries were not the same as simulated.

Secondly we had to integrate over a range of re-collision momenta (± 0.1 a.u.) in order to gain statistics. Although slightly narrower or wider ranges did not significantly change the observed patterns (or the absence thereof), any realistic interval of momenta may be able to cancel the intricate fringes predicted by theory.

A third potential explanation is the fact not all electrons were born at the same laser intensity. On the one hand, the laser focus provides a range of intensities, all contributing to the final distribution of electrons. On the other hand, our pulses were relatively long, having a slowly rising envelope. Although we were assuming the opposite, significant population may have ionized at various points in time before the envelope reached its maximum. These two intensity averaging effects are not too problematic as long as re-collision and streaking momentum are roughly in a linear relationship with each other. The latter becomes increasingly problematic the more we approach tunneling at the field maximum, corresponding to lower streaking momenta.

Fourthly, we assumed contributions only form the "long" electron trajectories. It is possible "short" trajectories are causing some background.

(a) N_2^+, 7 eV, Aligned.

(b) O_2^+, 7 eV, Aligned.

(c) N_2^+, 7 eV, Anti-Aligned.

(d) O_2^+, 7 eV, Anti-Aligned.

(e) N_2^+, 7 eV, Normalized Differences.

(f) O_2^+, 7 eV, Normalized Differences.
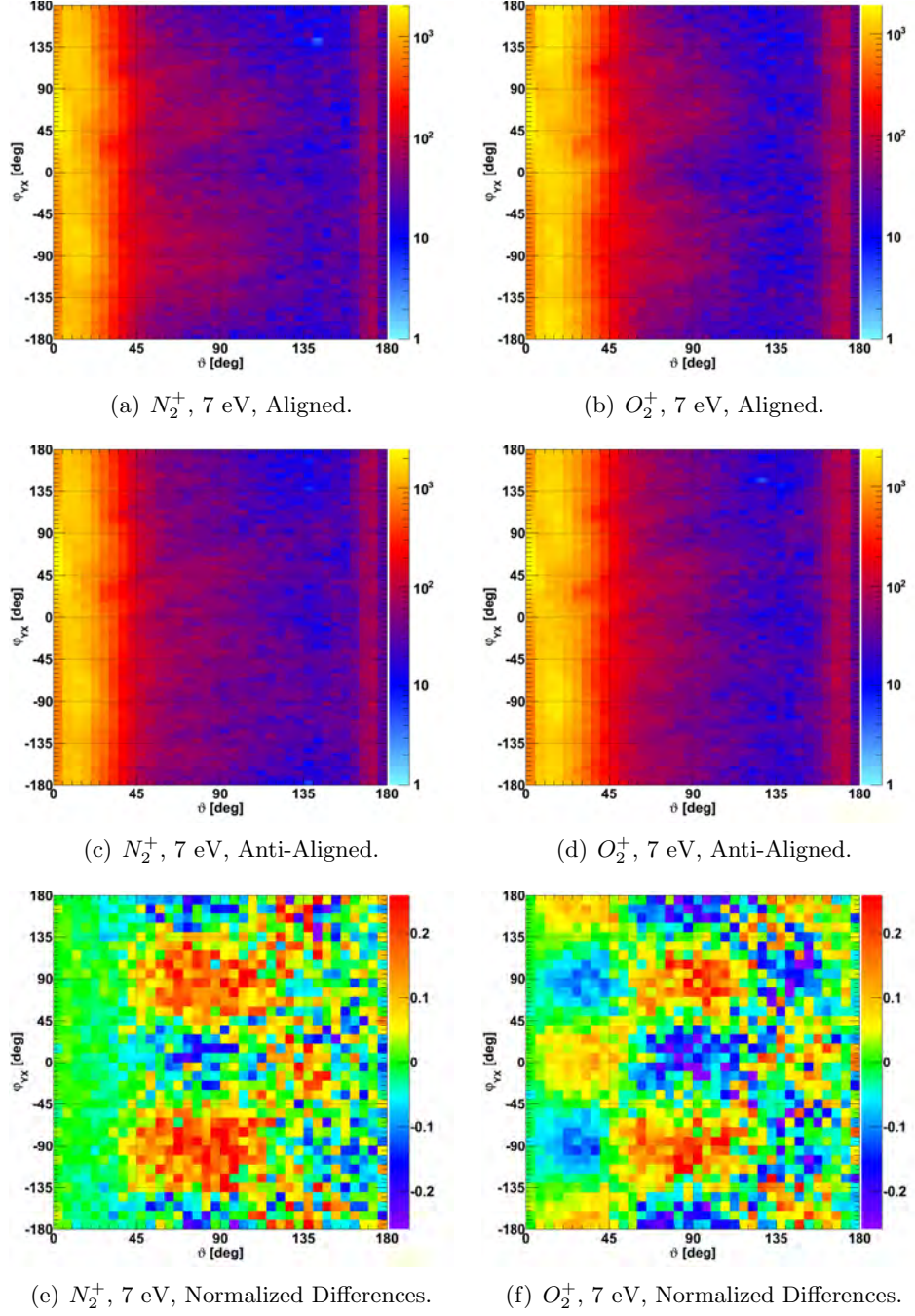
Figure C.6.: Experiment A: Electron re-scattering data in spherical coordinates within a diffraction sphere. The re-collision energy is 7 eV. Column on the *left* (*right*): Electrons correlated with N_2^+ (O_2^+) ions. *Top* row: Electrons from aligned molecules; *middle*: From anti-aligned molecules; *bottom*: Normalized differences between the above.

(a) N_2^+, 14 eV, Aligned.

(b) O_2^+, 14 eV, Aligned.

(c) N_2^+, 14 eV, Anti-Aligned.

(d) O_2^+, 14 eV, Anti-Aligned.

(e) N_2^+, 14 eV, Normalized Differences.

(f) O_2^+, 14 eV, Normalized Differences.
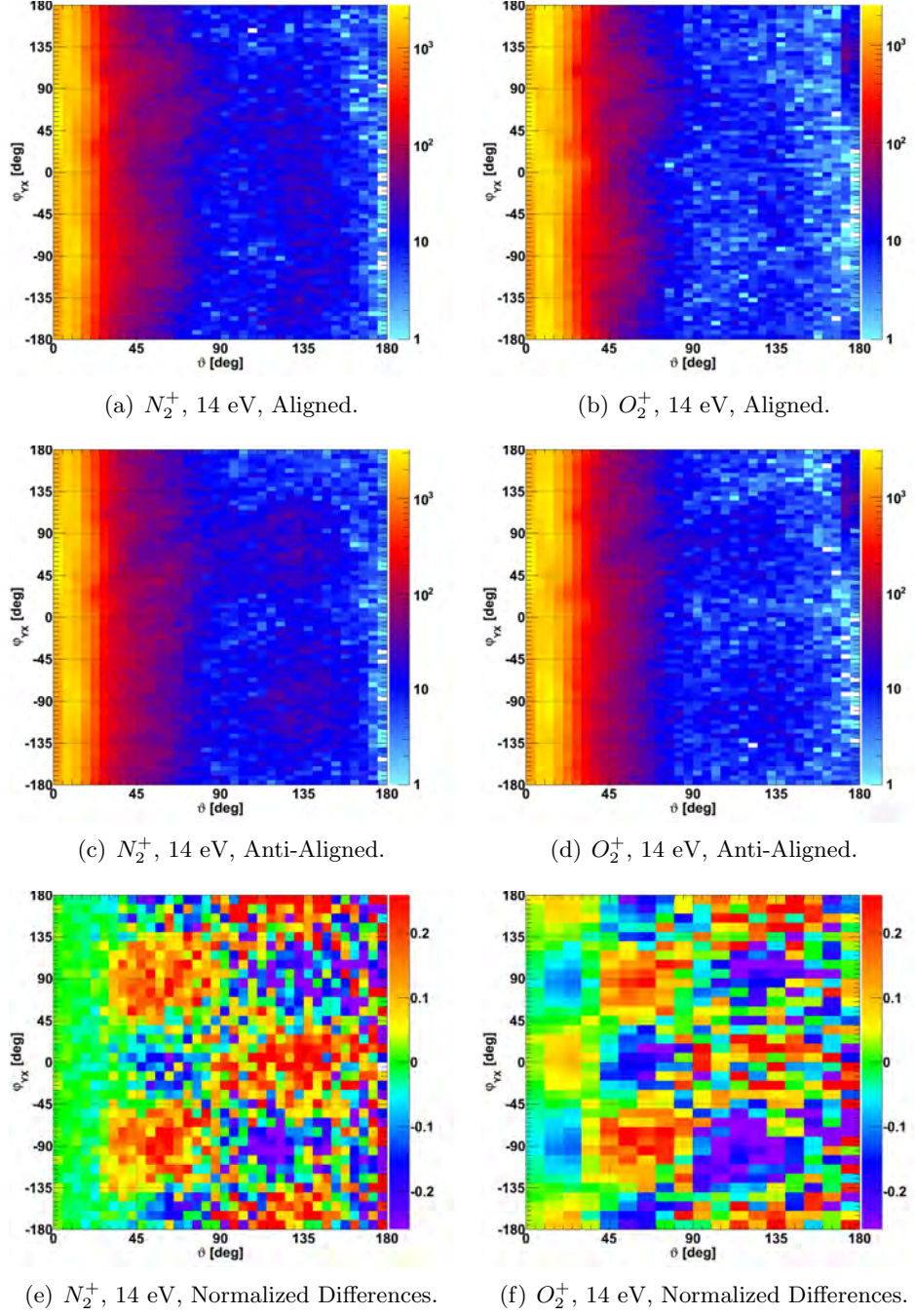
Figure C.7.: Experiment A: Electron re-scattering data in spherical coordinates within a diffraction sphere. The re-collision energy is 14 eV. Column on the *left* (*right*): Electrons correlated with N_2^+ (O_2^+) ions. *Top* row: Electrons from aligned molecules; *middle*: From anti-aligned molecules; *bottom*: Normalized differences between the above.

(a) N_2^+, 18 eV, Aligned.

(b) O_2^+, 18 eV, Aligned.

(c) N_2^+, 18 eV, Anti-Aligned.

(d) O_2^+, 18 eV, Anti-Aligned.

(e) N_2^+, 18 eV, Normalized Differences.

(f) O_2^+, 18 eV, Normalized Differences.
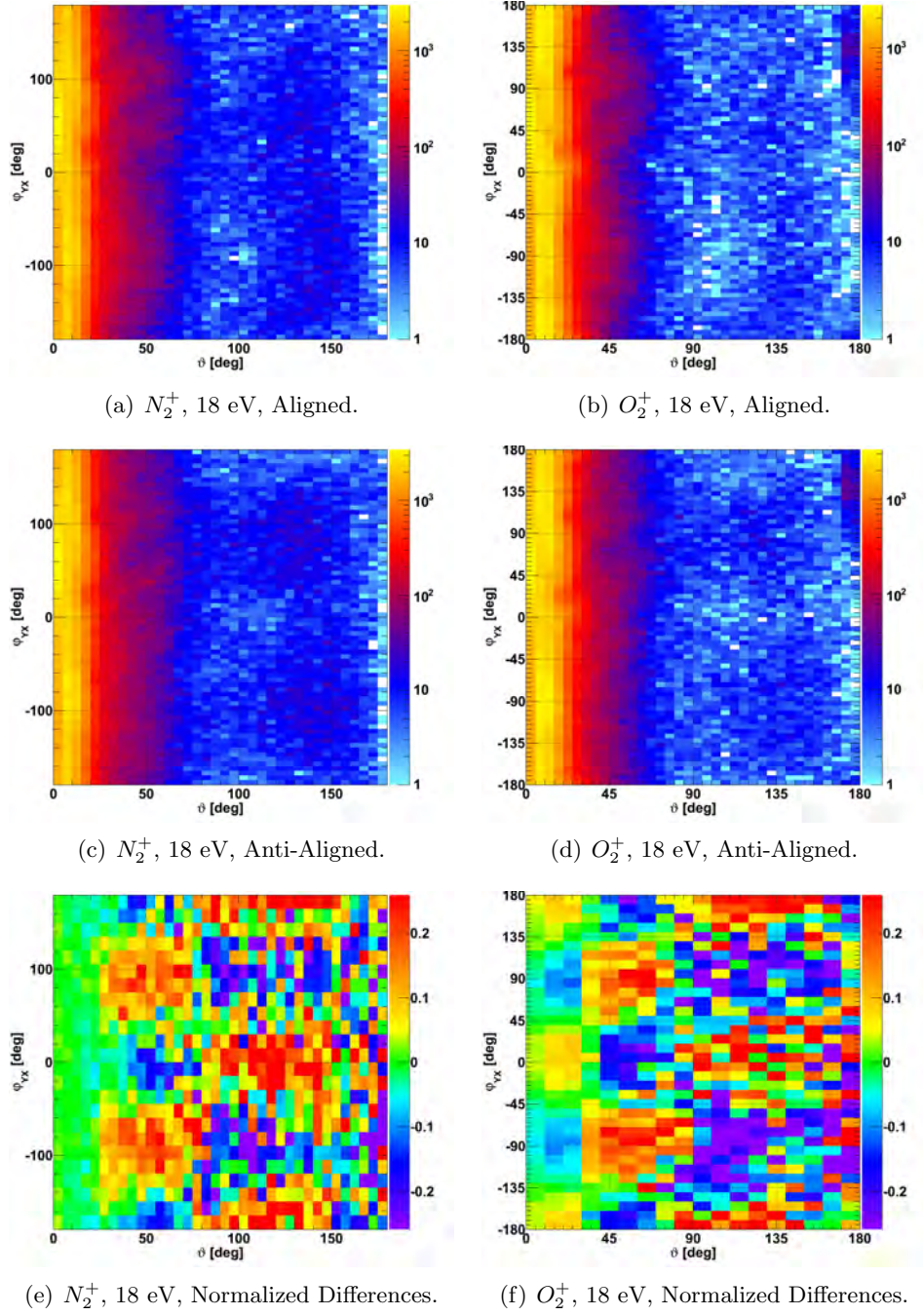
Figure C.8.: Experiment A: Electron re-scattering data in spherical coordinates within a diffraction sphere. The re-collision energy is 18 eV. Column on the *left* (*right*): Electrons correlated with N_2^+ (O_2^+) ions. *Top* row: Electrons from aligned molecules; *middle*: From anti-aligned molecules; *bottom*: Normalized differences between the above.

(a) N_2^+, 22 eV, Aligned.

(b) O_2^+, 22 eV, Aligned.

(c) N_2^+, 22 eV, Anti-Aligned.

(d) O_2^+, 22 eV, Anti-Aligned.

(e) N_2^+, 22 eV, Normalized Differences.

(f) O_2^+, 22 eV, Normalized Differences.
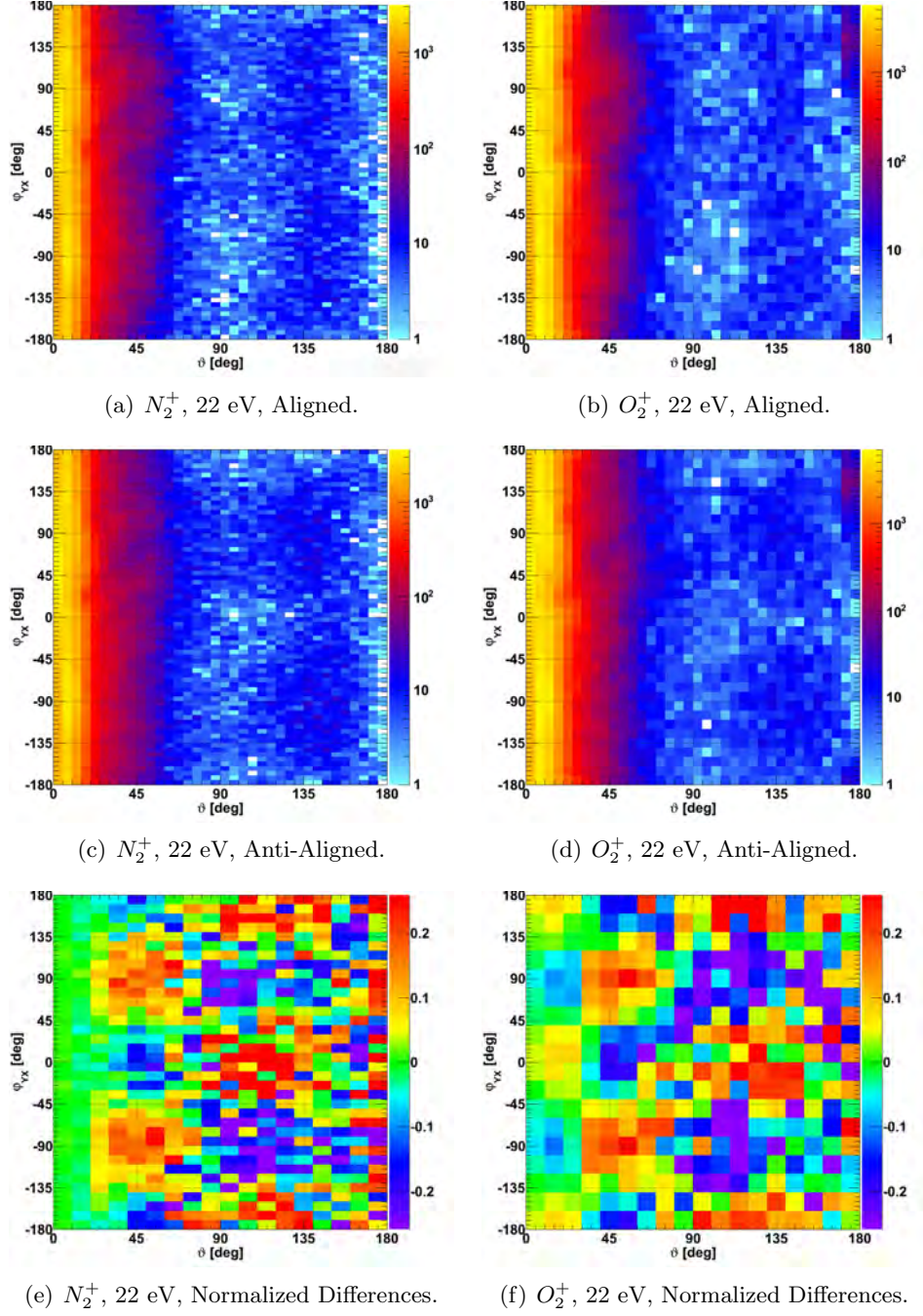
Figure C.9.: Experiment A: Electron re-scattering data in spherical coordinates within a diffraction sphere. The re-collision energy is 22 eV. Column on the *left* (*right*): Electrons correlated with N_2^+ (O_2^+) ions. *Top* row: Electrons from aligned molecules; *middle*: From anti-aligned molecules; *bottom*: Normalized differences between the above.

C.4. Conclusion

Despite being a very rough approximation, using a double-slit model is not entirely illegitimate. This way we will not be able to retrieve the full information on the scattering potential that is contained in the structures being missed as compared to the real cross sections. However, our experiment did not uncover these extra fringes, anyway. The most likely explanation are the angular distributions of molecules contributing to the electron spectra, which are not perfectly narrow. In oder to check this, it would be desirable to average exact scattering calculations over the angular distributions of ionizing molecules and then calculate normalized differences.

Hence, the rather gross simplification of describing the scattering molecular ion as a double-slit is currently not limiting the model's ability to reproduce the experiment. It is remarkable the similarity between the double-slit and the full scattering calculation can be improved by increasing the electron energy in the simple model.

D. The Pulse Envelope and Streaking

In chapter 2.3.1, we stated that the effect of streaking on a long pulse can be reasonably approximated by the relationship

$$p_{streak}(t_0) \approx p_{osc} \sin \omega t_0$$

given in equation (2.12) before. This shall be shown here.

Let us assume a Gaussian-shaped temporal pulse profile as in equation (2.2) with zero carrier-envelope phase. According to the computer algebra system MAPLE, the solution of equation (2.11) for this case is[1]

$$p_{streak}(t_0) = -\frac{1}{2} p_{osc} \sigma \sqrt{\pi} e^{-\frac{1}{4}\omega^2 \sigma^2} \left\{ 1 - Re \left[erf \left(\frac{t_0}{\sigma} - \frac{1}{2} i\omega\sigma \right) \right] \right\} \qquad \text{(D.1)}$$

with the so-called error function

$$erf(x) = \frac{2}{\sqrt{\pi}} \int_o^x e^{-\tilde{x}^2} \mathrm{d}\tilde{x}.$$

This result is not very convenient to use. We compare it graphically to the above approximation in figure D.1 for pulse conditions used in the experiment.

If we assume that ionization occurs preferentially in the central laser cycle, the approximation works perfectly. Otherwise, the effective streaking electric field is reduced with respect to its peak value within the pulse. This relates to ionization by a less intense pulse or outside the center of the focus.

---

[1]after significant manual cleanup...
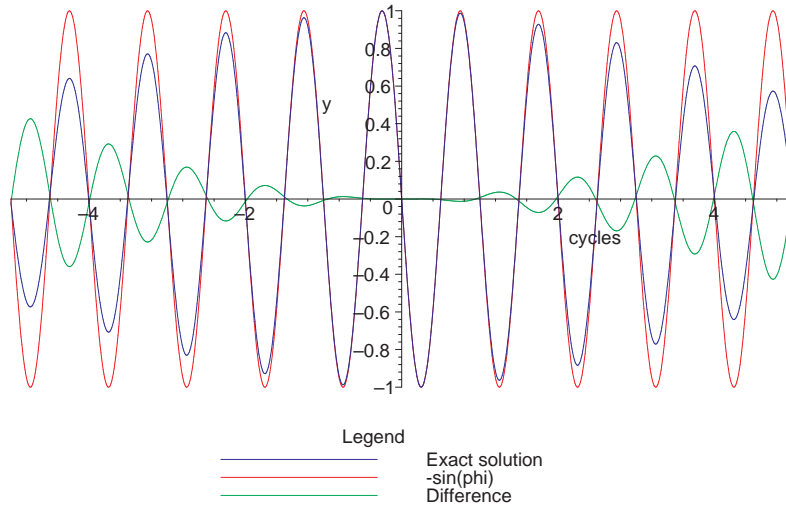
Figure D.1.: Calculation of the electron streaking by the laser field. *Horizontal axis*: Phase in optical cycles. *Vertical axis*: Final electron momentum in units of p_{osc}. *Blue* curve: Exact calculation according to equation (D.1), assuming a Gaussian-shaped fifteen-cycle (40 fs at 800 nm) pulse envelope. *Red*: Approximation as a continuous-wave field according to equation (2.12). *Green*: Difference between the two methods. It can be seen that the approximate method works well as long as electrons do not ionize more than about two optical cycles before or after the envelope maximum.

E. Technical Details

E.1. Programming of the Stage Controller

For experiment A, we used a stage controller of type Newport ESP 7000. A Newport ESP 300 motion controller was used in experiment B. Both controllers were programmable in the same language via a utility program from the host computer. The stage controller program used in experiment A is given in listing E.1, while the one for the N_2 measurement in experiment B is shown in listing E.2 and the respective one for the O_2 measurement is shown in listing E.3.

```
2ep              //Enter program #2.
3pa−0.442        //Axis 3: Move to absolute pos. −0.442 mm.
3ws              //Axis 3: Wait for it to stop.
3wt10000         //Wait for 10,000 milliseconds.
3pa−0.578        //Axis 3: Move to absolute pos. −0.578 mm.
3ws              //Axis 3: Wait for it to stop.
3wt10000         //Wait for 10,000 milliseconds.
3pa−1.313        //Axis 3: Move to absolute pos. −1.313 mm.
3ws              //Axis 3: Wait for it to stop.
3wt10000         //Wait for 10,000 milliseconds.
3pa−0.673        //Axis 3: Move to absolute pos. −0.673 mm.
3ws              //Axis 3: Wait for it to stop.
3wt10000         //Wait for 10,000 milliseconds.
qp               //Quit programming mode (prog. #2 complete).
2EX9999999       //Execute program #2 many times.
```

Listing E.1: Programming of the stage controller for experiment A. "Axis 3" is our translation stage. The comments were added later for comprehensibility.

```
23ep                  //Enter program #23.
1pa−0.582             //Axis 1: Move to absolute pos. −0.582 mm.
2pa0                  //Axis 2: Move to absolute pos. 0 deg.
1dl                   //Define label #1
2ws                   //Axis 2: Wait for it to stop.
2wt3000               //Axis2: Wait for 3,000 milliseconds.
2pr1                  //Axis2: Move by +1 deg.
1jl179                //Jump to label #1. Repeat this 179 times.
2ws                   //Axis 2: Wait for it to stop.
2pa180                //Axis 2: Move to absolute pos. 180 deg.
2dl                   //Define label #2
2ws                   //Axis 2: Wait for it to stop.
2wt3000               //Axis2: Wait for 3,000 milliseconds.
2pr−1                 //Axis2: Move by −1 deg.
2jl179                //Jump to label #2. Repeat this 179 times.
qp                    //Quit programming mode.
23EX9999999           //Execute program #23 many times.
```

Listing E.2: Programming of the stage controller for experiment B - N_2 measurement. "Axis 1" is our translation and "axis 2" the rotation stage. Comments were added later for comprehensibility.

```
23ep                  //Enter program #22.
1pa−0.439             //Axis 1: Move to absolute pos. −0.439 mm.
2pa0                  //Axis 2: Move to absolute pos. 0 deg.
1dl                   //Define label #1
2ws                   //Axis 2: Wait for it to stop.
2wt3000               //Axis2: Wait for 3,000 milliseconds.
2pr1                  //Axis2: Move by +1 deg.
1jl179                //Jump to label #1. Repeat this 179 times.
2ws                   //Axis 2: Wait for it to stop.
2pa180                //Axis 2: Move to absolute pos. 180 deg.
2dl                   //Define label #2
2ws                   //Axis 2: Wait for it to stop.
2wt3000               //Axis2: Wait for 3,000 milliseconds.
2pr−1                 //Axis2: Move by −1 deg.
2jl179                //Jump to label #2. Repeat this 179 times.
qp                    //Quit programming mode.
22EX9999999           //Execute program #22 many times.
```

Listing E.3: Programming of the stage controller for experiment B - O_2 measurement. "Axis 1" is our translation and "axis 2" the rotation stage. The only difference is the position of the translation stage (axis 1). Comments were added later for comprehensibility.

E.2. Custom List Mode File Format for Experiment B

Terminology

Channels are the inputs (= LEMO plugs) of the TDC. *Hits* are trigger signals applied to channels. *Events* are the hits of all channels, grouped within a certain time frame.

Data Types

Data types as used below (after MS VC++ on intel 32-bit architecture):

Type	Description / layout in file
short	16-bit integer
int	32-bit integer
long long	64-bit integer
float	32-bit floating point number
double	64-bit floating point number
string	unsigned int for length, followed by 8-bit ASCII characters
CString	Microsoft MFC CString class
CTime	Microsoft MFC CTime class. Apparently 32-bit integer.

LMF Header

In a COBOLD LM file, the event data section is preceeded by a header (one per file).

Non-User Header (COBOLD Standard)

Note: Offsets are given in bytes from the starting point of the file.

Offset	C++ Type	Contents	Comment
0	unsigned int	ArchiveFlag	> 0
4	int	DataFormat	-1 (=UserDefined)
8	unsigned int	Number of coordinates	Now irrelevant.
12	unsigned int	Header size [bytes]	
16	unsigned int	User header size [bytes]	
20	unsigned int	Number of events	
24	CTime	Starting time of LMF	
32	CTime	Stopping time of LMF	
40	CString	LMF Version String	Variable size!
?	CString	LMF file path (original)	Variable size!
?	CString	LMF Comment	Variable size!

User Header

The LMF user header contains all standard and some new pieces of information which were added for delaystage support. The user header starts at the offset 0+HeaderSize in the file. All offsets given are in bytes and relative to the beginning of the user header.

	Offset	C++ Type	Meaning
COBOLD Standard	0	int	User header size in bytes.
	4	int	DAQ version (should be 20080708).
	8	int	DAQ ID.
	12	double	Counter frequency in ticks/second.
	28	string	DAQInfo (variable length!)
	+0	int	LMF Version
	+4	116 bytes	116 bytes of uninterpreted data.
	+120	string	TDC config file (variable length!)
	+0	string	INL file (variable length!)
	+0	string	DNL file (variable length!)
	+0	4 bytes	4 bytes of uninterpreted data.
Delaystage - Custom!	+4	int	Number of axes (delaystages) used.
	+8	int	ID of COM port for stage controller.
	+12	int	ID of program in stage controller to be run.
	+16	unsigned int	Maximum age of position - axis 1.
	+20	double	Scaling factor of axis 1 (e.g. mm $\rightarrow$ ps).
	+28	double	Initial velocity of axis 1
	+36	unsigned int	Maximum age of position - axis 2.
	+40	double	Scaling factor of axis 2 (e.g. mm $\rightarrow$ ps).
	+48	double	Initial velocity of axis 2
	+56	unsigned int	Maximum age of position - axis 3.
	+60	double	Scaling factor of axis 3 (e.g. mm $\rightarrow$ ps).
	+68	double	Initial velocity of axis 3
	+76	unsigned int	Maximum age of position - axis 4.
	+80	double	Scaling factor of axis 4 (e.g. mm $\rightarrow$ ps).
	+88	double	Initial velocity of axis 4
	+96	string	Program source code the stage controller is to execute.

Event Datasets

After the headers (i.e., starting at the offset HeaderSize + UserHeaderSize in the file), the event datasets follow.

Assume we have k channels. Be n_k the number of hits caught by channel k. h_{kn} contains these hits. a is the number of axes (delaystages).

Each event dataset consists of four main sections:

	C++ Type	Meaning		
I	unsigned int	Event-header		= 0xf0f0f0f0 or event invalid.
	long long	hpTimestamp		in clock-ticks; see user header.
II	unsigned short	$n_1,$	$\ldots,$ n_k	Numbers of hits for each channel
III	int	$h_{11},$	$\ldots,$ h_{1n_1}	Hits of channel 1.
	int	$h_{21},$	$\ldots,$ h_{2n_2}	Hits of channel 2.
		$\vdots$		
	int	$h_{k1},$	$\ldots,$ h_{kn_k}	Hits of channel k.
IV	double	AxisPosition 1		Position of axis 1
	long long	Time of last poll 1		hpTimeStamp of pos. Ax. 1
		$\vdots$		
	double	AxisPosition a		Position of axis a
	long long	Time of last poll a		hpTimeStamp of pos. Ax. a

Part I is always written. It starts with the number $0xf0f0f0f0$ (hexadecimal) $=$ $11110000111100001111000011110000b$ (binary) $= 4042322160d$ (decimal). This can be used to make sure all reading is done accurately. The fixed number is followed by a 64 bit high precision time stamp. The conversion factor to seconds can be found in the LMF user header. Note this is NOT a unix timestamp, i.e., the unit is NOT milliseconds! (By tweaking .ccf files the time stamp can be cut down to 32 bit. However, this would make the resulting files incompatible with the analysis code as-is.)

Part II is always written, too. It consists of the number of hits for each channel. The data type is 16 bit integer, no sign. We are writing 17 channels, i.e., this section always consists of 17 successive unsigned short numbers. (Can be changed by tweaking .ccf files.)

Part III contains the actual hit data. All aquired hits for one channel up to a maximum of currently 16 (adjustable in .ccf files) are written successively, followed by the hits for the next channel, and so forth. The data type is signed 32 bit integer. No non-existing hits are written, e.g., if channel 3 caught no hits, there are no data from channel 3.

Part IV contains data from the delaystage(s). Only as many data sets are written as we have active delaystages (number of which is stored in the LMF header). The position of the respective axis is written as a 64-bit floating point number, followed by a 64 bit bigh precision time stamp dating back to the time when the computer inquired about the position for the last time.

References

[1] H. Stapelfeldt and T. Seideman, "Colloquium: Aligning molecules with strong laser pulses," Rev. Mod. Phys. **75**, 543–557 (2003). `doi:10.1103/RevModPhys.75.543`

[2] P. B. Corkum, "Plasma perspective on strong field multiphoton ionization," Phys. Rev. Lett. **71**, 1994–1997 (1993). `doi:10.1103/PhysRevLett.71.1994`

[3] M. Spanner, O. Smirnova, P. B. Corkum, and M. Y. Ivanov, "Reading diffraction images in strong field ionization of diatomic molecules," J. Phys. B **37**, L243–L250 (2004). `doi:10.1088/0953-4075/37/12/L02`

[4] M. Y. Ivanov, M. Spanner, and O. Smirnova, "Anatomy of strong field ionization," J. Mod. Opt. **52**, 165 (2005). `doi:10.1080/0950034042000275360`

[5] A. Staudte, *Subfemtosecond Electron Dynamics of H_2 in Strong Fields*, Ph.D. thesis, Institut für Kernphysik, J. W. Goethe Universität, Frankfurt am Main, Germany (2005).

[6] H. N. Chapman, P. Fromme, A. Barty, T. A. White, R. A. Kirian, A. Aquila, M. S. Hunter, J. Schulz, D. P. DePonte, U. Weierstall, R. B. Doak, F. R. N. C. Maia, A. V. Martin, I. Schlichting, L. Lomb, N. Coppola, R. L. Shoeman, S. W. Epp, R. Hartmann, D. Rolles, A. Rudenko, L. Foucar, N. Kimmel, G. Weidenspointner, P. Holl, M. Liang, M. Barthelmess, C. Caleman, S. Boutet, M. J. Bogan, J. Krzywinski, C. Bostedt, S. Bajt, L. Gumprecht, B. Rudek, B. Erk, C. Schmidt, A. Homke, C. Reich, D. Pietschner, L. Struder, G. Hauser, H. Gorke, J. Ullrich, S. Herrmann, G. Schaller, F. Schopper, H. Soltau, K. Kuhnel, M. Messerschmidt, J. D. Bozek, S. P. Hau-Riege, M. Frank, C. Y. Hampton, R. G. Sierra, D. Starodub, G. J. Williams, J. Hajdu, N. Timneanu, M. M. Seibert, J. Andreasson, A. Rocker, O. Jonsson, M. Svenda, S. Stern, K. Nass, R. Andritschke, C. Schroter, F. Krasniqi, M. Bott, K. E. Schmidt, X. Wang, I. Grotjohann, J. M. Holton, T. R. M. Barends, R. Neutze, S. Marchesini, R. Fromme, S. Schorb, D. Rupp, M. Adolph, T. Gorkhover, I. Andersson, H. Hirsemann, G. Potdevin, H. Graafsma, B. Nilsson, and J. C. H. Spence, "Femtosecond X-ray protein nanocrystallography," Nature **470**, 73–77 (2011). `doi:10.1038/nature09750`

[7] A. H. Zewail, "4D Ultrafast Electron Diffraction, Crystallography, and Microscopy," Ann. Rev. Phys. Chem. **57**, 65–103 (2006). `doi:10.1146/annurev.physchem.57.032905.104748`

[8] P. Baum and A. H. Zewail, "Attosecond electron pulses for 4D diffraction and microscopy," PNAS **104**, 18 409 (2007). `doi:10.1073/pnas.0709019104`

[9] T. Zuo, A. D. Bandrauk, and P. B. Corkum, "Laser-induced electron diffraction: a novel tool for probing ultrafast molecular dynamics," Chem. Phys. Lett. **259**, 313–320 (1996). `doi:10.1016/0009-2614(96)00786-5`

[10] M. Lein, J. P. Marangos, and P. L. Knight, "Electron diffraction in above-threshold ionization of molecules," Phys. Rev. A **66**, 051 404 (2002). `doi:10.1103/PhysRevA.66.051404`

[11] M. Meckel, D. Comtois, D. Zeidler, A. Staudte, D. Pavicic, H. C. Bandulet, H. Pepin, J. C. Kieffer, R. Dörner, D. M. Villeneuve, and P. B. Corkum, "Laser-Induced Electron Tunneling and Diffraction," Science **320**, 1478–1482 (2008). `doi:10.1126/science.1157980`

[12] J. D. Jackson, *Classical Electrodynamics* (Wiley, 1999).

[13] R. R. Freeman and P. H. Bucksbaum, "Investigations of above-threshold ionization using subpicosecond laser pulses," J. Phys. B **24**, 325–347 (1991). `doi:10.1088/0953-4075/24/2/004`

[14] D. B. Milosevic, G. G. Paulus, D. Bauer, and W. Becker, "Above-threshold ionization by few-cycle pulses," J. Phys. B **39**, 14 (2006). `doi:10.1088/0953-4075/39/14/R01`

[15] L. V. Keldysh, "Ionization in the Field of a Strong Electromagnetic Wave," Sov. Phys. JETP **20**, 1307–1314 (1965).

[16] N. B. Delone and V. O. Krainov, "Tunneling and barrier-suppression ionization of atoms and ions in a laser radiation field," Physics-Uspekhi **41**, 469 (1998). `doi:10.1070/PU1998v041n05ABEH000393`

[17] X. M. Tong, Z. X. Zhao, and C. D. Lin, "Theory of molecular tunneling ionization," Phys. Rev. A **66**, 033 402 (2002). `doi:10.1103/PhysRevA.66.033402`

[18] J. D. Louck, *Springer Handbook of Atomic, Molecular and Optical Physics* (Springer, 2006), chap. 2: Angular Momentum theory, pp. 9–74.

[19] Z. X. Zhao, X. M. Tong, and C. D. Lin, "Alignment-dependent ionization probability of molecules in a double-pulse laser field," Phys. Rev. A **67**, 043 404 (2003). `doi:10.1103/PhysRevA.67.043404`

[20] R. Murray, W.-K. Liu, and M. Y. Ivanov, "Partial Fourier-transform approach to tunnel ionization: Atomic systems," Phys. Rev. A **81**, 023 413 (2010). `doi:10.1103/PhysRevA.81.023413`

[21] R. Murray, M. Spanner, S. Patchkovskii, and M. Ivanov, "Tunnel ionization of molecules and molecular imaging," Phys. Rev. Lett. **Accepted** (2011).

[22] D. Pavicic, K. F. Lee, D. M. Rayner, P. B. Corkum, and D. M. Villeneuve, "Direct Measurement of the Angular Dependence of Ionization for N_2, O_2, and CO_2 in Intense Laser Fields," Phys. Rev. Lett. **98**, 243 001 (2007). `doi:10.1103/PhysRevLett.98.243001`

[23] A. Scrinzi, M. Y. Ivanov, R. Kienberger, and D. M. Villeneuve, "Attosecond physics," J. Phys. B **39**, R1–R37 (2006). `doi:10.1088/0953-4075/39/1/R01`

[24] J. Itatani, F. Quéré, G. L. Yudin, M. Y. Ivanov, F. Krausz, and P. B. Corkum, "Attosecond streak camera." Phys. Rev. Lett. **88**, 173 903 (2002). `doi:10.1103/PhysRevLett.88.173903`

[25] Z. Chen, A.-T. Le, T. Morishita, and C. D. Lin, "Quantitative rescattering theory for laser-induced high-energy plateau photoelectron spectra," Phys. Rev. A **79**, 033 409 (2009). `doi:10.1103/PhysRevA.79.033409`

[26] G. G. Paulus, W. Becker, W. Nicklich, and H. Walther, "Rescattering effects in above-threshold ionization: a classical model," Journal of Physics B: Atomic, Molecular and Optical Physics **27**, L703 (1994). `doi:10.1088/0953-4075/27/21/003`

[27] D. Ray, B. Ulrich, I. Bocharova, C. Maharjan, P. Ranitovic, B. Gramkow, M. Magrakvelidze, S. De, I. V. Litvinyuk, A. T. Le, T. Morishita, C. D. Lin, G. G. Paulus, and C. L. Cocke, "Large-Angle Electron Diffraction Structure in Laser-Induced Rescattering from Rare Gases," Phys. Rev. Lett. **100**, 143 002 (2008). `doi:10.1103/PhysRevLett.100.143002`

[28] T. Morishita, A.-T. Le, Z. Chen, and C. D. Lin, "Accurate retrieval of structural information from laser-induced photoelectron and high-order harmonic spectra by few-cycle laser pulses." Phys. Rev. Lett. **100**, 013 903 (2008). `doi:10.1103/PhysRevLett.100.013903`

[29] C. Ramsauer, "Über den Wirkungsquerschnitt der Gasmoleküle gegenüber langsamen Elektronen," Annalen der Physik **369**, 513 (1921). `doi:10.1002/andp.19213690603`

[30] C. Ramsauer and R. Kollath, "Die Winkelverteilung bei der Streuung langsamer Elektronen an Gasmolekülen," Naturwissenschaften **19**, 688–689 (1931), 10.1007/BF01516371. `doi:10.1007/BF01516371`

[31] C. Ramsauer and R. Kollath, "Die Winkelverteilung bei der Streuung langsamer Elektronen an Gasmolekülen. II. Fortsetzung," Annalen der Physik **404**, 529–561 (1932). `doi:10.1002/andp.19324040502`

[32] M. Fink, R.-D. Heuer, H. Kleinpoppen, K.-P. Lieb, N. Risch, and P. Schmüser, *Bestandteile der Materie*, Vol. 4 of Bergmann / Schaefer Lehrbuch der Experimentalphysik (de Gruyter, 2003), 2 edn.

[33] I. Hargittai, *Stereochemical Applications of Gas-Phase Electron Diffraction - Part A* (VCH, 1988), chap. 1 - A Survey: The Gas-Phase Electron Diffraction Technique of Molecular Structure Determination, pp. 1–54.

[34] F. Krausz and M. Ivanov, "Attosecond physics," Rev. Mod. Phys. **81**, 163 (2009). `doi:10.1103/RevModPhys.81.163`

[35] P. B. Corkum and F. Krausz, "Attosecond science," Nature Phys. **3**, 381 (2007). `doi:10.1038/nphys620`

[36] M. Lein, "Molecular imaging using recollision electrons," J. Phys. B **40**, R135 (2007). `doi:10.1088/0953-4075/40/16/R01`

[37] M. Hentschel, R. Kienberger, C. Spielmann, G. Reider, N. Milosevic, T. Brabec, P. Corkum, U. Heinzmann, M. Drescher, and F. Krausz, "Attosecond metrology," Nature **414**, 509–513 (2001). `doi:10.1038/35107000`

[38] J. Itatani, J. Levesque, D. Zeidler, H. Niikura, H. Pépin, J. C. Kieffer, P. B. Corkum, and D. M. Villeneuve, "Tomographic imaging of molecular orbitals," Nature **432**, 867–871 (2004). `doi:10.1038/nature03183`

[39] T. Nubbemeyer, K. Gorling, A. Saenz, U. Eichmann, and W. Sandner, "Strong-Field Tunneling without Ionization," Phys. Rev. Lett. **101**, 233 001 (2008). `doi:10.1103/PhysRevLett.101.233001`

[40] H. Niikura, F. Legare, R. Hasbani, A. D. Bandrauk, M. Y. Ivanov, D. M. Villeneuve, and P. B. Corkum, "Sub-laser-cycle electron pulses for probing molecular dynamics," Nature **417**, 917–922 (2002). `doi:10.1038/nature00787`

[41] S. N. Yurchenko, S. Patchkovskii, I. V. Litvinyuk, P. B. Corkum, and G. L. Yudin, "Laser-Induced Interference, Focusing, and Diffraction of Rescattering Molecular Photoelectrons," Phys. Rev. Lett. **93**, 223 003 (2004). `doi:10.1103/PhysRevLett.93.223003`

[42] S. X. Hu and L. A. Collins, "Imaging Molecular Structures by Electron Diffraction Using an Intense Few-Cycle Pulse," Phys. Rev. Lett. **94**, 073 004 (2005). `doi:10.1103/PhysRevLett.94.073004`

[43] M. Meckel, *Strong-Field Ionization of Aligned Oxygen Molecules*, Master's thesis, Institut für Kernphysik, J. W. Goethe Universität, Frankfurt am Main, Germany (2006).

[44] H. Hetzheim, C. Figueira de Morisson Faria, and W. Becker, "Interference effects in above-threshold ionization from diatomic molecules: Determining the internuclear separation," Phys. Rev. A **76**, 023 418 (2007). `doi:10.1103/PhysRevA.76.023418`

[45] T. Morishita, A.-T. Le, Z. Chen, and C.-D. Lin, "Potential for ultrafast dynamic chemical imaging with few-cycle infrared lasers," New J. Phys. **10**, 025 011 (2008). `doi:10.1088/1367-2630/10/2/025011`

[46] M. Busuladžić, A. Gazibegović-Busuladžić, D. B. Milošević, and W. Becker, "Angle-Resolved High-Order Above-Threshold Ionization of a Molecule: Sensitive Tool for Molecular Characterization," Phys. Rev. Lett. **100**, 203 003 (2008). `doi:10.1103/PhysRevLett.100.203003`

[47] M. Busuladžić, A. Gazibegović-Busuladžić, D. B. Milošević, and W. Becker, "Strong-field approximation for ionization of a diatomic molecule by a strong laser field. II. The role of electron rescattering off the molecular centers," Phys. Rev. A **78**, 033 412 (2008). `doi:10.1103/PhysRevA.78.033412`

[48] M. Okunishi, T. Morishita, G. Prümper, K. Shimada, C. D. Lin, S. Watanabe, and K. Ueda, "Experimental retrieval of target structure information from laser-induced rescattered photoelectron momentum distributions." Phys. Rev. Lett. **100**, 143 001 (2008). `doi:10.1103/PhysRevLett.100.143001`

[49] M. Okunishi, R. Itaya, K. Shimada, G. Pruemper, K. Ueda, M. Busuladzic, A. Gazibegovic-Busuladzic, D. B. Milosevic, and W. Becker, "Angle-resolved high-order above-threshold ionization spectra for N-2 and O-2: measurements and the strong-field approximation," J. Phys. B **41**, 201 004 (2008). `doi:10.1088/0953-4075/41/20/201004`

[50] M. Okunishi, R. Itaya, K. Shimada, G. Prümper, K. Ueda, M. Busuladžić, A. Gazibegović-Busuladžić, D. B. Milošević, and W. Becker, "Two-Source Double-Slit Interference in Angle-Resolved High-Energy Above-Threshold Ionization Spectra of Diatoms," Phys. Rev. Lett. **103**, 043 001 (2009). `doi:10.1103/PhysRevLett.103.043001`

[51] C. Cornaggia, "Electron-ion elastic scattering in molecules probed by laser-induced ionization," J. Phys. B **42**, 161 002 (2009). `doi:10.1088/0953-4075/42/16/161002`

[52] C. D. Lin, A.-T. Le, Z. Chen, T. Morishita, and R. Lucchese, "Strong-field rescattering physics - self-imaging of a molecule by its own electrons," J. Phys. B **43**, 122 001 (2010). `doi:10.1088/0953-4075/43/12/122001`

[53] M. Okunishi, H. Niikura, R. R. Lucchese, T. Morishita, and K. Ueda, "Extracting Electron-Ion Differential Scattering Cross Sections for Partially Aligned Molecules by Laser-Induced Rescattering Photoelectron Spectroscopy," Phys. Rev. Lett. **106**, 063 001 (2011). `doi:10.1103/PhysRevLett.106.063001`

[54] P. W. Dooley, I. V. Litvinyuk, K. F. Lee, D. M. Rayner, M. Spanner, D. M. Villeneuve, and P. B. Corkum, "Direct imaging of rotational wave-packet dynamics of diatomic molecules," Phys. Rev. A **68**, 023 406 (2003). `doi:10.1103/PhysRevA.68.023406`

[55] K. F. Lee, *Controlling Molecular Alignment*, Ph.D. thesis, McMaster University, Hamilton, ON, Canada (2006).

[56] P. W. Dooley, *Molecular Imaging using Femtosecond Laser Pulses*, Ph.D. thesis, McMaster University, Hamilton, ON, Canada (2003).

[57] M. Spanner, *Field-Free Alignment and Strong Field Control of Molecular Rotors*, Ph.D. thesis, University of Waterloo, Waterloo, ON, Canada (2004).

[58] P. Linstrom and W. Mallardeds.,, *NIST Chemistry WebBook, NIST Standard Reference Database Number 69* (National Institute of Standards and Technology, Gaithersburg MD, 20899, USA, http://webbook.bist.gov, 2011).

[59] S. Backus, C. G. Durfee, M. M. Murnane, and H. C. Kapteyn, "High power ultrafast lasers," Rev. Sci. Instrum. **69**, 1207 (1998). `doi:10.1063/1.1148795`

[60] A. E. Siegman, *Lasers* (University Science Books, Sausalito, CA, 1986).

[61] D. Strickland and G. Mourou, "Compression of amplified chirped optical pulses," Opt. Commun. **56**, 219 – 221 (1985). `doi:10.1016/0030-4018(85)90120-8`

[62] ThorLabs, 435 Route 206, P.O. Box 366, Newton, NJ 07860-0366, *ThorLabs Catalog*, 20 edn.

[63] G. Tejeda, B. Maté, J. M. Fernández-Sánchez, and S. Montero, "Temperature and Density Mapping of Supersonic Jet Expansions Using Linear Raman Spectroscopy," Phys. Rev. Lett. **76**, 34 (1996). `doi:10.1103/PhysRevLett.76.34`

[64] "MCP Assembly Selection Guide," Tech. rep., Hamamatsu Photonics K.K., Electron Tube Center (2002).

[65] J. L. Wiza, "Microchannel Plate Detectors," Nuclear Instruments and Methods **162**, 587–601 (1979).

[66] RoentDek Handels GmbH, *TDC8 ISA & PCI and TDC8PCI2 Manual*, 6.2.90.2 edn.

[67] A. Czasch, *Documentation for the Resort-Routine used for square and hexagonal Delayline-Detectors*, Institut für Kernphysik, J. W. Goethe Universität, Frankfurt am Main, Germany.

[68] L. Foucar, *Ionisation und Anregung von Wasserstoff- und Deuteriummolekülen mit Synchrotronstrahlung*, Master's thesis, Institut für Kernphysik, J. W. Goethe Universität, Frankfurt am Main, Germany (2003).

[69] R. Brun and F. Rademakers, *ROOT: An Object-Oriented Data Analysis Framework*, CERN. http://root.cern.ch/

[70] M. Lundqvist, D. Edvardsson, P. Baltzer, M. Larsson, and B. Wannberg, "Observation of predissociation and tunnelling processes in O_2^{2+} : a study using Doppler free kinetic energy release spectroscopy and ab initio CI calculations," J. Phys. B **29**, 499–514 (1996). doi:10.1088/0953-4075/29/3/016

[71] M. Lundqvist, D. Edvardsson, P. Baltzer, and B. Wannberg, "Doppler-free kinetic energy release spectrum of N_2^{2+}," J. Phys. B **29**, 1489 (1996). doi:10.1088/0953-4075/29/8/013

[72] A. S. Alnaser, S. Voss, X. M. Tong, C. M. Maharjan, P. Ranitovic, B. Ulrich, T. Osipov, B. Shan, Z. Chang, and C. L. Cocke, "Effects Of Molecular Structure on Ion Disintegration Patterns In Ionization of O_2 and N_2 by Short Laser Pulses," Phys. Rev. Lett. **93**, 113 003 (2004). doi:10.1103/PhysRevLett.93.113003

[73] A. S. Alnaser, X. M. Tong, T. Osipov, S. Voss, C. M. Maharjan, B. Shan, Z. Chang, and C. L. Cocke, "Laser-peak-intensity calibration using recoil-ion momentum imaging," Phys. Rev. A **70**, 023 413 (2004). doi:10.1103/PhysRevA.70.023413

[74] D. Zeidler, *Private Communication* (Steacie Institute for Molecular Sciences, National Research Council, 100 Sussex Drive, Ottawa, ON, Canada K1A0R6).

[75] M. Meckel, D. Comtois, D. Zeidler, A. Staudte, D. Pavicic, H. C. Bandulet, H. Pepin, J. C. Kieffer, R. Dörner, D. M. Villeneuve, and P. B. Corkum, "Laser-Induced Electron Tunneling and Diffraction: Supplementary Online Material," (2008). http://www.sciencemag.org/cgi/content/full/320/5882/1478/DC1

[76] D. Comtois, D. Zeidler, H. Pépin, J. C. Kieffer, D. M. Villeneuve, and P. B. Corkum, "Observation of Coulomb focusing in tunnelling ionization of noble

gases," J. Phys. B **38**, 1923–1933 (2005). `doi:10.1088/0953-4075/38/12/008`

[77] D. Comtois, *Private Communication* (Institut National de la Recherche Scientifique - Énergie, Matériaux et Télécommunication, 1650 boulevard Lionel-Boulet, Varennes, Québec, Canada, J3X 1S2).

[78] Y. Huismans, A. Rouzée, A. Gijsbertsen, J. H. Jungmann, A. S. Smolkowska, P. S. W. M. Logman, F. Lépine, C. Cauchy, S. Zamith, T. Marchenko, J. M. Bakker, G. Berden, B. Redlich, A. F. G. van der Meer, H. G. Muller, W. Vermin, K. J. Schafer, M. Spanner, M. Y. Ivanov, O. Smirnova, D. Bauer, S. V. Popruzhenko, and M. J. J. Vrakking, "Time-Resolved Holography with Photoelectrons," Science **331**, 61–64 (2011). `doi:10.1126/science.1198450`

[79] C. Smeenk, *Private Communication* (Steacie Institute for Molecular Sciences, National Research Council, 100 Sussex Drive, Ottawa, ON, Canada K1A0R6).

[80] C. Smeenk, L. Arissian, A. Staudte, D. M. Villeneuve, and P. B. Corkum, "Momentum space tomographic imaging of photoelectrons," Journal of Physics B: Atomic, Molecular and Optical Physics **42**, 185 402 (2009). `doi:10.1088/0953-4075/42/18/185402`

[81] T. N. Rescigno, C. W. McCurdy, A. E. Orel, and B. H. Lengsfield, *Computational Methods for Electron-Molecule Collisions* (Plenum Press, New York, 1995).

[82] T. N. Rescigno, *Private Communication* (Lawrence Berkeley National Lab, Berkeley, CA, USA).

[83] A. E. Orel, *Private Communication* (University of California, Davis, CA, USA).

Acknowledgements

I am indebted to the people at Frankfurt who made the experiments possible by developing and supporting the required components. Amongst others, this is *Lothar Ph. H. Schmidt* (signal decoupling, amplification and discrimination electronics), *Till Jahnke* / Cronologic (time to digital converters), *Achim Czasch* (data analysis software development), *Klaus Ullmann-Pfleger* (data acquisition software development) and *Ottmar Jagutzki* (everything). *Magdalene Zimmer* made the three-dimensional drawings of the setup.

I have to thank more members of the research groups both at Frankfurt and Ottawa for making work enjoyable (and possible) than I can list here. Special thanks go to *Andrew Shiner* for lending me various lab supplies whose shortage tended to turn out after hours and the "inhabitants" of office 01.313 for many good chats.

The *German National Academic Foundation* (Studienstiftung) provided me with funding for three years. But almost more importantly, their social and scientific program was an opportunity to learn about different disciplines and make friends with some of the crazyest individuals on the planet. Prof. *D.-H. Rischke* and his group of Frankfurt "Stiftis" added to this. After all, it is quite sad being an alumnus now. . .

I would also like to thank my parents and family for almost three decades of encouragement and support of whatever I was doing.

And ultimately: Thank you for reading!

                                                                            The end.

Ausführliche Zusammenfassung

Hinweis: Eine gekürzte Zusammenfassung ist dieser Arbeit sowohl in deutscher, als auch in englischer Sprache vorangestellt.

Allgemeines

In der vorliegenden Arbeit wird die Ionisation von Stickstoff- und Sauerstoff-Molekülen in starken, nicht-resonanten Laserlicht-Pulsen untersucht.

Als Strahlungsquelle diente ein gepulstes Titan-Saphir-Lasersystem mit einer Wellenlänge von $\lambda = 800$ nm und einer Pulslänge von $\tau = 40$ fs. Die Energie eines Photons betrug $W_{Ph} = 1,55$ eV.

Molekül-Ausrichtung

Das Hauptaugenmerk galt dem Kanal der Einfachionisation, der neben einem Elektron ein stabiles Molekülion (N_2^+ / O_2^+) erzeugt. Da in diesem Fall keine Dissoziation des Ions stattfindet, kann nicht aus der Flugrichtung ionischer Fragmente auf die Ausrichtung der Molekülachse geschlossen werden. Die Abhängigkeit des Prozesses vom Winkel zwischen der Molekülachse und der Polarisationsrichtung des ionisierenden Lichtes ist nur dann zugänglich, wenn die Ausrichtung der Molekülachsen vor dem Zeitpunkt der Ionisation aktiv beeinflusst werden kann.

Hierzu wurde die Technik der „nichtadiabatischen Molekülausrichtung" („nonadiabatic molecular alignment") angewandt. Ein erster, mäßig intensiver Lichtpuls bewirkte die Ausrichtung der Molekülachsen im Laborsystem. In einem definierten zeitlichen Abstand folgte ein zweiter, hochintensiver „Probe"-Puls, der die ausgerichteten Moleküle ionisierte.

In einem ersten Experiment („Experiment A") waren nur zwei Verteilungen von Molekülachsen möglich. In einem zweiten, sehr ähnlichen Versuch („Experiment B") wurde diese Einschränkung aufgehoben.

Spektrometer

Die Impulse der durch den „Probe"-Puls freigesetzten Elektronen und Ionen wurden mittels eines sogenannten COLTRIMS Spektrometers vermessen. Die wichtigste Eigenschaft eines solchen ist die Möglichkeit, Impuls-Vektoren von Elektronen und Ionen in Koinzidenz zu rekonstruieren. Dies ermöglicht die kinematisch vollständige Betrachtung von Reaktionen.

Überprüfung der Ausrichtung

Mit niedriger Rate fanden Doppelionisationen statt. Diese waren nicht der hauptsächliche Gegenstand der Untersuchungen. Sofern das Doppelion in zwei einfach geladene Fragmente aufbrach, konnten deren Flugrichtungen jedoch genutzt werden, um auf die Ausrichtung der Molekülachse vor der Ionisation zu schließen. Auf diese Weise wurde der erreichte Grad an Ausrichtung vermessen.

Experimente „A" und „B"

In „Experiment A" wurden Elektronen-Impulsverteilungen für zwei verschiedene Molekülausrichtungen von N_2 und O_2 bestimmt. Um sicher zu gehen, dass die experimentellen Bedingungen für Stickstoff- und Sauerstoff-Moleküle exakt identisch waren, kam ein Gasgemisch zum Einsatz. Erst in der auf die Datenaufnahme folgenden Analyse wurden die Messdaten nach Molekül- bzw. Ionenarten sortiert.

„Experiment B" bestand hingegen aus zwei sukzessiven Messungen für N_2 und O_2. Der gesamte Aufbau war hinreichend stabil um trotzdem direkte Vergleiche zuzulassen. Die Beschränkung auf zwei Molekülausrichtungen wurde aufgehoben. Die Polarisationsrichtung des ausrichtenden Lichtpulses und damit die Vorzugsrichtung der Molekülachsen-Verteilung wurde in Schritten von 2° rotiert.

Datenanalyse

Die mittels COLTRIMS unmittelbar erhobenen Rohdaten mussten zunächst im Rahmen einer aufwendigen Datenanalyse in Impulse umgerechnet werden.

Es stellte sich heraus, dass die Elektronen-Zählraten für höhere Impulse sehr stark abfielen. Dies machte es unmöglich, durch direkten visuellen Vergleich von Graphen solcher Verteilungen Unterschiede zwischen den untersuchten Molekülsorten und -Winkelverteilungen zu erkennen. Um die Unterschiede von Elektronen-Impulsverteilungen sichtbar zu machen wurden „Normierte Differenzen" verwendet. Diese sind definiert als

$$nd = \frac{\text{Signal} - \text{Referenz}}{\text{Signal} + \text{Referenz}}$$

und auch als „Kontrast" oder „Asymmetrie-Parameter" bekannt. Als Signal und Referenz dienten jeweils Elektronen-Verteilungen, die von unterschiedlich ausgerichteten Molekül-Ensembles stammten.

Wichtigste Ergebnisse

Die normierten Differenzen von Elektronen-Impulsverteilungen aus Experiment A sind für N_2 und O_2 in Abbildung E.1 reproduziert. Die Graphen für Stickstoff
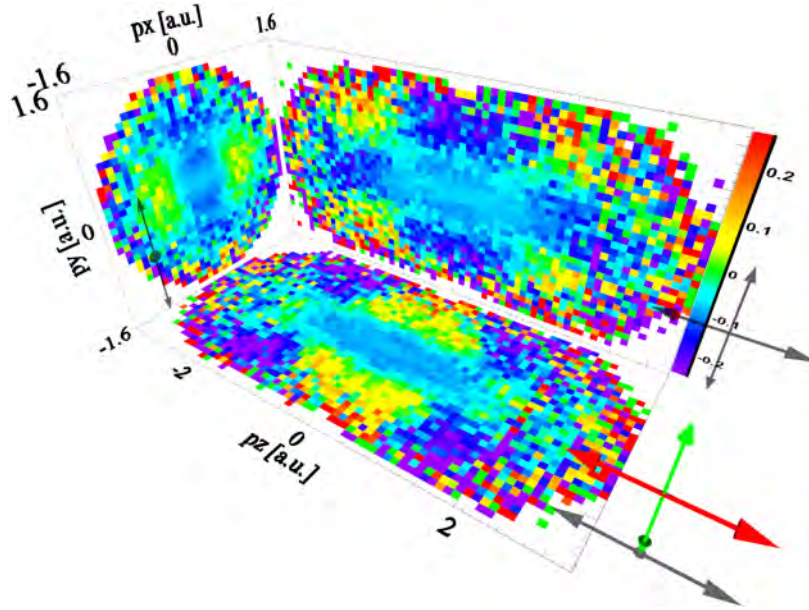
(a) Mit N_2^+-Ionen korrelierte Elektronen.
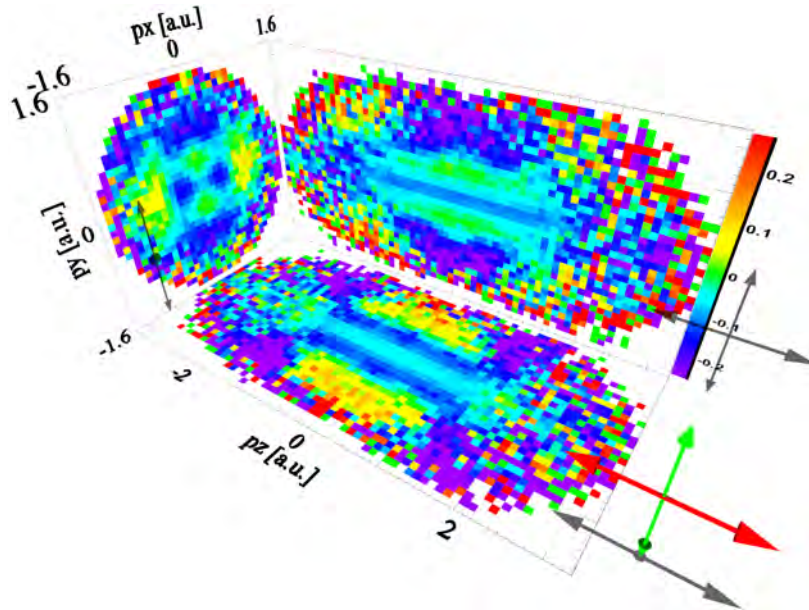
(b) Mit O_2^+-Ionen korrelierte Elektronen.

Abbildung E.1.: Ergebnis von Experiment A: „Normierte Differenzen" (siehe Text) von Elektronen-Impulsverteilungen aus dem Einfachionisationsprozess $X_2 \rightarrow X_2^+ + e^-$. *Rote* Doppelpfeile zeigen die Polarisationsrichtung des ionisierenden und *grüne* die Polarisationsrichtung des ausrichtenden Laserlicht-Pulses an. Die als „Signal" genutzte Elektronen-Verteilung wurde von Molekülen gewonnen, deren Achsen vorzugsweise entlang der Polarisation des ausrichtenden Pulses (grüner Pfeil) orientiert waren. Die „Referenz"-Verteilung wurde von Molekülen gewonnen, die verstärkt senkrecht zu jener Polarisationsrichtung orientiert waren. Siehe Text.

(a) und Sauerstoff (b) zeigen im Bereich niedriger Impulse sehr unterschiedliche und bei höheren Impulsen nahezu identische Strukturen. Dies wird, untermauert durch Simulationen, folgendermaßen interpretiert:

1. Im Bereich niedriger Elektronen-Impulse senkrecht zur Polarisationsrichtung des ionisierenden Lichtpulses ($x-y$ Ebene) wird der "Fingerabdruck" des ionisierten Molekülorbitals sichtbar.

   Die Ionisation des Elektrons geschieht durch Tunneln aus dem durch das elektrische Feld des intensiven Laserlicht-Pulses unterdrückten elektrostatischen Potential des Moleküls. Die Symmetrie der elektronischen Wellenfunktion bleibt dabei erhalten. Die Elektronen-Impulsverteilung in der Ebene senkrecht zur Polarisation des ionisierenden Lichtes entspricht einer Projektion des Orbitals in diese Ebene, multipliziert mit einer gaußförmigen Einhüllenden. Letztere hängt allerdings nicht von der Ausrichtung der Molekülachse ab und wird daher durch die Berechnung normierter Differenzen eliminiert.

   Die höchsten besetzten Molekülorbitale von N_2 und O_2 haben sehr unterschiedliche Formen (Symmetrien), was die unterschiedlichen Strukturen in den verglichenen Elektronen-Verteilungen bei niedrigen Impulsen begründet.

2. Die Strukturen bei höheren Impulsen können in erster Näherung als Doppelspalt-Interferenz interpretiert werden. Ein getunneltes Elektronen-Wellenpaket propagiert im oszillierenden elektrischen Feld des Lichtpulses. Von diesem kann es unter bestimmten Bedingungen auf das Ion hin zurück beschleunigt werden und dort streuen. Wir betrachten den Fall elastischer "Rückstreuung". In erster Näherung wirken die Bestandteile des diatomaren Molekülions wie ein Doppelspalt, an dem die streuende Elektronen-Welle gebeugt wird.

In Experiment B wurde die Molekülausrichtungs-Richtung in kleinen Schritten variiert. Sowohl der Effekt der Elektronenbeugung am Ion, als auch (im Falle von N_2 mit Einschränkungen) die Abbildung des ionisierten Orbitals wurde erneut beobachtet.

Auswirkungen

Die beobachteten Effekte ermöglichen interessante neue Messmethoden.

Laser-Induziertes Tunneln

Das in Experiment A beobachtete Tunneln der Wellenfunktion des äußersten Elektrons ermöglicht eine Messung der Elektronendichte des höchsten besetzten Molekülorbitals in Analogie zu einem Rastertunnelmikroskop (RTM). Anstatt

einer Spitze gibt die Polarisation des ionisierenden Laserlicht-Pulses die Richtung des Tunnelns vor. Durch ein Drehen der Molekülachse relativ zu dieser Richtung kann „gerastert" werden. In der vorgelegten Arbeit wurde nicht nur der „Tunnelstrom" (d.h. die Ionisationsrate), sondern auch die Impulsverteilung der getunnelten Elektronen bestimmt. Hierzu ist kein unmittelbares Analogon aus der konventionellen Rastertunnel-Mikroskopie ersichtlich.

Experiment B war ursprünglich von der Idee eines „Laser-RTMs" inspiriert. Es sollte möglich sein, aus den unter verschiedenen Winkeln aufgenommenen Projektionen des Molekülorbitals mittels einer tomographischen Inversion die dreidimensionalen Elektronen-Dichteverteilungen im Orbital zu rekonstruieren. Diesbezügliche Entwicklungen sind bei Kooperationspartnern im Gange.

Elektronenbeugung

Die beobachtete Beugung des rückgestreuten Elektrons ermöglicht den Rückschluss auf die Positionen der Kerne im Molekülion. Es besteht die Hoffnung, dass sich in Zukunft detailliertere Informationen über das streuende Potential jenseits des einfachen Doppelspalt-Modells gewinnen lassen. Rückstreuung höherenergetischer Elektronen sollte hingegen eine verbesserte Ortsauflösung ermöglichen.

Ausblick

Beide Informationen - Ionisiertes Orbital und Beugungsbild des Ions - werden simultan in ein- und derselben Messung gewonnen. Die zeitliche Auflösung wird durch rein optische Parameter (Licht-Wellenlänge, Pulslänge) determiniert. Sie kann mittels ultrakurzer, phasenstabiler Laserlicht-Pulse in den Bereich einer Femtosekunde oder darunter verbessert werden.

In der vorliegenden Arbeit wurden die prinzipielle Möglichkeit der vorgestellten Techniken (Tunneln und Beugung) gezeigt (proof-of-concept). An verschiedenen Stellen sind Verbesserungen möglich. Die Zukunft wird zeigen, ob der apparative und personelle Aufwand die erreichbaren Ergebnisse rechtfertigt.

Lebenslauf

Name	Jens Moritz Meckel
Geburtstag	07.10.1981
Geburtsort	Frankfurt am Main
Nationalität	deutsch
Familienstand	ledig

Bildungsweg

Abitur	29.05.2001, Humboldtschule, Bad Homburg
Vordiplom Physik	26.05.2003, J. W. Goethe-Universität, Frankfurt
Diplom Physik	05.09.2006, J. W. Goethe-Universität, Frankfurt

Auszeichnungen und Preise

03/2004	Aufnahme in die Studienstiftung des deutschen Volkes
11/2007	Promotionsstipendium der Studienstiftung des deutschen Volkes
01/2008	Philipp Siedler-Wissenschaftspreis 2007 für Diplomarbeit

Akademische Lehrer (Physik & Chemie)

Prof. Dr. B. Brutschy
Prof. Dr. P. B. Corkum
Prof. Dr. R. Dörner
Prof. Dr. C. Greiner
Prof. Dr. Dr. h.c. mult. W. Greiner
Prof. Dr. M. Huth
Prof. Dr. B. O. Kolbesen
Prof. Dr. M. Lang
Dr. J. Meyer
Prof. Dr. D. Schubert
Prof. Dr. Dr. h.c. R. Stock
Prof. Dr. H. Schmidt-Böcking
Prof. Dr. Th. Stöhlker
Prof. Dr. D. M. Villeneuve
Prof. Dr. J. Wachtveitl
Prof. Dr. J. Weidmann

Forschungsaufenthalte

2003	3 Wochen	National Research Council, Ottawa, Kanada
2004/05	1 Jahr	National Research Council, Ottawa, Kanada
2008	1 Woche	BESSY II, Berlin
	4 Monate	National Research Council, Ottawa, Kanada
2009	1 Woche	Freie Universität, Berlin
2010	1 Woche	BESSY II, Berlin

Eingeladene Vorträge

1. Workshop "Advances in Strong-Field and Attosecond Physics", University College London, London, England, 23.-25.06.2010.
   Titel: Laser-Induced Electron Tunneling and Diffraction.

2. Workshop "Studies of Atoms and Molecules with New Light Sources", Sandbjerg Estate, Sonderborg, Dänemark, 27.-29.05.2009.
   Titel: Laser-Induced Electron Tunneling and Diffraction.

3. Festveranstaltung zur Verleihung des Philipp Siedler-Wissenschaftspreises 2007, Physikalischer Verein, Frankfurt am Main, 16.01.2008.
   Titel: Ionisation ausgerichteter Sauerstoff-Moleküle in starken Laser-Feldern.

Sonstige Konferenzbeiträge

1. Ultra-Fast Dynamic Imaging of Matter II, Ischia, Italien, 30.04.-03.05.2009.
   Vortrag: Laser-Induced Electron Tunneling and Diffraction.

2. Gordon Conference on Multiphoton Processes, Tilton, NH, USA, 08.-13.06.2008.
   Poster: Laser-Induced Electron Tunneling and Diffraction.

3. DPG-Frühjahrestagung, Darmstadt, 10.-14.03.2008.
   Vortrag: Einfachionisation kleiner, ausgerichteter Moleküle in starken Laser-Feldern.

4. Gordon Conference on Quantum Control of Light and Matter, Waterville, ME, USA, 31.07.-05.08.2005.
   Poster: Photoelectron Emission from Aligned O2 Molecules.

Artikel in Fachzeitschriften (peer reviewed)

1. J. Titze, M. S. Schöffler, H.-K. Kim, F. Trinter, M. Waitz, J. Voigtsberger, N. Neumann, B. Ulrich, K. Kreidi, R. Wallauer, M. Odenweller, T. Havermeier, S. Schössler, **M. Meckel**, L. Foucar, T. Jahnke, A. Czasch, L. Ph. H. Schmidt, O. Jagutzki, R. E. Grisenti, H. Schmidt-Böcking, H. J.

Lüdde, R. Dörner: **Ionization Dynamics of Helium Dimers in Fast Collisions with He^{++}**. Phys. Rev. Lett. 106, 033201 (2011)

2. B. Ulrich, A. Vredenborg, A. Malakzadeh, **M. Meckel**, K. Cole, M. Smolarski, Z. Chang, T. Jahnke, and R. Dörner: **Double-ionization mechanisms of the argon dimer in intense laser fields.** Phys. Rev. A 82, 013412 (2010).

3. T. Jahnke, H. Sann, T. Havermeier, K. Kreidi, C. Stuck, **M. Meckel**, M. Schöffler, N. Neumann, R. Wallauer, S. Voss, A. Czasch, O. Jagutzki, A. Malakzadeh, F. Afaneh, Th. Weber, H. Schmidt-Böcking, R. Dörner: **Ultrafast energy transfer between water molecules**. Nature Physics 6, 139 (2010).

4. A. Staudte, S. Patchkovskii, D. Pavičić, H. Akagi, O. Smirnova, D. Zeidler, **M. Meckel**, D. M. Villeneuve, R. Dörner, M. Yu. Ivanov, P. B. Corkum: **Angular Tunneling Ionization Probability of Fixed-in-Space H$_2$ Molecules in Intense Laser Pulses**. Phys. Rev. Lett. 102, 033004 (2009).

5. **M. Meckel**, D. Comtois, D. Zeidler, A. Staudte, D. Pavicic, H. C. Bandulet, H. Pépin, J. C. Kieffer, R. Dörner, D. M. Villeneuve, P. B. Corkum: **Laser-Induced Electron Tunneling and Diffraction**. Science 320, 1478 (2008).

6. A. Staudte, C. Ruiz, M. Schöffler, S. Schössler, D. Zeidler, Th. Weber, **M. Meckel**, D. M. Villeneuve, P. B. Corkum, A. Becker, and R. Dörner: **Binary and Recoil Collisions in Strong Field Double Ionization of Helium**. Phys. Rev. Lett. 99, 263002 (2007).

7. A. Staudte, D. Pavicic, S. Chelkowski, D. Zeidler, **M. Meckel**, H. Niikura, M. Schöffler, S. Schössler, B. Ulrich, P. P. Rajeev, Th. Weber, T. Jahnke, D. M. Villeneuve, A. D. Bandrauk, C. L. Cocke, P. B. Corkum, R. Dörner: **Attosecond Strobing of Two-Surface Population Dynamics in Dissociating H$_2$$^+$**. Phys. Rev. Lett. 98, 073003 (2007).

8. M. Weckenbrock, D. Zeidler, A. Staudte, Th. Weber, M. Schöffler, **M. Meckel**, S. Kammer, M. Smolarski, O. Jagutzki, V. R. Bhardwaj, D. M. Rayner, D. M. Villeneuve, P. B. Corkum and R. Dörner: **Fully Differential Rates for Femtosecond Multiphoton Double Ionization of Neon**. Phys. Rev. Lett. 92, 213002 (2004).

9. D. Zeidler, M. Weckenbrock, A. Staudte, Th. Weber, M. Schöffler, **M. Meckel**, S. Kammer, M. Smolarski, O. Jagutzki, V.R. Bhardwaj, D. M. Rayner, D. M. Villeneuve, P. B. Corkum, R. Dörner: **Fully differential rates for femtosecond multiphoton double ionization of neon**. Proc. SPIE Vol. 5579, 708 (2004).

Artikel in sonstigen Zeitschriften

1. **M. Meckel**, R. Dörner und A. Staudte: **Kurzzeitaufnahmen von Molekülen**. Physik in unserer Zeit 39, 217 (2008).